Peculiarities of acoustic energy transmission from liquid helium to metals: A Review

K. N. Zinov'eva

P. Kapitza Institute of Physical Problems, Russian Academy of Sciences, 117334 Moscow, Russia)*
(Submitted November 18, 1996)
Fiz. Nizk. Temp. **23**, 485–498 (May–June 1997)

Experimental and theoretical studies of the coefficient α of phonon energy transmission from liquid helium to cubic-symmetry metals (tungsten, copper, and aluminum single crystals and gold polycrystals) are reviewed briefly. It is shown that the transmission coefficients for single crystals with a perfect surface are correctly described by the theory of acoustic impedance mismatch model, taking into account absorption of phonons by conduction electrons. Andreev's theory of electron resonant absorption of a Rayleigh wave by the surface of single crystal with $\alpha \sim 1$ is confirmed. In a strongly anisotropic copper single crystal, a resonant pseudo-surface wave absorption peak is also observed. It is shown for aluminum that phonon dissipation decreases sharply upon a transition from the normal to superconducting state, and the height of the Rayleigh peak decreases accordingly. It is found that the main mechanism of phonon scattering in a polycrystal is the Rayleigh scattering at grain boundaries, which is proportional to ω^4 and is much stronger than scattering at electrons. The form of angular dependence of the absorption coefficient $\alpha(\theta)$ changes significantly. © *1997 American Institute of Physics.* [S1063-777X(97)00105-9]

INTRODUCTION

In this paper, the latest publications by the author and her group devoted to the problem of the Kapitza boundary thermal resistance are reviewed briefly.

Kapitza[1] discovered a temperature gradient ΔT emerging at the boundary between two media with a thermal flux though the contact and proportional to the flux density $\dot{Q}$ with the proportionality factor R_K, which is called the thermal resistance of the boundary and which changes with temperature in proportion to T^{-3}:

$$\Delta T = R_K \dot{Q}. \tag{1}$$

In order to explain this effect, Khalatnikov[2,3] proposed a theory known as the acoustic mismatch model (AMM). According to this theory, heat transfer is executed by phonons that are incident at the interface at both sides. Heat transfer is strongly suppressed due to mismatch of acoustic impedances of the media (which differ by a factor of 10^3) and the smallness of the critical angle of incidence for phonons in liquid helium, starting from which total internal reflection takes place.

The heat flux from helium to a solid can be written in the form[4]

$$\dot{Q}_{l\to s} = \frac{\hbar}{(2\pi c)^2}\int_0^\infty n\left(\frac{\hbar\omega}{T}\right)\omega^3 d\omega \int_0^{\pi/2} w \times(\omega,\theta)\cos\theta \sin\theta d\theta. \tag{2}$$

Here n is the Planck function, c the velocity of light in helium, and $w(\omega,\theta)$ is the transmission coefficient for a phonon having a frequency ω and incident from liquid helium to the interface at an angle θ. (Henceforth, instead of $w(\omega,\theta)$ we shall consider the quantity $\alpha(\omega,\theta)=w(\omega,\theta)\cos\theta$).

In thermal equilibrium, counter fluxes of phonons are equal, and the resultant thermal flux is equal to zero. If the equilibrium is disturbed, the emerging resultant heat flux is given by

$$W = \frac{4\pi^5}{15}\frac{\rho c}{D}\frac{T^4}{(2\pi\hbar c_t)^3}F(\eta), \tag{3}$$

where ρ and D are the densities of liquid helium and the solid, respectively, c_l and c_t are the velocities of longitudinal and transverse waves in the solid, $\eta = c_l/c_t$, and $F(\eta)\approx 1$ is the function of elastic constants for the solid. In the case of small ΔT, we obtain

$$\Delta W = \frac{16\pi^5}{15}\frac{\rho c}{D}\frac{T^3\Delta T}{(2\pi\hbar c_t)^3}F(\eta), \tag{4}$$

$$R_K = \frac{15}{16\pi^5}\frac{DT^{-3}}{\rho c}(2\pi\hbar c_t)^3 F^{-1}(\eta). \tag{5}$$

In the notation used by Khalatnikov, we have

$$F = \frac{1}{2}\frac{D}{\rho}\left(\frac{c_t}{c}\right)\int_0^{\pi/2} w(\theta)\cos\theta \sin\theta d\theta = F_1(\eta)+F_2(\eta), \tag{6}$$

where $F_1(\eta)$ determines the contribution from volume waves (longitudinal and transverse) to the energy flux, and $F_2(\eta)$ is the contribution from surface waves. Khalatnikov calculated the value of F_2 under the assumption that the energy of a Rayleigh wave is absorbed by the solid completely, and $F_1 \approx F_2$.

It has been established reliably (see reviews in Refs. 5,6) that Khalatnikov's acoustic theory is valid for the interface between liquid helium and a perfect crystal with an ideal surface. The theory correctly describes the experimental data for $T<0.3-0.4$ K. Above this temperature, a large set of values of the Kapitza resistance differing from the values calculated at $T=1$ K by more than two orders of magnitude is observed. This can be explained by the fact that, in the case of thermal contact between real media, there exist energy-exchange channels associated with phonon dissipation and disregarded in the theory, such as the scattering of phonons at conduction electrons in metals, scattering at grain boundaries in polycrystals, scattering in the surface layer at roughnesses, at impurities, at crystal lattice defects and at the edges of the crystal. Energy dissipation due to scattering changes the acoustic transmission coefficient $\alpha(\theta)$, and hence the Kapitza resistance.

This was noted for the first time by Andreev[7,8] who proved that scattering of phonons at conduction electrons in metals leads to resonant absorption of the surface way for the supercritical Rayleigh angle θ_R with the energy transmission coefficient $\alpha\sim 1$ for a resonant peak width of the order of an angular minute. The contribution of Rayleigh waves to the heat flux is approximately equal to the contribution from volume waves. Later, some authors[9,10] obtained a similar pattern for transmission of acoustic phonons by introducing absorption of sound in the bulk of the solid into the phenomenological theory of acoustic mismatching. The energy of a Rayleigh wave is localized near the surface of the solid in a layer of thickness 2λ; in the case of dissipation, this energy is transferred to the bulk either by phonons or by conduction electrons. In the absence of dissipation, the energy stored in the solid is emitted to liquid helium.

The phenomenological theory, taking into account phonon dissipation in a solid, is known as the dissipative theory of acoustic mismatching. The results of this theory were used in our investigations.

This review contains the results of theoretical and experimental studies of the coefficient α of phonon transmission from liquid ^{4}He to metals with cubic symmetry (tungsten, copper and aluminum single crystals and gold polycrystals).

Before describing the results, let us consider briefly the methods of calculations and experimental technique.

2. CALCULATION OF TRANSMISSION COEFFICIENTS

Since $\alpha(\omega,\theta)$ determines the value of heat flux through the interface between ^{4}He and a solid (and hence the Kapitza resistance), it is important to compare the experimental values of transmission coefficient obtained by us with the theoretical values. Analytical formulas derived in Refs. 2–4 and 7–10 describe the interface between ^{4}He and an isotropic solid whose parameters are usually unknown. For this reason, we made measurements on crystals. However, crystals are acoustically anisotropic. In the general case of the helium–crystal interface, the transmission coefficient for a monochromatic plane wave depends on the plane along which the crystal is cut, the polar angle θ of incidence, and the direction φ of wave propagation.[11] In contrast to an isotropic medium, a solution of the wave equation for such an interface does not exists. Nevertheless, the problem can be solved numerically on a computer.

In our publications, we used the following general algorithm of calculating $\alpha(\omega,\theta,\varphi)$:

(1) the wave equation of an infinite anisotropic medium was written and solved;
(2) the boundary conditions for a plane boundary of the semi-infinite anisotropic medium were written;
(3) on the basis of the obtained solutions, a system of linear equations satisfying the boundary conditions was written.

Let us consider the main stages of calculations based on such an algorithm.

1. For an elastically deformed anisotropic medium (crystal), the dependence of the stress tensor σ_{ij} on the strain tensor u_{kl} has the form[12]

$$\sigma_{ij}=\lambda_{ijkl}u_{kl}, \tag{7}$$

where λ_{ijkl} is the tensor of elastic moduli. Crystals belonging to the cubic symmetry group have only three nonzero independent moduli of elasticity: λ_{1111}, λ_{1122}, and λ_{1212}. The anisotropy coefficient is defined as

$$\eta=\frac{2\lambda_{1212}}{\lambda_{1111}-\lambda_{1122}}. \tag{8}$$

We assume that an elastic monochromatic wave with frequency ω, wave vector $\mathbf{k}$, and polarization X_j ($u_j = X_j \exp[i(k_i x_i - \omega t)]$ propagates in an infinite medium with density D and elastic moduli λ_{ijkl}. The wave equation has the form

$$(k_i k_l \lambda_{ijkl} - D\omega^2 \delta_{jk}) X_k = 0. \tag{9}$$

This equation establishes the relation between ω,$\mathbf{k}$, and X_k. Since the right-hand side of Eq. (9) is equal to zero, nontrivial solutions X_k exist only when the determinant is equal to zero:

$$\det(k_i k_l \lambda_{ijkl} - D\omega^2 \delta_{jk}) = 0. \tag{10}$$

This equation can be regarded as a sixth-degree equation in the wave vector modulus $|\mathbf{k}|$ for a fixed frequency ω with the parameter $\mathbf{n}=\mathbf{k}/|\mathbf{k}|$ corresponding to the direction of propagation of the wave in the crystal. The equation has three pairs of roots $|\mathbf{k}|^{(m)}(\omega,\mathbf{n})$ corresponding to the one quasi-longitudinal and two quasi-transverse modes. Generally speaking, three different phase velocities of elastic waves correspond to an arbitrary direction $\mathbf{n}$ in the crystal.

2. Let us consider an anisotropic medium with a plane boundary. We direct the z-axis at right angles to the boundary (liquid helium is over the medium in the positive half-space) and the x-axis to the sagittal plane. In this case,

$$k_x c = \omega \sin\theta, \quad k_y = 0, \quad k_z c = \omega \cos\theta, \tag{11}$$

where θ is the angle of incidence of sound and c the velocity of sound in helium.

The boundary conditions at the interface are reduced to the conservation of the tangential component of wave vector (Snell's law) and of the phonon frequency, as well as to the continuity equation.

For a wave incident on the interface from the side of liquid helium, we have

$$k_x = k_x^{\mathrm{He}}, \quad k_y = k_y^{\mathrm{He}}, \quad \omega = \omega^{\mathrm{He}}. \tag{12}$$

In this case, the z-component of the wave vector of the reflected wave is equal to the z-component of the incident wave and has the opposite sign:

$$k_{z\mathrm{refl}}^{\mathrm{He}} = -k_z^{\mathrm{He}}, \tag{13}$$

while the z-component of waves transmitted through the crystal are determined from Eq. (10) which is regarded as a sixth-degree polynomial in k_z. From the six roots of Eq. (10), we choose three roots having a physical meaning: if a root is real-valued, the group velocity must be directed to the bulk of the metal (must be positive), but if the root is imaginary, the wave must attenuate during its propagation to the bulk of the metal (the imaginary component is negative).

The continuity equation is reduced to the equality of the normal displacement and stress on both sides of the interface and to the absence of tangential stress σ.

3. These conditions lead to a system of linear equations from which the amplitude of the reflected wave can be calculated. The ratio of the amplitude of the reflected wave to the amplitude of the incident wave gives the reflection coefficient for amplitude, while the square of its modulus gives the energy reflection coefficient α_{refl}. In this case, the transmission coefficient $\alpha(\theta,\varphi) = 1 - \alpha_{\mathrm{refl}}$. We assume that absorption of sound in liquid helium is equal to zero. The absorption in the solid was taken into account by introducing a small imaginary component to the elastic tensor of the medium λ_{ijkl} in the wave equation (9), namely, by multiplying the initial tensor λ_{ijkl} by the constant $(1+2pi)$. The dimensionless absorption parameter p can be expressed in terms of the coefficients $\gamma_{l,t}$ of bulk absorption of acoustic energy:

$$p_{l,t} = \gamma_{l,t} c_{l,t}/2\omega = \frac{\lambda_{l,t}}{4\pi l_{l,t}}, \tag{14}$$

where $\gamma_{l,t} = (1/x)\ln J_0/J$, $\lambda_{l,t}$ is the acoustic wave length and $l_{l,t}$ the characteristic length for energy absorption (the distance over which the intensity J decreases by a factor of e).

The algorithm described above was used to develop a program for calculating angular dependences of energy transmission for a plane monochromatic acoustic wave at the interface between liquid helium and various single crystals of cubic symmetry. By way of an example, Fig. 1 shows the results of calculations for tungsten, copper, aluminum, and gold crystals cut in the (001) plane for an azimuthal angle of wave propagation $\varphi = 0°$.

The coefficient $\alpha(\theta)$ vanishes for the angles $\theta_1 = \arcsin(c/c_l)$ and $\theta_2 = \arcsin(c/c_t)$, and the Rayleigh peak corresponds to the angle $\theta_R = \arcsin(c/c_R)$, where c_R is the velocity of a Rayleigh wave at the free surface of the metal.

The results of calculations presented in Fig. 1 are obtained for the absorption parameter $p = 6\cdot 10^{-4}$, and $\alpha \approx 1$ for $\theta = \theta_R$. Elastic constants for aluminum, copper, and gold at low temperatures were taken from the handbook[13] and for tungsten from Ref. 14 (at room temperature).

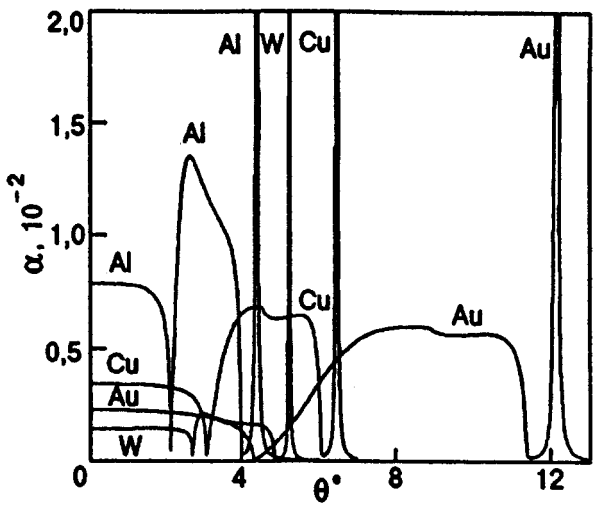

FIG. 1. Energy transmission coefficient for a plane acoustic wave propagating from liquid ^{4}He to tungsten, gold, copper and aluminum single crystals. The cut is made along the plane (001), the azimuthal angle of propagation $\varphi = 0°$, and $\alpha(\theta_R) \simeq 1$ (the absorption parameter $p = 6\cdot 10^{-4}$).

3. MEASURING TECHNIQUE

The method of measurements of angular spectra of the energy transmission coefficient for a plane monochromatic acoustic waves propagating from liquid ^{4}He to metals is described in detail in Refs. 15 and 16.

The measurements were made on a ^{3}He–^{4}He dilution refrigerator with a minimum temperature ~ 25 mK, in which the measuring chamber filled with ^{4}He and containing the sample and a piezoelectric quartz emitter was cooled.

The setup was mounted in a screened room. At a stabilized liquid helium temperature (with a stabilization level up to 1 μK), the overheating of the samples by phonons incident from ^{4}He on the crystal surface at various angles was measured with the help of sensitive semiconducting thermometers fixed to the sample with a conducting adhesive at the shadow side. The dependences of sample overheating ΔT on the angle of incidence θ were recorded at fixed frequencies. The recording time varied from 30 min to 1.5 h.

The method allowed us to measure small energy transmission coefficients ~ 0.003–0.005 with an angular resolution up to $1'$ at temperatures 60–400 mK under saturated vapor pressures at frequencies 10–300 MHz for the signal-to-noise ratio of the order of 100 with a high reproducibility.

The sample overheating ΔT is connected with the acoustic energy transmitted through the sample through the following relation:

$$\Delta T = \frac{S_{\mathrm{exp}}}{S_{\mathrm{sample}}} R_K \alpha(\omega,\theta)\dot{Q}, \tag{15}$$

where $\dot{Q}$ is the energy density of the acoustic flux incident at the angle θ to the surface, $\alpha(\omega,\theta)$ is the energy transmission coefficient, S_{exp} the area of the sample surface on which the

sound is incident, S_{sample} the total surface of the sample, and R_K the Kapitza boundary resistance. Relation (15) leads to

$$\alpha(\omega,\theta)=\frac{\Delta T}{R_K\dot{Q}}\frac{S_{\text{sample}}}{S_{\text{exp}}}. \tag{16}$$

In our experiments, we determined only the relative value of $\alpha(\omega,\theta)$. The absolute value of transmission coefficient can be obtained either by measuring all the parameters appearing in (16), or by comparing the experimental value of $\alpha(\omega,\theta)$ with the theoretical dependence.

While developing the method of measurements, we found that the following factors are most significant:

(1) helium temperature stabilization in the interval $3\cdot10^{-5}$–10^{-6} K;
(2) measurement of the angle θ with an error smaller than $1'$;
(3) simultaneous measurement of the temperature of helium and the crystal with sensitive semiconducting thermometers whose signals were supplied to low-temperature ac bridges and were recorded from the output of the instruments in the real time by a computer.

4. DISCUSSION OF RESULTS

4.1. Tungsten Single Crystal

Among metals with cubic symmetry, tungsten is the most isotropic crystal in the acoustic sense (the anisotropy coefficient $\eta=0.995$). The absence of anisotropy simplifies an analysis of theoretical dependences considerably.

The high-purity tungsten single crystal ($R_{300}/R_{4.2}=64000$) had the shape of a circular disk of diameter 8.6 mm and thickness 1.5 mm. The normal to the electrolytically polished face surface of the disk formed the angles 23° and 30° with the axes [100] and [101], respectively. The roughnesses and deviations from the plane were within 0.3 μm.

Measurements were made at frequencies 10 and 30 MHz in the temperature interval 60 mK–0.4 K.[15–18,31] The angle of incidence θ of a plane acoustic wave on the sample varied from $-20°$ to $+20°$.

The characteristic curves for 30 MHz are presented in Fig. 2a. Here, the sample overheating ΔT (in mK) relative to liquid helium is plotted along the ordinate axis to the left, while the acoustic energy transmission coefficient $\alpha(\theta)=w(\theta)\cos\theta$ is plotted along the ordinate axis to the right. (For the angle of incidence 6°, the difference between α and w amounts to less than 0.5%.) The magnitude of the angle $\alpha(\theta)$ was calculated from the value of ΔT after normalization at zero angle at which, according to the acoustic theory, the value of α was assumed to be

$$\alpha(0)=\frac{4\rho c D_{cl}}{(\rho c+Dc_l)^2}\approx\frac{4\rho c}{Dc_l}=1.4\cdot10^{-3}. \tag{17}$$

It can be seen from Fig. 2a that sound passes from helium to tungsten only in a narrow angular interval close to the normal incidence. For $\theta\simeq\pm6°$, sharp peaks of sample overheating are observed.

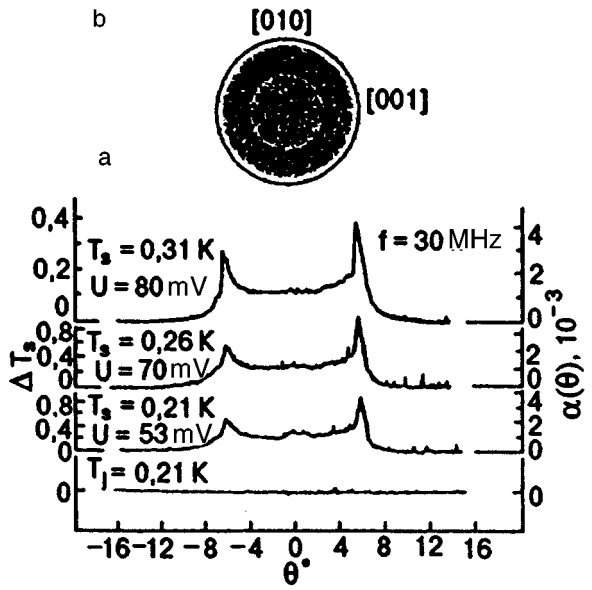

FIG. 2. (a)Experimental recording of the angular dependence of acoustic energy transmission coefficient $\alpha(\theta)$ (right scale) in tungsten single crystal for $f=30$ MHz and three different temperatures; the left scale corresponds to sample overheating ΔT by sound. The lower curve is recorded temperature of liquid helium and U is the voltage applied to quartz. (b) Two-dimensional theoretical spectrum of $\alpha(\theta,\varphi)$ for the interface between ^{4}He and tungsten in the angle of incidence θ in the sagittal plane vs. the radius r; φ is the azimuthal angle between the axis [001] and the sagittal plane.

Since the peaks are formed symmetrically relative to the normal for both frequencies under investigation and at different temperatures, and lie in the angular interval corresponding to total internal reflection, their formation can be associated with an increase in energy transmission due to absorption of the Rayleigh surface wave excited resonantly by the incident acoustic wave, i.e., the effect predicted by Andreev.

The following two peculiarities of experimental curves are worth noting. The first is that the peaks formed at $-\theta_R$ and $+\theta_R$ have different heights, which is apparently associated with the nonuniformity of radiation emitted by quartz.

The second peculiarity is the presence of small peaks at $\theta=0°$ formed at the lowest temperatures. The peaks are due to an increase in energy incident at the interface due to multiple reflection of the plane wave between the quartz emitter and the sample.

These peculiarities were subsequently observed for other samples (copper and aluminum) also. The peaks at $\theta=0°$ were studied by us in detail for a copper single crystal.

Let us compare the experimental results obtained for $\alpha(\theta)$ in tungsten with the theoretical dependence presented in Fig. 1. The spectrum in the figure correctly describes the observed $\alpha(\theta)$ dependence. However, the critical angles for longitudinal and transverse waves could not be observed, apparently, in view of imperfection of the plane wave emitted by quartz.

Figure 2b shows a two-dimensional theoretical spectrum of $\alpha(\theta,\varphi)$ for the interface between liquid ^{4}He and tungsten. The intensity of gray color corresponds to the value of α

(white background corresponds to $\alpha=0$, while black regions correspond to $\alpha=0.005$).

An attempt to choose the theoretical peaks corresponding to the experimental Rayleigh peaks (Fig. 2a) both in height and width proved futile mainly due to the fact that theoretical peaks have extended tails making a contribution to the integral of transmitted energy up to 30% beyond the critical angle. Such contributions are not observed in experiments.

It should be borne in mind that the theoretical analysis was carried out under the assumptions that the plane interface is infinitely large and the plane wave is perfect, which, strictly speaking, do not correspond to our experimental conditions. In actual practice, the sample has a size of the order of the characteristic length l for 30 MHz, and according to calculations, diffraction broadening λ/D of acoustic beam in helium was 6 and $2'$ for 10 and 30 MHz, respectively.

The minimum width of the experimental Rayleigh peak for 30 MHz was $25'$. The reason behind additional peak broadening beyond the diffraction broadening could be the imperfection of the emitter as well as wavy roughness of the electrochemically polished sample surface.

In spite of a considerable (by an order of magnitude) broadening of the acoustic beam as compared to diffraction broadening, we can compare the experimental results with the dissipative acoustic theory by using the invariability of the integral of transmitted energy and estimate the absorption parameter p (and γ) corresponding to the given sample.

An estimate of the integral $\int_0^{2\theta_R}\alpha(\theta)d\theta$ for experimental and theoretical values of $\alpha(\theta)$ was obtained for 10 and 30 MHz at different temperatures. The experimental curves were preliminarily normalized at $\theta=0°$.

The absorption parameters determined in this way vary from $(1.0–1.25)\cdot10^{-4}$ for 10 MHz to $(2–6)\cdot10^{-4}$ for 30 MHz, which is in satisfactory agreement with the measured value for the bulk acoustic absorption coefficient ($p=3\cdot10^{-4}$).[19] The integral of the total energy for experimental values is twice as large as the energy integral up to the critical angle, which is in accord with calculations made by Khalatnikov and Andreev.

4.2. Copper Single Crystal

Experiments[18,20,21] were made on a copper single crystal whose properties can be described correctly by the free electron theory.

The sample of diameter 10 mm and thickness 1.4 mm was cut from a single crystal by the electric-spark method so that the surface under investigation coincided with the basal plane (001). The sample was polished mechanically by diamond paste and then etched electrochemically. The removed layer of copper of thickness 10 μm was several times larger than the grain size of the coarsest diamond paste. It can be assumed that the obtained surface contained no mechanical stresses.

Investigations on a Linnik interference microscope proved that the main part of the surface is smooth to within 100 nm; scratches of depth up to 200–500 nm were present, their density being approximately 1 scratch/mm. Thus, scattering at defects for ultrasonic waves of length up to 1 μm corresponding to frequency 500 MHz was weak.

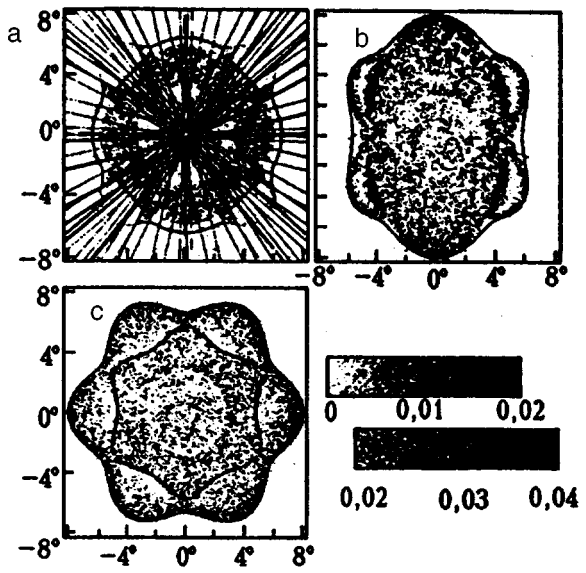

FIG. 3. The result of theoretical calculation of acoustic energy transmission through the interface between liquid ^{4}He and a copper single crystal cut along the planes (001) (a), (011) (b), and (111) (c). The two components of the angle of incidence of sound at the interface are plotted along the coordinate axes. The calculations are made for the absorption parameter $p=5\cdot10^{-4}$. Bold lines show the direction of scanning in experiments, while fine lines show equivalent directions for a cubic crystal.

The sample surface was smooth to within 10 μm over a length of 100 mm.

Copper is an acoustically strongly anisotropic crystal with the anisotropy coefficient $\eta=3.2$. The form of angular absorption spectra is determined by the shape of constant-frequency surfaces of the crystal in the space of wave vectors **k**. For a strongly anisotropic crystal, constant-frequency surfaces differ from the spherical surface both for the longitudinal and for two transverse modes. The constant-frequency surface for the slowest transverse mode is not convex, and hence a transition is made from conventional surface waves to generalized waves.[22]

Figure 3 shows the results of calculation of acoustic energy transmission through the three principal planes of the copper single crystal in the form of two-dimensional patterns. The following peculiarities of two-dimensional spectra are worth mentioning. A region of transmission of longitudinal sound is observed at the center, for angles close to the normal. As a result of anisotropy, the shape of this region differs from circular. The region of longitudinal sound is separated from the region of transverse sound by a band with zero transmission coefficient. In the region of transverse waves, the transmission coefficient is slightly larger than in the region of longitudinal waves as in the case of an isotropic medium.

Narrow black bands framing the continuous spectrum correspond to sharp peaks of resonant transmission of sound in the case of excitation of a surface Rayleigh wave.

The distinction of the spectrum of an anisotropic crystal (copper) from that of an isotropic crystal lies in the forma-

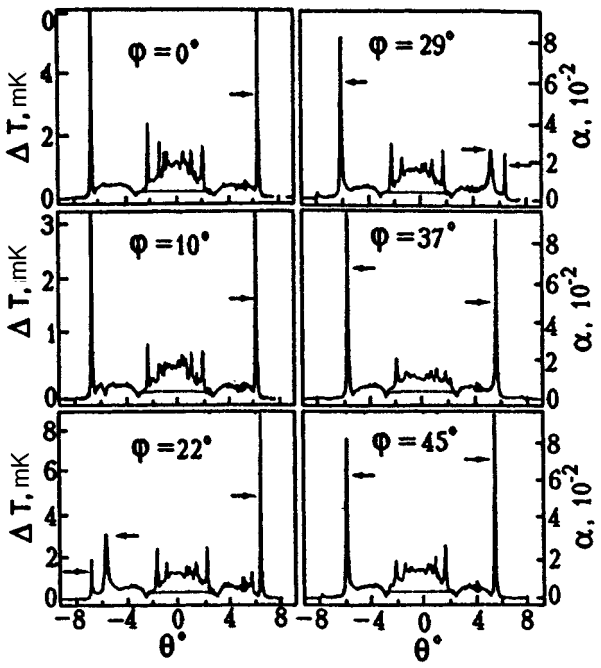

FIG. 4. (a) Experimental spectra of phonon transmission to a copper single crystal ((001) plane) along various azimuthal directions $\varphi=0$, 10, 22, 29, 37, and 45° at temperature $T=140$ mK and frequency $f=39$ MHz. Dotted lines correspond to the results of calculations. The arrows indicate the tops of experimental Rayleigh and pseudo-surface peaks.

tion of additional resonant peaks in the continuous spectral region, which correspond to pseudo-surface waves.[11] The term ''pseudo-surface waves'' is usually applied to waves which are localized at the surface incompletely, but are coupled only slightly with bulk mode.

In Fig. 3, pseudo-surface peaks in the form of narrow black bands can be seen in the (001) plane in the vicinity of the [110] direction. In the same directions, the intensity of transmission of Rayleigh waves vanishes. Pseudo-Rayleigh peaks can also be seen in the (111) plane and are absent in the (011) plane. The velocity of Rayleigh waves is smaller than the velocities of the longitudinal and two transverse modes in the crystal; for this reason, Rayleigh peaks always lie at the edges of the spectrum.

Solid curves in Fig. 4 present the results of measurements of the acoustic energy transmission coefficient in a copper single crystal for the (001) plane and azimuthal directions $\varphi=0$, 10, 22, 29, 37 and 45°. These results were obtained during measurements at temperature 140 mK and frequency 39 MHz. The dashed lines in same figures correspond to theoretical dependences $\alpha(\theta)$ calculated for a plane wave. It can be clearly seen that the experimental and theoretical dependences are in excellent agreement and repeat the finest details everywhere except the central region of angles $\pm 2°$. Such an agreement was reached for the first time in the present publication.

In the central region, $\alpha(\theta)$ has additional resonant peaks at $\theta_R/3, \theta_R/5, \theta_R/7$, etc. These peaks are larger in absolute value than the theoretical value $\alpha(0)=5\cdot 10^{-3}$ by a factor of 2–3. This is due to close spacing of the sample and quartz (~ 10 mm), which leads to multiple reflections of ultrasound between these two surfaces.

As a result of multiple reflections, the spectrum of transmission coefficient for angles θ_R/n (n is an odd number) acquires additional resonant peaks associated with excitation of surface Rayleigh waves; as a result, the transmission energy increases in the region $\pm 2°$. This is confirmed by calculations.[21] Thus, the theoretical and experimental values of α in a specific geometry coincide in the central region also.

The pattern asymmetry relative to $\theta=0°$, which is noticeable in Fig. 4, is due to the fact that the scanning in the given directions is carried out not exactly through the center ($\theta=0°$). The deviations measured for six azimuthal angles lie within $20-40'$. As a result, the pattern to the left and right of $\theta=0°$ corresponds to slightly different azimuthal angles, which was taken into account in the calculation of theoretical dependences.

An analysis of the experimental curves in Fig. 4 shows that the overheating of the single copper crystal by sound is observed only in the range of allowed angles $|\theta|<7°$ as in the case of tungsten. In contrast to tungsten, (1) a sharper interface exists for the critical cone of energy transmission in copper, and (2) the resonant peaks for surface waves are much sharper and higher. The maximum Rayleigh peak had the amplitude $\alpha\approx 0.1$ (see Fig. 4a). The observation of such sharp and high peaks confirms the predictions of Andreev's theory.[7]

Along with purely surface Rayleigh peaks, Fig. 4 also shows pseudo-surface peaks. Excellent agreement with the theory should be noted as regards the angles θ for which resonant peaks are excited as well as the shape of these peaks (height and width). The suppression of Rayleigh peaks can be clearly seen as we approach $\varphi=45°$ ([110] direction). In the directions $\varphi=37$ and 45°, resolved peaks have amplitudes amounting only to 1/100 of the maximum amplitude.

It should be noted that in the region of continuous spectrum ($|\theta|<6°$), minima separating longitudinal ($|\theta|<3°$) and transverse ($3°<|\theta|<6°$) modes were observed for the first time. A minimum between transverse and Rayleigh waves was also observed (the critical angle was 6–6.5°). In the absence of damping ($p\approx 0$), the transmission coefficient $\alpha=0$ at the minima θ_1 and θ_2, i.e., total internal reflection of longitudinal and transverse waves takes place. This is an additional evidence in favor of the validity of the acoustic theory for the description of heat-transfer processes.

The temperature and frequency dependences are illustrated in Fig. 5. The spectra are repeated exactly both for temperature and for frequency. The attenuation of the signal upon an increase in temperature is due to absorption of ultrasound in helium, which is proportional to ωT^4, while the attenuation with increasing frequency is due to the deterioration of the emitter quality for small wave lengths.

The theoretical dependence of the transmitted energy integral $I=\int \alpha(\theta)d\theta$ on the azimuthal angle $\varphi°$ on the (001) surface for various values of the absorption parameter p is shown in Fig. 6. For purely surface Rayleigh waves (left curves), the integral transmission decreases abruptly in the region $\varphi\approx 30°$, vanishing for the direction $\varphi=45°$. As we

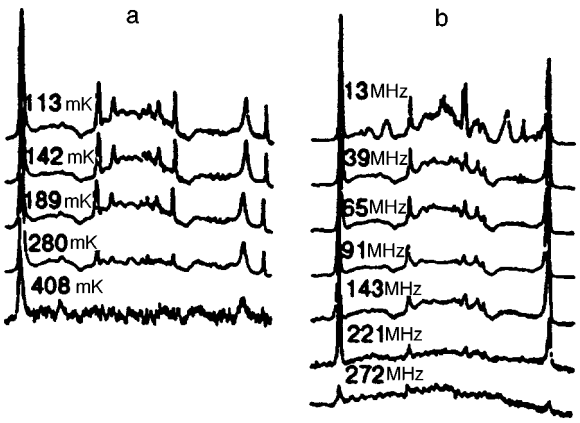

FIG. 5. (a) Experimental spectra of transmission of ultrasound to a copper single crystal ((001) plane): in the direction $\varphi = 29°$ at a frequency 39 MHz at various temperatures (a) and $\varphi = 37°$ at $T = 140$ mK for various frequencies (b).

approach $\varphi = 45°$, the Rayleigh peak becomes infinitely narrow (for $\alpha \sim 1$), the magnitude of integral transmission I_R decreasing simultaneously with decreasing peak width. Since the transverse component k_z of the wave vector is real-valued in this case, there is no localization, the wave penetrates the crystal to a large depth and becomes purely volume wave for $\varphi = 45°$.

The integral transmission of a pseudo-surface wave (right curves in Fig. 6) in the directions $\varphi = 30–42°$ does not depend on absorption since the radiation emission into the solid in this angular interval exceeds the radiation emission into the liquid. In the angular range 42–45°, I is a function of dissipation if its magnitude is smaller than the radiation emission into the liquid, but larger than the radiation emission into the crystal.

4.3. Aluminum Single Crystal

Aluminum is an acoustically weakly anisotropic crystal with the absorption coefficient $\eta = 1.22$.

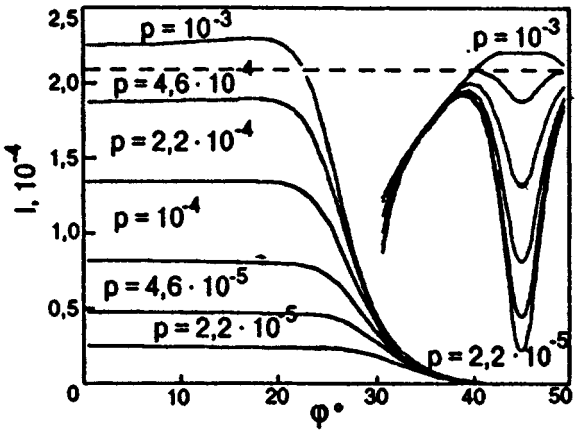

FIG. 6. Dependence of the integral energy transmission $I = \int \alpha(\theta) d\theta$ on the azimuthal angle φ on the (001) surface for various values of the absorption parameter p. The integral for a purely surface wave is shown on the left and for a pseudo-surface wave on the right. The dashed line shows average integral transmission for volume waves (longitudinal and transverse).

The aluminum single crystal was grown from a high-purity metal melt ($R_{300}/R_{4.2} = 40\,000$). The sample had the shape of a disk of diameter 18 mm and thickness 2 mm, whose free surface was close to the basal plane (001) of the crystal. The [100] axis was on the free surface, and the (010) plane formed an angle approximately equal to 2° with the normal to the surface.

As usual, the sample was first mechanically polished on a buffing machine (the grain size in the polishing paste was approximately 1 μm). Then the sample was subjected to electrochemical polishing as a result of which a layer of thickness 15 μm was removed. After such a treatment, the sample acquired the mirror surface without scratches and with a surface defect size smaller than 0.1 μm.

Since the effect of anisotropy was studied in detail earlier for the copper single crystal, and anisotropy of aluminum is small, the transmission coefficient for phonons through the basal plane (001) in the given sample was studied only for sound propagating along the [100] axis (the azimuthal angle $\varphi = 0°$).

We were mainly interested in analyzing of the effect of the superconducting phase transition in aluminum on the transmission coefficient.

In order to transform the sample to the normal state ($T_c = 1.19$ K, $H_c = 100$ Oe), the magnetic field $H \sim 1$ kOe $\gg H_c$ of a solenoid was applied in the direction perpendicular to the surface under investigation for $\theta = 0°$.

The transmission coefficient was measured in the temperature range 100–300 mK at frequencies varying from 13 to 91 MHz.[18,23]

The results of measurements of $\alpha(\theta)$ in the normal and superconducting states at two frequencies (39 and 65 MHz) at $T = 140$ mK and the theoretical dependences are presented in Fig. 7.

It can be clearly seen that as for the tungsten and copper single crystals investigated earlier, sound propagates in aluminum inside a narrow cone (with the angle approximately equal to $\pm 5°$). The region of continuous spectrum (angle $\pm 4.3°$) with a minimum between the longitudinal and transverse waves for the critical angle of incidence $\pm 2°$ for longitudinal waves is clearly outlined. Sharp peaks associated with resonant absorption of Rayleigh waves excited by the incident sound lie on both sides of the critical angle. It should be noted that experimental curves exactly coincide with calculated theoretical dependences.

As in the previous experiments with tungsten and copper, the region corresponding to transmission to longitudinal modes ($|\theta| < 2°$) contains additional peaks at angles θ_R/n (n is an odd number) associated with the excitation of Rayleigh waves by the sound experiencing multiple reflections between the surfaces of the sample and the quartz emitter (the separation between these objects was approximately 10 mm.

In the normal state of aluminum, the principal Rayleigh peaks for $\theta_R \approx \pm$ 4.5° attain the amplitude $\alpha \approx 0.18$ for a width approximately equal to 30′, while the absorption parameter $p = (5–8) \cdot 10^{-3}$, which coincides with the results of direct measurements.[24] The absolute values of $\alpha(\theta)$ were determined by normalization of the experimental dependence

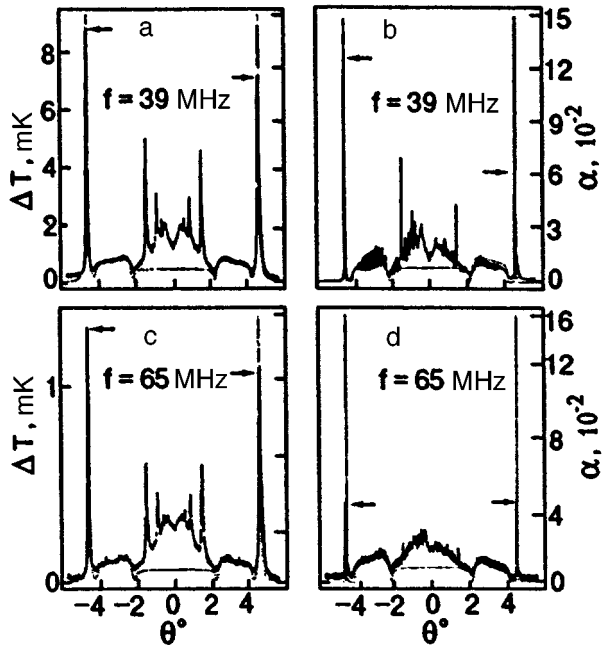

FIG. 7. Angular spectrum for the phonon transmission coefficient $\alpha(\theta)$ to aluminum for the normal (a,c) and superconducting (b,d) states at frequencies 39 and 65 MHz at $T=140$ mK. Solid curves correspond to experiments and dotted curves to the theory. The arrows indicate the tops of experimental Rayleigh peaks.

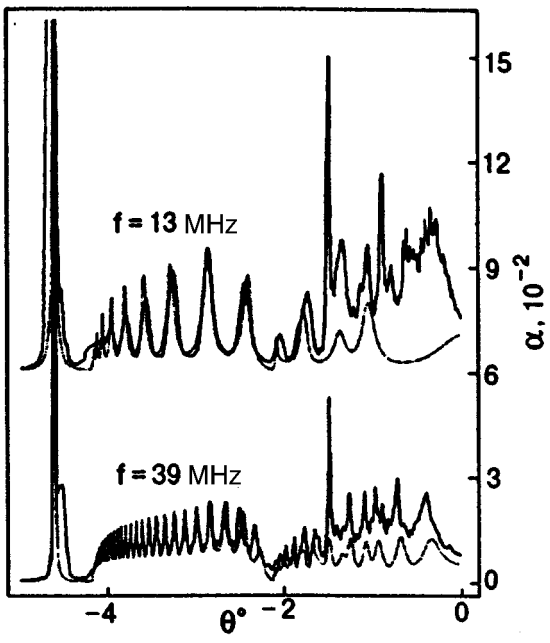

FIG. 8. Angular oscillations of the transmission coefficient $\alpha(\theta)$ for superconducting aluminum, associated with interference of waves in a finite-thickness plate, $T=195$ mK. The solid curves correspond to experiments, and dotted curves to the theory. (For both frequencies, $\alpha=0$ on the left of the Rayleigh peak.)

to the theoretical dependence in the region of transmission to the transverse mode (which does not contain distortions associated with secondary Rayleigh peaks), and the absorption parameter p was determined from a comparison of the normalized experimental curve with the theoretical one.

Thus, experiments with aluminum confirm the validity of Andreev's theory once again. The experimental angular spectra for aluminum in the superconducting state (see Figs. 7b and 7d) differ considerably from the $\alpha(\theta)$ spectra in the normal state. The Rayleigh peaks become much narrower (their width amounts approximately to $5'$), and their height exceeds that in the continuous spectrum region only slightly (for high frequencies).

The absorption parameter p for the superconducting state is smaller by a factor of 60–70 than for the normal state, and the contribution of Rayleigh peaks to the thermal flux is virtually equal to zero.

Besides, in the superconducting state, angular oscillations of the quantity $\alpha(\theta)$ (''crest'') are observed in the region of continuous spectrum (see Fig. 8), the oscillation frequency increasing in proportion to the frequency of sound. The oscillations of $\alpha(\theta)$ emerge due to the finite width of the plate. The sound transmitted in the plate and reflected multiply between its parallel plates interferes in the metal (in analogy with the Fabry–Perot interferometer). The calculated interference pattern for both frequencies (dotted curve in Fig. 8) coincides to a considerable extent with the experimental curve. In the normal state, no oscillations are observed in view of much stronger absorption of sound in the metal.

Thus, it has been proved experimentally that the absorption of a Rayleigh wave by conduction electrons in the normal state is the dominating dissipation mechanism. In the superconducting state, absorption decrease abruptly and is associated with different scattering mechanisms (mainly, with the scattering at the sample edges, periodic nonuniformities and roughnesses). In this case, the absorption parameter can be a function of the frequency of incident sound, which was actually observed in experiments at low frequencies.

The abrupt decrease in absorption during the transition to the superconducting state leads to an increase in the Kapitza resistance (approximately two-fold).

A comparison of experimental angular spectra $\alpha(\theta)$ for the three metals investigated by us (tungsten, copper, and aluminum) shows that the transmission coefficients for ideal monocrystalline samples with a perfect surface are close and are correctly described by the dissipative acoustic theory. The values of $p \approx 3\cdot 10^{-4}$–$5\cdot 10^{-3}$ obtained for tungsten, copper, and aluminum coincide with the results of direct measurements on sound absorption. It should be noted that Andreev's theory gives narrower resonant peaks for $\alpha \simeq 1$ (of width 4–30″) corresponding to smaller parameters p.

4.4. Gold Polycrystal

The analysis of single crystals with perfect surfaces, which confirmed the validity of the dissipative acoustic theory, provoked the natural question as to what will be the transmission coefficients $\alpha(\omega,\theta)$ for acoustic energy in polycrystals?

Remarkably, the acoustic properties of the interface between ^{4}He and a polycrystal have not been investigated until recently in spite of the fact that most of measurements of Kapitza resistance were made on polycrystalline samples.

We investigated the helium–polycrystal interface for high-purity polycrystalline gold ($R_{300}/R_{4.2}=36\,000$) prepared from melt.[25] The sample was in the shape of a parallelepiped of the size $13\times10\times1.9$ mm. In the process of manufacturing, the sample was rolled through rollers, levelled under a press with polished quartz plates, and then annealed in vacuum. The quality of the surface was controlled by a Linnik interference microscope; the size of roughnesses and deviations from the plane did not exceed 0.5 μm.

According to rings on the Laue diffraction patterns recorded from two different points of the sample (the lines are continuous and have the same thickness), we could estimate the average size of crystallites: $\overline{a}\leqslant10$ μm. In addition, after the experiments the surface was subjected to fine mechanical polishing and etching and was investigated under a microscope with a large magnification. A typical size of grains formed as a result of recrystallization and annealing was 5–10 μm. Each crystallite was a single crystal with strongly anisotropic acoustic properties. The anisotropy coefficient for gold is $\eta=2.85$. Figure 1 shows the $\alpha(\theta)$ spectrum for a gold single crystal in the direction $\varphi=0°$. It is assumed that crystallites in a polycrystal are oriented at random, as a result of which the acoustic properties of the polycrystal become isotropic.

The polycrystalline gold sample described above was studied by us twice.[15,25] The first experiments[15] did not lead to positive results. Only subsequent measurements[25] in the same sample, using a more perfect measuring technique, made it possible to obtain a stable pattern of angular dependence $\alpha(\omega,\theta)$ for a plane monochromatic wave for three frequencies in the range 13–65 MHz.

The main distinguishing feature of the spectra for transmission coefficient $\alpha(\omega,\theta)$ in a gold polycrystal was that the overheating ΔT for the gold polycrystal by sound was very small relative to ^{4}He. For the same acoustic flow rate, the overheating for the gold polycrystal was smaller than for single crystals by a factor of 10^2–10^3, which indicated a small Kapitza resistance in the polycrystalline sample. Rough estimates obtained on the basis of our experiments give $R_KT^3\sim80$ cm^{2}K^4/W, which is close to the value $R_KT^3=46$ cm^{2}K^4/W obtained by Folinsbee and Anderson[26] for a mechanically polished annealed gold foil of thickness 0.6 mm at $T\sim40$–300 K.

Figure 9 shows the experimental curves $\alpha(\theta)$ normalized (by coincidence at $\theta=0$) for frequencies 13, 39, and 65 MHz in the region of positive angles θ. For $\theta=0$, we have $\alpha_{\text{theor}}=2.13\cdot10^{-3}$.

The form of the $\alpha(\omega,\theta)$ spectra for a polycrystal differs from typical angular spectra for single crystals. For polycrystals, we do not observe sharp and high peaks of resonant absorption of a Rayleigh wave at the spectral edges, deep minima separating the regions of longitudinal and transverse surface waves, and resolved secondary Rayleigh peaks near zero angle of incidence. The spectra are asymmetric, all singularities are strongly blurred, and resonant peaks are broad and low.

Beyond the critical cone $\theta_c=12°$, the function $\alpha(\theta)$ decreases very slowly, tending to zero. The construction of the instrument did not allow us to investigate the spectra for angles of incidence $\theta>30$–$40°$.

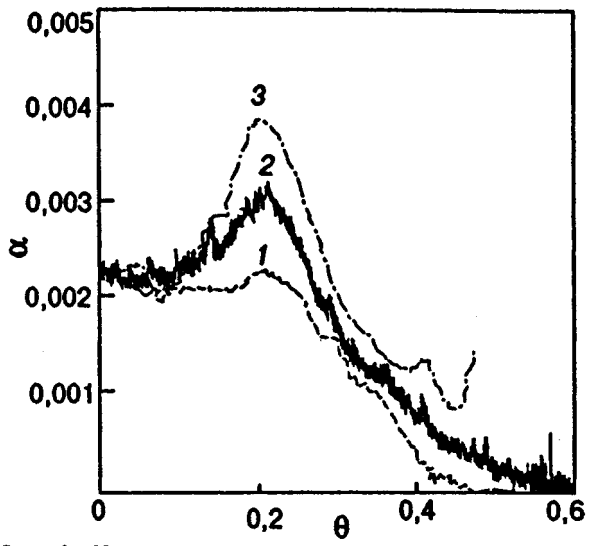

FIG. 9. Normalized experimental $\alpha(\theta)$ curves for a gold polycrystal: $f=13$ MHz, $T=150$ mK (curve *1*), $f=39$ MHz, $T=200$ mK (curve *2*), and $f=65$ MHz, $T=150$ mK (curve *3*).

The form of the $\alpha(\theta)$ spectra in Fig. 9 indicates strong absorption of sound in the gold polycrystal. The sound absorption parameters p can be determined by comparing the transmitted energy integrals $\int_0^{0.5}\alpha(\theta)d\theta$ for theoretical and experimental dependences (we assume that the integral of transmitted energy is conserved). The shape of the experimental $\alpha(\theta)$ curve can differ from that of the theoretical curve mainly due to the expansion of the interval of angles of incidence on a rough surface.

It was found that as the frequency changes from 13 to 65 MHz, the parameter p changes from $2\cdot10^{-4}$ to 0.15, i. e. strongly depends on frequency. For the frequencies 39 and 65 MHz, it is one or two orders of magnitude larger than the electron absorption parameter ($p\sim10^{-4}$).[27] The increase of the tails in the $\alpha(\theta)$ spectrum with frequency beyond the critical cone also confirms this statement.

Such a strong sound absorption in the gold polycrystal and its increase with frequency are due to scattering of sound at grain boundaries.

It was proved in the theoretical works by Lifshits and Parkhomovskii,[28] Papadakis,[29] and Kaganova and Maradudin[30] that scattering takes place at nonuniformities of the elastic medium in view of random orientation of crystallites each of which is a strongly anisotropic single crystal. At high frequencies, this absorption mechanism becomes predominant.

Papadakis[29] proved that absorption of sound depends on the average grain size $\overline{a}$: $\gamma=Vf^4S$ for low frequencies ($\lambda\gg\overline{a}$, Rayleigh scattering) and $\gamma=\overline{a}f^2\Sigma$ for high frequencies ($\lambda\ll\overline{a}$), where V and $\overline{a}$ are the average volume and diameter of a grain, and S and Σ are constant coefficients characterizing the material and varying insignificantly from sample to sample. The boundary between the two regions is determined by the condition $\lambda_b=2\pi\overline{a}$. In our case, $\lambda=90$,

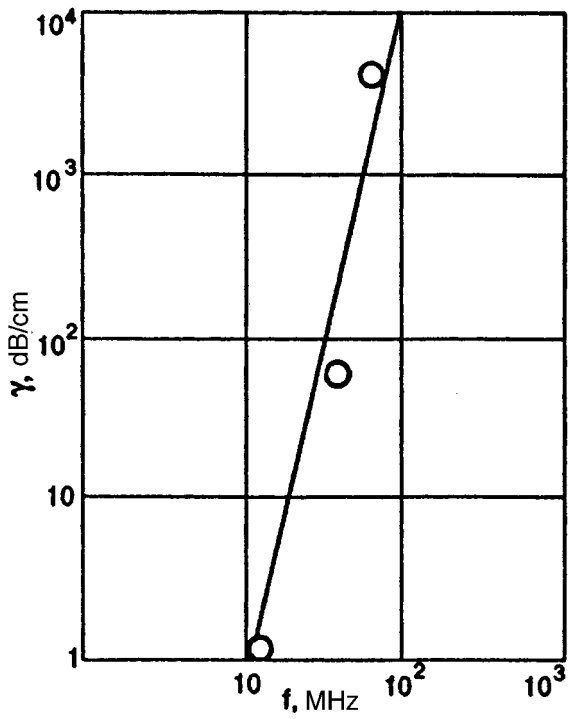

FIG. 10. Experimental values of absorption for a Rayleigh wave in a gold polycrystal ($f=13,39,65$ MHz) and the theoretical straight line $\gamma=\overline{V}f^4S$[29] for the grain size 5 μm.

30, and 18 μm, i.e., we are in the intermediate region for the grain size $\overline{a}=5$ μm.

Figure 10 shows the theoretical straight line $\gamma=\overline{Vf}^4S$ for the grain size $\overline{a}=5$ μm. The values of S are borrowed from Ref. 29. The same figure shows the points obtained from a comparison of I_{exp} and I_{theor}. The error in the evaluation of integrals is approximately 100%. The maximum error is observed in the range of parameters p from 10^{-3} to 10^{-1}, in which the integral varies only by 10%. It can be seen from the figure that satisfactory agreement is observed between the experimental values of γ and the theoretical straight lime $\gamma=\overline{Vf}^4S$.[29]

A virtually complete absorption of sound even at the frequency $f=65$ MHz explains the considerable increase in the integral contribution of phonons to the thermal flux through the boundary of the polycrystal. It increases due to the tail extending from the critical angle to $\pi/2$, which is in accord with the dissipative acoustic theory. From this point of view, the small value of the Kapitza resistance for polycrystalline gold is obvious.

The following peculiarities of the $\alpha(\theta)$ spectra of the polycrystal are worth noting.

(1) The overheating of the gold polycrystal by sound relative to liquid helium is 2–3 orders of magnitude weaker than that of single crystals, which corresponds to a large absorption parameter p and a small Kapitza resistance.
(2) The $\alpha(\theta)$ curves do not exhibit a complete angular symmetry in view of anisotropy of the polycrystal due to residual preferred orientation after rolling. Individual peaks on the $\alpha(\theta)$ curves are rather due to absorption of a Rayleigh wave by groups of crystallites with close orientation of principal axes.
(3) The height of the gently sloping Rayleigh absorption peak at θ_c increases with frequency, which is typical of spectra for which p is a function of frequency. The maximum transmission ($\alpha\approx 1$) for polycrystalline gold apparently corresponds to the frequency region $f>65$ MHz.
(4) Rayleigh peaks have a larger angular width, which can be explained not only by large values of p, but also by the blurring of the incident beam due to imperfections of the surface formed by individual grains (single crystals) oriented at different angles to the surface.

5. CONCLUSION

The main results can be formulated as follows.

(1) Resonant absorption of sound by the surface of a tungsten single crystal for a Rayleigh supercritical angle of incidence was observed and investigated for the first time at frequencies 10 and 30 MHz,[15–17,31] thus confirming Andreev's theory.[7,8] It was established experimentally that only bulk longitudinal and transverse waves with small ($\sim 10^{-3}$) and virtually constant transmission coefficients depending weakly on absorption are excited in the critical cone in an acoustically isotropic single crystal. Outside the critical cone, a sharp peak of resonant absorption of a Rayleigh wave with the width $\sim 30'$ and with $\alpha\sim 0.01$ is observed. The width and height of the peak are determined by the absorption of sound in the single crystal, which is equal to attenuation at electrons and holes in the bulk. It is shown that Rayleigh waves make approximately the same contribution to the transmitted energy flux as the bulk waves in the subcritical angular range.
(2) The coefficient of acoustic energy transmission through the (001) plane in a copper single crystal is investigated experimentally at frequencies 10–300 MHz and theoretically (by computer calculations methods using the acoustic dissipative theory) for various azimuthal directions of propagation.[18,20,21] It is shown that two resonant modes are excited on the (001) and (111) surfaces in an acoustically anisotropic single crystal: A Rayleigh surface wave and a pseudo-surface wave with $\alpha\approx 0.1$ and with peak widths $10–20'$. At the (011) surface, only a Rayleigh wave is excited. Good agreement between the experimental spectra and those calculated according to dissipative acoustic theory[4,7–10] with a phenomenological absorption parameter $p\sim 10^{-4}–10^{-3}$ was attained for the first time. The width of Rayleigh peaks was independent of temperature and virtually independent of frequency. We managed to observe for the first time two symmetric minima corresponding to critical angles for longitudinal and transverse waves. For angles of incidence close to zero, numerous peaks of lower intensity were observed; these are Rayleigh peaks associated with the incidence of ultrasound multiply reflected between the sample and the emitter.

(3) The acoustic energy transmission coefficient to an aluminum single crystal in the normal and superconducting states was investigated for the first time at frequencies up to 90 MHz.[18,23] It was shown that a Rayleigh wave indeed attenuates at conduction electrons. In the superconducting state, Rayleigh peaks become vanishingly small and make virtually zero contribution to the thermal flux, while in the normal state the height of these peaks is of the same order of magnitude as in copper. Interference effects which are absent in the normal state were observed in superconducting aluminum in which the scattering at electrons is small.

(4) Angular and frequency dependences of the energy transmission coefficient for a plane monochromatic acoustic wave propagating from liquid ^{4}He to a gold polycrystal with a crystallite size 5–10 μm were analyzed.[25] It was proved that the form of absorption spectra is determined by the strong attenuation of sound in the polycrystal due to scattering at the boundaries of strongly anisotropic and randomly oriented grains. The absorption parameter at the frequency 65 MHz ($p\sim 10^{-1}$) is 2–3 orders of magnitude higher than the parameter of absorption at conduction electrons. It was proved experimentally that the absorption of sound is proportional to ω^4, i.e., corresponds to Rayleigh scattering in an elastically nonuniform medium.

The author is sincerely grateful to A. F. Andreev, Yu. A. Kosevich, A. S. Semenov, and V. Kondrat'ev for fruitful discussions and to V. N. Krutikhin for his assistance in the preparation of experiments. Thanks are due to all authors of publications covered in this review. Special thanks are due to V. Kondrat'ev for his help in preparing the manuscript. This research was carried out under a Soros Foundation grant awarded by the American Physical Society, Grant No. N8G000 of the International Science Foundation, and Grant No. N8G300 of the International Science Foundation and Russian Foundation of Fundamental Studies.

*)E-mail: zinoveva@kapitza.ras.ru

[1] P. L. Kapitza, Zh. Éksp. Teor. Fiz. **11**, 1 (1941).
[2] I. M. Khalatnikov, Zh. Éksp. Teor. Fiz. **22**, 687 (1952).
[3] I. M. Khalatnikov, *Introduction to the Theory of Superfluidity* [in Russian], Nauka, Moscow (1965): *Theory of Superfluidity* [in Russian], Nauka, Moscow (1971).
[4] I. M. Khalatnikov and I. N. Adamenko, Zh. Éksp. Teor. Fiz. **63**, 745 (1972) [Sov. Phys. JETP **36**, 391 (1972)].
[5] E. T. Swartz and R. O. Pohl, Rev. Mod. Phys. **61**, 605 (1989).
[6] Ts. Nakayama, in: Progr. in Low Temp. Phys.**XII** (ed. by D. F. Brewer), Elsevier Science Publ., Amsterdam.
[7] A. F. Andreev, Zh. Éksp. Teor. Fiz. **43**, 358 (1962) [Sov. Phys. JETP **16**, 257 (1962)].
[8] A. F. Andreev, Zh. Éksp. Teor. Fiz. **43**, 1535 (1962) [Sov. Phys. JETP **16**, 1084 (1962)].
[9] H. Haug and K. Weiss, Phys. Lett. A **40**, 19 (1972).
[10] R. E. Peterson and A. C. Anderson, J. Low Temp. Phys. **11**, 639 (1973).
[11] G. W. Farnell, in *Acoustic Surface Waves* (ed. by A. A. Oliner), New York (1978).
[12] L. D. Landau and E. M. Lifshitz, *Theory of Elasticity*, 3rd ed. Pergamon, Oxford (1986).
[13] *Handbuch der Physik* **VIa**, p. 385, Springer Verlag, Berlin– Heidelberg–New York (1973).
[14] T. Truell, Ch. Elbaum, and B. Chick, *Ultrasonic Methods in Solid State Physics*, Academic Press, New York (1969).
[15] K. N. Zinov'eva, Zh. Éksp. Teor. Fiz. **79**, 1973 (1980) [Sov. Phys. JETP **52**, 996 (1980)].
[16] K. N. Zinov'eva, in *Low Temperature Physics* (ed. by Borovik–Romanov), Mir Publishers, Moscow (1985).
[17] K. N. Zinov'eva, Pis'ma Zh. Éksp. Teor. Fiz. **28**, 294 (1978) [JETP Lett. **28**, 269 (1978)].
[18] K. N. Zinov'eva, D. A. Narmoneva, and A. S. Semenov, in *Springer Series in Solid State Science*, **112**: *Phonon Scattering in Condensed Matter VII* (ed. by M. Meissner and R. O. Pohl), Springer Verlag, Berlin–Heidelberg (1993).
[19] C. K. Jones and Y. A. Rayne, Phys. Lett. **13**, 282 (1964).
[20] K. N. Zinov'eva, G. È. Karstens, A. V. Kashlyuk, and A. V. Semenov, Pis'ma Zh. Éksp. Teor. Phys. **51**, 332 (1990) [JETP Lett. **51**, 379 (1990)].
[21] K. N. Zinov'eva, D. A. Narmoneva, and A. V. Semenov, Zh. Éksp. Teor. Phys. **105**, 1280 (1994) [JETP **78**, 690 (1994)].
[22] A. M. Kosevich, Yu. A. Kosevich, and E. S. Syrkin, Zh. Éksp. Teor. Phys. **88**, 1089 (1985) [Sov. Phys. JETP **61**, 639 (1985)].
[23] K. N. Zinov'eva, D. A. Narmoneva, and A. V. Semenov, Pis'ma Zh. Éksp. Teor. Fiz. **59**, 118 (1994) [JETP Lett. **59**, 125 (1994)].
[24] R. David, H. R. van der Laar, and N. J. Poulis, Physica **28**, 330 (1962).
[25] K. N. Zinov'eva and I. N. Shvetsov, Zh. Éksp. Teor. Fiz. **105**, 886 (1994) [JETP **78**, 475 (1994)].
[26] J. T. Folinsbee and A. C. Anderson, J. Low Temp. Phys. **17**, 409 (1974).
[27] R. F. Mac Farlane and J. A. Rayne, Phys. Rev. **162**, 532 (1967).
[28] I. M. Lifshits and G. D. Parkhomovskiĭ, Zh. Éksp. Teor. Fiz. **20**, 175 (1950).
[29] E. Papadakis, in *Physical Acoustics. Principles and Methods* (ed. by W. Mason and R. Thurnston), Academic Press, New York (1968–1970).
[30] I. M. Kaganova and A. A. Maradudin, in *Statistical Physics, Elasticity and Dislocations Theory* (ed. by T. Jossanef and D. M. Barnete), Universitas Osloems, Oslo (1991).
[31] K. N. Zinov'eva and V. I. Sitnikova, Zh. Éksp. Teor. Fiz. **84**, 576 (1983) [Sov. Phys. JETP **57**, 332 (1983)].

Translated by R. S. Wadhwa

Superfluid ^{3}He in the zero temperature limit (Review Article)

G. R. Pickett

School of Physics and Chemistry, Lancaster University, Lancaster, LA1 4YB United Kingdom[1)]
(Submitted December 19, 1996)
Fiz. Nizk. Temp. **23**, 499–508 (May–June 1997)

In this paper we discuss some (and only a small fraction) of the interesting properties of superfluid ^{3}He at the low-temperature limit. We concentrate on the unique behavior and applications of the very dilute excitation gas at the lowest temperatures. This gas has been used for among other things, the probing of the $A-B$ phase interface, the detection of low-energy particle events and in the simulation of the creation of cosmic strings. © *1997 American Institute of Physics.* [S1063-777X(97)00205-3]

INTRODUCTION

We can think of the classes of quantum fluids as existing in a distinct hierarchy of complexity. The simplest is superfluid ^{4}He. Here the starting material of the condensate, the ^{4}He atoms are bosons. They have no spin, no charge and are spherically symmetrical, filled-shell, noble gas atoms. In the condensate they offer no labels other than their mass. Thus the superfluid component in liquid ^{4}He has a wave function which gives information only on the distribution and motion of the mass in the system. A distortion of the wave function may therefore generate a response only in terms of mass, in this case a mass superflow.

The next most complex system in our hierarchy is the superconducting electron gas in a conventional superconductor. Here the component particles, the electrons, are fermions and may only contribute to a boson condensate by coupling in Cooper pairs. Here we have the possibility of more structure since a pair may have orbital and spin angular momentum. However, in conventional superconductors at least, the Cooper pairs choose the simple solution and couple with spins opposed. The total spin is thus zero, and to maintain the correct symmetry the orbital angular momentum must be even, and also takes the value zero. The Cooper pairs in a superconductor are thus also very simple. They carry mass, and more importantly charge. Therefore, a distortion of the wave function can lead to a supercurrent (the associated mass current is unimportant in comparison). In more exotic forms of superconductivity, where the pairs may have nonzero spin, the situation could in principle be much more complex. The fact that the Cooper pairs carry a charge couples the condensate into electromagnetism, yielding all the exotic quantum-electrical properties for which the superconductors are valued. Further, on the mundane practical level, this means that we can examine superconductivity by including the superconducting element under examination in a simple electric circuit. Our measurement of the current and voltage then allows us to infer what is happening inside the superconductor. Direct observation of the superconducting behavior *in situ* is much more difficult.

The third class in our hierarchy is exemplified by superfluid ^{3}He. Here the starting particles are again fermions, the ^{3}He atoms which carry a nuclear spin. However, in this case the coupling of the pairs yields, not zero spin, but spin 1. To maintain the correct symmetry the pair angular momentum must be odd and in fact in the ground state is 1. Therefore, the Cooper pairs comprising the condensate are characterized by mass, nuclear spin and orbital angular momentum. This a) makes for a much richer structure and b) allows us to examine the very essence of the superfluidity by providing us with a window into the internal structure of the condensate itself by NMR.

THE LOW TEMPERATURE REGIME

Experimentalists working with quantum fluids generally think about the subject in terms of the two-fluid model, the interplay between the normal fluid and superfluid components being one of the characteristic features of these unique systems. However, near zero temperature we have a new regime. The normal fluid density is negligible and we are left with 'pure' superfluid. In the case of superfluid ^{3}He this turns out to be a very rewarding region since the condensate itself has such a rich structure. In fact, the behavior turns out to be increasingly interesting as the disturbing interference of the normal fluid is removed with falling temperature.

Some of the most arresting properties of the quantum fluids remain the persistent phenomena, persistent mass flow in superfluid ^{4}He and persistent currents in the superconductors. In superfluid ^{4}He the normal fluid and superfluid components are coupled together via the mechanism known as mutual friction. Since the normal fluid flow is dissipative, this coupling acts, in general, to prevent persistent flow in the superfluid. (The process is mediated by vortices which carry a circulation of 2π of wave function phase around the vortex axis. If a vortex can cross the path of the superflow, then 2π of phase is either added or removed from the phase gradient, thus mediating the decay of the flow.) To see real, persistent flow phenomena in superfluid ^{4}He, we must either restrict the discussion to low flow velocities or make experiments in very restricted geometries, which inhibit the flow of vortices. In the superconductors, on the other hand, the normal and supercurrents are almost completely decoupled and persistent currents in loops can be maintained for very long periods. Which of us has not been impressed when, as students, we learned for the first time that currents could be maintained circulating in loops for periods of many years?

The properties characteristic of, and unique to, superfluid ^{3}He at the very lowest temperatures are associated with the magnetic behavior of the nuclear spins and with the dilute gas of residual thermal excitations. Unfortunately, magnetic interactions are long range and during dynamic motion of the spin system, say after an NMR pulse, the magnetizations associated with the normal and superfluid components are very tightly coupled. Under certain circumstances these can be separated,[1] but this is the exception. The possibility of persistent magnetic phenomena is very interesting. The only straightforward means to observe such behavior is to resort to very low temperatures where the dissipative effect of the normal fluid is so weak as to be negligible on the time scale of an experiment. We cannot reach this regime yet, but we have approached close enough that persistent behavior of several minutes can be observed, giving us a tantalizing insight into what might lie in store for us at lower temperatures. At temperatures close to zero, the quasiparticle excitations above the ground state form a fascinating dilute gas. Since the excitation dispersion curve is of the ''double minimum'' BCS type, the dynamics of the particles is very unlike that of a conventional ''Newtonian'' gas where the dispersion curve is the familiar, $E = p^2/2m$, parabola. This leads to many non-intuitive properties, as we discuss below.

These two low-temperature properties of superfluid ^{3}He are those which have attracted most of our interest at Lancaster. In collaboration with Yuri Bunkov, formerly of the Kapitza Institute and currently working in Grenoble, we have been studying the magnetic properties of the condensate at the very lowest temperatures through NMR. However, what we are concerned with in this paper is the unique behavior of the extremely dilute gas of the quasiparticle excitations. This gas not only has very unusual properties in its own right, but also provides a convenient probe for studying other properties of the superfluid. In this context, we have been examining the thermal behavior of the superfluid which we believe can be used as a very sensitive particle detector. Finally, jointly with CRTBT, Grenoble, we have been exploiting the particle absorption techniques developed earlier for studying the simulation of cosmic string creation, via the Kibble mechanism, by looking at the formation of vortices after a sudden crossing of the superfluid transition.

THE EXCITATION GAS

We start by considering the properties of the very low-temperature excitation gas. This is one of the few in nature in which an entire assembly of particles with non-Newtonian dynamics is completely accessible. There are similar ensembles of excitations in condensed matter physics, but almost all are trapped in a lattice. The ^{3}He excitation gas is contained only in a superfluid condensate, which for most mechanical purposes can be treated as a vacuum, and the independent dynamics of the excitations can be studied. This is especially the case at low temperatures, where the low excitation density ensures that collisions are rare and the excitations behave entirely ballistically.

The unusual behavior of the quasiparticle excitation gas is a result of the double minimum dispersion curve, shown in Fig. 1. This curve is quite different from the Newtonian parabola in having the energy minimum not at zero momentum but at the Fermi momentum. Furthermore, this leads to two different types of excitation: quasiparticles with group velocity and momentum parallel and quasiholes with group velocity and momentum opposed. The gas has rather different properties in the two phases of superfluid ^{3}He. However, in the B-phase the excitation curve is virtually isotropic and the energy gap to the excitation energy minimum is the same in all directions. The curve in Fig. 1 holds also for the A-phase, but in this case the gap is dependent on the direction relative

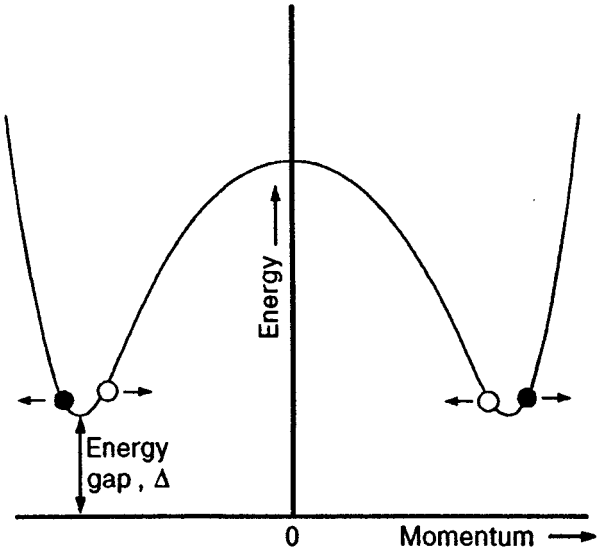

FIG. 1. The excitation dispersion curve in superfluid ^{3}He. The minimum on the curve occurs not at zero momentum, as for a conventional Newtonian object, but rather at the Fermi momentum. This means that there are two classes of excitation; quasiparticles (filled circles) with momentum and velocity in the same direction and quasiholes (open circles) with momentum and velocity in the opposite direction.

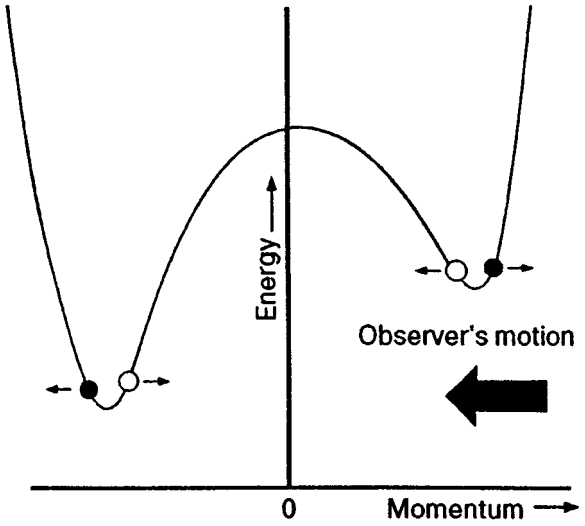

FIG. 2. When observed in a moving frame, the dispersion curve in Fig. 1 is seen to be canted. Excitations with momenta directed toward the moving observer have higher energies in this frame and those with momenta directed away have lower energies.

to the direction of the Cooper pair angular momentum, with two polar nodes of zero gap and a maximum gap around the equator.

In the B-phase the energy gap to the minimum excitation energy implies at low temperatures an excitation density dominated by the gap Boltzmann factor $\exp(-\Delta/kT)$. At the lowest accessible temperatures (about 100 μK at zero pressure) the density of excitations is vanishingly small, the number of unpaired ^{3}He atoms being of the order of 1 in 10^7. The mean free paths of the excitations are therefore very long, orders of magnitude longer than any experimental dimension. Thus we may carry out experiments with beams of excitations.

Near the minimum in the dispersion curve it can be seen that an excitation may have its group velocity reversed for a negligible change in momentum. This is the so-called Andreev reflection, in which a quasiparticle (quasihole) incident on a region of increasing gap is reflected as a quasihole (quasiparticle). This process was first discussed by Andreev in the context of electron reflection at a normal-superconducting interface. However, in the superfluid ^{3}He context such reflection processes have a very strong influence on the dynamical properties, since they permit an excitation to be reflected with virtually no change of momentum.

A further interesting aspect of the dispersion curve in Fig. 1 is the fact that it is not invariant but may be changed. When we move relative to the superfluid ^{3}He, in contrast with a normal gas, the excitation dispersion curve in our frame of reference assumes a different shape. While we move, excitations with momenta approaching are seen to have increased energies and those with momenta receding have decreased energies. For a Newtonian particle this simply translates the energy/momentum parabola. In the superfluid ^{3}He case, however, the excitation dispersion curve becomes canted, as shown in Fig. 2. The effective gap for approaching excitations increases and that for receding excitations decreases.

THE VIBRATING WIRE RESONATOR

We can make use of these properties of the dispersion curve to create a very sensitive mechanical quasiparticle detector. The device we use is a vibrating wire resonator which is a simple semicircle of very fine superconducting wire, as shown in Fig. 3. The loop has a mechanical resonance in which the wire moves perpendicularly to the plane by the flexure of the wire legs. If the loop is placed in a magnetic field, as shown, then a current at the appropriate frequency through the wire will set it into oscillation from the Lorentz force on the current. The motion of the loop through the field sets up a voltage across the loop (from the cutting of the field lines) which we can monitor to infer the velocity. From this simple device we can infer the behavior of the excitation gas from its damping effect on the motion of the resonator. We sweep the frequency through the mechanical resonance of the wire loop and measure the width at half-height of the in-phase signal, Δf_2.

Since the density of the excitation gas at the lowest accessible temperatures is comparable to that of a moderately good vacuum, one might assume that a mechanical method

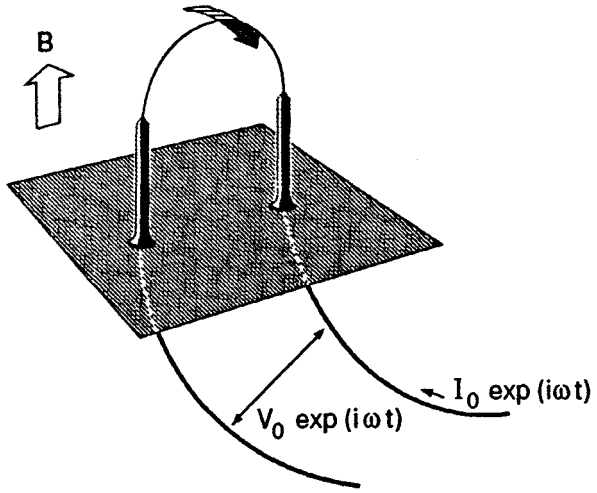

FIG. 3. A vibrating wire resonator.

of detection is unlikely to be very effective. Paradoxically, quasiparticle excitations produce a very large mechanical effect on such a resonator. First, from the shape of the dispersion curve, the excitations have very large momenta for their energies compared to 'conventional' excitations. Furthermore, when the wire is moving through the excitation gas the dispersion curve in the frame of the wire becomes canted, as discussed above. This has a large effect on the dynamics of the response of the gas to the motion of the wire. The situation is illustrated schematically in Fig. 4. The canted dispersion curve has the effect that for quasiholes approaching the wire from the forward side there are no outgoing hole states with similar energies and the quasiholes must be reflected by Andreev processes and thus exchange negligible momentum with the wire. Similarly quasiparticles approaching from the rear must also be Andreev reflected. This has the effect that even at modest velocities normally scattering processes are

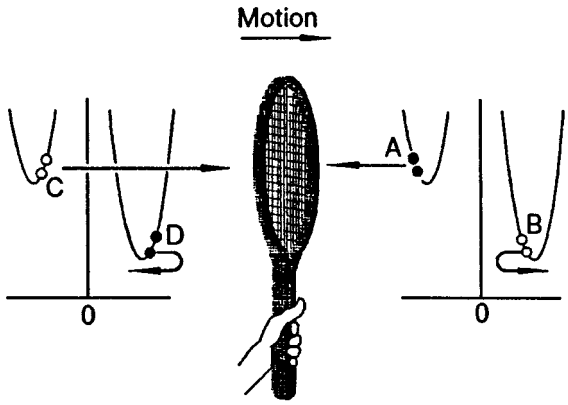

FIG. 4. A schematic diagram of an object moving through superfluid ^{3}He-B. For simplicity, a tennis racket is used as the representative object since it can be assumed that it does not displace the condensate, but only reflects the excitations. In the rest frame of the moving racket (in which scattering is elastic) we see that for excitations approaching from the front only quasiparticles (filled circles) may be normally reflected. Quasiholes must be Andreev reflected with virtually no exchange of momentum with the racket. The converse holds on the opposite side. This multiplies the force on the racket by several orders of magnitude over that expected for a similar ''conventional'' excitation gas.

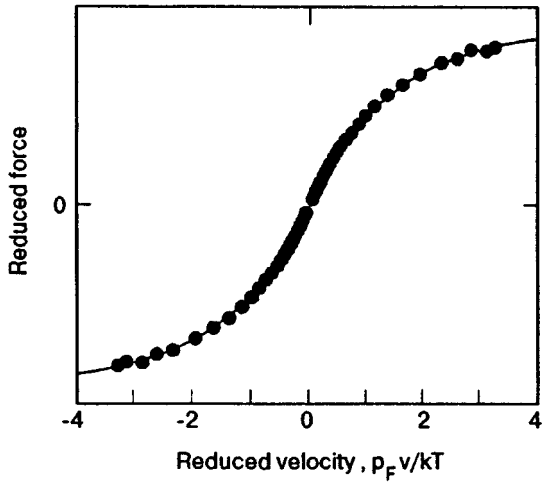

FIG. 5. The measured force velocity-curve for an object moving in the excitation gas. The velocity-independent force above a velocity of $v = kT/p_F$ is quite apparent.

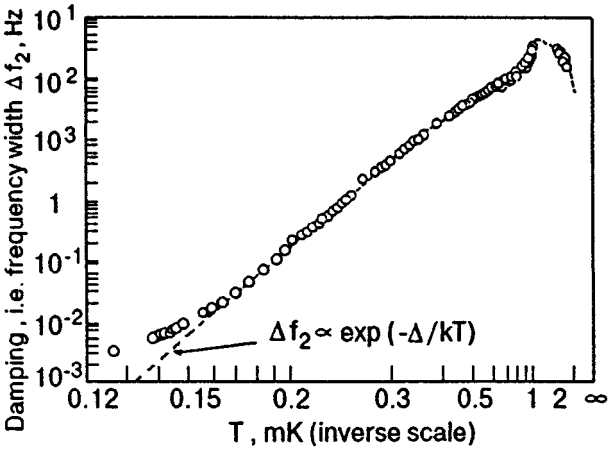

FIG. 6. The frequency width, Δf_2, of a vibrating wire resonator plotted as a function of temperature, as measured by Pt NMR. These very old data are rather poor at the lower temperatures, where the damping becomes very small and we have to measure for many hours in order to determine the frequency width. More modern resonators are made of much thinner wire, giving a larger damping, which is much easier to measure.

biased to give a preponderance of quasiparticle scatterings on the forward side and quasihole scatterings on the rear side. *Both* these processes impede the motion of the wire.

This has two effects, first the resistive force opposing the motion of the wire becomes a constant, independent of velocity, above a velocity of $^2 v = kT/p_F$, which is quite unlike the behavior in conventional gases. This can be seen in Fig. 5, where we plot a typical force-velocity curve.[3] Furthermore, at more modest velocities there remains the imbalance of scattering processes of the quasiparticles and quasiholes, which amplifies the damping effect of the excitations on the wire by many orders of magnitude over the effect of a conventional gas of particles with similar energies.[2] Taking all these factors into account, we find that the density of quasiparticle excitations in the superfluid is very easy to detect by mechanical methods even at the lowest temperatures.

At low velocities, if we do the full calculation,[2] the damping turns out to be proportional to the gap Boltzmann factor, $\exp(-\Delta/kT)$. This means that we can simply calculate the width from the known properties of the wire resonator and the temperature. However, we have measured the damping against an NMR temperature scale, as shown in Fig. 6. This measurement was made many years ago[4] and confirmed the $\exp(-\Delta/kT)$ dependence of the damping. This variation of damping with temperature provides us with a very accurate thermometer for the lower temperature regions, since $\exp(-\Delta/kT)$ changes very rapidly with temperature. For example, there is a change of a factor of 16 between 100 μK and 120 μK for the B-phase at zero pressure.

QUASIPARTICLE BEAMS

In recent years we have extended our interest to examining the behavior of quasiparticle beams. To do this, we need a spectrometer which has a quasiparticle beam source and a quasiparticle beam detector. The device we currently use was developed by S. N. Fisher at Lancaster.[5] This is essentially a blackbody radiator for quasiparticles. The device consists of a box immersed in the superfluid B-phase with a small hole in one wall, as shown in Fig. 7. Inside the box are two vibrating wire resonators. One acts as a thermometer to measure the temperature (or quasiparticle density). The other acts as a heater and makes use of the following principle. If a resonator is driven at high enough velocity, the liquid can be locally accelerated above the Landau critical velocity for pair-breaking. Beyond this velocity the moving wire can create a shower of excitations, both quasiparticles and quasiholes. In other words we can use a heavily driven resonator as a heater. Such a heater has the great advantage that the heat is generated directly in the liquid. This is important, since at the lowest temperatures the Kapitza conductance between the superfluid and solid heater is so poor that thermal contact is too weak for a well-defined quantity of heat to be emitted into the liquid.

The blackbody radiator is thus a small enclosure of about 0.1 cm^3 volume containing a heater and thermometer.

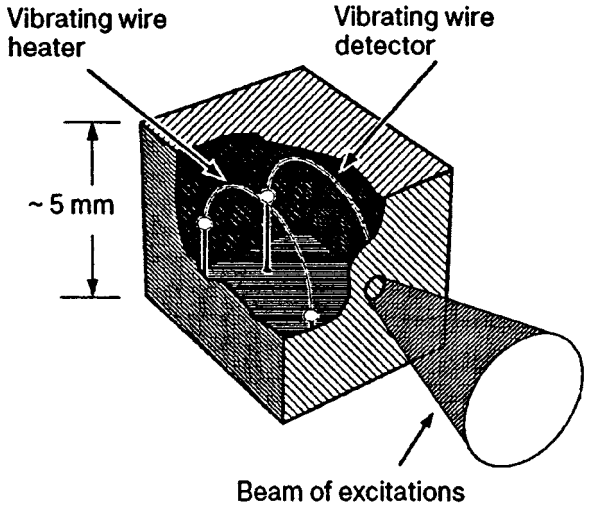

FIG. 7. A quasiparticle blackbody radiator. The box contains a heater and thermometer vibrating wire resonator. When heated, a beam of thermal excitations (quasiparticles and quasiholes) is emitted from the small hole.

The device can be used in the detector or emitter mode. When used as a detector, the flux of excitations incident on the hole can be deduced from the temperature rise inside the enclosure. In emitter mode heat is introduced into the liquid in the enclosure by the heater. This generates a flux of excitations leaving the small hole. The flux of excitations leaving the hole is determined by the temperature inside, T, and is given by

$$\dot{n} = AkT \exp(-\Delta/kT),$$

where A is a constant. (For simplicity in presenting the argument here, we assume that the temperature of the superfluid outside the enclosure is zero.) Since the excitations emerge with a thermal distribution of energies, the mean energy is simply $\Delta + kT$, and the energy flux can thus be written as follows:

$$W = AkT(\Delta + kT)\exp(\Delta/kT). \tag{1}$$

To calibrate the radiator as a quasiparticle source we need to determine the value of A. This we do by applying a steady energy input to the liquid via the heater resonator and observing the temperature inside. If we plot the values for Eq. (1) for such a calibration we find that the experimental fit is linear over many orders of magnitude of input heater power. Furthermore, the lowest detectable power is of the order of 10^{-16} watts or below,[6] which means, as we shall see below, that these devices can be used as particle detectors.

BEAM EXPERIMENTS; DIRECT OBSERVATION OF ANDREEV REFLECTION

We have made a number of experiments with such devices. The two easiest to understand are those designed to allow the direct observation of Andreev reflection and that designed to probe the $B-A$ phase interface, since these experiments need only a source radiator. For the observation of Andreev reflection we set up a radiator which had a small paddle in front of the hole from which the thermal beam is emitted. The setup[6] is shown in Fig. 8. If we move the paddle towards the hole, then the backflow around the paddle ensures that the quasiparticles leaving the radiator find that states near the paddle have their energies decreased (since the liquid is approaching the emitted beam), while quasiholes find their energies increased. This means that quasiholes in the beam are Andreev reflected by the velocity gradient and are returned along the line of the beam back into the radiator. (A feature of Andreev reflection is the almost perfect reversal of the group velocity of the excitation so reflected.) The situation is illustrated in Fig. 9. Since a fraction of the emitted beam is thereby returned to the radiator, the excitation density inside is increased above the density observed when the paddle is stationary and there is no Andreev reflection. From the temperature rise we can, in principle, calculate the fraction of the beam Andreev reflected. In practice, the paddle cannot be moved steadily toward the radiator indefinitely but must be oscillated back and forth. The fraction reflected must therefore be integrated over a complete cycle of the motion of the paddle. When this is done, the rise in temperature inside the box is found to be in good agreement with a simple one-dimensional model of the behavior.[6] A plot of the fraction of excitations Andreev reflected as a function of paddle velocity is shown in Fig. 10 along with a calculation of the expected behavior, as discussed in Ref. 6. This experiment constituted the first direct observation of Andreev reflection in superfluid ^{3}He and provided a much less equivocal result than similar experiments made in superconductors.

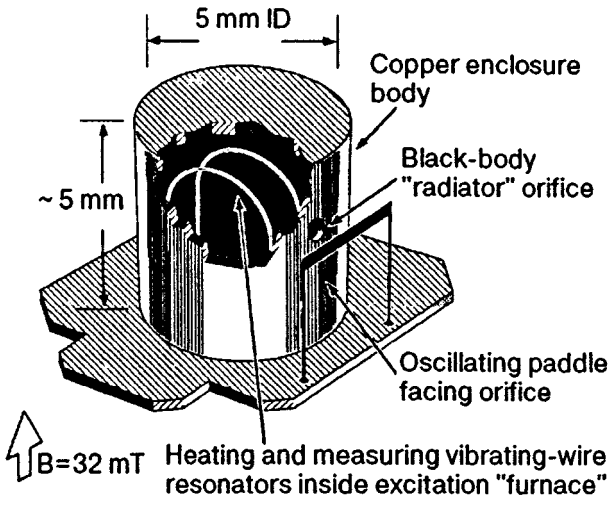

FIG. 8. The experiment for direct observation of the Andreev reflection. An oscillating paddle faces the blackbody radiator beam hole. When the paddle is moved, the velocity field around it causes the Andreev reflection of excitations back into the radiator and the temperature inside thus rises.

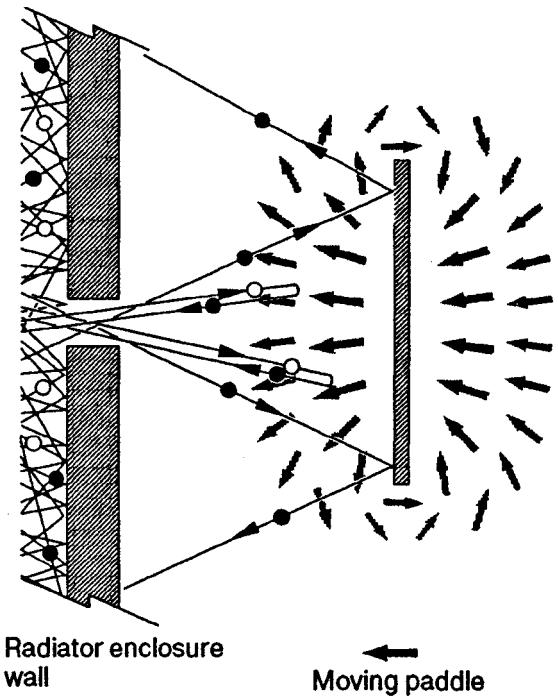

FIG. 9. A schematic diagram of the Andreev experiment. The flow around the paddle causes the Andreev reflection of excitations (in the case illustrated the quasiholes are reflected). Since the Andreev reflection is an accurate retroreflection process, the reflected excitations return to the radiator enclosure.

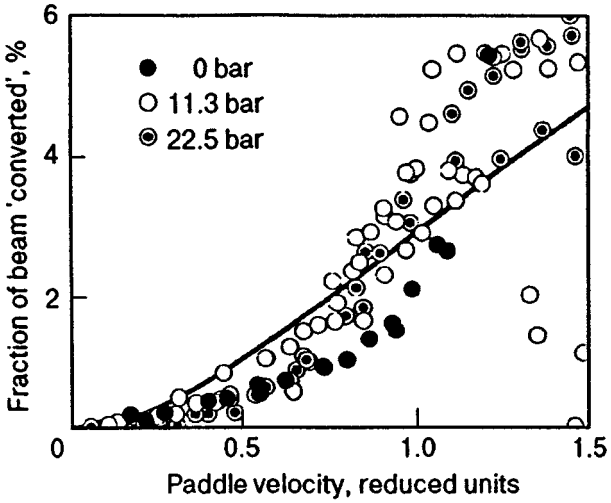

FIG. 10. The measured fraction of excitations reflected by the Andreev processes in the blackbody radiator and paddle experiment, as discussed in the text. The solid line represents a theoretical estimate using a simple one-dimensional model.

BEAM EXPERIMENTS; PROBING THE *A*–*B* PHASE INTERFACE

For the experiment to probe the phase interface between the two superfluid phases, the *B*-phase and the *A*-phase, we stabilized a small region of *A*-phase liquid by applying a very localized magnetic field.[7] The region was arranged to be directly in front of the beam hole of a blackbody radiator, as shown in Fig. 11. In this case the actual gaps in the liquid are changed by the magnetic field. In the *B*-phase the gap is decreased along the direction of a magnetic field, but the excitation spectrum is split according to whether the spin is parallel or antiparallel to the field. The parallel gap in the *A*-phase is 15% larger than the undisturbed gap in the *B*-phase. We can measure these gaps since we have set them up along the beam trajectory. Excitations approaching the region of increasing gap must be Andreev reflected when the effective gap becomes equal to the excitation energy. The

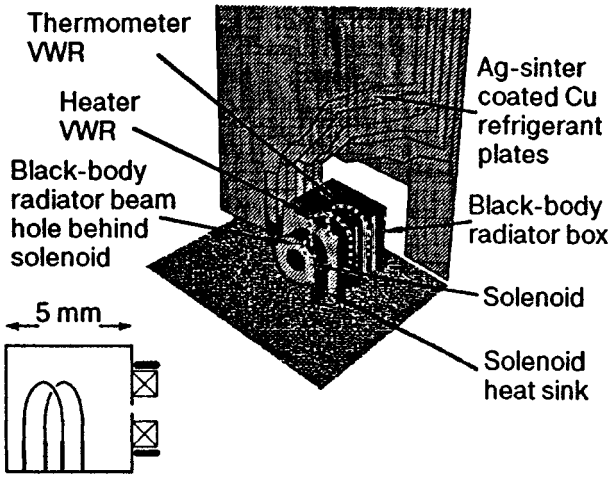

FIG. 11. The experiment used to probe the superfluid ^{3}He A-B phase interface. A blackbody radiator has a small solenoid that encloses the beam hole. It can be used to a create a phase interface across the beam (see text).

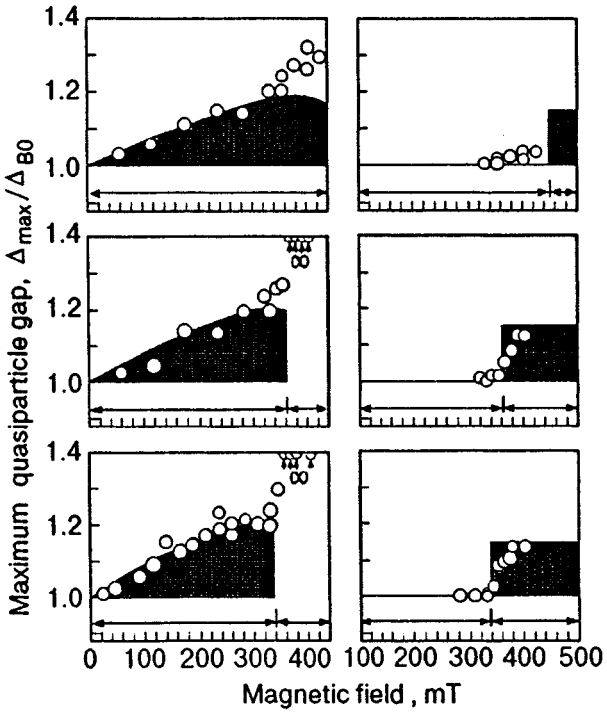

FIG. 12. The A- and B-phase gaps, as measured in the *A*–*B* phase interface experiment (see text).

excitation is thereby returned to the radiator which raises its temperature. A measurement of the temperature in the radiator as a function of magnetic field along the trajectory gives us the value of the maximum gap along the beam. Since in the *B*-phase the gap change depends on the spin value we have to split the calculation into two parts for the *B*-phase part of the problem. Thus we can measure both the maximum *B*-phase gap as a function of field and the *A*-phase gap in the same experiment again by exploiting the unique properties of Andreev reflection. The measured gaps, as shown in Fig. 12 turn out to be in good agreement with the accepted values. However, the maximum gaps in an excitation spectrum have not been readily measurable earlier. In usual spectroscopic methods the minimum gap tends to dominate the response of the system to any input radiation. The present method opens up a new range of experiments where quasiparticles are used as probes. This pilot experiment on the *A*–*B* interface indicates that the method will work and further sophistication can now be considered. It is of course important to remember that the *A*–*B* interface in superfluid ^{3}He is unique in that it is a high symmetry interface between two very different but also high-symmetry Bose condensates. This is the most complex high-symmetry interface to which we currently have experimental access.

PARTICLE DETECTION IN SUPERFLUID ^{3}He

The work with the calibration of the blackbody radiator, with its very high energy resolution, led us to think that this device might provide a possible particle detector. We had suggested long ago[8] that superfluid ^{3}He would provide an ideal working material for the detection of low-energy recoil interactions. The ''working fluid'' is simple, consisting only

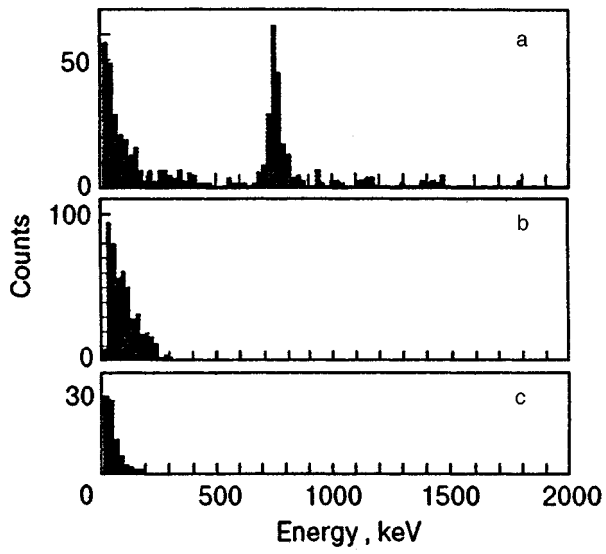

FIG. 13. Spectra of particle events measured in a blackbody radiator in superfluid ^{3}He. The top spectrum is that taken with a neutron source, the middle is that taken with a gamma-ray source, and the bottom is a background spectrum. The large peak in the neutron spectrum can be seen at about 800 keV, which represents the neutron capture process (see text).

of the superfluid ground state and the dilute gas of excitations. The excitations have energies comparable to that of the superfluid energy gap, $\Delta = 1.4 \times 10^{-7}$ eV, which is virtually the lowest which we can currently utilize. Finally, the only significant impurity in superfluid ^{3}He is ^{4}He. Extrapolation of the known high-temperature solubility of ^{4}He in liquid ^{3}He to 100 μK suggests that ^{4}He is only soluble to one part in 10^{2000}. The purity of the working fluid is thus absolute.

Our first attempt at such an experiment was to take the blackbody radiator used for the Andreev reflection experiment described above and monitor the temperature inside the enclosure while exposing the cryostat to the output of an AmBe neutron source. What we would expect to see would be as follows: a particle interacts inside the box, heats the liquid (i.e., increases the excitation density), causing a sudden fall in the amplitude of the thermometer resonator. The excess excitations in the radiator enclosure so-produced subsequently diffuse out of the hole and the amplitude recovers exponentially. The time constant for the quasiparticles to leak out of the box is governed by the geometry and the hole size and in a typical experiment is a few tenths of a second at the lowest temperatures.

The size of the jumps in the thermometer trace can be calibrated in terms of deposited energy by the application of a short known pulse of heating to the heater wire in the enclosure. When exposed to a source, the events can thus be calibrated and presented as a spectrum in the usual way. Figure 13 shows spectra for a gamma source, a neutron source, and a background spectrum for comparison taken in this way.[9] The neutron spectrum shows a very prominent peak at about $\sim$ 800 keV, which arises from low-energy neutrons undergoing the nuclear reaction $n + {}^3_2\mathrm{He} \rightarrow p + {}^3_1\mathrm{H}$. This process releases an energy of 764 keV into the liquid.

When we used the device to monitor the background radiation level, we found that we could resolve events releasing energies of only 500 eV. This is rather a good performance for a device which was neither optimized nor intended for these experiments. With various improvements we are convinced that we could improve the performance by many orders of magnitude and have proposed a dark matter detector based on this principle.[9]

SIMULATION OF COSMIC STRING CREATION

An interesting further application of the blackbody radiator has been in the simulation of the creation of cosmic strings via the Kibble mechanism. This mechanism was first proposed by Kibble[10] to describe the creation of topological defects during the series of phase transitions which the Universe is thought to have undergone shortly after the big bang.

There are profound analogies between the structure of superfluid ^{3}He and the structure of the metric of the Universe. Because of the spin and orbital angular momentum properties, ^{3}He shows a superposition of broken spin rotation, broken orbital rotation and broken gauge symmetries, which provide a close approximation to the superposition of broken rotational and gauge symmetries used to describe the Universe. Similar types of linear defects (vortices), point defects (monopoles) and textures may be generated in superfluid ^{3}He, by analogy with the various types of defects which may have been created (some of which may survive to the present) in the structure of the Universe.

The background of this experiment[11] depended on a certain level of serendipity. Fisher, working with Bunkov and Godfrin in Grenoble, built an experiment similar to that used in Lancaster for the detection of neutrons,[9] which described above. However, the hole in the enclosure was made much smaller than that used in the Lancaster experiment. The smaller hole made this experiment less effective as a particle detector but allowed a much more accurate energy calibration to be made since the time constant of the system was much longer than that of the earlier version.

When a neutron interacts inside the blackbody enclosure of the Grenoble experiment via the exothermic neutron capture process, the better calibration allows us to ascertain that the energy taken up by the superfluid as thermal excitations is significantly lower than 764 keV, which is known to be released by this process. We know that some of this energy is released as ultraviolet photons which are lost to the helium. However, even after this fraction is taken into account there is still a significant ''missing energy.'' We found that this energy has gone into producing topological defects in the liquid, in this case, vortices. The defects are formed when the liquid cools through the superfluid transition. The interaction of a neutron with a ^{3}He atom in the cold superfluid leads initially to the creation of a very energetic proton and tritium nucleus. These particles rapidly lose this energy to create a small volume of the liquid (a few microns in extent) which is heated above the transition temperature of 0.94 mK. As the liquid cools back through the transition, fluctuations in the temperature mean that many regions of the cooling ''fireball'' independently become superfluid and since these regions of superfluid are nucleated independently, the order parameter is random. As the regions grow and coalesce, grain boundaries in the order parameter are formed. These

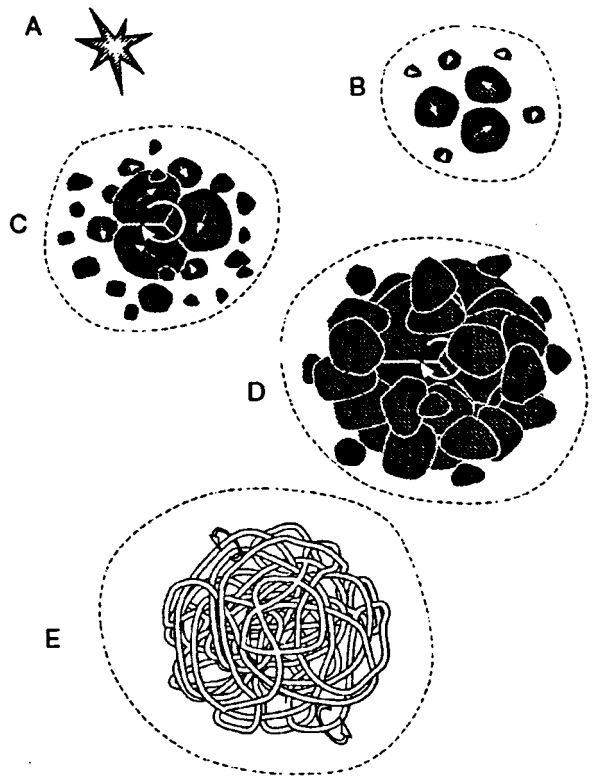

FIG. 14. Simulation of the creation of cosmic strings in superfluid ^{3}He. A small region of the liquid is heated by a neutron capture process. This leads to the heating of a small volume of the liquid above the transition temperature. As this volume cools, independently nucleated regions of the superfluid are created. The order parameter in each ''grain'' is also independent. When the regions coalesce, the mismatch of the order parameters leads to the formation of a vortex tangle.

may relax to some extent by the bending of the order parameter but along every line around which there is a 2π circulation of the order parameter angle there is no possibility of relaxation and a vortex remains. The various domain contacts thus relax to form a vortex tangle. Since the background liquid is much colder than the transition temperature (about 100 μK compared with the transition temperature of 940 μK), the vortex tangle is rapidly cooled through the region near the transition and reaches a temperature regime where the lifetime becomes very long. This process is shown schematically in Fig. 14.

Zurek[12] has translated the Kibble mechanism for application to phase transitions in quantum fluids. Zurek's scenario allows us to predict the density of topological defects as a function of the cooling rate and the characteristic time of the superfluid medium. We can independently estimate the typical distance separating the topological defects, since we know the energy deposited in the liquid (the 764 keV released by the capture process). We can estimate from the liquid heat capacity what volume is heated above the transition and from the ''missing energy'' the length of vortex line can be calculated. When these two numbers are compared (of the order of 1 to 10 coherence lengths in both cases), the agreement is found to be remarkably good.[11]

POSTAMBLE

Much interest in the quantum fluids has been directed toward the behavior at higher temperatures, where the order parameter is rapidly changing with temperature and the properties are dominated by the interaction between normal and superfluid components. For the ''structureless'' superfluids such as liquid ^{4}He and the conventional superconducting electron gas the low-temperature regime might be thought of as of lesser interest since the condensate is very simple. Certainly in the case of superfluid ^{3}He the very low-temperature regime reveals many interesting properties which have many implications for other areas of physics.

ACKNOWLEDGMENTS

We would like to thank all the members of the Lancaster group who have contributed to our work over the years, including I. Bradley, Y. Bunkov, D. Cousins, M. Enrico, S. Fisher, M. Follows, T. Guénault, W. Hayes, C. Kennedy, S. Phillipson, N. Shaw, T. Sloan, P. Thibault, and K. Torizuka. We also thank the Grenoble group of C. Bäuerle, Y. Bunkov, S. Fisher, and H. Godfrin, who carried out the cosmic strings experiment described above.

[1)]E-mail: gpickett@lancaster.ac.uk

[1] Yu. M. Bunkov, S. N. Fisher, A. M. Guénault, C. J. Kennedy, and G. R. Pickett, Phys. Rev. Lett. **68**, 600 (1992).
[2] S. N. Fisher, A. M. Guénault, C. J. Kennedy, and G. R. Pickett, Phys. Rev. Lett. **64**, 2566 (1989).
[3] S. N. Fisher, G. R. Pickett, and R. J. Watts-Tobin, J. Low Temp. Phys. **83**, 225 (1991).
[4] A. M. Guénault, V. Keith, C. J. Kennedy, I. E. Miller, and G. R. Pickett, Nature **302**, 695 (1983).
[5] S. N. Fisher, A. M. Guénault, C. J. Kennedy, and G. R. Pickett, Phys. Rev. Lett. **69**, 1073 (1992).
[6] M. P. Enrico, S. N. Fisher, A. M. Guénault, G. R. Pickett, and K. Torizuka, Phys. Rev. Lett. **70**, 1846 (1993).
[7] D. J. Cousins, M. P. Enrico, S. N. Fisher, S. L. Phillipson, G. R. Pickett, N. S. Shaw, and P. J. Y. Thibault, Phys. Rev. Letters **77**, 5245 (1996).
[8] G. R. Pickett, *Proceedings of the Second European Workshop on Low Temperature Devices for the Detection of Low Energy Neutrinos and Dark Matter*, Editions Frontières, Ed L. Gonzalez-Mestres and D. Perret-Gallix 377 (1988).
[9] D. I. Bradley, Yu. M. Bunkov, D. J. Cousins, M. P. Enrico, S. N. Fisher, M. R. Follows, A. M. Guénault, W. M. Hayes, G. R. Pickett, and T. Sloan. Phys. Rev. Lett. **75**, 1887 (1995).
[10] T. W. B. Kibble, J. Phys. A **9**, 1387 (1976).
[11] C. Bäuerle, Yu. M. Bunkov, S. N. Fisher, H. Godfrin, and G. R. Pickett, Nature **382**, 332 (1996).
[12] W. H. Zurek, Nature **317**, 505 (1985).

This article was published in English in the original Russian journal. It was edited by S. J. Amoretty.

Neutron scattering study of liquid helium. Analysis of new data

N. M. Blagoveshchenskii, A. V. Puchkov, and A. N. Skomorokhov

Russian State National Science Center ''Power Physics Institute,'' 249020 Obninsk, Russia

I. V. Bogoyavlenskii and L. V. Karnatsevich

National Science Center ''Kharkov Physicotechnical Institute,'' 310108 Kharkov, Ukraine
(Submitted November 15, 1996)
Fiz. Nizk. Temp. **23**, 509–514 (May–June 1997)

A new analysis of neutron scattering data obtained earlier for liquid ^{4}He is presented. The experiments were made on the time-of- flight spectrometer DIN-2PI in the pulsed reactor IBR-2. The results are analyzed by using a consistent data processing technique including the representation of the dynamic structural factor $S(Q,\omega)$ with a constant wave vector Q. The one-phonon component of $S(Q,\omega)$ is approximated by using the damped harmonic oscillator function taking into account the instrumental resolution. It is shown that the experimental values of $S(Q,\omega)$ are in good agreement with the fitting model, i.e., have a simple one-component structure. The presented results indicate a peculiarity in the temperature dependence of $S(Q,\omega)$ for liquid helium in the wave vector region 0.5–0.8 Å^{-1}. Various explanations of such a peculiarity are discussed.
[S1063-777X(97)00305-8]

INTRODUCTION

The results of analysis of liquid helium by using the inelastic neutron scattering method were reported by us earlier.[1] The experiments were carried out on the time-of-flight direct geometry spectrometer DIP-2PI[2] (reactor IBR-2, Dubna). An important feature of the method used is that the measurements are made at a constant scattering angle, i.e., under the conditions when the transferred momentum is not strictly constant within the measuring spectrum. In Ref. 1, we made an attempt to obtain preliminary qualitative results on the structure of the helium excitation spectrum without taking into account these changes in the momentum. In view of inaccuracies emerging in this case, we approximated the spectrum of scattered neutrons by using the simplest fitting model in which the helium excitation lines and resolution functions have the Gaussian shape. Under these assumptions, the excitation spectrum of liquid helium acquired a complex structure. Such an approach made it possible to analyze a large body of experimental data in the range of the wave vector Q from 0.08 to 1.6 Å^{-1} for initial energies of neutrons $E_0=2.08$, 2.45, and 3.5 meV at liquid helium temperatures ranging from 0.44 to 2.25 K.[1] The spectral structure obtained as a result of such an analysis did not contradict the semiphenomenological theory[3,4] predicting a complex structure of the excitation spectrum for liquid helium.

As the simplified method of spectral analysis leads to considerable errors, we carried out a new, more consistent experimental data processing taking into account the peculiarities of the time-of-flight technique (transition of spectra to the scale with $Q=\text{const}$, taking into account momentum indeterminacy, etc.) and using the real resolution function and a physically substantiated fitting model for the one-phonon component of $S(Q,\omega)$ (the so-called damped harmonic oscillator function).

In this paper, we report on the results of new analysis of the experimental spectra obtained earlier. The data processing is carried out for several typical values of the transferred momentum, for which a complete set of data required for the application of the data processing method described below is available.

EXPERIMENTAL DATA PROCESSING

The basic microscopic parameter of a substance, which can be extracted from neutron experiments, is the dynamic structural factor (or scattering law) $S(Q,\omega)$ which is directly connected with the fundamental parameters of the system such as the dynamic susceptibility function and the radial distribution function. Using model concepts, we can obtain from $S(Q,\omega)$ the information on the structure of the excitation spectrum of the system and on relaxation characteristics of excitations. The dynamic structural factor $S(Q,\omega)$ can be presented as a superposition of the one-phonon part of the scattering law, which corresponds to scattering of a neutron accompanied by the generation of an excitation, and the multiphonon part corresponding to neutron scattering with the generation of two or more excitations in helium. In this communication, we analyze the one-phonon part of $S(Q,\omega)$. The separation of these components of the scattering law is a complicated problem involving a number of assumptions and conjectures. The doubly differential scattering cross section used in experiments is connected with $S(Q,\omega)$ through the well-known relation

$$\frac{d^2\sigma}{d\Omega\, d\omega}=N\frac{\sigma}{4\pi\hbar}\frac{k_f}{k_i}S(Q,\omega),$$

where N is the number of atoms in the system, σ the cross section of scattering at a bound nucleus, and k_i and k_f are the values of the wave vectors of the incident and scattered neutrons, respectively.

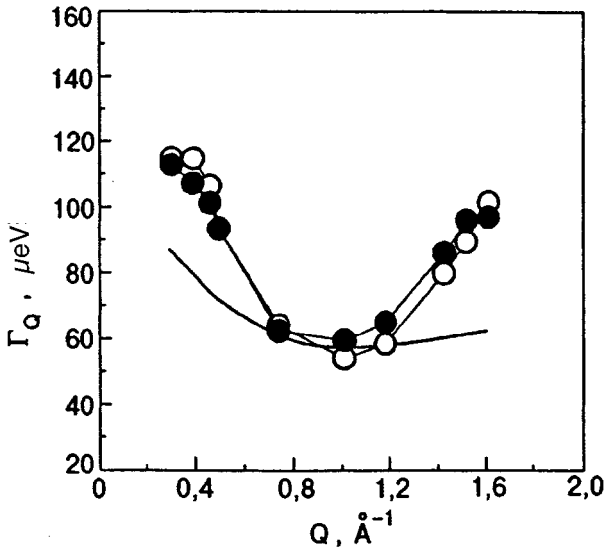

FIG. 1. The dependence of the half-width of resolution function on the transferred momentum Q, taking into account the indeterminacy dQ in the wave vector transfer (●) and without it (solid curve); light circles correspond to the values of experimental peak width at $T=0.44$ K.

In order to obtain the dynamic structural factor $S(Q,\omega)$ for liquid helium from experimental spectra measured on the time-of-flight scale at a constant scattering angle θ, we carried out the following standard operations. First, the scattering law $S(\theta,t)|_{\theta=\text{const}}$ at a constant angle and on the time-of-flight scale was transformed to the representation $S(\theta,\omega)|_{\theta=\text{const}}$. Second, the phonon component was taken into account, for which we used the procedure of background subtraction in accordance with the expression

$$I=(I_s-I_{0f})-B(I_0-I_{0f}), \tag{1}$$

where I_s and I_0 are the flux-normalized spectra of neutrons scattered by the container with and without helium, respectively, I_{0f} is the time-independent background of fast neutrons, and B the correction for container screening by helium. Third, the spectra of $S(\theta,\omega)|_{\theta=\text{const}}$ were transformed by interpolation to the scattering law $S(Q,\omega)|_{Q=\text{const}}$ with a constant transfer of wave vector.

The experimental spectra $S(Q,\omega)$ obtained in this way were approximated by convolution of the model dynamic structural factor for liquid helium with the spectrometer resolution function $R(E_0,\omega)$:

$$S(Q,\omega)=S_1(Q,\omega)\otimes R(E_0,\omega). \tag{2}$$

For the model of the one-phonon component of the dynamic structural factor for liquid helium, we chose the function of an attenuating harmonic oscillator

$$S_1(Q,\omega)=\frac{[(1/\pi)Z_Q][n_B(\omega)+1]4\omega\omega_Q\Gamma_Q}{[\omega^2-(\omega_Q^2+\Gamma_Q^2)]^2+[2\omega\Gamma_Q]^2}, \tag{3}$$

where Z_Q is the intensity of one-phonon scattering, Γ_Q the peak half-width at half-height points, ω_Q the excitation energy, ω the transferred energy, and $n_B(\omega)$ the Bose factor.

The spectrometer resolution function was calculated by using the Monte Carlo method, taking into account the

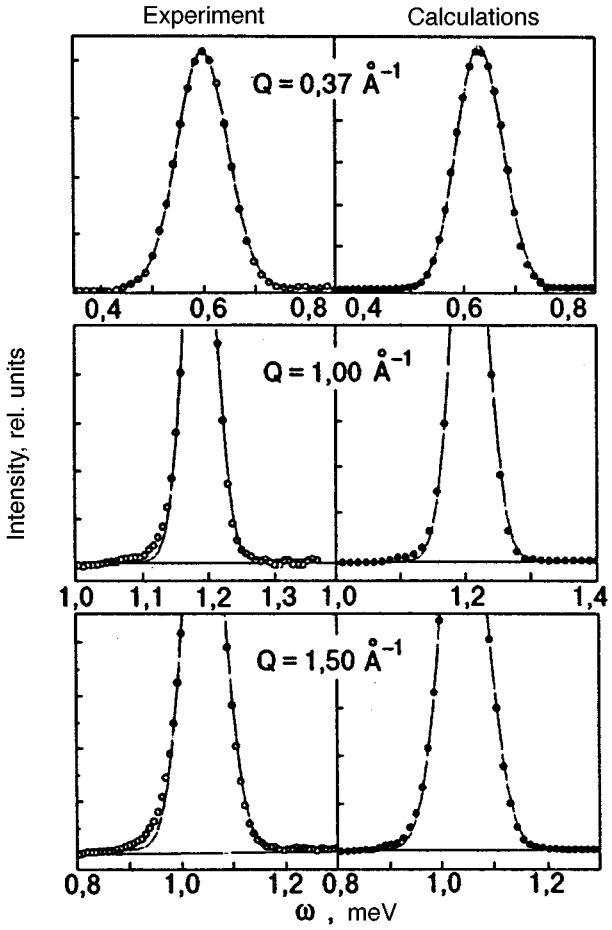

FIG. 2. Comparison of the shape of resolution function calculated by the Monte Carlo method (●) with the experimental dependences $S(Q,\omega)$ recorded at liquid helium temperature $T=0.44$ K(○) for three values of the wave vector Q. The solid curve describes the result of approximation of calculated and experimental values of $S(Q,\omega)$ by a Gaussian function.

energy-momentum relation for energy excitations in liquid helium. For systems with a strong dispersion, the resolution function is usually determined not only by the energy resolution of the spectrometer, but also by the momentum- transfer resolution dQ which depends on the energy–momentum relation $E(Q)$ for the scatterer.[5] The scale of this contribution to the resolution function in our case, when the substance under investigation is liquid helium, is clearly seen from a comparison of the curves in Fig. 1 showing the values of the half-width of theoretical resolution functions, taking into account dQ and without it. It can be seen from the figure that this contribution is close to zero in the maxon region, where grad $\omega_Q=0$, i.e., in the absence of dispersion of excitations, and becomes significant for larger and smaller values of Q upon an increase in the dispersion of excitations.

The correctness of the values of resolution function calculated by the Monte Carlo method can be verified by comparing them with the real neutron scattering spectrum for helium at a low experimental temperature for which the intrinsic excitation line width in helium can be neglected as compared to the resolution function width. Such a comparison was carried out for the lowest temperature 0.44 K attained in our experiments, at which the intrinsic excitation

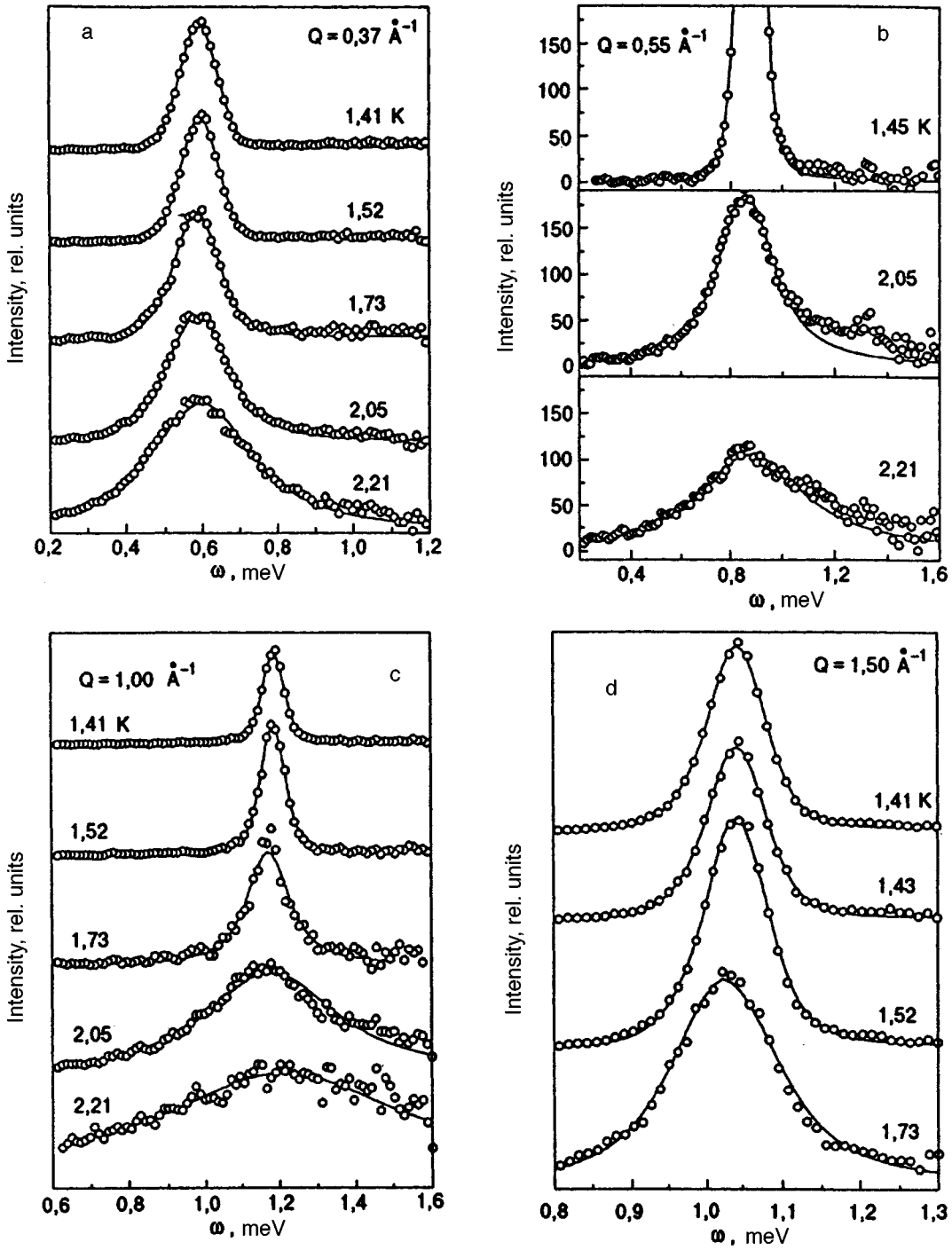

FIG. 3. Experimental spectra of $S(Q,\omega)|_{Q=\text{const}}$ for liquid helium at various temperatures. Solid curve describes the result of approximation of spectra by formula (2) for the values of wave vector $Q=0.37$ (a), 1.00 (b), and 1.50 Å^{-1} (c) (the spectra are in relative units) and for $Q=0.55$ Å^{-1} (the spectra are normalized in area).

width is apparently smaller than 2 μeV,[6,7] while the resolution function width in the region of elastic scattering amounts to $\sim$120 μeV (Fig. 2). The solid curve in the figure corresponds to the Gaussian approximation of the theoretical and experimental curves. It can be seen that for a wave vector transfer of 0.37 Å^{-1}, the Gaussian function correctly describes both dependences. For large values of wave vector transfer, the low-energy parts of the curves deviate considerably from the Gaussian curves in both cases. For an analysis of experimental spectra recorded at higher temperatures, a superposition of two Gaussian functions were used as an adequate representation of the resolution function taking into account its asymmetry.

RESULTS

Figures 3a–3d show the $S(Q,\omega)$ spectra for liquid He in the temperature interval 1.41–2.21 K for the wave vector

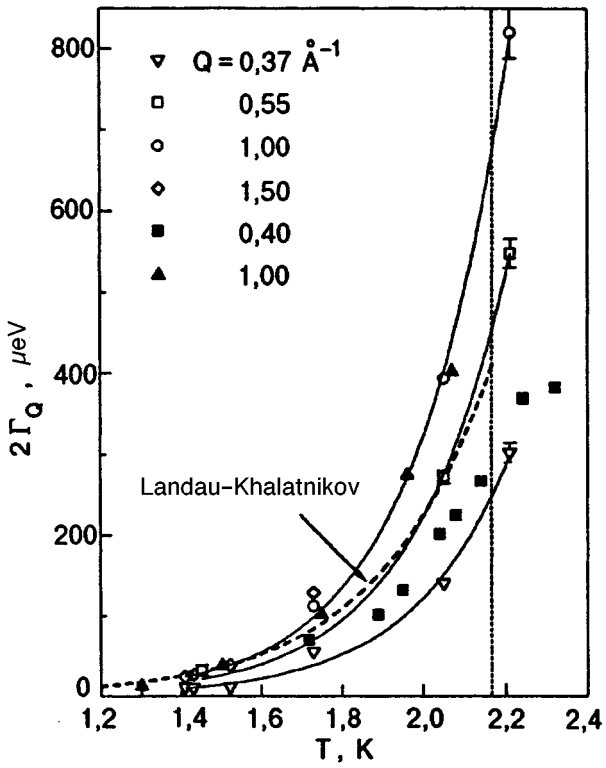

FIG. 4. Temperature dependence of the one-phonon peak width for several values of wave vector Q (*light symbols*). Solid curve describes the approximation of experimental values for $Q=0.37, 0.55$, and 1.00 Å^{-1} by an exponential function. Dark symbols correspond to the results obtained by other authors (in Ref. 8 (■) and in Ref. 9 (dark triangles)) for close values of wave vectors. The dashed curve is the Landau–Khalatnikov theoretical curve for rotons.

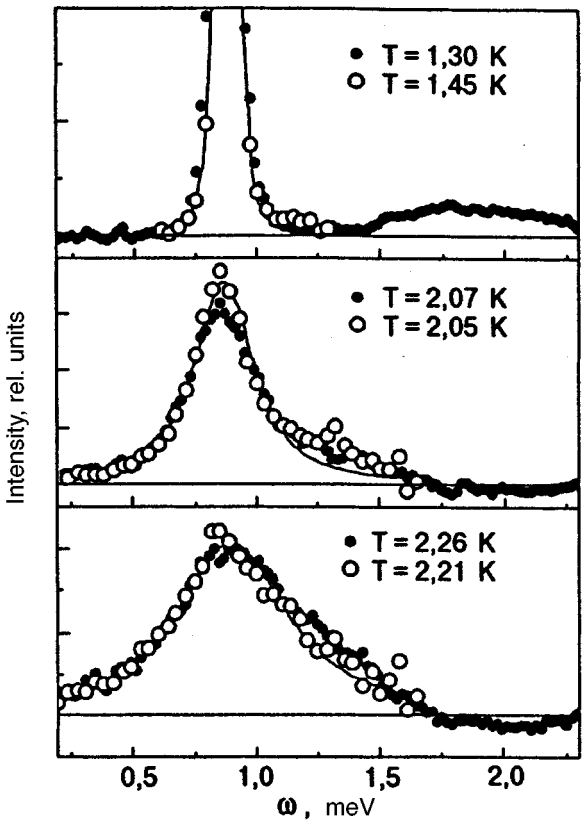

FIG. 5. Comparison of experimental dependences $S(Q,\omega)$ obtained by using different spectrometers for $Q=0.55$ Å^{-1} and close temperature values: our results (○) and the results obtained by Andersen *et al.*[8] (●). The spectra are normalized in area. The solid curve describes the results of approximation of our results by formula (2).

values $Q=0.37, 0.55, 1.0$, and 1.5 Å^{-1} for characteristic regions on the dispersion curve for liquid helium. It can be seen that experimental one-phonon peaks are described correctly by expression (2). Thus, the above approach to experimental data processing does not suggest a complex structure of the one-phonon component of the dynamic structural factor $S(Q,\omega)$ following from the results of earlier analysis.[1] Figure 4 shows the temperature dependence of the one-phonon peak width. It can be seen that the peak width increases exponentially with temperature for all values of the wave vector. The obtained results are in good agreement with the data obtained by other authors (dark symbols). The excitation energy weakly depends on temperature to within the experimental error in the entire range of temperature under investigation, including the λ-transition region. The high-energy wing of the peak at $T \geqslant 1.73$ K contains an additional low-intensity contribution, which is observed for all values of wave vector except $Q=1.5$ Å^{-1}. This additional contribution is manifested most clearly for $Q=0.55$ Å^{-1}, i.e., in the transition region between the phonon and maxon regions on the dispersion curve. The effect is observed at $T=1.45$ K, has the maximum intensity at 2.05 K, and is preserved at $T=2.21$ K, i.e., above the temperature corresponding to the λ-transition.

Let us consider this effect in greater detail by comparing our data with the results obtained in Refs. 8 and 9 for these values of wave vector (Fig. 5). It can be seen that the main part of multiphonon scattering at temperatures 1.3–1.45 K corresponds to higher values of energy than the one-phonon peak and the observed singularity. The additional contribution to intensity observed in our experiments corresponds to the energy range 1.2–1.4 meV and exhibits a strong temperature dependence. It should be noted that our data are in good agreement with the results obtained in Refs. 8 and 9, especially at $T=2.05$ and 2.21 K, for which the results obtained in Refs. 8 and 9 are presented after the procedure of ''simple subtraction of multiphonon component'' (SSM).[10] It should be emphasized that our data and the results in Refs. 8 and 9 were obtained on different spectrometers and for different initial energies. This allows us to suggest that the singularity observed in $S(Q,\omega)$ has a physical origin.

It is difficult to propose an unambiguous explanation of the observed phenomenon on the basis of the available experimental data at present. We shall indicate some of the possible interpretations of the effect.

The additional contribution to intensity can be associated with interference between one-phonon and multiphonon scattering. According to the predictions of the theory, the contribution to scattering associated with these processes becomes significant for $Q=0.5$ Å^{-1}.[11] It should also be observed that such a contribution should be manifested starting from the energy of one-phonon excitation.

Grevecoeur *et al.*[12] observed an additional contribution to intensity at energies above that corresponding to the one-phonon peak in experiments on liquid helium under pressure. These authors attribute the emergence of this peak to a damping mode of zeroth sound in accordance with the results obtained by Glyde and Griffin.[3] While the singularity observed by us is associated with this mode, the singularity in Ref. 12 was observed for values of energy and momentum shifted as a result of applied pressure.

Finally, the effect under investigation can be due to two-phonon processes in the low-energy range of $S(Q,\omega)$. The theory[11] predicts an increase in the intensity of these processes with temperature.

Thus, the available experimental data do not allow us to interpret unambiguously the nature of the observed singularity. We believe that this publication will arouse interest and stimulate further theoretical and experimental investigation of the behavior of $S(Q,\omega)$ in the phonon–maxon transition region.

In conclusion, the authors express their deep gratitude to Henry Glyde for fruitful discussions at Dubna, to Ken Andersen for providing the experimental data, and to Sergei Pupko who created the program for calculating the resolution function by the Monte Carlo method.

This research was supported by the Russian State Science and Technology program ''Modern Trends in Physics of Condensed Media'' under the project ''Neutron Studies of Matter'' and the Ukrainian State Foundation of Fundamental Studies.

[1] N. M. Blagoveshchenskii, I. V. Bogoyavlenskii, L. V. Karnatsevich *et al.*, Phys. Rev. B **50**, 16550 (1994).
[2] A. V. Abramov, N. M. Blagoveshchenskii, B. K. Blinov *et al.*, Atomnaya Energiya **66**, 316 (1989).
[3] H. R. Glyde and A. Griffin, Phys. Rev. Lett. **65**, 1454 (1990).
[4] H. R. Glyde, Phys. Rev. B **45**, 7321 (1992).
[5] R. Grevecoeur, I. de Shepper, L. de Graaf *et al.*, Nucl. Inst. Meth. A **356**, 415 (1995).
[6] F. Mezei and W. G. Stirling, in *75th Jubilee Conf. on Helium-4* (ed. by Y. G. M. Armitage), World Scientific, Singapore (1983).
[7] K. H. Andersen *et al.*, Phys. Rev. Lett. (to be published).
[8] K. H. Andersen, W. G. Stirling, R. Scherm *et al.*, J. Phys: Cond. Matter **6**, 821 (1994).
[9] K. H. Andersen and W. G. Stirling, J. Phys: Cond. Matter **6**, 5805 (1994).
[10] A. Miller, D. Pines, and P. Nozieres, Phys. Rev. **108**, 1452 (1962).
[11] H. Glyde, *Excitations in Liquid and Solid Helium*, Clarendon Press, Oxford (1994).
[12] R. M. Grevecoeur, H. E. Smorenburg, I. M. de Schepper, and E. C. Svensson, Czech. J. Phys. **46**, 257 (1996).

Translated by R. S. Wadhwa

Structure and superfluidity of ^{4}He films on plated graphite

J. Nyéki,[a] R. Ray, G. Sheshin,[b] V. Maidanov,[b] V. Mikheev,[c] B. Cowan, and J. Saunders[d]

Millikelvin Laboratory, Department of Physics, Royal Holloway University of London, Egham, Surrey, 7W20 OEX, United Kingdom

(Submitted January 20, 1997)
Fiz. Nizk. Temp. **23**, 515–526 (May–June 1997)

The results of an experimental study using torsional oscillators of the superfluidity of ^{4}He films adsorbed on hydrogen plated graphite are reported. The evolution of superfluidity with the growth of the film shows considerable structure arising from the atomic layering of the film. There is evidence that the superfluidity of a single fluid layer is strongly suppressed, possibly due to the influence of the periodic potential arising from the underlying solid layer. The behavior of two fluid layers is quite distinct, but shows similarities to that of thicker films on heterogeneous substrates; we suggest that the usual theory of the superfluidity of two-dimensional ^{4}He should be extended to account for superfluid onset temperatures in such a film.
 [S1063-777X(97)00405-2]

DEDICATION

In this paper we give a brief review of one aspect of the results of a research collaboration between scientists from the B. I. Verkin Institute for Low Temperature Physics and Engineering, Kharkov and Royal Holloway University of London. This has been made possible by the support of the Royal Society (London), and the Engineering and Physical Sciences Research Council (United Kingdom). The low-temperature experiments reported here were cooled using a cryogenic cycle, sorption pumped, dilution refrigerator of the type pioneered by Professor Eselson and his group. This was initially constructed in Kharkov, modified and developed at Royal Holloway, and provided an excellent low mechanical noise environment for these studies involving sensitive, high-Q, mechanical oscillators. Further developments and the commercialization of this refrigerator technique are described elsewhere in this volume. This paper is intended as a tribute to the memory of Professor Eselson and the tradition of low-temperature helium research at Kharkov, to which he contributed so significantly.

1. INTRODUCTION

The superfluid transition of a thin ^{4}He film on a planar surface is understood in terms of a Kosterlitz–Thouless (KT) two-dimensional phase transition.[1] Above some critical temperature, vortex-antivortex pairs become unbound, the film cannot support a superflow and the superfluid density drops discontinuously to zero. Clear confirmation of these ideas was primarily due to the experiments of Reppy and coworkers, at Cornell.[2] They adsorbed the helium film on a sheet of mylar which was contained inside a torsional oscillator. Associated with the superfluid transition of the film is a shift in the period of the oscillator, resulting from the drop in its effective moment of inertia as the film decouples from the substrate. This method was a development of a method first used by Andronikashvili[3] to determine the superfluid density of bulk liquid ^{4}He. The key features of the Cornell torsional oscillators were their high-quality factor, $Q \geqslant 10^5$, and a typical frequency in the range 0.5–2 kHz outside that of most vibrational noise on a typical cryostat. This technique allowed the resolution of the small period shifts due to the superfluid transition in the film (typically of the order of ns, compared to a period of the order of 1 ms), as well as a characteristic dissipation peak at the superfluid transition. The discontinuous period jump predicted by KT is somewhat rounded by the finite frequency at which the superfluid response is measured. However, it was possible to confirm the universal relation for the jump $\rho_s(T_c)/T_c = 2m^2 k_B/\pi\hbar^2$. A comparison of the results with the dynamic KT theory can be found in Agnolet, McQueeney and Reppy (AMR).[4]

The mylar substrate used in this early work is extremely heterogeneous, i.e., the substrate is disordered due to atomic scale roughness. One consequence of this is that up to some threshold coverage the helium film is localized and no superfluid transition is observed. This threshold coverage is commonly known as the ''dead layer'' or ''inert layer.'' It has been suggested that superfluid onset, as a function of coverage at $T=0$, may be regarded as a transition between an insulating, disordered (Bose glass) phase and the superfluid.[5]

Recently, attention has turned to the study of ^{4}He films adsorbed on the basal plane of graphite using these sensitive torsional oscillator methods. The first such study of superfluidity in this system was performed by Crowell and Reppy (CR),[6] while Mohandas *et al.*[7] concentrated on submonolayer films and found no evidence for superfluidity in them. Exfoliated graphite substrates were used to provide a sufficiently large surface area to allow measurements of adequate sensitivity. It is well established that this substrate consists of atomically flat crystallites of typical dimension a few hundred angstroms and thus provides a homogeneous binding potential for the adsorbate. Residual heterogeneity, at the crystallite edges, localizes about 2% of the first helium layer, and so is a relatively weak effect. The important point is that the film on this substrate is atomically layered; clear periodic structure has been seen in the compressibility of the film, as determined from vapor pressure adsorption isotherms,[8] as well as in the heat capacity[8,9] and third sound velocity.[8] Lay-

ering of the film is also seen in first principles calculations of film structure.[10] Thus, in contrast with heterogeneous substrates, the structure of the film is, in principle, well defined. This structure turns out to have a profound influence on the development of superfluidity. Exfoliated graphite substrates have been widely used in the study of adsorbed gases.[11] In principle, it is possible to modify the surface binding potential, in a reasonably controlled and well characterized way, by preplating with either an inert gas or hydrogen. The objective is to coat the graphite with an integral number of atomic layers of the preplating gas and to provide a composite substrate of weaker binding potential. This binding potential can be varied from that of bare graphite to that of the preplating material for a sufficiently thick film, so long as it wets the graphite surface. This is the method used by us. We have plated the graphite with a bilayer and a trilayer of HD. Here we used HD rather than H_2 or D_2 because of the absence of any ortho-para conversion and associated heating at ultralow temperatures.

Our use of hydrogen plating has also been motivated, in part, by previous studies of the superfluidity of ^{4}He on hydrogen films. The expected advantage of using a thick hydrogen film as a substrate was to avoid solidification of the first ^{4}He layer, offering the prospect of observing superfluidity in a submonolayer ^{4}He film. Brisson *et al.*[12] studied third sound propagation in helium films adsorbed on hydrogen-plated glass, while Mochel and co-workers,[13] Adams and Pant[14] have investigated helium on metallic surfaces plated with thick hydrogen films using third sound and torsional oscillators, respectively. These last two studies indeed give evidence of submonolayer superfluidity of the ^{4}He film. In addition, Mochel and Chen[13] found evidence for a second transition below the superfluid transition and also observed two third sound modes under certain conditions. Although these experiments rely on the formation of a uniform hydrogen film, it is in fact not clear that hydrogen wets metallic substrates. Indeed, there is some clear experimental evidence to the contrary.[15] Thus, the philosophy behind the present experiment was to start with well characterized thin hydrogen films, up to three atomic layers, adsorbed on graphite. The structure of such films has been investigated by neutron scattering and their density determined.[16] It was established that they wet the surface. The goal to grow a thick hydrogen film on graphite remains a challenge for the future. The first study of the superfluidity of ^{4}He on hydrogen-plated graphite was the third sound measurements of Zimmerli, Mistura, and Chan[8] (ZMC). Heat capacity measurements have also been performed by Vilches and co-workers,[17] providing valuable insights into the structure of the ^{4}He film.

One disadvantage of the exfoliated graphite substrate is that, on length scales greater than of the order of 1 μm it is extremely disordered. This results in a tendency for the superfluid film to be entrained by the oscillator, so that the full period shift due to the onset of superfluidity is not observed. This effect is parameterized by a quantity, conventionally referred to as the χ factor, which reflects the fraction of the superfluid which does not decouple from the surface. For mylar[4] $\chi \sim 0.14$, while for Grafoil CR[6] $\chi = 0.989$, which reflects the poor connectivity of the surface. The present work gives a value of about 0.95, depending on the preplating [see Sec. 3.4 for more details]. However, although these χ factors are relatively close to unity, tending to reduce the observed period shifts due to superfluidity, this is compensated for by the large specific surface area of the substrate.

A broad overview of the growth of helium films on graphite is as follows. The submonolayer film has a rich phase diagram that has been characterized by heat capacity[18] and neutron scattering measurements.[19] At the coverage at which a second layer begins to form (second layer promotion) the first layer consists of an incommensurate solid on a triangular lattice.[20] At third layer promotion the second layer is also solid at sufficiently low temperatures.[9] Subsequent layers are fluid; thus only two layers solidify on bare graphite. In the present work we have preplated the graphite by a bilayer and a trilayer of HD. In contrast to bare graphite, it appears that in this case only one helium layer solidifies due to the weaker binding potential of the preplated graphite surface. Note that, as previously mentioned, it is believed that for a bulk hydrogen surface the binding potential is weak enough to prevent solidification of the first helium layer.[21]

A further important detail concerns the evolution of the fluid layers. Consider the second layer on bare graphite, which at low densities is fluid (the layer begins to solidify at about 5.5 nm^{-2}). Theory predicts that, at sufficiently low temperatures, this fluid is self condensed[22] with a density of roughly 4 nm^{-2}, which is supported by measurements of the heat capacity.[9] On cooling, at second layer coverages of less than 4 nm^{-2}, it is therefore expected that the second layer fluid first phase will separate into a low density ''gas'' and a high density ''fluid''. (At $T=0$ the density of the ''gas'' component vanishes and that of the fluid is of the order of 4 nm^{-2}.) Following phase separation, the superfluid transition subsequently occurs in the high density liquid component. Thus, superfluid onset in this case is controlled by the intersection in the temperature-coverage plane of the boundary of the 2D gas-liquid coexistence region and the line of superfluid transitions of a uniform fluid film.[23,24] Intriguingly, Clements *et al.*[25] found such a coexistence region in each of the first three fluid layers on bare graphite, or layer by layer condensation. The possible interplay between such phase transitions in the film and its superfluidity is an important factor in the interpretation of these experiments.

The organization of this paper is as follows. A brief description of the experimental method is given in Sec. 2, including details of the torsional oscillator, the *in situ* pressure gauge for sample characterization and the method of data collection. Section 3 contains the main experimental results together with their interpretation. Although the observed behavior is rich in detail, we believe the systematics of the interplay between superfluidity and film structure emerge quite clearly. For clarity this section is split into a number of subsections dealing with (i) the method adopted to preplate the graphite with a bilayer or trilayer of HD, (ii) the characterization of the growth of the ^{4}He film on these preplated substrates by vapor pressure adsorption isotherms. Next is the longest subsection (iii) which describes the evolution of the superfluidity in the first two fluid layers. These results appear to show that a periodic potential strongly sup-

presses superfluidity and that the superfluid transition of two fluid layers is no longer described by Kosterlitz-Thouless theory in its simplest form. In subsection (iv) we discuss our determination of the χ factor of the substrate. A number of further interesting experimental observations are collected in (v), including features which may signify the layer by layer condensation in the film, the observation of periodicity of the third sound speed and a coverage dependence of the vortex dynamics. Section 4 summarizes the main conclusions of the paper, with suggestions for future work.

2. EXPERIMENTAL METHOD

The torsional oscillator is of conventional design, consisting of a stycast 1266 shell, with internal diameter 18 mm and height 12 mm, packed with Grafoil and mounted on a hollow BeCu torsion rod. The torsion mode or floppy mode are driven and detected capacitatively. The frequencies are 1056 and 605 Hz, respectively. The device is operated in a self-resonant oscillator circuit, at constant drive voltage, with the torsional oscillator as the frequency determining element. The period of the oscillator is measured with a HP5335A counter. The response of the oscillator is preamplified, and then lock-in detected. The oscillation amplitude is proportional to the quality factor of the oscillator, and is calibrated by observing the ring down of the oscillator on removing the drive. The Grafoil sample is in the form of disks 0.15 mm in thickness, providing a total surface area of 65 m^2. It was baked in vacuum at 1100 °C to remove impurities, before loading it in the cell. It is necessary to measure the background period and dissipation (both are smooth with no anomalous features) of the oscillator as a function of temperature between 12 K and 20 mK. When the adsorbed film is not superfluid, the torsional oscillator simply acts as a sensitive microbalance, with a period shift proportional to the coverage (mass) of the adsorbed film. For our oscillator the sensitivity with respect to the areal density of the ^{4}He film is 26 ns·nm^2.

The cell is attached via a massive vibration isolator to a cell plate, which in turn is connected to the mixing chamber of a cryogenic-cycle, sorption-pumped dilution refrigerator[26] via a weak thermal link. This enables the temperature of the cell to be swept slowly, using a heater attached to the cell plate, to accumulate period and dissipation data. The sweep rate is such that there is negligible hysteresis between data taken on warming and cooling. The temperature is measured by a 470-Ω Speer resistor and a GaAs chip resistor,[27] calibrated by a ^{3}He melting curve thermometer between 0.05 and 0.8 K and by a calibrated germanium resistance thermometer between 0.3 and 4 K.

An *in situ* pressure gauge similar in design to that used by Zimmerli[28] and Crowell[6] was connected to the cell and mounted on the cell plate. The deflection of the gold-plated kapton membrane was detected capacitatively and yielded a pressure resolution of 5 nbar. The reference volume of this gauge was connected by a capillary to room temperature for rough evacuation, a small graphite pelletplaced inside the reference volume ensured a good vacuum at low temperatures and provided a better reference pressure than simply connecting one side of the diaphragm to the vacuum can (in our case it was pumped by a graphite cryopump attached to the 1-K pot). The gauge was calibrated against the vapor pressure of liquid ^{4}He (actually a thick ^{4}He film of 20 layers in the torsional oscillator), in the temperature range 0.75–1.25 K. This gauge was used for vapor pressure adsorption isotherms to characterize the growth of the HD preplating film and the ^{4}He film. In addition, the in situ gauge monitored the vapor pressure of the film during collection of period data, enabling corrections to be made to the oscillator period due to desorption of the film at higher temperatures. The system was also equipped with a room-temperature Paroscientific pressure gauge.[29] The cell fill line was equipped with a series of heaters, which were used for preplating the graphite with hydrogen during the performance of isotherms (at 12 K and 10 K) and when cooling the cell to 4.2 K, to ensure that the cell is the coldest point, thus avoiding the formation of bulk hydrogen in the fill line. The period of the torsional oscillator, which effectively acts as a microbalance, is an extremely sensitive detector of any unwanted loss of hydrogen from the cell.

3. RESULTS

3.1. Preplating with HD

Measurements on ^{4}He films were made with preplatings of a bilayer and a trilayer of HD. The procedure for determining these preplatings is as follows. The surface area of the sample is determined by a 4.2 K ^{4}He isotherm, taking point B[18] as the indicator of first layer promotion. We use this as the reference for all surface densities in this paper. The density of H_2 and D_2 films on graphite (one, two and three layers) has been measured by neutron scattering.[16] With this information and the bulk molar volume, we generate the density per layer as a function of the reciprocal number of layers. These data can be interpolated to estimate the values for HD films, with a precision of about 2% (18.3 and 27.1 nm^{-2} for bilayer and trilayer, respectively). Scaling the dose for ^{4}He monolayer completion by the ratio of these densities and the neutron scattering density of a completed ^{4}He monolayer[20] (11.25 nm^{-2}), gives the required estimated dose for a bilayer or trilayer of HD. Further, we have obtained a HD vapor pressure isotherm at 12 K and 10 K and found compressibility minima in good agreement with these estimates (corresponding to densities 18.9 and 27.2 nm^{-2} for the bilayer and trilayer). The preplating coverages which we chose were those corresponding to these compressibility minima.[30] Following these procedures, we can be confident that the chosen preplatings are very close to exactly two and three layers.

3.2. Characterization of ^{4}He film

For each HD preplating case a helium isotherm was used to characterize the growth of the film, locating the layer promotions. Results for the bilayer and trilayer preplating of isotherms at 940 mK are shown in Fig. 1. Layer promotions were determined from compressibility minima, and a ^{4}He coverage scale was defined. These coverages are referred to the 4.2 K ^{4}He isotherm on bare graphite, for which first layer promotion is taken as 11.4 nm^{-2}. For the bilayer preplating these promotions occur at 7.3, 12.5, 18.7 and 25.2 nm^{-2}. The last three values are 20% smaller than those obtained by

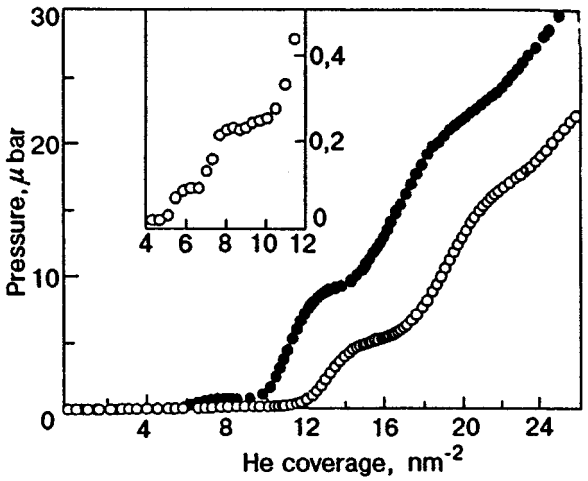

FIG. 1. ^{4}He vapor pressure isotherms, taken at 940 mK, for graphite plated with a bilayer (open circles) and trilayer (closed circles) of HD. Inset shows detail for bilayer preplating, near first layer promotion. Structure is believed to arise from solidification of film, followed by promotion at 7.3 nm^{-2}.

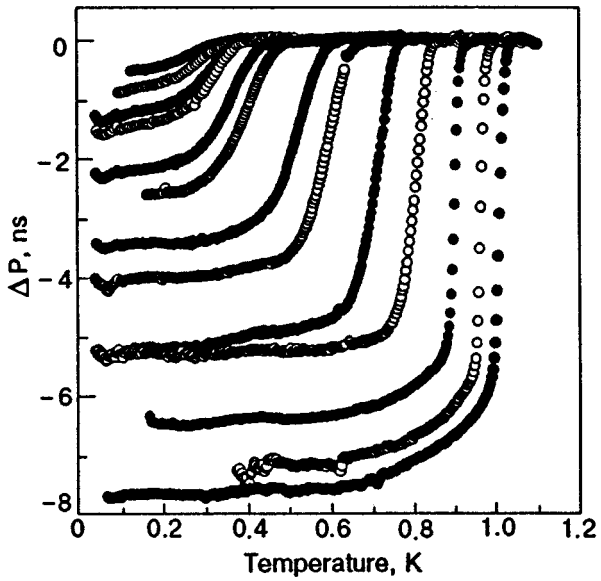

FIG. 2. Period shift due to superfluid transition for trilayer preplating. Coverages; 7.02, 7.50, 8.15, 8.47, 9.11, 9.35, 9.61, 9.74, 10.16, 10.60, 11.71, 12.58, and 13.11 nm^{-2}.

ZMC for ^{4}He on graphite preplated by a bilayer of hydrogen. Thus, our coverage scales are consistent within a constant scaling factor. For the trilayer preplating we found shifted compressibility minima at 5.65, 10.3, 16.7, 24.0 nm^{-2}. Most of the coverage offset between these two isotherms for different preplatings is attributable to a significantly lower density of the first ^{4}He layer for the trilayer preplating. For both preplatings no superfluid signature is observed from the first ^{4}He layer fluid, at lower coverages. This layer is believed to be solid on completion. The low density of second layer promotion for the trilayer preplating may arise from a registered structure which resists compression. In the following we assume that the first layer is solid; the second and third layers are thus the first and second fluid layers. The development of superfluidity in these fluid layers is discussed in the next subsection.

We should note that CR detected superfluidity in the second layer of ^{4}He on bare graphite prior to solidification; the period shifts associated with superfluidity have an anomalous temperature dependence. According to the phase diagram of Greywall,[9] these superfluid transitions occur when the film is a coexistence of gas and liquid. This may be responsible for the anomalous behavior observed. For the present case of HD preplated substrates we currently believe that the observation of superfluidity in the first ^{4}He layer is precluded by the solidification of the film, which in this case occurs at lower second layer coverages. On the basis of experiments on ^{3}He films on a HD bilayer preplated graphite substrate, we expect to enter a commensurate solid-fluid coexistence region at 4.8 nm^{-2}, in the low-temperature limit.[31]

3.3. Evolution of superfluidity in the first two fluid layers

The results for the period shift due to the superfluid transition and the associated dissipation peak are shown in Figs. 2 and 3 for a selection of lower coverages for the trilayer preplating.[32] The temperature dependence of the period shift for the three highest coverages, after formation of the second fluid layer, are most characteristic of a KT transition. The dissipation peak associated with the transition is relatively narrow, with the temperature half-width of about 30 mK. For each coverage these data allow us to determine the total period shift due to the onset of superfluidity, $\Delta P(0)$. This quantity is the difference between the estimated $T=0$ limit of the period and the period immediately above the super-

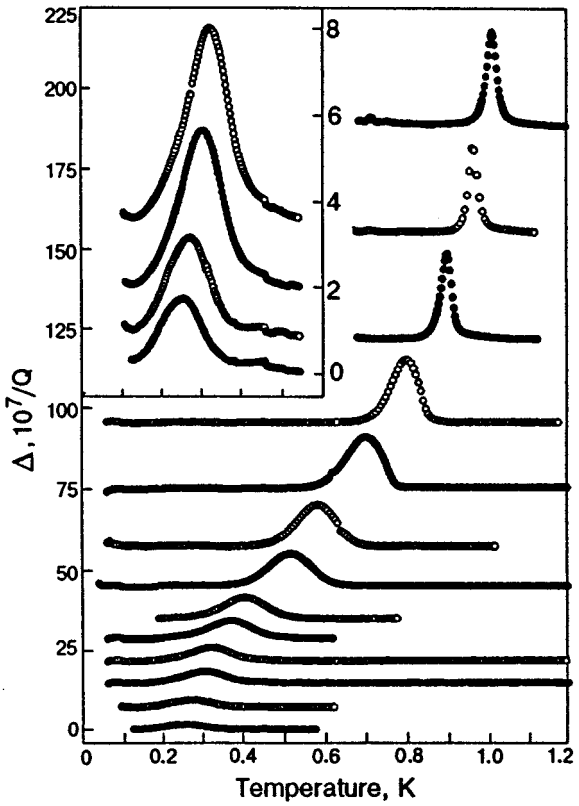

FIG. 3. Dissipation peaks at the superfluid transition, with trilayer preplating. Coverages are the same as for Fig. 2. Data we displaced for clarity. The inset shows data for the first four coverages on an enlarged scale.

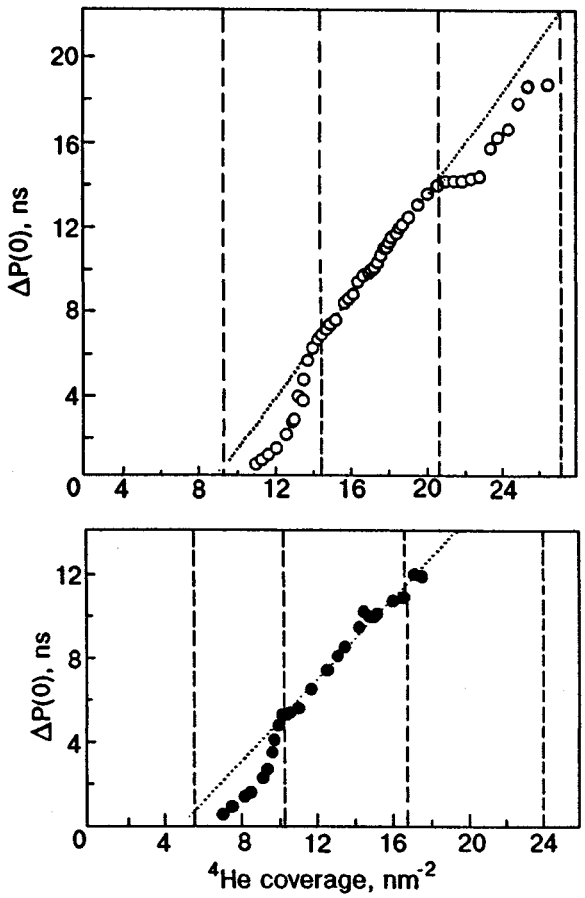

FIG. 4. Total period shift as a function of coverage. Upper plot (open circles); bilayer preplating. Lower plot (filled circles); trilayer preplating. Vertical dashed lines indicate coverages of layer promotions, inferred from vapor pressure isotherms. Dotted line is a linear fit to period shift data in the third layer (second fluid layer).

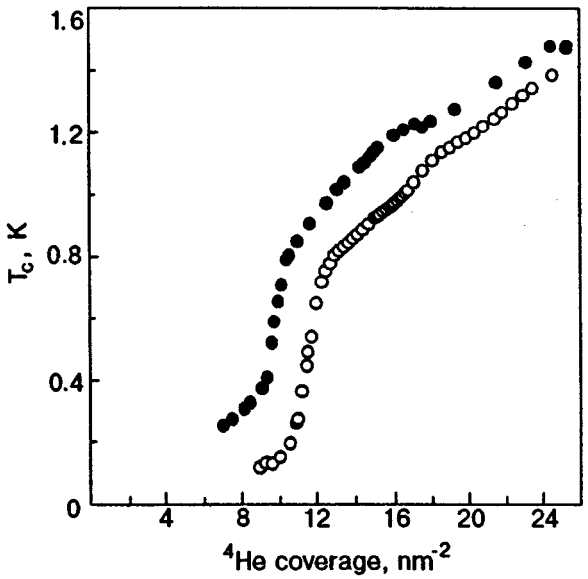

FIG. 5. Temperature of dissipation peak, used to locate superfluid transition temperature, as a function of coverage. Open circles; bilayer preplating. Closed circles; trilayer preplating.

fluid transition, after applying the vapor pressure correction. These data are plotted as a function of the total ^{4}He coverage in Fig. 4. The values of T_c, here defined as the temperature of the dissipation maximum, are shown in Fig. 5.

a) First fluid layer

It can be seen that the behavior is rather similar for the two preplatings, apart from a coverage shift referred to earlier, and is attributed to difference in densities of the first solid layer. The behavior in the second ^{4}He layer (first fluid layer) is very similar to that observed in the third layer (again first fluid layer) by CR on bare graphite. We interpret the break in the coverage dependence of $\Delta P(0)$ and T_c part through filling of the fluid layer as due to the two-dimensional condensation (''puddling'') of that layer at lower coverages, as previously proposed by CR. Thus, up to a total coverage 10.8(9.3) nm^{-2} for the bilayer (trilayer) preplating, the fluid layer separates on cooling into a low-density ''gas'' and high-density ''liquid.'' The superfluid transition observed is that of the high-density ''liquid'' component. The break then corresponds to the point in the $T-n$ plane at which a line of superfluid transitions emerges from the two phase coexistence regime. These results are broadly consistent with the third sound measurements of ZMC[8] on H_2 plated graphite, which also find superfluidity in the second ^{4}He layer.

Recent heat capacity measurements on this system,[17] with preplatings slightly in excess of exact bilayer and trilayers of hydrogen, also provide evidence of such a layer condensation, with a critical temperature of 0.8 K. From our data, for both preplatings, we estimate the minimum density of the second layer fluid, at which a uniform fluid is stable to $T=0$, to be $n_2=4\pm0.5$ nm^2, where the error largely comes from uncertainties in the precise density of the first solid layer. This is in reasonable agreement with theory.[22,25]

Examination of the period shift curves for the four coverages studied below the break for the trilayer preplating (Fig. 2) shows that ''superfluid onset,'' now defined as the temperature at which a shift in period is first resolved, occurs at the same temperature, $\sim$0.4 K, at each coverage. Similar behavior is seen for the bilayer preplating. This observation supports the model of a superfluid transition occurring in puddles of condensed liquid, whose density remains constant as a function of coverage. Note that the values of T_c plotted in Fig. 5 are the temperatures of the dissipation maxima, which show a coverage dependence in this regime. This is clearly attributable to changes in the temperature width of the superfluid transition. The decrease in width of the transition as the coverage is increased may be associated with the increasing size of the puddles or with the effects of percolating superflow between puddles.

We cannot be sure of the morphology of these superfluid puddles but our results suggest that they decouple from the substrate. Either the high-density component forms in a single patch, perhaps at the edge of a Grafoil platelet or it is not necessary for superfluid patches to percolate in order to slip relative to the surface. Thus, while it is clear that percolation is necessary for dc superfluid mass transport, it might be expected that a torsional oscillator will continue to detect superfluidity, even if the liquid separates into a set of non-

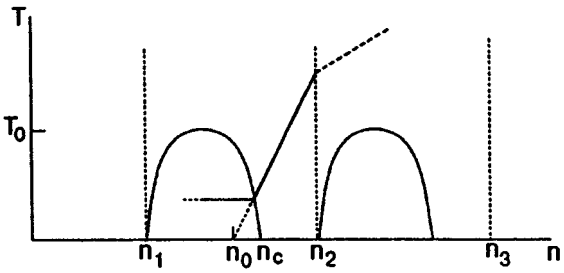

FIG. 6. Schematic diagram to illustrate proposed interaction of superfluidity and 2D condensation phenomena. Layer promotions occur at n_1, n_2, n_3. At n_1 the first layer is solid. For $n_1<n<n_c$ the second layer consists of a self-condensed fluid - gas coexistence. For $n_c<n<n_2$ the second layer is a uniform fluid. After promotion to a third layer at n_2 the third layer fluid is also self condensed, as suggested in Ref. 25. The critical temperature of both gas-liquid coexistence regions is T_0, probably of the order of 0.8 K. A line of superfluid transition temperatures T_c is also shown; T_c is constant in the coexistence region and on entering the uniform fluid phase increases with coverage faster than the KT slope, extrapolating to zero at n_0 (dead layer). There is a break in the coverage dependence of Tc at promotion, $n=n_2$.

percolating patches.

At higher fluid layer coverages above the break in the regime where we expect a uniform fluid layer, there is a rapid increase in T_c and $\Delta P(0)$. For both preplatings, this continues until the formation of a second fluid layer. At this point (the third layer promotion), there is a second break in the coverage dependence. Similar behavior was seen on bare graphite by CR.[6] We interpret this data immediately before the third layer promotion (formation of second fluid layer) as follows. If in Fig. 4 the line of period shifts (following the break indicating emergence from the coexistence region) is extrapolated to zero, this determines the density at which the onset of superfluidity might be expected for a uniform fluid layer. The line of transition temperatures extrapolates to essentially the same coverage. They are 10.5 nm^{-2} and 8.5 nm^{-2} for the bilayer and trilayer, respectively, and we interpret them as the ''dead layer'' prior to the third layer promotion. Clearly, superfluid onset as a function of coverage is not directly observable because of the intervention of 2D condensation. This is schematically illustrated in Fig. 6. We believe that this suggests that superfluidity is suppressed in the uniform two dimensional fluid. For both preplatings the extrapolated fluid density, which corresponds to the ''dead layer'' coverage, is 3 nm^{-2}.

This value is comparable to that obtained from third sound measurements on a (nominally) thick hydrogen film by Shirron and Mochel[13] (this gives a dead layer of 3.9 nm^{-2}, after scaling their surface densities by a factor 1.67, as suggested by Cheng *et al.*[33]). Torsional oscillator measurements on a thick H_2 film[14] give a dead layer of about 1/2 ''layer.'' Note that in the present experiment we have a high degree of confidence in the quality of the surface. In the present measurement, for the bilayer and trilayer preplatings, the apparent inert layer corresponds to about 0.6 of the density of the fluid layer at promotion plus the first solid layer. One might call the fluid component of this inert layer as the ''nontrivial'' component. The results of CR on bare graphite are consistent with these observations.

In the coverage range under consideration, which corresponds to a uniform fluid layer before the promotion, the increase of T_c with coverage is significantly faster than the KT line, $T_c=0.156\,n(\mathrm{K\cdot nm^2})$. This relation assumes[2] $\rho_s(T_c)=0.82\rho_s(0)$. It also assumes the bare mass of the ^{4}He atom. The width of the dissipation peak temperature at the superfluid transition also decreases rapidly with increasing coverage. The origin of this strong suppression of superfluidity and the rapid increase in T_c with increasing coverage remains an open question. It may arise from residual heterogeneity of the surface; however, the observed behavior is similar for the two preplatings reported here and for bare graphite. The observations may indicate that the periodic potential of the underlying solid layer influences the superfluid onset. The rapid increase in T_c may stem from the fact that the film become more delocalized normal to the surface; theory suggests[25] that such an effect can occur at a coverage significantly lower than that of the layer promotion.

Note that, although we refer to this fluid layer as being uniform, we expect on the basis of Monte Carlo simulations of a ^{4}He monolayer on hydrogen[34] that the local density will show structure arising from the periodic surface potential. These simulations show an effective ^{4}He mass up to twice that of the bare mass and a 20% suppression in the superfluid density, as well as condensation below 4.6 nm^{-2}.

From the above discussion, it appears that there is overall consistency between this and previous experiments, with evidence for a strong suppression of superfluidity in a single fluid layer at lower coverages. In the present case this suppression is small at third layer promotion, when a second fluid layer forms [see more detailed discussion in the following section (b)]. In our opinion, theoretical work on the influence of the periodic potential on the superfluidity of a single fluid layer, taking into account the delocalization of the film normal to the substrate, would be of great interest.

b) Two fluid layers

At a coverage of 12.5(10.3) nm^{-2} the third layer forms for the bilayer (trilayer) preplating. We now have two fluid layers above a solid ^{4}He layer above the preplated graphite substrate. The coverage dependence of both T_c and $\Delta P(0)$ show a sharp break at this third layer promotion for both preplatings. As the third layer (second fluid layer) grows, the total period shift $\Delta P(0)$ increases linearly with coverage to a good level of accuracy. The quantity $\Delta P(0)$ is a measure of the mass of the film participating in the superfluidity in the $T=0$ limit. A linear fit to this period data in this coverage range extrapolates to zero at a coverage of 6.7 (4.8) nm^{-2} for the bilayer (trilayer) preplating. In both cases this value is close to, but slightly smaller than, the coverage at which second layer promotion was observed: 7.3 (5.65) nm^{-2}. This is powerful evidence that in the low-temperature limit, the film now consists of two superfluid layers above a solid ^{4}He layer. All of the fluid participates in the superfluidity; the ''dead'' layer is merely the first solid layer. This contrasts with the nontrivial dead layer we have argued for in the first fluid layer and is clear evidence for a shift in the density of the inert layer as a function of the coverage of the film.

If a line of transitions with the KT slope is drawn in Fig. 5, $T_c=0.156\ (n-n_{\mathrm{dead}})$ with $n_{\mathrm{dead}}=6.7$ (4.8) nm^{-2} for the bilayer (trilayer) preplating, the transition temperature is closest to that observed just at third layer promotion, as the

second fluid layer forms. Indeed, for the trilayer preplating the line almost coincides with the data at this point. This suggests, therefore, that at third layer promotion the first fluid layer is completely superfluid, in marked contrast with the situation at slightly lower coverages. The behavior of ^{4}He on bare graphite as a second fluid layer forms (corresponding to fourth layer promotion in that system) is somewhat more complex. (Clearly, in comparing the evolution of superfluidity in the two systems it is the number of fluid layers that is important: it is $l-2$ for bare graphite and $l-1$ for preplated graphite, where l is the total number of layers.) The results of CR for T_c and ΔP show a plateau in the vicinity of third layer promotion, which is possibly attributable to a reconstruction of the film. We see a similar feature at fourth layer promotion for the bilayer preplating [see section 3.5.]. The absence of such an effect in the present experiment as the second fluid layer forms simplifies the interpretation.

It is interesting to compare the coverage dependence of T_c with that observed for ^{4}He on mylar.[2,4] In this case the ''dead layer'' is typically in the range 25–30 μmol·m^{-2}. A simple picture is that this is in the form of an amorphous coating of the substrate, which screens the heterogeneous substrate potential in such a way that additional ^{4}He atoms are delocalized. These fluid atoms undergo a superfluid transition via the KT mechanism; the data of Bishop and Reppy[2] show a linear $T-n$ dependence, which is well described by the KT relation $T=0.156n$ (K·nm^2). AMR[4] report data over a wider coverage range. In this case the dead layer is 28 μmol·m^{-2}; the initial $T-n$ relation is again reasonably consistent with the KT line. However, at about 40 μmol·m^{-2}, which corresponds to a fluid density of 7 nm^{-2}, the slope of the $T-n$ line decreases. Above 40 μmol·m^{-2} AMR found the slope of the $T-n$ line to be 0.071 Knm^2. This behavior is reminiscent of the sharp decrease in dT_c/dn as a result of formation of a second fluid layer in the present hydrogen preplated graphite experiment. In all cases this occurs at $T_c \sim 0.8$ K. It is intriguing, and we believe significant, that for both preplatings we have investigated T_c increases linearly with coverage as the second fluid layer fills with a slope quite close to that seen on mylar (0.084 Kn·m^2 and 0.060 Kn·m^2 for trilayer and bilayer preplating, respectively). This suggests that the transition in behavior is a direct result of the formation of two fluid layers. According to this view, the coverage dependence of T_c above promotion is an intrinsic feature of the superfluid transition in two coupled fluid layers. On the mylar substrate the film is not so highly layered. Therefore, in this case a sharp kink in the $T-n$ curve is not observed. Rather a more gradual but still pronounced change in slope occurs.

In contrast, below this feature, for just one fluid layer, the behavior is entirely different for the two substrates. The mylar substrate, which is screened by the ^{4}He inert layer, provides a disordered potential. There is no $2D$ condensation of the fluid, and the transition temperature follows the KT line. In contrast, the atomically flat plated graphite substrate provides a periodic potential. At fluid coverages below of about 4 nm^{-2} the uniform fluid is unstable at sufficiently low temperatures and 2D condensation occurs. Above this coverage there is a strong suppression of both the superfluid transition temperature and the superfluid density, possibly because of the influence of the periodic potential due to the solid underlayer. These results challenge our understanding of superfluidity in helium films and hopefully will stimulate more theoretical work.

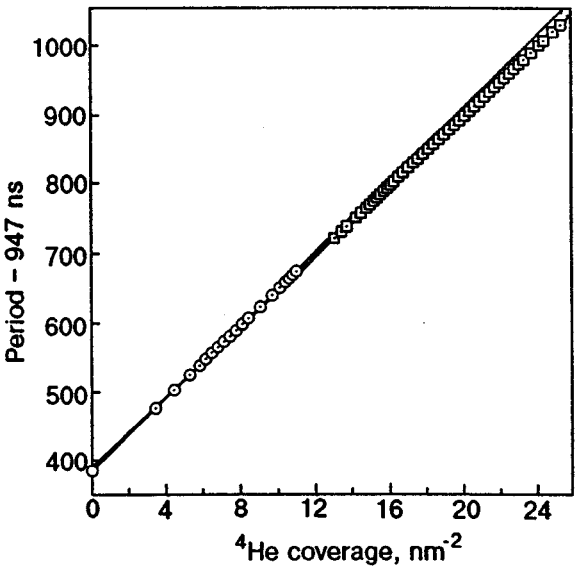

FIG. 7. Determination of the χ factor. ^{4}He filling curve at 940 mK (for trilayer preplating), showing change in the period as a function of coverage. Circles; nonsuperfluid coverages. Squares; superfluid coverages. Linear fit to each of these sets of data are shown. The results in the vicinity of a superfluid transition are omitted from analysis.

3.4. Determination of the χ factor

Let us now discuss measurements of the χ factor of the surface. It is obtained from an isotherm of the oscillator period as a function of coverage, taken at the same time as the vapour pressure isotherm. This filling curve data refers to fully annealed films; this procedure was possible because of the good long-term stability of the cell period. (An alternative is to fill the cell at a constant temperature, which can lead to nonuniform coverages.) The results for the trilayer are given in Fig. 7. In this case the superfluid transition temperature at the temperature of the measurement is about 12 nm^{-2}. A linear fit to data below 11 nm^{-2} (normal film at this temperature) gives a mass sensitivity of 26.01 ns·nm^2. For coverages above 13 nm^{-2}, for which the film is superfluid, a linear fit gives a slope of 25.014 ns·nm^2. This gives a χ factor of 0.9617. For the bilayer preplating we obtain a normal mass sensitivity of 26.00 ns·nm^2, in excellent agreement with the trilayer result. In this case the χ factor is 0.9519. With this data the expected slopes of the $\Delta P(0)$-vs-n lines after third layer promotion are 1.25 (0.995) ns·nm^2 for the bilayer (trilayer) preplating. These values compare quite well with those obtained from Fig. 4, 1.176 (0.949) ns·nm^2. It is possible that the superfluid fraction at $T=0$ is suppressed in these films, but this cannot be measured directly since it cannot be separated from the effects represented by the χ factor. CR report a χ factor of 0.989 for ^{4}He on bare graphite. For our Grafoil sample with no preplating we find $\chi=0.956$, a result obtained from a filling curve on bare graphite in the same cell following the

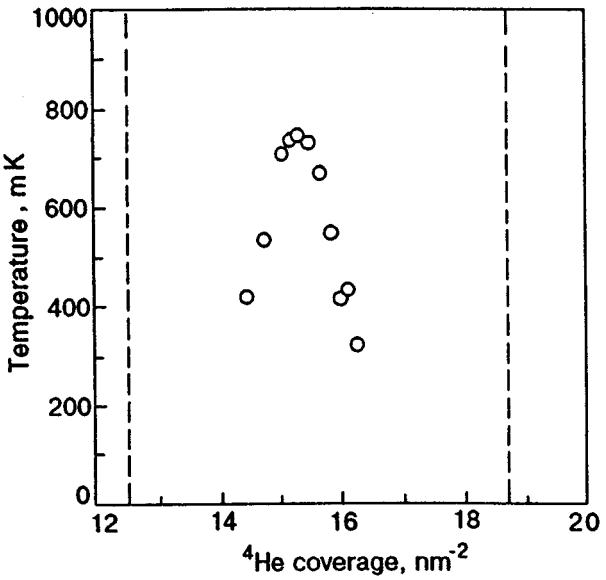

FIG. 8. Locus in $T-n$ plane of the features in the oscillator (small period step, sharp peak in dissipation) tentatively associated with puddling transition in third layer.

same procedures. It seems, therefore, that the preplating does not have a big effect on the χ factor. It is likely that most of the difference between our result and that of CR stems from the substrate quality or from the effects of different heat treatments.

3.5. Other experimental features

In the third layer (second fluid layer) for bilayer preplating we find a set of small steps in the period data, which are associated with small, sharp peaks in the dissipation. Because we have studied a large number of closely spaced coverages, we can follow the evolution of this feature. The locus in the $T-n$ plane, shown in Fig. 8, is suggestive of that of a two-phase coexistence region or layer-by-layer fluid condensation, as predicted by Clements *et al.*[25] Thus, in this region the second layer would be a uniform fluid and the third layer is puddled. The width of the coexistence region is $4\ \mathrm{nm}^{-2}$ and the critical temperature of 0.8 K is close to that found from the heat capacity measurements in the second layer. We emphasize that this attribution is extremely tentative. We should point out that in this coverage regime the period shift and amplitude data suffer from contamination by third sound resonances.[35] They could be eliminated in an oscillator with a lower operating frequency. Driving the oscillator in its floppy mode helps separate out third sound resonances. However, we can exploit the observed mode crossings, whose most pronounced signature is a dramatic decrease in the Q factor of the torsion mode, to trace the evolution of the third sound velocity. For the bilayer preplating the temperature of the mode crossing exhibits a maximum at $16.7\ \mathrm{nm}^{-2}$; this arises from a compressibility minimum in perfect agreement with that determined from the vapor pressure isotherm that locates the third layer promotion, as expected. In contrast, the measurements of ZMC[8] show a coverage offset between the maxima in the third sound velocity and the compressibility minima. This may arise because the measurements are dominated from different graphite surfaces in the same cell. The velocity data comes from a cleaved HOPG (highly oriented pyrolytic graphite) crystal, while that for the vapor pressure is dominated by the graphite foam ballast in the same cell. Above fourth layer promotion (formation of the third fluid layer), the bilayer preplating period shift data show a plateau of width $2.5\ \mathrm{nm}^{-2}$. Additional ^{4}He atoms added to the film appear not to contribute to the superfluidity. This most likely arises from a reconstruction of the film, which involves an increase in the density of the first solid layer. A similar plateau of comparable width was seen by CR, also at fourth layer promotion, which in this case corresponds to the formation of the second fluid layer. These authors suggested a number of possible explanations for such a structure in the period shift isotherms, including that of film reconstruction just mentioned. It seems that the absence of a plateau in these data above third layer promotion should impose additional constraints on the possible explanation of such features. On the one hand, it appears to favor less strongly the model of Zimanyi *et al.*,[36] who calculated the superfluid density in Bose–Hubbard model. On the other hand, we do not believe that the plateau can arise from puddling, one of the possibilities suggested in Ref. 6 and by Clements *et al.*,[25] since we observed a linear dependence of ΔP on coverage in the second fluid layer. Puddling is predicted in this layer, and as discussed, we have signatures in the torsional oscillator response, which can tentatively be attributed to the onset of puddling.

Another striking feature of the evolution of superfluidity concerns the width of the dissipation peak at superfluid onset. It should be sensitive to the vortex dynamics in the film. For both preplatings the data show a rather similar coverage dependence (Fig. 9). Following the end of the second layer puddling, the peak half-width decreases dramatically through third layer promotion. As the next fluid layer (third layer) fills, the dissipation exhibits a minimum, near 0.3 layer filling, followed by a maximum, near 0.7 layer filling for both preplatings. Since as the third layer fills the superfluid transition temperature exceeds 0.8 K above the critical temperature for gas-liquid coexistence, the second and third fluid layers should be uniform fluids at superfluid onset, and therefore there should be no effect of puddling on the dissipation near the onset.

4. CONCLUSIONS

The present experiment and the previous results of Crowell and Reppy reveal a wealth of new phenomena in atomically layered superfluid ^{4}He films on graphite. Varying the substrate potential by preplating has proved to be a valuable tool to extract ''universal'' features of the behavior of this system.

On the hydrogen bilayer and trilayer preplated surfaces we have studied there is no evidence for superfluidity in the first ^{4}He layer. The second layer appears to condense into a 2D liquid at sufficiently low temperatures for a layer filling below $4\ \mathrm{nm}^{-2}$. At higher coverages in this layer we believe it to be a uniform fluid. There is a rapid increase in the superfluid signal and T_c with coverage, much faster than that expected from KT theory. This may indicate a strong influence of the periodic substrate potential on superfluidity,

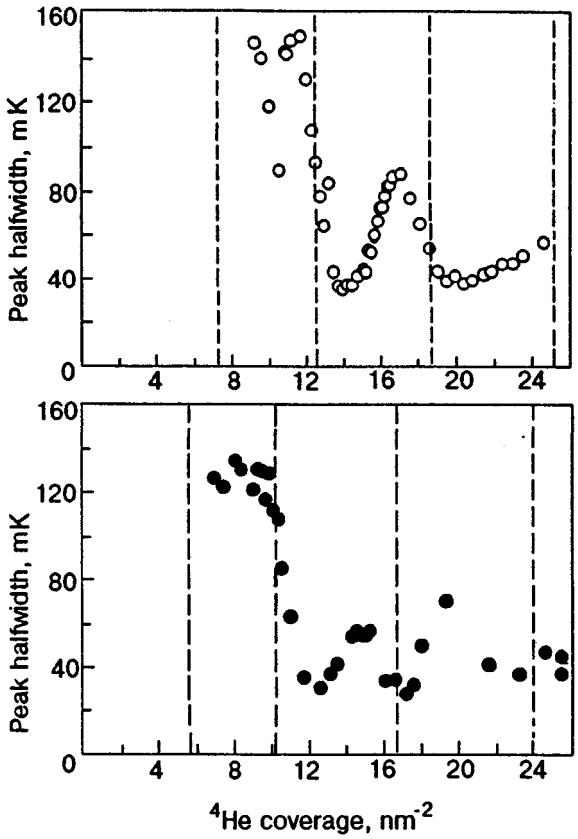

FIG. 9. Coverage dependence of the width of the superfluid transition. Temperature half-width of the dissipation peak at superfluid transition plotted as a function of coverage. Open (closed) circles are for bilayer (trilayer) preplating.

which by extrapolation would completely suppress the superfluidity of a uniform fluid layer at a layer filling of about 0.6. However, upon completion of the second layer (first fluid layer), the transition temperature is close to the KT line, with a dead layer corresponding simply to the first solid layer.

On formation of the third layer, the period shift data show that the system consists of two superfluid layers above an inert layer, which is assumed to be solid for both preplatings. The increase of the superfluid transition temperature with coverage is now significantly slower than the KT line, but similar to the behavior observed on mylar substrates. The superfluid transition temperature of the film would only appear to fit the expectation from KT theory at essentially one coverage, third layer promotion, for which the ^{4}He film consists of a single fluid layer atop a single solid layer above the preplated substrate.

We believe that more theoretical study is required to understand the superfluid transition of a single fluid layer subject to a crystalline potential. It would also appear that the system of two fluid layers of ^{4}He would merit further study. To what extent are the layers, in particular, the vortices, coupled? There are possible analogies with high-T_c materials here. A future experimental objective is to attempt to grow a thick hydrogen film and to study the expected submonolayer superfluidity with torsional oscillator techniques.

ACKNOWLEDGMENTS

We thank C. Lusher for help with the data acquisition system and M. Siqueira for suggestions and comments. We should also especially like to thank P. Crowell, G. Mistura, P. S. Ebey, and O. E. Vilches for useful advice and discussions. Technical assistance was provided at various stages by J. Taylor, T. Wilkinson, and A. Betts. This work was supported by EPSRC (UK) and the Royal Society, and supported, in part, by INTAS program (project 94-3416).

[a]Permanent address: Institute of Experimental Physics, Slovak Academy of Sciences, Kosice, Slovak Republic.
[b]Permanent address: B. I. Verkin Institute of Low Temperature Physics, Kharkov, Ukraine.
[c]Permanent address: Oxford Instruments plc, Eynsham, U.K. Former address: B. I. Verkin Institute of Low temperature Physics, Kharkov, Ukraine.
[d]Corresponding author: J. Saunders@rhbnc.ac.uk

[1] J. M. Kosterlitz and D. J. Thouless, J. Phys. C **6**, 1181 (1973), *ibid*. 7, 1046 (1974).
[2] D. J. Bishop and J. D. Reppy, Phys. Rev. Lett. **40**, 1727 (1980); Phys. Rev. B **22**, 5171 (1980).
[3] E. L. Andronikashvili, Zh. Éksp. Teor. Fiz. **16**, 780 (1946).
[4] G. Agnolet, D. F. McQueeney, and J. D. Reppy, Phys. Rev. B **39**, 8934 (1989).
[5] M. P. A. Fisher, P. B. Weichmann, G. Grinstein, and D. S. Fisher, Phys. Rev. B **40**, 546 (1989).
[6] P. A. Crowell and J. D. Reppy, Phys. Rev. Lett. **70**, 3291 (1993); Physica B**197**, 269 (1994); Phys. Rev. B**53**, 2701 (1996).
[7] P. Mohandas, C. Lusher, B. Cowan, and J. Saunders, J. Low Temp. Phys. **89**, 613 (1992); P. Mohandas, C. P. Lusher, B. Cowan, and J. Saunders, J. Low Temp. Phys. **101**, 481 (1995).
[8] G. Zimmerli, G. Mistura, and M. H. W. Chan, Phys. Rev. Lett. **68**, 60 (1991).
[9] D. S. Greywall and P. A. Busch, Phys. Rev. Lett. **67**, 3535 (1991); D. S. Greywall, Phys. Rev. B **47**, 309 (1993).
[10] E. Krotscheck, Phys. Rev. B **32**, 12453 (1991).
[11] For a recent review see M. H. W. Chan, *Phase Transitions in Surface Films 2*, Ed., H. Taub, G. Torzo, H. J. Lauter, and S. C. Fain Jr., Plenum, 1991.
[12] J. G. Brisson, J. C. Mester, and I. F. Silvera, Phys. Rev. B **44**, 12453 (1991).
[13] P. J. Shirron and J. M. Mochel, Phys. Rev. Lett. **67**, 1118 (1991); J. M. Mochel and M. T. Chen, Physica B **197**, 278 (1994); M. T. Chen, J. M. Roesler, and J. M. Mochel, J. Low Temp. Phys. **89**, 125 (1992).
[14] P. W. Adams and V. Pant. Phys. Rev. Lett. **68**, 2350 (1992).
[15] R. N. J. Conradt, U. Albrecht, S. Herminghaus, and P. Leiderer, Physica B **194–196**, 679 (1994).
[16] H. Wiechert in *Excitations in 2D and 3D Quantum Fluids*, Eds. A. F. G. Wyatt and H. J. Lauter, Plenum (1990).
[17] P. S. Ebey and O. E. Vilches, J. Low Temp. Phys. **101**, 469 (1995); P. Ebey, thesis, University of Washington and O. E. Vilches, private communication (1995).
[18] M. Bretz, J. G. Dash, D. C. Hickernell, E. O. McClean, and O. E. Vilches, Phys. Rev. A**8**, 1589 (1973).
[19] M. Nielsen, J. P. McTague, and W. Ellerson, J. Phys. (Paris) Colloq. C4-10 (1997); H. J. Lauter, H. Godfrin, V. L. Franck, and H. P. Schildberg, Physica B **165&166**, 597 (1990).
[20] H. J. Lauter, H. P. Schildberg, H. Godfrin, H. Wiechert, and R. Haensel, Can. J. Phys. **65**, 1435 (1987).
[21] E. Cheng, M. W. Cole, W. F. Saam, and J. Treiner, Phys. Rev. B **46**, 13967 (1992).
[22] P. A. Whitlock, G. V. Chester, and M. H. Kalos, Phys. Rev. B **38**, 2418 (1988).
[23] J. G. Dash, Phys. Rev. Lett. **41**, 1178 (1978).
[24] M. Schick and O. E. Vilches, Phys. Rev. B **48**, 9910 (1993).
[25] B. E. Clements, E. Krotscheck, and H. J. Lauter, Phys. Rev. Lett. **70**, 1287 (1993); B. E. Clements, J. L. Epstein, E. Krotscheck, and M. Saarela, Phys. Rev. B**48**, 7450 (1993); B. E. Clements and B. E. Clements, *ESF*

Workshop on Quantum Fluids and Solids (Interfaces), unpublished (1994).
[26] P. Mohandas *et al.* Physica B **194–196**, 55 (1994); V. A. Maidanov *et al.*, Sov. J. Low Temp. Phys. **20**, 527 (1994).
[27] Obtained from R. Rentzsch, see R. Rentzsch, K. J. Friedland, A. N. Ionov, M. N. Mateev, I. S. Shlimak, C. Gladun, and H. Vinkelberg, Physica Status Solidi, B **137**, 691 (1986).
[28] G. Zimmerli, thesis, Penn. State University.
[29] Paroscientific, Inc., Redmond, WA 98502 (USA).
[30] The compressibility is $(\partial n/\partial \ln p)/k_B T n^2$, where n is the coverage and p the vapour pressure.
[31] M. Siqueira, C. P. Lusher, B. P. Cowan, and J. Saunders, Phys. Rev. Lett. **71**, 1407 (1993) and unpublished heat capacity data.
[32] R. Ray, J. Nyéki, G. A. Sheshin, B. Cowan, and J. Saunders, Czech. J. Phys. **46** (Supp. S1), 422 (1996).
[33] E. Cheng, W. F. Saam, M. W. Cole, and J. Treiner, J. Low Temp. Phys. **92**, 11 (1993), and Ref. 12.
[34] M. Wagner and D. M. Ceperley, J. Low Temp. Phys. **94**, 185 (1994).
[35] We can now identify additional features in the dissipation and period shift below the superfluid transition, reported in J. Nyéki, R. Ray, V. Maidanov, M. Siqueira, B. Cowan, and J. Saunders, J. Low Temp. Phys. **101**, 279 (1995), as arising from such mode crossings between third sound resonances and the driven torsion mode. Note that these data were obtained with a different Grafoil sample to that used in the work reported in the present paper.
[36] G. Zimanyi, P. A. Crowell, R. T. Scalettar, and G. G. Batrouni, Phys. Rev. B **50**, 6515 (1994).

This article was published in English in the original Russian journal. It was edited by S. J. Amoretty.

Quantum nucleation of cavities in a liquid helium at low temperatures

S. N. Burmistrov and L. B. Dubovskii

Department of Superconductivity and Solid State Physics, Kurchatov Institute, Moscow 123182, Russia[1)]
(Submitted November 18, 1996)
Fiz. Nizk. Temp. **23**, 527–536 (May–June 1997)

The rate of the quantum cavitation in normal fluid ^{3}He and superfluid ^{4}He at temperatures down to absolute zero has been studied. The effect of energy dissipation due to viscosity and the effect of the finite compressibility of a fluid are incorporated into the calculation of the quantum cavitation rate. Because of the dissipative processes, the kinetics of the quantum cavitation in ^{3}He and ^{4}He proves to be qualitatively different. In normal ^{3}He it corresponds to the dissipative tunneling through a potential barrier. In contrast, in superfluid ^{4}He the effect of dissipation is of minor importance. In both liquids the role of the compressibility of a fluid enhances significantly for the small critical nuclei, which have several interatomic distances and can provide us the nucleation rates sufficient for the experimental observation of the homogeneous cavitation in the quantum regime. © *1997 American Institute of Physics.*
[S1063-777X(97)00505-7]

1. INTRODUCTION

Considerable theoretical discussion on the macroscopic quantum nucleation has recently been focused on the low-temperature cavitation in liquid helium at negative pressures.[1–4] Some intriguing problems, such as the tensile strength of liquid helium, i.e., the magnitude of the negative pressure required to produce nucleation of cavities, and the critical pressure at which liquid helium becomes thermodynamically unstable against the density fluctuations, have aroused special interest. Various cavitation experiments have also been performed.[5–7]

According to the first estimates[8] of the rates at which bubbles nucleate in a liquid ^{4}He, it is expected that quantum nucleation should dominate over the thermally activated nucleation at temperatures below ≈ 0.3 K and that in this temperature range the pressure providing the noticeable nucleation rate or the tensile strength should be about $P \approx -15$ atm. Later, Maris and Xiong[2] pointed out the possibility that, before this pressure can be attained, the liquid ^{4}He is unstable against the long-wavelength fluctuations of density since the square of the sound velocity becomes negative. The extrapolations of the sound velocity into the negative pressure range and some numerical calculations suggest that the sound velocity at pressure P goes to zero as

$$c(P) \propto (P - P_c)^{\nu}. \tag{1}$$

Here the exponent ν is close from 1/3 to 1/4. The critical pressure P_c, i.e., the pressure at the lability point, is estimated to be $P_c = -(8-9)$ atm at absolute zero. For liquid ^{3}He, it is expected that $P_c = -(2-3)$ atm.[2]

In order to find the tensile strength, one needs a theory on the nucleation of cavities in the liquid. So far all the calculations of the nucleation rate and tensile strength in the region of the quantum tunneling regime have been performed within the framework of the Lifshitz–Kagan theory[9] of first-order phase transitions. However, in this well-known theory there were several assumptions that reduced its general validity. In particular, metastable liquid phase was assumed to be absolutely incompressible or, in other words, sound velocity in the liquid is infinite. Clearly, a more realistic theory of the quantum cavitation should involve the effect of the finite compressibility, especially in the closest vicinity of the instability point at which the sound velocity vanishes.

As follows from the recent studies involving the effect of finite compressibility on the quantum decay rate of a metastable phase, the ratio of the nucleus growth rate $\dot{R}$ to the sound velocity c is a physical parameter which governs the magnitude of the compressibility in the case of three-dimensional nucleation.[10] In turn, for the decay of low-dimensional metastable systems the involvement of nonzero compressibility of a medium in the calculation of the decay rate is of principal importance since the approximation of an incompressible medium has no applicability.[11] Furthermore, compared with the standard theories[9,12] based on the models of an incompressible medium, in which the decay kinetics of a metastable phase has a dissipationless character, the sound retardation due to the finite velocity of sound propagation produces qualitative changes in the quantum decay, which becomes completely analogous to the dissipative quantum tunneling through a potential barrier. The mechanism of energy dissipation is associated with the emission of sound during the growth of the stable phase. On the whole, this leads to the time nonlocality of the effective Euclidean action and, as a result, to the appearance of the explicit temperature dependence for the nucleation rate in the quantum tunneling regime.

The examination of the compressibility effect on the quantum nucleation of cavities in a metastable liquid, which has not been made yet, is the main topic considered in this paper. In order to investigate quantum-mechanical tunneling between the metastable and stable states of a condensed medium and to calculate the rate at which cavities nucleate, we employ the formalism based on the use of the finite-action solutions (instantons) of equations continued to the imaginary time. (For review see, for example, Ref. 13.) This approach[14,15] for describing quantum-mechanical tunneling

in the systems with macroscopic number of degrees of freedom was used for incorporating the influence of energy dissipation in a metastable, condensed medium on the quantum kinetics of first-order phase transitions at low temperatures.[11,16]

2. DYNAMICS OF A THIN-WALL BUBBLE IN THE LIQUID

The growth of a bubble in the liquid, as well as the formation of a bubble, is a very complex process. The growth of a bubble occurs in a condensed medium representing a system of many particles. As a result, the growth of a bubble is accompanied by nondissipative and dissipative processes, including the nonhomogeneous outflow of the liquid from the bubble, the viscosity, the heat conduction, and sound emission due to the compressibility of the liquid. Thus, even for a spherical bubble that expands uniformly in all directions, the derivation of the general growth equation, which is valid for an arbitrary expansion rate, is a complex problem. We therefore start from a number of simplifying assumptions.

Let us consider a normal fluid, say, ^{3}He held at arbitrary pressure P, either positive or negative. As the next step, we assume that a spherical bubble of radius $R(t)$ has been produced and that its radius is growing at certain rate $\dot{R}(t)$. For simplicity, we disregard the possible presence of the helium vapor inside the bubble, since the density of the vapor is much smaller compared to that of the bulk liquid. We can then consider the bubble within a thin-wall approximation assuming that the bubble has an abrupt boundary between a void and the liquid surrounding the bubble. In other words, we will describe the liquid-vacuum interface in the terms of the surface energy coefficient α. Of course, this is reasonable only if the bubble radius is much larger than the interface thickness.

The total energy of the system will then be

$$\varepsilon = \int_{r>R(t)} d^3r \left[\frac{1}{2}\,\rho(\mathbf{r})\mathbf{v}^2(\mathbf{r}) + \rho(\mathbf{r})\varepsilon(\rho(\mathbf{r})) \right] + 4\pi\alpha R^2(t), \tag{2}$$

where the velocity and density of the liquid at point $\mathbf{r}$ are $\mathbf{v}(r)$ and $\boldsymbol{\rho}(r)$, respectively. The first bulk term represents a sum of the kinetic and internal energies of the liquid, and $\boldsymbol{\epsilon}$ is the internal energy per unit mass. The second term is the surface energy of the bubble. To make the further simplification of the bubble growth, we disregard all the heat effects which, in general, can accompany the growth of a bubble. For this purpose, one should ignore the possible temperature dependence in the coefficient of surface energy α and the heat transfer due to the viscosity of the medium.

Let us now turn to the derivation of the equation which the growth of a bubble obeys. First of all, we note that, according to the conservation of the mass flux across the boundary of a bubble, we have an equality between the fluid velocity and the growth rate at $r=R(t)$, i.e.,

$$v(R)=\dot{R}(t). \tag{3}$$

Next, one possible way to obtain the growth equation is to use the conservation of the momentum density flux across the boundary at $r=R(t)$:

$$P(R)+\tau_{rr}(R)+\frac{2\alpha}{R}=0. \tag{4}$$

Here $P(R)$ is the pressure, and $\tau_{rr}(R)$ is the radial component of the viscous stress tensor at the surface of the bubble. The viscous stress tensor τ_{ik} is defined by the standard expression[17] as

$$\tau_{ik}=-\eta\left(\frac{\partial v_i}{\partial x_k}+\frac{\partial v_k}{\partial x_i}-\frac{2}{3}\,\delta_{ik}\,\frac{\partial v_l}{\partial x_l}\right)-\zeta\,\delta_{ik}\,\frac{\partial v_l}{\partial x_l}, \tag{5}$$

here η and ζ are the viscosity coefficients, and the subscripts i, k and l run over the values of 1, 2, and 3 corresponding to the components of the radius vector. The last term in Eq. (4) takes into account the existence of the Laplace pressure due to the curvature of the surface.

The boundary condition (4) is essentially an equation of the bubble growth. We must express the pressure $P(R)$ and the viscous stress $\tau_{rr}(R)$ in terms of the variables describing the growth of a bubble, i.e., $\dot{R}(t)$ and $R(t)$. For this purpose one should employ two equations which govern the motion of a fluid. The first is the equation of continuity

$$\frac{\partial\rho}{\partial t}+\nabla\cdot(\rho\mathbf{v})=0 \tag{6}$$

and the second is the Navier–Stokes equation[17]

$$\rho\left[\frac{\partial\mathbf{v}}{\partial t}+(\mathbf{v}\cdot\nabla)\mathbf{v}\right]=-\nabla P+\eta\nabla^2\mathbf{v}+\left(\zeta+\frac{\eta}{3}\right)\nabla(\nabla\cdot\mathbf{v}). \tag{7}$$

We are now in the position to calculate the unknown quantities $P(R)$ and $\tau_{rr}(R)$, using Eqs. (6) and (7), and the boundary condition (3). However, the derivation of the general analytic solution for an arbitrary dependence of the growth rate $\dot{R}$ on time t is unfeasible and we restrict the analysis to the limit of sufficiently low growth rates, $\dot{R}\to 0$. In what follows, only the quantities of the order not smaller than $\dot{R}/c\ll 1$ will be kept, where c is the sound velocity. The time derivatives of $R(t)$ to third order are also retained. Each term of the decomposition has its own physical meaning and, in addition, its relative contribution to the bubble growth kinetics depends on several factors, including the bubble radius, growth rate, temperature, and kinetic properties of the liquid near the bubble.

As usual, to solve Eqs. (6) and (7), it is convenient to introduce the velocity potential $\varphi(\mathbf{r}t)$ according to

$$v=\nabla\varphi.$$

In the above approximations the motion of a fluid medium can be reduced to the linear equation corresponding to the propagation of sound under damping

$$\nabla^2\varphi-\frac{\ddot{\varphi}}{c^2}+\frac{(4/3)\,\eta+\zeta}{\rho c^2}\,\nabla^2\dot{\varphi}=0. \tag{8}$$

The general solution for the sound that propagates from the bubble and vanishes at infinity can be represented as

$$\varphi(rt)=\int_{-\infty}^{\infty}\frac{d\omega}{2\pi}\,e^{-i\omega t}\,\frac{e^{-i\lambda_\omega r}}{r}\,\Phi(\omega),$$

$$\lambda_\omega=\frac{\omega}{c}\left(1-2i\gamma_\omega\frac{c}{\omega}\right)^{-1/2},\quad \gamma_\omega=\frac{4\eta/3+\zeta}{2\rho c^3}\,\omega^2, \tag{9}$$

where γ_ω is the sound absorption coefficient due to the viscosity of a fluid. The unknown function $\Phi(t)$ must be determined from the boundary condition (3) setting $\partial\varphi/\partial r=\dot{R}(t)$ at $r=R(t)$. The involvement of first-order time derivative alone is sufficient in our approximation; i.e.,

$$\Phi(t)\approx-\frac{\dot{V}(t)}{4\pi},\quad V(t)=\frac{4\pi}{3}R^3(t), \tag{10}$$

where $V(t)$ is the volume of an expanding bubble. Using the usual relation for the pressure in a fluid

$$P(rt)-P=-\rho\dot{\varphi}-\rho\frac{(\nabla\varphi)^2}{2}+\left(\frac{4}{3}\eta+\zeta\right)\nabla^2\varphi$$

and Eq. (5) for the viscous stress tensor, we obtain for the equation of the bubble growth

$$\frac{2\alpha}{R}+P+4\eta\frac{\dot{R}}{R}+\rho\left(R\ddot{R}+\frac{3}{2}\dot{R}^2\right)-\frac{\rho}{4\pi c}\dddot{V}(R)+\ldots=0, \tag{11}$$

where P is the external pressure. In the absence of the surface, viscous, and sound terms the equation for the radial growth of a bubble was derived for the first time by Lord Rayleigh. Later, the growth equation was generalized by M. Plesset with allowance for the surface tension.

For further analysis, let us rewrite the growth equation in a more general form. Multiplying Eq. (11) by $4\pi R^2$, we obtain

$$U'(R)+\mu_1(R)\dot{R}+\mu_2(R)\left[\ddot{R}+\frac{1}{2}\frac{\mu_2'(R)}{\mu_2(R)}\dot{R}^2\right]-\mu_3(R)\times\left[\dddot{R}+\frac{3}{2}\frac{\mu_3'(R)}{\mu_3(R)}\ddot{R}\dot{R}+\frac{1}{2}\left(\frac{\mu_3''(R)}{\mu_3(R)}-\frac{\mu_3'^2(R)}{2\mu_3^2(R)}\right)\dot{R}^3\right]+\ldots=0. \tag{12}$$

The expression which we derived essentially represents a general form for lowest terms of the expansion of the equation of bubble growth in a series in the slowness of variation of the bubble radius $R(t)$ in time; i.e., expression (12) is a low-frequency expansion.

The term $U'(R)$ which remains finite at $\dot{R}\equiv0$ originates from

$$U(R)=\frac{4\pi}{3}PR^3+4\pi\alpha R^2. \tag{13}$$

Accordingly, $U(R)$ can be treated as a potential energy of the bubble. Note that for negative pressures the bubbles with radii exceeding the critical size

$$R_c=3\alpha/|P| \tag{14}$$

prove to be energetically favorable and cavitation becomes unavoidable.

The second term with the first derivative represents the drag force, which hinders the growth of a bubble and which is completely analogous to the Stokes force, which is proportional to the growth rate

$$\mu_1(R)\dot{R}=16\pi\eta R\dot{R}. \tag{15}$$

It is obvious that the drag force governs the evolution of a bubble at sufficiently small growth rate when the other terms which depend on the temporal derivatives, can be disregarded. As we shall see below, such situation for the quantum cavitation is possible provided the critical size R_c of a bubble is large enough or, identically, in the limit of small negative pressures $|P|\to0$.

We would like to make an important remark concerning the behavior of the friction coefficient $\mu(R)$ as a function of the bubble radius and temperature. The point is that in the course of deriving the Rayleigh–Plesset equation (11) we employed the Navier–Stokes equation with the viscous stress tensor (5) in the form of the expansion in the gradients of the fluid velocity. This implies, however, that the hydrodynamic approximation is satisfied; i.e., the bubble radius should be much larger compared with the mean free path $l(T)$ of excitations in the medium surrounding the bubble. Since the mean free path increases rapidly at low temperatures, in particular, $l(T)\propto1/T^2$ for ^{3}He, the crossover from the hydrodynamic $R\gg l$ regime to the ballistic or Knudsen regime of $R\ll l$ should occur at a certain temperature $T_l(R)$.

In the ballistic regime the friction coefficient is governed by the interaction of excitations with the surface of a bubble and is proportional to the area of the bubble surface. The general expression for the friction coefficient $\mu_1(R)$ can be represented as[16]

$$\mu_1(R)=16\pi\eta Rf(R/l),$$

$$f(x)=\begin{cases}1, & \text{if } x\gg1\\ ax, & \text{if } x\ll1.\end{cases} \tag{16}$$

Here $f(x)$ is a dimensionless function of the ratio of the bubble radius to the mean free path of excitations in the liquid. The numerical factor a is of the order of unity and depends on the particular features of the interaction of excitations with the bubble surface. It should be noted that in the ballistic regime the friction coefficient $\mu_1(R)$ is independent of the mean free path $l(T)$ since $\eta\sim\rho cl$.

The terms with the second derivative and with the square of the first derivative in Eq. (12) are standard terms and can be described in terms of the variable mass of a bubble:[9]

$$\mu_2(R)=4\pi\rho R^3. \tag{17}$$

These terms can be attributed to the kinetic energy of the fluid that flows away from the bubble.

The other third-order terms are associated mainly with the finite velocity of the propagation of sound in a medium. The corresponding coefficient $\mu_3(R)$ is given by

$$\mu_3(R)=\frac{4\pi\rho}{c}R^4. \tag{18}$$

Clearly, the smaller the sound velocity, the larger the effect of this term on the growth of a bubble and on the cavitation kinetics.

To gain further physical insight, we represent the growth equation in terms of the bubble energy dissipated per unit time,

$$\frac{d}{dt}\left(U(R)+\frac{1}{2}\,\mu_2(R)\dot{R}^2-\mu_3(R)\dot{R}\ddot{R}-\frac{1}{2}\,\mu_3'(R)\dot{R}^3\right)$$

$$=-\mu_1(R)\dot{R}^2-\frac{\rho}{4\pi c}\,\ddot{V}^2. \tag{19}$$

As one can see, the right-hand side of Eq. (19) is described by the dissipative function. The first term of the dissipative function corresponds to the standard ohmic dissipation with the variable friction coefficient. The second term is exactly equal to the total intensity of the sound emission as the volume of the body immersed in the fluid changes[17] if the wavelength λ of the sound emitted is much larger than the size of the body; i.e., $\lambda \gg R$. In our case the latter is identical to the inequality $R \ll c$.

In conclusion, we would like to emphasize two important points. First, the growth equation (12) has a limited region of applicability, which is restricted by the low growth rates so that the growth time of a bubble would be longer than the characteristic times of the relaxation processes in the medium surrounding the bubble. Second, the kinetic coefficients $\mu_n(R)$, in general, are different in various media, for example, in the normal or superfluid liquid.

3. QUANTUM NUCLEATION RATE

In this section we shall estimate the thermal-quantum crossover temperature and calculate the rate at which a bubble nucleates at zero temperature. The quantum cavitation problem is treated within the approach elaborated for describing the decay of a metastable state in the presence of energy dissipation[14,15] and used for the analysis of the quantum nucleation processes during first-order phase transitions.[16] This approach is based on finding the extremum values of the effective Euclidean action determined in imaginary time and on using one-to-one correspondence between the classical equation of growth in real time and the Euler-Lagrange equation for the effective action due to the principle of the analytic continuation $(|\omega_n| \to -i\omega)$ into imaginary time.

The rate of the quantum nucleation can be written as

$$\Gamma(T)=\Gamma_0(T)\exp(-S(T)/\hbar), \tag{20}$$

where the preexponential factor Γ_0 is the rate of cavitation per unit volume and unit time. According to the general theory of the nucleation kinetics, the factor Γ_0 can be evaluated approximately as the attempt frequency ν_0 multiplied by the number of centers at which the independent cavitation events can occur.

In turn, the exponent S is the extremum value of the effective Euclidean action

$$S_{\rm eff}|R_\tau|=\int_{-\beta\hbar/2}^{\beta\hbar/2} d\tau\left[U(R_\tau)+\frac{1}{2}\,\mu_2(R_\tau)\left(\frac{dR}{d\tau}\right)^2\right]$$

$$+\frac{1}{4\pi}\int\int_{-\beta\hbar/2}^{\beta\hbar/2} d\tau d\tau'[\,\gamma_1(R_\tau)$$

$$-\gamma_1(R_{\tau'})]^2\,\frac{(\pi T)^2}{\hbar^2\,\sin^2\,\pi T(\tau-\tau')/\hbar}$$

$$-\frac{1}{4\pi}\int\int_{-\beta\hbar/2}^{\beta\hbar/2} d\tau d\tau'\left[\frac{\partial\gamma_3(R_\tau)}{\partial\tau}\right.$$

$$\left.-\frac{\partial\gamma_3(R_{\tau'})}{\partial\tau'}\right]^2\,\frac{(\pi T)^2}{\hbar^2\,\sin^2\,\pi T(\tau-\tau')/\hbar}, \tag{21}$$

where $\beta=T^{-1}$ is the inverse temperature. The path $R(\tau)$ which is defined in imaginary time τ satisfies the periodic boundary conditions $R(-\beta\hbar/2)=R(\beta\hbar/2)$. It should be emphasized that all the parameters of the effective action are associated unambiguously with the corresponding parameters in the classical equation of growth (12). The correspondence can readily be settled with the analytic continuation $(|\omega_n| \to -i\omega)$ of the Euler–Lagrange $(\delta S_{\rm eff}/\delta R_\tau=0)$ equation for the effective action to real time, which entails the classical equation of growth. The substitution $(|\omega_n| \to -i\omega)$ of the Matsubara frequencies with the real frequencies must be performed in the frequency representation of the corresponding equations.

It is clear that the first two terms in Eq. (21) can be attributed to the potential and kinetic energies of a bubble. The other terms, nonlocal in time, are due to the energy dissipation during the bubble growth. The parameters $\gamma_1(R)$ and $\gamma_3(R)$ are determined by the kinetic coefficients $\mu_1(R)$ and $\mu_3(R)$, respectively,

$$\mu_1(R)=\left(\frac{\partial\gamma_1(R)}{\partial R}\right)^2, \quad \mu_3(R)=\left(\frac{\partial\gamma_3(R)}{\partial R}\right)^2. \tag{22}$$

Depending on whether the hydrodynamic or ballistic regime takes place, as it follows from Eq. (16), we obtain

$$\gamma_1(R)=\begin{cases} \dfrac{2}{3}\,\sqrt{16\pi\eta}R^{3/2}, & \text{if } R\gg l \\ \dfrac{1}{2}\,\sqrt{16\pi a\,\eta/l}R^2, & \text{if } R\ll l. \end{cases}$$

Similar effective actions have been studied in the application to the general theory of the quantum kinetics of first-order phase transitions. However, the various authors[9,10,16] used the kinetic terms separately. It is interesting to note that, in contrast to the term with the ohmic dissipation which is related to the dissipative function proportional to the square of the first-order time derivative, the contribution due to the finite compressibility of a fluid to the effective action is negative. The latter results in enhancing the quantum nucleation rate compared with the one calculated in the framework of the Lifshitz–Kagan model of an incompressible fluid. Some hints for such conclusion can be seen from the fact that the finiteness of the velocity of the sound restricts the region of the bubble environment that can be disturbed and set in motion. The size of this region is approximately $\Lambda=c\tau$, where τ is a typical growth time. In a sense, one can say that the total kinetic energy of the fluid flowing away from the expanding bubble becomes smaller than in the case of an

incompressible fluid where the perturbation induced by the formation of the bubble extends instantaneously to infinity.

To be closer to what can actually be observed in low-temperature experiment, we consider only the case of the ballistic $R_c \gg l$ regime, when the critical radius is much larger than the mean free path of excitations. In fact, at low temperatures, $T<1$ K, the mean free path increases drastically in the normal ^{3}He and in the superfluid ^{4}He. Hence, the opposite case of the hydrodynamic regime requires large values for the critical bubble radius, which increases progressively as the temperature decreases. In addition, the large critical radius of a bubble results in such negligible nucleation rates that the homogeneous cavitation becomes unobservable on the scale of the reasonable experimental times. In the quantitative manner, the impossibility of the hydrodynamic quantum regime is expressed by the inequality of $T_l(R_c)>T_0(R_c)$, where $T_0(R_c)$ is the thermal-quantum crossover temperature.

Eventually, it is convenient to represent the effective action in the following way:

$$S_{\rm eff}[R_\tau]=\int_{-\hbar/2T}^{\hbar/2T} d\tau\left[\frac{4\pi}{3}PR_\tau^3+4\pi\alpha R_\tau^2+2\pi\rho R_\tau^3\dot{R}_\tau^2\right]+\frac{1}{4\pi}\int\int_{-\hbar/2T}^{\hbar/2T} d\tau d\tau'\left\{\frac{\rho}{4\pi}u\left[A(R_\tau)-A(R_{\tau'}]^2-\frac{\rho}{4\pi c}[\dot{V}(R_\tau)-\dot{V}(R_{\tau'})]^2\right\}\frac{(\pi T)^2}{\hbar^2\sin^2\pi T(\tau-\tau')/\hbar},\qquad(23)$$

where $A=4\pi R^2$ is the area of the surface, and $V=4\pi R^3/3$ is the volume of a bubble. The quantity $u\sim\eta/\rho l$ is approximately the characteristic velocity of excitations in a medium. For a normal liquid like ^{3}He, the order of magnitude of the velocity u is the Fermi velocity and the possible temperature corrections to the zero temperature are associated with the quantities of about $(T/T_F)^2$, where T_F is the degeneration temperature of the Fermi-like excitations.

In the superfluid ^{4}He where the energy dissipation of the ohmic type is due to the presence of the normal component alone, we have a different behavior of the quantity u:

$$u(T)\approx c\rho_n(T)/\rho.\qquad(24)$$

Here $\rho_n(T)$ is the density of the normal component and at low temperatures $T<0.5$ K the normal density is determined mainly by phonons[18]

$$\rho_n(T)=\frac{2\pi^2}{45}\frac{T^4}{\hbar^3c^5}.$$

It should be noted that since $u\sim c^{-4}$, the relative role of this ohmic term increases in the vicinity of the lability point because of the reduction of the sound velocity.

First, we consider the high-temperature region in which there is only a classical extremum path. The path which satisfies the condition $R(\tau)\equiv R_0=2R_c/3$ goes through the maximum U_0 of the potential energy (13) and yields the action $S=\hbar U_0/T$ resulting in the standard Arrhenius law for the nucleation rate,

$$\Gamma=\Gamma_0\exp(-U_0/T);\quad U_0=\frac{16\pi\alpha^2}{3|P|^2}.\qquad(25)$$

We begin the study of the low-temperature quantum behavior of the nucleation rate by analyzing the classical $R(\tau)\equiv R_0$ extremum path with respect to small oscillations about the maximum of the potential energy. For this purpose, we represent an arbitrary path as

$$R(\tau)=R_0+r(\tau).$$

Next we expand the effective action $S_{\rm eff}[R(\tau)]$ in a series in small powers of deviation of $r(\tau)$. Truncating a series in $r(\tau)$ at second order and turning to the Fourier representation

$$r(\tau)=\frac{T}{\hbar}\sum_n r_n\exp(-i\omega_n\tau),$$

$$r_n^*=r_{-n};\quad \omega_n=2\pi Tn/\hbar,\quad n=0,\pm1,\pm2,\ldots,$$

we obtain after some calculations the expression

$$S_{\rm eff}=\frac{\hbar U_0}{T}+\frac{T}{2\hbar}\sum_n\alpha_n|r_n|^2.\qquad(26)$$

Here the coefficients α_n are given by

$$\alpha_n=U_0''+16\pi\rho uR_0^2|\omega_n|+4\pi\rho R_0^3\omega_n^2-\frac{4\pi\rho R_0^4}{c}|\omega_n|^3.\qquad(27)$$

As the temperature is lowered, the coefficients $\alpha_{\pm1}$ vanish first at $T=T_1$, which is determined by the equation

$$-\alpha+4\rho uR_0^2\omega_1+\rho R_0^3\omega_1^2-\frac{\rho R_0^4}{c}\omega_1^3=0,\quad T_1=\frac{\hbar\omega_1}{2\pi}.\qquad(28)$$

Below the temperature T_1 the classical path $R(\tau)=R_0$ becomes absolutely unstable against the oscillations of mode $r_{\pm1}$.

Depending on the type of the quantum-classical path transition,[16] the genuine thermal-quantum crossover temperature T_0 coincides with the temperature T_1 if the effective action matches smoothly the exponent of the Arrhenius law or lies at a temperature slightly higher than the temperature T_1 if the quantum-classical path transition has a discontinuous, jump-like character, i.e., $T_0\leqslant T_1$. Although the action (23) we are concerned with refers to the last case and although the crossover temperature T_0 should be found from $S(T_0)=\hbar U_0/T_0$, the approximate estimate of $T_0\approx T_1$ is fully sufficient for our purpose.

According to Eq. (28), in the limit of sufficiently large radius $R_0\to\infty$ or, correspondingly, small negative pressures $|P|\to0$ we obtain the following estimate of the crossover temperature:

$$T_0\approx\frac{\hbar\alpha}{8\pi\rho uR_0^2}=\frac{\hbar}{32\pi\alpha\rho u}|P|^2.\qquad(29)$$

For the above formula to be correct, it is necessary that the growth rate $\dot{R}$ be smaller than the velocity of excitations and the sound velocity. Since the characteristic time of the underbarrier evolution of a bubble is $(2\pi\omega_1)^{-1}$, we have

$$\frac{2\pi\omega_1 R_0}{u}=\frac{\pi\alpha}{2\rho u^2 R_0}\ll 1. \tag{30}$$

Obviously, this inequality restricts the magnitude of the pressure

$$|P|\ll \rho u^2, \tag{31}$$

for which our approximations hold true. If the strong inequality (30) breaks down, in Eq. (28) we must use terms of higher orders in ω_1, and the estimate (29) of the thermal-quantum crossover temperature ceases to be valid.

In contrast with normal ^{3}He, in superfluid ^{4}He the density of the normal component $\rho_n(T)$ vanishes as $T\to 0$ and therefore the contribution of the ohmic term in Eq. (28) decreases. In order to analyze all the facts of the case, let us rewrite Eq. (28) for temperature T_1, taking into account Eq. (24) for $\rho_n(T)$

$$-\alpha+\frac{R_0^2}{90\pi^2 c^4}\hbar\omega_1^5+\rho R_0^3\omega_1^2-\frac{\rho R_0^4}{c}\omega_1^3=0. \tag{32}$$

Of course, the condition $\omega_1 R_0/c\ll 1$ is assumed to be satisfied.

As one can see, the dissipative ohmic term linear in ω_1 has no significant influence on the thermal-quantum crossover temperature T_0 provided that $R_0\gg R_*$ where the radius R_* is given by

$$R_*\approx\left(\frac{\hbar^2\alpha^3}{8100\pi^4 c^8\rho^5}\right)^{1/11}. \tag{33}$$

For the radius $R_0\gg R_*$, the thermal-quantum crossover temperature is found to be approximately the same, as it follows from the nondissipative model of the quantum cavitation[1,4]

$$T_0\approx\frac{\hbar}{2\pi}\sqrt{\frac{\alpha}{\rho R_0^3}}=\frac{\hbar}{4\pi}\frac{|P|^{3/2}}{\sqrt{\alpha\rho}}. \tag{34}$$

To satisfy the approximation of the low growth rate $\omega_1 R_0\ll c$, we must impose a restriction on the radius R_0 or on the negative pressure P:

$$R_0\gg\frac{\alpha}{\rho c^2}\ \text{ or }|P|\ll\rho c^2. \tag{35}$$

Numerically, if the physical parameters of ^{4}He are measured at zero pressure $P=0$, we find that $R_*\approx\alpha/\rho c^2$. Since $\alpha/\rho c^2\approx 0.5$ Å, the validity of the estimate (34) is connected with the applicability of the macroscopic description, which is correct for large bubble radii compared with the interface thickness. Note that the condition (35) can be satisfied only in the range of pressures far enough from the lability point at which the sound velocity vanishes.

Let us now focus our attention on the low-temperature $T\ll T_0$ behavior of the nucleation rate. First, we consider the case of $u(T)=\text{const}$, which corresponds to the normal ^{3}He. Since we should remain within the approximation of the low growth rate, the main contribution to the effective action originates from the dissipative ohmic term which is nonlocal in time. The other two kinetic terms can therefore be treated as perturbations. Accordingly, for temperature $T=0$ we have approximately

$$S(T=0)\approx 4\pi\rho u R_c^4\left[1+\frac{\alpha}{2\rho u^2 R_c}-\frac{u}{9c}\left(\frac{\alpha}{\rho u^2 R_c}\right)^2\right]$$
$$\propto|P|^{-4}. \tag{36}$$

This result represents the decomposition of the effective action in $\dot{R}/u\ll 1$ if we take into account that the typical time of the bubble growth or, identically, the transit time along the extremum underbarrier path is about

$$\tau_c=\frac{\rho u R_c^2}{\alpha}. \tag{37}$$

In contract with the dissipationless kinetics[1,4,9] the energy dissipation during the bubble growth leads to the effective action in which the kinetic terms depend on temperature in an explicit form. It is natural therefore to expect a temperature-dependent behavior of the nucleation rate in the quantum tunneling regime below the crossover temperature T_0. We thus can expect[16]

$$\Delta S(T)=S(T)-S(0)\approx -S(0)(T/T_0)^2. \tag{38}$$

It is obvious that the temperature correction affects essentially the nucleation rate, while $|\Delta S(T)|>\hbar$. Introducing the temperature T_2 at which $|\Delta S(T_2)|\approx\hbar$, i.e.,

$$T_2\approx\frac{\alpha}{R_c^4}\left(\frac{\hbar}{4\pi\rho u}\right)^{3/2}\propto P^4, \tag{39}$$

we obtain a noticeable range of temperatures $T_2<T\ll T_0$, for which the enhancement of nucleation rate $\Gamma(T)$ follows the law of $\log[\Gamma(T)/\Gamma(0)]\propto T^2$.

Let us turn now to the case of the cavitation in a superfluid ^{4}He. In contrast to a normal fluid, where the density of excitations remains finite down to zero temperature, the density of the normal component in superfluid ^{4}He vanishes at zero temperature and the nucleation kinetics is governed mainly by the well-known nondissipative term, which is related to the kinetic energy of the liquid.[1,4,9] Using the correction due to the finite velocity of the sound propagation, we can describe the effective action at $T=0$ approximately by

$$S(T=0)\approx\frac{5\sqrt{2}\pi^2}{16}(\alpha\rho)^{1/2}R_c^{7/2}\left(1-\frac{4}{9c}\sqrt{\frac{2\alpha}{\rho R_c}}\right). \tag{40}$$

The order of magnitude of the second term is a ratio of the underbarrier growth rate to the sound velocity. On the whole, the model of an incompressible liquid,[4,9] as one can see underrates the cavitation rate in the quantum regime. As the pressure decreases, the underestimate of the cavitation rate increases due to the reduction of the critical radius and the sound velocity. For large critical radii, although the relative correction to the quantum nucleation rate is small, the absolute value of the correction is very large because of an exponential dependence of the nucleation rate on the effective action.

To conclude the section, we shall analyze the low $T\ll T_0$ temperature behavior of the nucleation rate. The

temperature-dependent behavior for the nucleation rate is entirely due to the terms in the effective action (23), which are nonlocal in time and which describe the energy dissipation processes occurring in the superfluid ^{4}He during the bubble growth.

The temperature correction from the ohmic dissipation term is governed, initially by the temperature behavior of the normal density $\rho_n(T)$[16]

$$\Delta S_{\rm ohm}(T) \approx 4\pi\rho u(T) R_c^4 = 4\pi c \rho_n(T) R_c^4.$$

This contribution reduces the nucleation rate. In contrast, the temperature correction resulting from the sound emission term has a negative sign and increases the nucleation rate[10]

$$\Delta S_s(T) \approx \frac{\rho^2 R_c^9}{c\alpha}\left(\frac{T}{\hbar}\right)^4.$$

The temperature dependence of the correction is the same as for $\rho_n(T)$. The total temperature correction is determined by a sum

$$\Delta S(T) = S(T) - S(0) \approx \left(\frac{8\pi^3\hbar}{45c^3} - \frac{\rho^2 R_c^5}{\alpha}\right)\frac{R_c^4}{c}\left(\frac{T}{\hbar}\right)^4. \quad (41)$$

Note that at least in the immediate vicinity of the lability point, when $P \to P_c$ and $c(P) \to 0$, the correction associated with the existence of the normal component will dominate over the sound emission mechanism. In contrast, in the range of the small negative pressures of $p < -3\alpha/R_*$ or large critical radii,

$$R_c > R_* \approx \left(\frac{8\pi^3}{45}\frac{\alpha\hbar}{\rho^2 c^3}\right)^{1/5}, \quad (42)$$

the sound emission mechanism governs the temperature behavior of the nucleation rate. If we take the parameters of ^{4}He at zero pressure, the numerical estimate gives the value of about 2.4 Å for radius R_*, which is comparable with the interatomic distance a. In the whole region of the macroscopic $R_c \gg a$ approximation the contribution from the ohmic dissipation is therefore negligible and the nucleation rate $\Gamma(T)$ should increase with increasing temperature.

Let us now evaluate the temperature T_2 at which the temperature correction for the exponent becomes significant, i.e., if $|\Delta S(T_2)| \approx \hbar$. Using Eq. (41), we obtain

$$T_2 \approx \hbar\left(\frac{\hbar\alpha c}{\rho^2 R_c^9}\right)^{1/4}. \quad (43)$$

However, the temperature T_2 is smaller than the temperature T_0 of the thermal-quantum crossover only for the sufficiently large critical radii which exceed a certain radius R_2

$$R_c > R_2 \approx \frac{4\pi}{3}\left(\frac{16\pi\hbar c}{3\alpha}\right)^{1/3}. \quad (44)$$

The estimate for pressures $|P| \approx 0$ yields $R_2 \approx 40$ Å. Thus, only for macroscopically large bubbles of radius $R_c \gg a$ there is a noticeable range of temperatures $T_2 < T < T_0$ where $|\Delta S(T)| > \hbar$. For $R_c < R_2$, the scale of the $\log\Gamma(T)/\Gamma(0) \propto T^4$ variation is not large. Note that the radius R_2 decreases near the lability point $c(P_c) = 0$.

4. SUMMARY

In this paper we have examined the effect of the dissipative processes and finite compressibility on the rate at which bubbles can nucleate via quantum tunneling in the normal ^{3}He and superfluid ^{4}He at negative pressures and sufficiently low temperatures. In conclusion, we would like to emphasize several important points common and distinct for the kinetics of the quantum cavitation in the normal and superfluid liquids.

The common feature of quantum kinetics is that the dissipative processes, which are associated with the viscosity of a fluid, hinder the quantum nucleation of bubbles. The viscous phenomena have an origin entirely in the spatially nonuniform flow of the fluid which has to spread in the radial directions away from the expanding bubble.

In contrast, the finite compressibility of a fluid facilitates the quantum nucleation of the bubbles since it is easier to push the fluid out from the cavity if the medium surrounding it is light-compressible. This phenomenon is accompanied by the excitation and emission of the sound waves induced by an expanding sphere.

This effect is essential for the negative pressures of about several atmospheres when the critical sizes of the bubbles should be approximately equal to several interatomic distances and the rate of tunneling is comparable with the sound velocity. On the whole, these two processes result in the appearance of the explicit temperature-dependent behavior of the cavitation rate in the quantum regime.

On the other hand, it is the dissipative processes that make the quantum cavitation kinetics diverse in the normal and superfluid liquids. In the normal fluid ^{3}He, where the density of excitations does not vanish at low temperatures, the quantum cavitation kinetics corresponds entirely to the dissipative tunneling through a potential barrier in the overdamped regime. Compared with the calculations[1,2,4,9] performed on the basis of the dissipationless models of quantum cavitation, the quantum cavitation rate for the bubbles of the large critical sizes proves to be significantly smaller and, correspondingly, the tensile strength should be also somewhat smaller.

In addition, the temperature necessary for observing the quantum tunneling regime instead of thermal activation decreases and should be below about 70 mK. The $\log\Gamma(T)/\Gamma(0) \propto T^2$ behavior for the nucleation rate is expected in the low-temperature limit.

In contrast with the normal ^{3}He, in superfluid ^{4}He, where all excitations are frozen out as the temperature tends to absolute zero, the dissipative processes do not play an essential role with the exception of the range of small negative pressures. This range of pressures of about $P > -1$ atm refers to the sufficiently large critical sizes of the bubbles which have an astronomically large lifetime and thereby do not determine the tensile strength of ^{4}He under ordinary experimental conditions.

Although the compressibility and sound excitation effects during the nucleation must undoubtedly be involved in the cavitation kinetics of the bubbles of small critical sizes, the quantum cavitation rate $\Gamma(T)$ and therefore the tensile strength of ^{4}He remain, as in the case of the incompressible

liquid models, nearly independent of the temperature. The involvement of the compressibility of superfluid ^{4}He leads to the thermal-quantum crossover temperature which is somewhat higher than that calculated on the basis of the incompressible liquid model. The last two consequences for the quantum cavitation in the homogeneous ^{4}He together with the estimate of the crossover temperature of about $T_0 \approx 0.3$ K for the small critical bubbles do not contradict the recent low-temperature cavitation experiments.[19]

We are grateful to Yu. Kagan for many important discussions. The research described in this publication was made possible in part by Grant No. MAA300 from the International Science Foundation. This study is also supported in part by the Grant No. 96-02-18511a from the Russian Foundation for Basic Research. This work was supported by ISI Foundation and INTAS Contract No. 1010-CT930055.

[1)]E-mail: burmi@kurm.polyn.kiae.su

[1] V. A. Akulichev, Ultrasonics **24**, 8 (1986).
[2] H. J. Maris and Q. Xiong, Phys. Rev. Lett **63**, 1078 (1989); Q. Xiong and H. J. Maris, Low Temp. Phys. **77**, 347 (1989).
[3] M. Guilleumas, M. Pi, M. Barranco, J. Navarro, and M. A. Solis, Phys. Rev. **B47**, 9116 (1993).
[4] H. J. Maris, J. Low Temp. Phys. **98**, 403 (1995).
[5] J. A. Nissen, E. Bodegom, L. C. Brodie, and J. S. Semura, Phys. Rev. **B40**, 6617 (1989).
[6] Q. Xiong and H. J. Maris, J. Low Temp. Phys. **82**, 105 (1991).
[7] M. S. Pettersen, C. Naud, S. Balibar, and H. J. Maris, Physica **B194–196**, 575 (1994).
[8] V. A. Akulichev and V. A. Bulanov, Sov. Phys. Acoust. **20**, 501 (1975).
[9] I. M. Lifshitz and Yu. Kagan, Sov. Phys. JETP **35**, 206 (1972).
[10] S. E. Korchunov, Sov. J. Low Temp. Phys. **14**, 316 (1988).
[11] S. N. Burmistrov and L. B. Dubovskii, J. Low Temp. Phys. **96**, 131 (1994).
[12] A. F. Andreev, in *Quantum Theory in Solids*, I. M. Lifshitz (ed.), MIR Publishers, Moscow (1982), p. 11; M. Uwaha, J. Low Temp. Phys. **52**, 15 (1983).
[13] *Quantum Tunneling in Condensed Medium*, Yu, Kagan and A. J. Leggett (eds.), North-Holland, Amsterdam (1992).
[14] A. O. Caldeira and A. J. Leggett, Phys. Rev. Lett. **46**, 211 (1981); Ann. Phys. **149**, 374 (1983).
[15] A. I. Larkin and Yu. N. Ovchinnikov, JETP Lett. **37**, 382 (1983); Sov. Phys. JETP **59**, 420 (1984).
[16] S. N. Burmistrov and L. B. Dubovskii, Sov. Phys. JETP **66**, 414 (1987).
[17] L. D. Landau and E. M. Lifshitz, *Hydrodynamics*, Pergamon, New York (1986).
[18] I. M. Khalatnikov, *An Introduction to the Theory of Superfluidity*, Addison, New York (1989).
[19] S. Balibar, G. Guthmann, H. Lambare, P. Roche, E. Rolley, and H. J. Maris, J. Low Temp. Phys. **101**, 271 (1995).

This article was published in English in the original Russian journal. It was edited by S. J. Amoretty.

Viscosity and ultrasonic attenuation in ^{4}He below 0.6 K

Chung-In Um

Department of Physics, College of Science, Korea University Seoul 136-701, Korea

Soo-Young Lee

The Research Institute of Basic Science, Korea University Seoul 136-701, Korea

Sahng-Kyoon Yoo

Department of Physics, Seonam University Namwon, Chunbuk 590-170, Korea

Thomas F. George

*Office of the Chancellor/Departments of Chemistry and Physics & Astronomy, University of Wisconsin-Stevens Point, Stevens Point, Wisconsin 54481-3897, USA**

Lakshmi N. Pandey

Departments of Chemistry and Physics, Washington State University, Pullman, Washington 99164-4630, USA

Igor N. Adamenko

Department of Physics and Technology, Kharkov State University, Kharkov 310077, Ukraine
(Submitted November 29, 1996)
Fiz. Nizk. Temp. **23**, 537–545 (May–June 1997)

Through a treatment of three-phonon processes, the wide-angle scattering rates and the absorption rates of phonons, which characterize viscosity and ultrasonic attenuation, respectively, are calculated for ^{4}He below 0.6 K. These rates are obtained from the collision matrix which is constructed approximately from an integral eigenvalue equation for the collision operator. The sequence of the lowest eigenvalues of the collision matrix as the angular momentum quantum number (l) increases shows a saturated behavior which has not been reported before. The calculated viscosity and ultrasonic attenuation are compared with previous theoretical and experimental results. [S1063-777X(97)00605-1]

1. INTRODUCTION

Since the anomalous phonon energy spectrum for ^{4}He was proposed,[1] its transport properties have been studied on the basis of that spectrum.[2–4] For the case of the anomalous phonon spectrum, the lowest-order phonon processes are three-phonon processes (3PP), while for the case of the normal spectrum they are four-phonon processes (4PP). Thus, in order to investigate the properties of superfluid ^{4}He at low temperatures, we must completely understand 3PP.

Maris[5] explained the temperature dependence of the viscosity of ^{4}He below 0.6 K in terms of the eigenvalues of the 3PP collision operator. Later, using a variational calculation, Benin[6] obtained similar results. Their fundamental idea is that the relaxation rate characterizing the viscosity is the eigenvalue of the 3PP collision operator with angular momentum quantum number $l = 2$. Although their results provide a good explanation for viscosity experimental data,[7] in the development of their theories oversimplified approximations were used for simplicity of the numerical calculation. Maris, for example, used only the linear term in the expression for the anomalous phonon energy spectrum in the matrix element calculation, and for the procedure of transforming an integral eigenvalue problem into a matrix form he divided the range of the integral into a relatively small number of summing points (10–20). In Benin's theory, rather rough trial wave functions were used. The effects of these rough approximations in both theories can be shown in the behavior of the sequence of the lowest eigenvalues with increasing l at a given temperature. Maris's theory[3,8] shows increasing behavior of the sequence with l, i.e., no saturation, and in Benin's variational theory this increasing behavior is more severe.

In general, as l increases, the angular distance θ_m between the maximum point and minimum point of the variation of the phonon distribution from an equilibrium value decreases inversely with l ($\theta_m = \pi/l$). Roughly speaking, when $\theta_m/2$ becomes smaller than the average value of the scattering angle of 3PP at a given temperature, the lowest relaxation rates may be constant, which shows a saturated behavior. We provide our numerical results showing this saturated behavior in Sec. 3.

For the eigenvalues of the 3PP collision operator, Maris[8] obtained a discrete spectrum. According to our calculation, the spectrum of the eigenvalues with $l = 2$ is a continuous spectrum with a finite positive minimum value. This continuous property of the eigenvalue spectrum seems to be in accordance with the theoretical work of Buot[9] about the relaxation rate spectrum of phonons. For the first-sound attenuation in ^{4}He, a shoulder observed by Roach *et al.*[10] was found to be the result of the restriction of 3PP, which

means that the zero-temperature spectrum depends on pressure.[11]

In this paper we obtain, using a similar method to Maris, the integral expression of the eigenvalue problem and convert it into a matrix form. From this collision matrix we calculate the eigenvalues and phonon viscosity for ^{4}He below 0.6 K. From the diagonal elements of the collision matrix, we also give a natural explanation for the shoulder of the ultrasonic attenuation. In Sec. 2 the collision matrix for 3PP is constructed. The numerical analysis of the eigenvalues for the matrix is given in Sec. 3. In Sec. 4 we evaluate the viscosity and ultrasonic attenuation, and compare them with available experimental data. Conclusions are given in Sec. 5.

2. COLLISION MATRIX FOR THREE-PHONON PROCESSES

In the long-wavelength limit the interaction for 3PP is given by

$$\mathbf{V}_3=\int d\mathbf{r}\left[\frac{1}{2}\,m_4\mathbf{v}_s(\mathbf{r})\rho_4(\mathbf{r})\mathbf{v}_s(\mathbf{r}) + \frac{1}{6}\,\frac{\partial}{\partial n_4}\left(\frac{m_4 s^2}{n_4}\right)\rho_4(\mathbf{r})^3\right], \tag{2.1}$$

where m_4 is the ^{4}He mass, and $\mathbf{v}_s(\mathbf{r})$ and $\rho_4(\mathbf{r})$ are the local superfluid velocity and local density variation of ^{4}He from equilibrium density n_4, which are small quantities. These small variations can be expanded within a volume V in terms of phonon annihilation and creation operators, $b_{\mathbf{q}}$ and $b_{\mathbf{q}}^+$, as

$$\rho_4(\mathbf{r})=\sum_{\mathbf{q}}\left(\frac{q^2 n_4}{2m_4\omega_{\mathbf{q}}V}\right)^{1/2}(b_{\mathbf{q}}e^{i\mathbf{q}\cdot\mathbf{r}}+b_{\mathbf{q}}^+e^{-i\mathbf{q}\cdot\mathbf{r}}), \tag{2.2}$$

and

$$\mathbf{v}_s(\mathbf{r})=\sum_{\mathbf{q}}\left(\frac{\omega_{\mathbf{q}}}{2m_4 n_4 V}\right)^{1/2}\hat{q}(b_{\mathbf{q}}e^{i\mathbf{q}\cdot\mathbf{r}}+b_{\mathbf{q}}^+e^{-i\mathbf{q}\cdot\mathbf{r}}), \tag{2.3}$$

where $\omega_{\mathbf{q}}$ is the energy of a phonon with momentum $\mathbf{q}$. We can then obtain the matrix element for 3PP by a straightforward calculation as

$$\langle\mathbf{q}',\mathbf{q}''|V_3|\mathbf{q}\rangle=\left(\frac{T(\mathbf{q},\mathbf{q}',\mathbf{q}'')}{V}\right)^{1/2}\delta_{\mathbf{q}'+\mathbf{q}'',\mathbf{q}}, \tag{2.4}$$

where

$$T(\mathbf{q},\mathbf{q}',\mathbf{q}'')=\left(\frac{1}{8m_4n_4}\right)\left[\left(\frac{\omega_{\mathbf{q}}\omega_{\mathbf{q}''}}{\omega_{\mathbf{q}'}}\right)^{1/2}q'\hat{q}\cdot\hat{q}'' + \left(\frac{\omega_{\mathbf{q}}\omega_{\mathbf{q}'}}{\omega_{\mathbf{q}''}}\right)^{1/2}q''\hat{q}\cdot\hat{q}' + \left(\frac{\omega_{\mathbf{q}'}\omega_{\mathbf{q}''}}{\omega_{\mathbf{q}}}\right)^{1/2}q\hat{q}' \times\hat{q}''+s^2(2u-1)\,\frac{qq'q''}{(\omega_{\mathbf{q}}\omega_{\mathbf{q}'}\omega_{\mathbf{q}''})^{1/2}}\right]^2, \tag{2.5}$$

and u is the Grüneisen constant defined by

$$u=\frac{n_4}{s}\,\frac{\partial s}{\partial n_4}, \tag{2.6}$$

with a value of[12] 2.84.

The collision integral due to the 3PP is given by

$$I_{3\mathrm{PP}}(\mathbf{q})=\frac{1}{2}\sum_{\mathbf{q}',\mathbf{q}''}2\pi|\langle\mathbf{q}',\mathbf{q}''|V_3|\mathbf{q}\rangle|^2\delta(\varepsilon_f-\varepsilon_i)[n_{\mathbf{q}'}n_{\mathbf{q}''}(1+n_{\mathbf{q}})-n_{\mathbf{q}}(1+n_{\mathbf{q}'})(1+n_{\mathbf{q}''})] + \sum_{\mathbf{q}',\mathbf{q}''}2\pi|\langle\mathbf{q}'|V_3|\mathbf{q}\mathbf{q}''\rangle|^2\delta(\varepsilon_f-\varepsilon_i)[n_{\mathbf{q}'}(1+n_{\mathbf{q}''})(1+n_{\mathbf{q}})-n_{\mathbf{q}'}n_{\mathbf{q}''}(1+n_{\mathbf{q}'})], \tag{2.7}$$

where ε_i and ε_f are the phonon energies of the initial and final states, respectively, and $n_{\mathbf{q}}$ is the distribution of phonons with momentum $\mathbf{q}$. In Eq. (2.7), the first term represents the process $\mathbf{q}\rightleftharpoons\mathbf{q}'+\mathbf{q}''$ and the second term the process $\mathbf{q}'\rightleftharpoons\mathbf{q}+\mathbf{q}''$.

If the phonons are in their equilibrium state, i.e., $n_{\mathbf{q}}=n_{\mathbf{q}}^0$, where $n_{\mathbf{q}}^0$ is the equilibrium phonon distribution, the collision integral vanishes by detailed balance. If we consider a small variation from the equilibrium as

$$n_{\mathbf{q}}=n_{\mathbf{q}}^0+\delta n_{\mathbf{q}}, \tag{2.8}$$

then the collision integral can be rewritten to first order in $\delta n_{\mathbf{q}}$ as

$$I_{3\mathrm{PP}}(\mathbf{q})=-\frac{1}{2(2\pi)^2}\int_{(1)}dq'\,d\Omega_{q'}q'^2T(\mathbf{q},\mathbf{q}',\mathbf{q}'')\,\delta(\varepsilon_f-\varepsilon_i)[\,\delta n_{\mathbf{q}}(1+n_{\mathbf{q}'}^0+n_{\mathbf{q}''}^0)-\delta n_{\mathbf{q}'}(n_{\mathbf{q}''}^0-n_{\mathbf{q}}^0) - \delta n_{\mathbf{q}''}(n_{\mathbf{q}'}^0-n_{\mathbf{q}}^0)]-\frac{1}{(2\pi)^2}\int_{(2)}dq'\,d\Omega_{q'}q'^2T \times(\mathbf{q},\mathbf{q}',\mathbf{q}'')\,\delta(\varepsilon_f-\varepsilon_i)[\,\delta n_{\mathbf{q}}(n_{\mathbf{q}''}^0-n_{\mathbf{q}'}^0) - \delta n_{\mathbf{q}'}(1+n_{\mathbf{q}}^0+n_{\mathbf{q}''}^0)+\delta n_{\mathbf{q}''}(n_{\mathbf{q}}^0-n_{\mathbf{q}'}^0)]. \tag{2.9}$$

Because of the momentum conservation, $\mathbf{q}''=\mathbf{q}-\mathbf{q}'$ in the first integral and $\mathbf{q}''=\mathbf{q}'-\mathbf{q}$ in the second integral, which are denoted by (1) and (2), respectively, in Eq. (2.9).

The variation of the distribution function from the equilibrium state can be expanded by spherical harmonics as

$$\delta n_{\mathbf{q}}=q\overline{n_{\mathbf{q}}^0}\sum_{l,m}\Phi_{lm}(q)Y_{lm}(\Omega_q), \tag{2.10}$$

where for simplicity we define

$$\overline{n_{\mathbf{q}}^0}\equiv\frac{\partial n_{\mathbf{q}}^0}{\partial\omega_{\mathbf{q}}}. \tag{2.11}$$

$Y_{lm}(\Omega_q)$ is a spherical harmonic, and Ω_q is the solid angle of $\mathbf{q}$. Using the addition theorem, we transform the spherical harmonics for $\mathbf{q}'$ and $\mathbf{q}''$ to those for $\mathbf{q}$ as follows:

$$Y_{lm}(\Omega_{q'})\rightarrow P_l(\cos\,\theta)Y_{lm}(\Omega_q), \tag{2.12}$$

$$Y_{lm}(\Omega_{q''})\rightarrow P_l(\cos\,\theta')Y_{lm}(\Omega_q), \tag{2.13}$$

where P_l is the Legendre polynomial, and θ and θ' are the angles between momenta $(\mathbf{q},\mathbf{q}')$ and momenta $(\mathbf{q},\mathbf{q}'')$, respectively.

After performing the angular integration, we obtain the collision integral as

$$I_{3\mathrm{PP}}(\mathbf{q}) = -q\overline{n}_{\mathbf{q}}^{0}\sum_{l,m} Y_{lm}(\Omega_q) \times\Bigg\{\frac{1}{2(2\pi)}\int_{(1)} dq'q'^2\,\frac{T(\mathbf{q},\mathbf{q}',\mathbf{q}'')}{B(\mathbf{q},\mathbf{q}',\mathbf{q}'')}\Bigg[(1+n_{\mathbf{q}'}^{0}+n_{\mathbf{q}''}^{0})\Phi_{lm}(q) - \frac{q'\overline{n}_{\mathbf{q}'}^{0}}{q\overline{n}_{\mathbf{q}}^{0}}(n_{\mathbf{q}''}^{0} - n_{\mathbf{q}}^{0})P_l(\cos\theta)\Phi_{lm}(q') - \frac{q''\overline{n}_{\mathbf{q}''}^{0}}{q\overline{n}_{\mathbf{q}}^{0}}(n_{\mathbf{q}'}^{0} - n_{\mathbf{q}}^{0})P_l(\cos\theta')\Phi_{lm}(q'')\Bigg] + \frac{1}{2\pi}\int_{(2)} dq'q'^2\,\frac{T(\mathbf{q},\mathbf{q}',\mathbf{q}'')}{B(\mathbf{q},\mathbf{q}',\mathbf{q}'')}\Bigg[(n_{\mathbf{q}''}^{0} - n_{\mathbf{q}'}^{0})\Phi_{lm}(q) - \frac{q'\overline{n}_{\mathbf{q}'}^{0}}{q\overline{n}_{\mathbf{q}}^{0}}(1+n_{\mathbf{q}}^{0} + n_{\mathbf{q}''}^{0})P_l(\cos\theta)\Phi_{lm}(q') + \frac{q''\overline{n}_{\mathbf{q}''}^{0}}{q\overline{n}_{\mathbf{q}}^{0}}(n_{\mathbf{q}}^{0} - n_{\mathbf{q}'}^{0})P_l(\cos\theta')\Phi_{lm}(q'')\Bigg]\Bigg\}, \tag{2.14}$$

where $B(\mathbf{q},\mathbf{q}',\mathbf{q}'')$, which originates from the delta function representing energy conservation through $3PP$, is defined by

$$B(\mathbf{q},\mathbf{q}',\mathbf{q}'') = \left|\frac{\partial(\varepsilon_f - \varepsilon_i)}{\partial\cos\theta}\right|. \tag{2.15}$$

If we represent the collision integral in terms of the relaxation time τ_l i.e.,

$$I_{3\mathrm{PP}}(\mathbf{q}) = -q\overline{n}_{\mathbf{q}}^{0}\sum_{l,m}\frac{Y_{lm}(\Omega_q)\Phi_{lm}(q)}{\tau_l}, \tag{2.16}$$

we can then obtain the eigenvalue equation for each l. Because the different values of m do not change the form of the eigenvalue equation, we can suppress the index m.

The eigenvalue equation for a given l becomes

$$\frac{1}{2(2\pi)}\int_{(1)} dq'q'^2\,\frac{T(\mathbf{q},\mathbf{q}',\mathbf{q}'')}{B(\mathbf{q},\mathbf{q}',\mathbf{q}'')}\Bigg[(1+n_{\mathbf{q}'}^{0}+n_{\mathbf{q}''}^{0})\Phi_l(q) - \frac{q'\overline{n}_{\mathbf{q}'}^{0}}{q\overline{n}_{\mathbf{q}}^{0}}(n_{\mathbf{q}''}^{0} - n_{\mathbf{q}}^{0})P_l(\cos\theta)\Phi_l(q') - \frac{q''\overline{n}_{\mathbf{q}''}^{0}}{q\overline{n}_{\mathbf{q}}^{0}}(n_{\mathbf{q}'}^{0} - n_{\mathbf{q}}^{0})P_l(\cos\theta')\Phi_l(q'')\Bigg] + \frac{1}{2\pi}\int_{(2)} dq'q'^2\,\frac{T(\mathbf{q},\mathbf{q}',\mathbf{q}'')}{B(\mathbf{q},\mathbf{q}',\mathbf{q}'')}\Bigg[(n_{\mathbf{q}''}^{0} - n_{\mathbf{q}'}^{0})\Phi_l(q) - \frac{q'\overline{n}_{\mathbf{q}'}^{0}}{q\overline{n}_{\mathbf{q}}^{0}}(1+n_{\mathbf{q}}^{0}+n_{\mathbf{q}''}^{0})P_l(\cos\theta)\Phi_l(q') + \frac{q''\overline{n}_{\mathbf{q}''}^{0}}{q\overline{n}_{\mathbf{q}}^{0}}(n_{\mathbf{q}}^{0} - n_{\mathbf{q}'}^{0})P_l(\cos\theta')\Phi_l(q'')\Bigg] = \lambda_l\Phi_l(q), \tag{2.17}$$

where the eigenvalue $\lambda_l = \tau_l^{-1}$.

Since this integral eigenvalue equation cannot be solved analytically, we use a numerical method. If we replace the integral on the left-hand side by a sum over a finite set of points, we obtain a matrix eigenvalue equation

$$M_l\Phi_l = \lambda_l\Phi_l, \tag{2.18}$$

where M_l denotes the collision matrix with a given l symbolically. The diagonal elements of the matrix M_l come from the terms containing $\Phi_l(q)$ in Eq. (2.17), while the terms containing $\Phi_l(q')$ or $\Phi_l(q'')$ give the off-diagonal elements. The number of eigenfunctions and eigenvalues will then be equal to the matrix size j_m, the number of points to be summed over.

3. NUMERICAL ANALYSIS OF THE EIGENVALUES

A. Phonon energy spectrum

In order to perform numerical calculations we should choose an anomalous phonon energy spectrum to use. As will be seen below, the wide-angle scattering rate depends sensitively on the phonon energy spectrum. Among the various spectra proposed by many authors, we take two forms, one suggested by Greywall[13] and another by Maris.[3] The phonon energy spectrum suggested by Greywall is

$$\omega_{\mathbf{q}} = sq(1+\alpha_2 q^2 + \alpha_4 q^4 + \alpha_6 q^6), \tag{3.1}$$

where

$$s = 237.0 \text{ m/s for } P = 0 \text{ atm},$$

$$s = 298.9 \text{ m/s for } P = 10 \text{ atm},$$

$$\alpha_2 = 1.30 - 0.065\ P,$$

$$\alpha_4 = -10.25\alpha_2 + 108.5(s_4/s - 1) - 28.44(s_5/s - 1),$$

$$\alpha_6 = 25.0\alpha_2 - 434.0(s_4/s - 1) + 177.8(s_5/s - 1),$$

$$s_4 = 247.0 + 2.86\ P,$$

$$s_5 = 242.0 + 2.20\ P.$$

Here s is the velocity of first sound, and P is the pressure. Since this spectrum has pressure dependence, it is available under arbitrary pressure. Another spectrum given by Maris is

$$\omega_{\mathbf{q}} = sp\left(1 + \gamma p^2\,\frac{1-(p/p_A)^2}{1+(p/p_B)^2}\right), \tag{3.2}$$

where

$$s = 238.3 \text{ m/s},$$

$$\gamma = 10\times 10^{37} \text{ cgs units},$$

$$p_A/\hbar = 0.542 \text{ Å}^{-1},$$

$$p_B/\hbar = 0.332 \text{ Å}^{-1}.$$

Let us test the properties of the above two spectra. Figure 1 shows the phase velocities of the two spectra and the group velocity of Greywall's spectrum at $P = 0$ atm. The phase velocity of Greywall's spectrum at $P = 10$ atm is also presented. It is shown that the phase velocities are consistent with neutron scattering experiments.[14] For the case of $P = 0$ atm, the maximum positions of the phase velocities, v_p, of the two spectra are almost the same at about $q = 0.3$ Å^{-1}, while the maximum value of Greywall's spec-

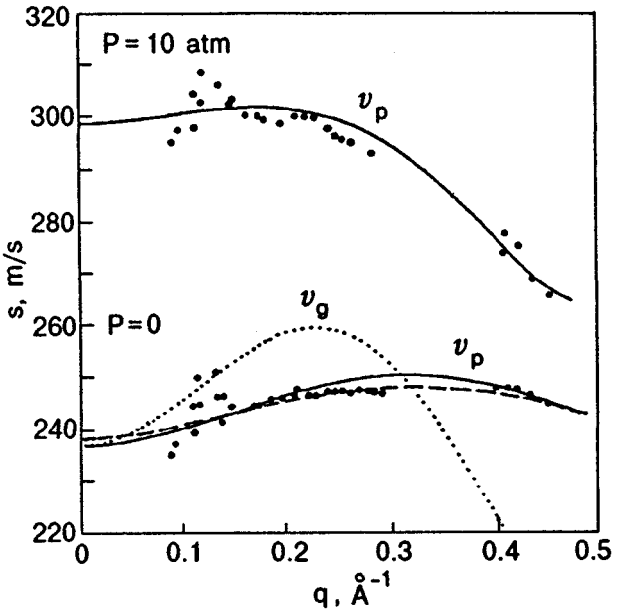

FIG. 1. Phase and group velocities at $P = 0$ atm and $P = 10$ atm. The solid lines are the phase velocities of Greywall's spectrum: the upper curve is for $P = 10$ atm and the lower curve for $P = 0$ atm. The dashed line is Maris's phase velocity. The phase velocities of both spectra are consistent with neutron scattering experiments.[14] The dotted line represents Greywall's group velocity.

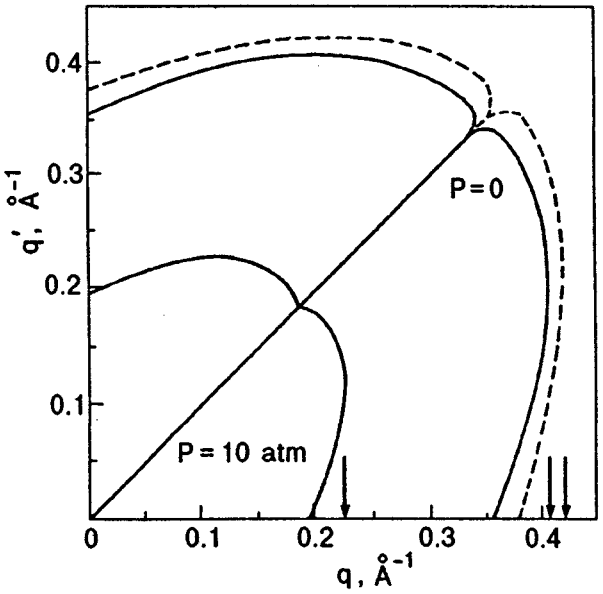

FIG. 2. The allowed range of 3PP for Greywall's spectrum (solid lines) at $P = 0$ atm and $P = 10$ atm and that of Maris's spectrum (dashed lines). The vertical arrows indicate the cutoff momenta. The lower part ($q > q'$) denotes the allowed range of the first process and the upper part ($q' > q$) that of the second process.

trum is larger than that of Maris's spectrum. For $P = 10$ atm, the range of v_p/s is reduced considerably compared to the case of $P = 0$ atm, which is related closely to the cutoff momentum, q_c, above which 3PP do not occur.

For the above spectra we obtain the allowed range for 3PP and 3PP scattering angle, using conditions of energy and momentum conservation. Since the 3PP do not change the total momentum and total energy, the momentum and energy of the initial state equal those of the final state. For convenience, we denote $\mathbf{q} = \mathbf{q}' + \mathbf{q}''$ as the first process and $\mathbf{q}' = \mathbf{q} + \mathbf{q}''$ as the second process. For the case of the first process, for example, the energy and momentum conserve as

$$\mathbf{q} = \mathbf{q}' + \mathbf{q}'', \tag{3.3}$$

$$\omega_{\mathbf{q}} = \omega_{\mathbf{q}'} + \omega_{\mathbf{q}''}. \tag{3.4}$$

Using the above equations, we can determine the allowed range for 3PP in the qq'-plane, which is shown in Fig. 2. The lower part of the diagonal line in Fig. 2 is the region in which the first process is allowed, and the upper part corresponds to the second process. The allowed regions have symmetry about the diagonal line, i.e., under exchange of q and q', as expected. The changes of the range with pressure also are shown. As pressure increases, the allowed range for 3PP becomes smaller, which can be expected from the behavior of the phase velocity with pressure in Fig. 1. We can see the cutoff momentum, q_c, for 3PP, which is represented by a vertical arrow in Fig. 2. We note that the allowed range for 3PP and cutoff momentum from Maris's spectrum are larger than those of Greywall's spectrum.

From the conditions of momentum and energy conservation we also obtain the 3PP scattering angle distribution. The distribution of the 3PP scattering angle of the first process, i.e., the angle between $\mathbf{q}$ and $\mathbf{q}'$, is shown in Fig. 3. The maximum scattering angle for Greywall's spectrum is 23.8°, which is larger than 19.6° for Maris's spectrum.

B. Numerical calculation of the eigenvalue

The eigenvalues of the 3PP collision matrix with $l = 2$, M_2, are the relaxation rates characterizing the viscosity, because they are related to the phonon momentum transfer in the perpendicular direction. We note that the eigenvalues depend on the matrix size j_m. As we can see in Fig. 4, the eigenvalue spectrum becomes denser as j_m increases. Such behavior of the eigenvalues indicates that the eigenvalue spectrum at infinite j_m is continuous, in contrast with the result of Maris,[8] in which a discrete eigenvalue spectrum is obtained. Only the lowest eigenvalue has physical importance, because the corresponding eigenfunction, which has no node, is appreciable in the range of momenta considered, while the eigenfunctions corresponding to the eigenvalues just above the lowest one are negligible except for a very small momentum. A similar argument for the eigenvalues with $l = 1$ was given by Maris.[8]

The temperature variation of the lowest eigenvalue $\lambda_2(T)$ with j_m is shown in Fig. 5. We see that $\lambda_2(T)$ converges with increasing j_m. This fact is different from Maris's argument that for $j_m = 15$ $\lambda_2(T)$ is independent of the details of the mesh to better than 1%.

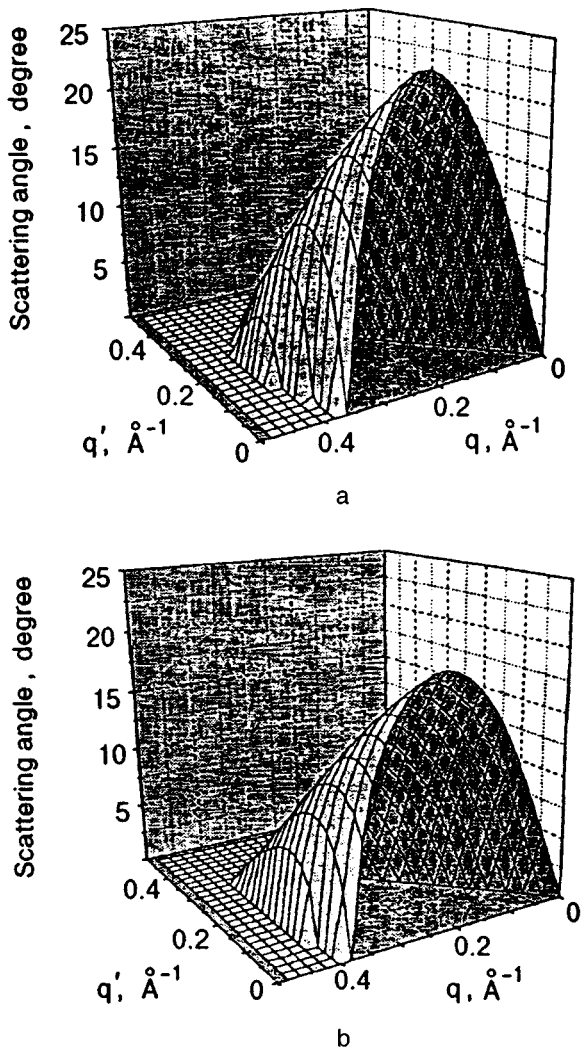

FIG. 3. 3PP scattering angle distribution of the first processes. a) Greywall's spectrum. b) Maris's spectrum.

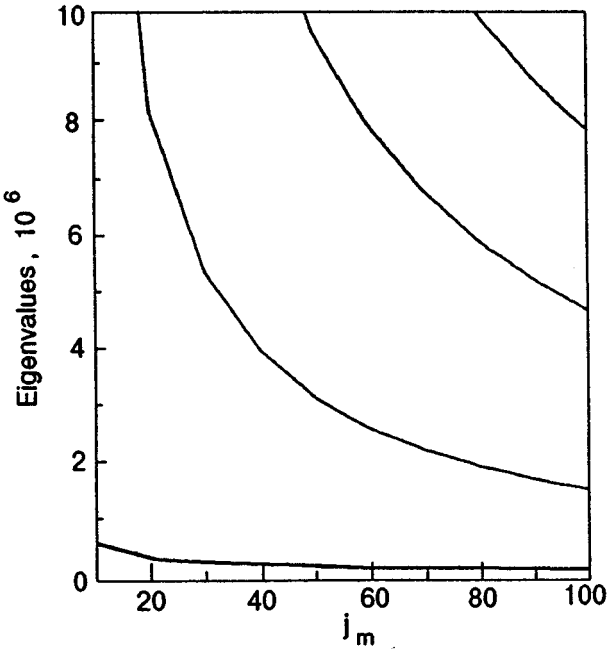

FIG. 4. Several eigenvalues, including the lowest one, plotted as matrix size j_m.

We also obtain the lowest eigenvalues for several l, as shown in Fig. 6. A saturated behavior appears when we set $j_m = 100$, which means that the phonons relax sufficiently in one collision time. At higher temperatures this saturated behavior may begin to appear at smaller l, since the typical 3PP scattering angle increases due to the higher average value of momentum (Fig. 3). Figure 6 shows this behavior correctly. On the other hand, the results obtained by Maris[8] and Benin[6] have no saturated behavior. Their results are very similar to the case $j_m = 10$ in our calculation. But $j_m = 10$ is too small to reveal the properties of the anomalous spectrum correctly. Therefore, we guess that their results with no saturation are due to the rough approximations in their numerical calculations.

Using both spectra presented before, we calculate the lowest eigenvalues λ_2 as a function of temperature by taking $j_m = 300$ and the upper bound of the integral of Eq. (2.17), $q_m = 0.45$ Å^{-1}; i.e., $\Delta_q = 0.0015$ Å^{-1}. This value of q_m is enough to cover the effective range of the integral, because the cutoff momentum q_c at $P = 0$ atm is about 0.4 Å^{-1}, as shown in Fig. 2. The results are shown in Fig. 7. When Greywall's spectrum is used, the values of $\lambda_2(T)$ are larger than those of Maris. This can be understood from the fact that the maximum value of the 3PP scattering angle distribution for Greywall's spectrum is greater than that of Maris's spectrum. Using Greywall's spectrum with $P = 10$ atm, we obtain a smaller $\lambda_2(T)$ than for the case $P = 0$ atm, which is a trivial result, because the cutoff momentum and 3PP scattering angle become smaller as a pressure increases.

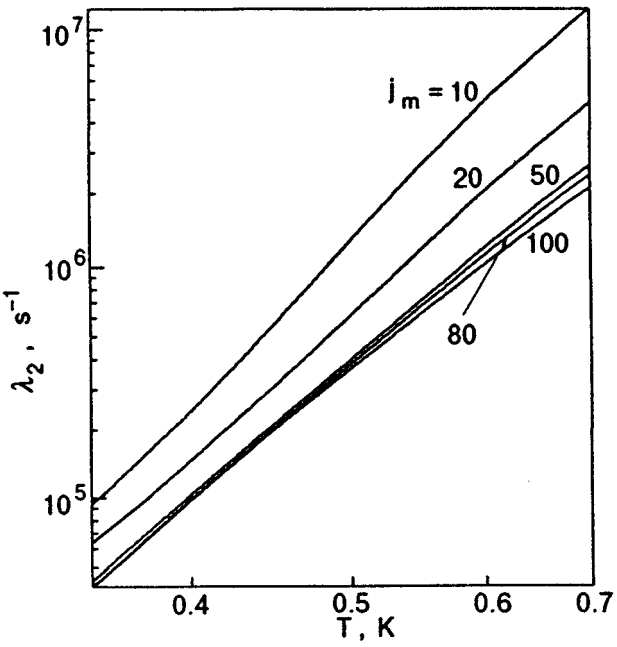

FIG. 5. Convergence of the lowest eigenvalues (λ_2) as a function of matrix size j_m.

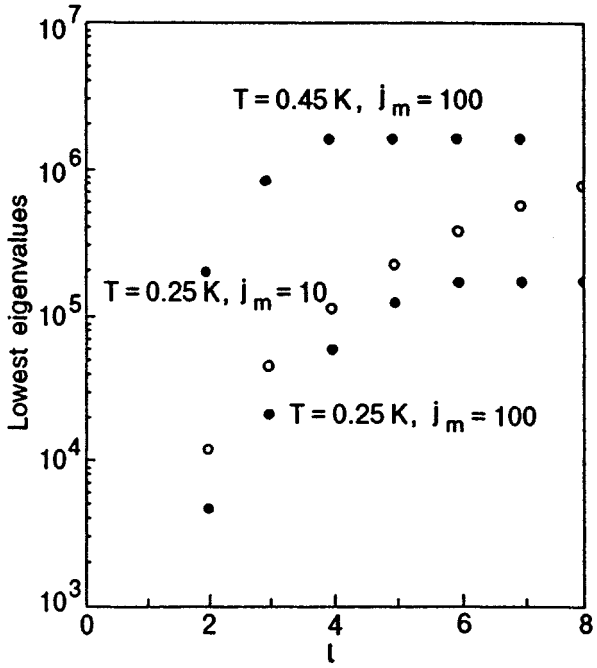

FIG. 6. Lowest eigenvalues versus l.

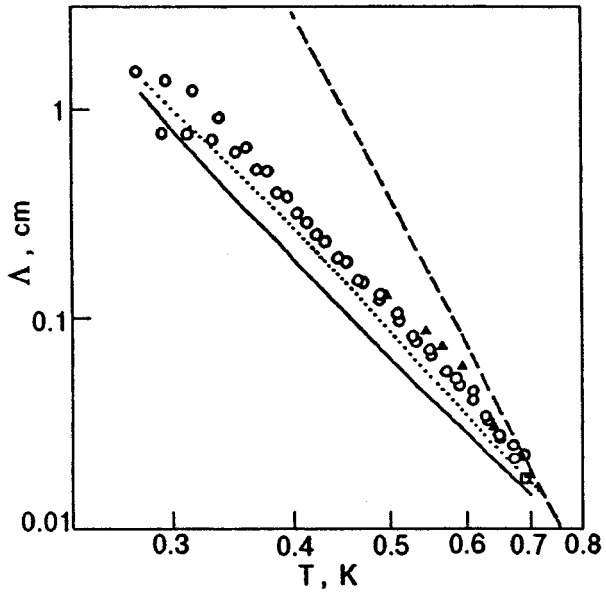

FIG. 8. Phonon mean free path resulting from 3PP. The solid line represents the result using Greywall's spectrum, and the dotted line that using Maris's spectrum. The open circles and the triangular marks indicate the experimental data on thermal conductivity by Greywall[13] and Whitworth,[7] respectively. The dashed line shows the theory of Landau and Khalatnikov based on 4PP.[15]

4. VISCOSITY AND ULTRASONIC ATTENUATION

A. Viscosity

The viscosity is written in terms of the phonon mean free path, which characterizes the viscosity[3] as

$$\eta = \frac{1}{5}\rho_{\rm ph}\langle v_g\rangle\Lambda, \tag{4.1}$$

where $\rho_{\rm ph}$ is the phonon mass density defined by

$$\rho_{\rm ph} = -\sum_{\mathbf{q}} \frac{q^2}{3}\frac{\partial n^0_{\mathbf{q}}}{\partial \omega_{\mathbf{q}}}, \tag{4.2}$$

and $\langle v_g\rangle$ is the average of the phonon group velocity

$$\langle v_g\rangle \equiv -\frac{1}{\rho_{\rm ph}}\sum_{\mathbf{q}} \frac{q^2}{3}\frac{\partial n^0_{\mathbf{q}}}{\partial \omega_{\mathbf{q}}}\frac{d\omega_{\mathbf{q}}}{dq}. \tag{4.3}$$

The mean free path for 3PP is related to the eigenvalues of the collision matrix as

$$\Lambda = \frac{\langle v_g\rangle}{\lambda_2}. \tag{4.4}$$

The results for Λ are shown in Fig. 8. The dashed line denotes the mean free path due to 4PP calculated by Landau and Khalatnikov,[15] which has a T^{-9} dependence. At $P = 0$ atm, the mean free path from Maris's spectrum, drawn by the dotted line, shows good agreement with the experiment performed on thermal conductivity by Greywall.[13] The mean free path from Greywall's spectrum appears to be lower than the experimental data. It can be well deduced, at least qualitatively, from the higher maximum value of the 3PP scattering angle in Fig. 3 and the larger phase velocity in Fig. 1.

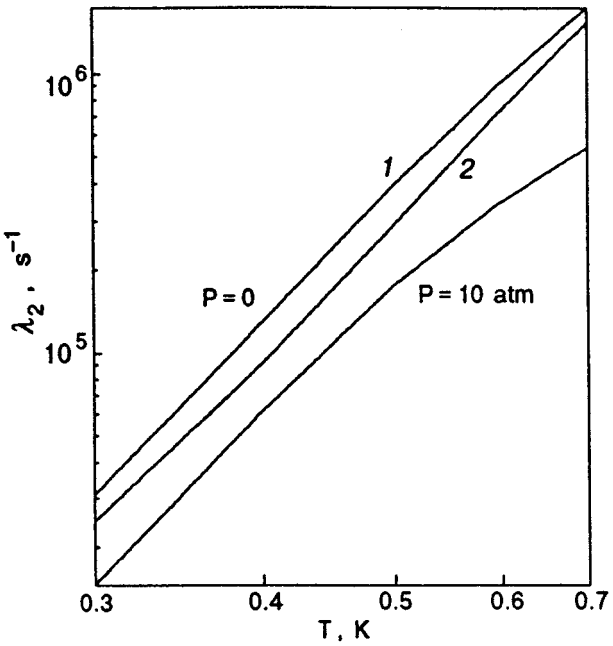

FIG. 7. Lowest eigenvalues (λ_2) as a function of T. a) Greywall's spectrum, b) Maris's spectrum. The case $P = 10$ atm from Greywall's spectrum is also shown.

B. Ultrasonic attenuation

At low pressures, the temperature dependence of the high-frequency ultrasonic attenuation (α) is approximately described by a T^4 law as under vapor pressure, whereas at higher pressures ($\geqslant$10 atm) the $\alpha(T)$ curve is significantly changed, and a shoulder occurs.[10] Roach *et al.*[10] suggested that the shoulder might indicate the existence of a new relaxation mechanism. However, Jäckle and Kehr[11] showed

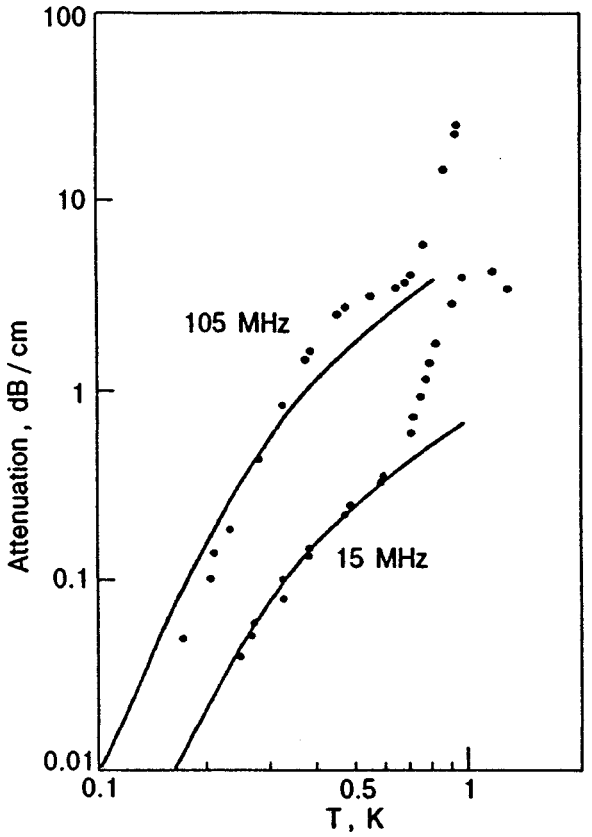

FIG. 9. Ultrasonic attenuation at 15 MHz and 105 MHz under pressure of 16.4 atm. The solid points are the experimental data of Roach *et al.*[10]

that the formation of the shoulder in $\alpha(T)$ is explained by assuming that the 3PP is allowed only for very long-wavelength phonons (''partially allowed 3PP'') due to deformation of the phonon spectrum under pressure.

Let us now consider the appearance of the shoulder using the collision matrix introduced in the previous section. The ultrasonic sound mens very long-wavelength phonons, which are injected from outside of the system. We can assume, therefore, that thermal phonons are in equilibrium, and only very long-wavelength phonons have variation from equilibrium due to the injected sound phonons.

Let the momentum of sound phonons be q. For thermal phonons with momenta q' and q'' in the equilibrium state we have

$$\Phi_l(q')=0, \tag{4.5}$$

$$\Phi_l(q'')=0 \tag{4.6}$$

in the collision integral of Eq. (2.17). Only the terms containing $\Phi_l(q)$ will then remain. This means that only the diagonal elements of the collision matrix are nonzero, and the l-dependence of the collision matrix equation will then disappear. The absorption rate, $\Gamma_a(q)$, of the sound phonon by a thermal phonon therefore becomes the diagonal part of the collision matrix.

The attenuation of sound is related to the absorption rate as

TABLE I. Phonon spectrum parameters used in the calculation of the sound attenuation at $P = 16.4$ atm.

s,(m/s)	α_2,(Å^2)	α_4,(Å^4)	α_6,(Å^6)	θ_m,(degree)	sq_c/k_B, (K)
332.4	0.0454	−8.3	22.35	0.83	1.59

$$\alpha=\frac{\Gamma_a(q)}{2s}. \tag{4.7}$$

Therefore, if we know the phonon energy spectrum under pressure, the attenuation of first sound can be obtained. Figure 9 shows the results for the attenuation of ultrasonic sound. For temperatures below 0.6 K the results show good agreement with experimental data. The parameters of the phonon energy spectrum used in this calculation are listed in Table I. The maximum scattering angle θ_m and cutoff momentum q_c calculated by these parameters are also listed in Table I. We find that for the case of attenuation of sound, the process $\mathbf{q}+\mathbf{q}''\rightarrow\mathbf{q}'$ is dominant. This means that the sound phonons are absorbed by thermal phonons. The scattering in this case is almost linear since the maximum scattering angle is $\theta_m = 0.83°$, and only very long-wavelength phonons, $q < 0.0625$ Å^{-1}, take part in the scattering. The cutoff momentum obtained here shows remarkable agreement with the result of Jäckle and Keher (within 1%). The rapidly increasing behavior at high temperature, $T > 0.6$ K, can be explained by considering the existence of rotons,[11] and so for this temperature range the contribution of rotons is essential.

5. CONCLUSIONS

We obtained the wide-angle scattering rates and the absorption rates of phonons in ^{4}He below 0.6 K by solving the eigenvalue equation for the 3PP collision matrix. The sequence of the lowest eigenvalues of the collision matrix along l shows a saturated behavior, which is different from the results given by Maris and Benin. Using Maris and Greywall's phonon spectra, we calculated the viscosity mean free paths and compared them with experimental data, where the Maris's spectrum seems to be in better agreement. For the result of ultrasonic attenuation, the phonon spectrum parameters at $P = 16.4$ atm are obtained from a fit, and the cutoff momentum calculated from the parameters is in excellent agreement with Ref. 11.

Since the 3PP are an important phonon-phonon mechanism in dilute ^{3}He–^{4}He mixtures at low temperatures, it is possible to apply this theory to such mixtures. This study is in progress.

ACKNOWLEDGMENTS

This work was supported by the Research Institute of Basic Science in Korea University and Nondirected Research Fund, Korea Research Foundation, 1995.

*E-mail: tgeorge@uwsp.edu

[1] H. J. Maris and W. E. Massey, Phys. Rev. Lett. **25**, 220 (1970).
[2] H. J. Maris, Phys. Rev. Lett. **28**, 277 (1972).
[3] H. J. Maris, Phys. Rev. Lett. **30**, 312 (1973).

[4] C. I. Um, C. W. Jun, and T. F. George, Phys. Rev. B **46**, 5746 (1992).
[5] H. J. Maris, Phys. Rev, A **8**, 1980 (1973).
[6] D. Benin, Phys. Rev. B **11**, 145 (1975).
[7] R. W. Whitworth, Proc. R. Soc. Lond. A **246**, 390 (1958).
[8] H. J. Maris, Phys. Rev. A **9**, 1412 (1974).
[9] F. A. Buot, J. Phys. C: Solid State Phys. **5**, 5 (1972).
[10] P. R. Roach, J. B. Ketterson, and M. Kuchnir, Phys. Rev. Lett. **25**, 1002 (1970).
[11] J. Jäckle and K. W. Kehr, Phys. Rev. Lett. **27**, 654 (1971).
[12] B. M. Abraham, Y. Eckstein, J. B. Ketterson, M. Kuchnir, and P. R. Roach, Phys. Rev. A **1**, 250 (1970); Phys. Rev. A **2**, 550 (1970).
[13] D. S. Greywall, Phys. Rev. B **23**, 2152 (1981).
[14] W. G. Stirling, J. R. D. Copley, and P. A. Hilton, *Proc. of the Int. Symp. on Neutron Inelastic Scattering*, I.A.E.A., Vienna (1977).
[15] L. D. Landau and I. M. Khalatnikov, JETP **19**, 637, 709 (1949).

This article was published in English in the original Russian journal. It was edited by S. J. Amoretty.

Orbital anisotropy of magnetically distorted superfluid ^{3}He-*B*

A. Gongadze, G. Kharadze, and G. Vachnadze

Institute of Physics, 6 Tamarashvili st., 380077 Tbilisi, Georgia[1)]
(Submitted November 18, 1996)
Fiz. Nizk. Temp. **23**, 546–552 (May–June 1997)

The orbital anisotropy of the magnetized superfluid *B*-phase of liquid ^{3}He is investigated theoretically for arbitrary fields and temperatures. The behavior of freely rotating *B*-phase under the action of magnetic field is considered. © *1997 American Institute of Physics.* [S1063-777X(97)00705-6]

1. INTRODUCTION

Ultralow-temperature superfluid phases of liquid ^{3}He are ordered states of a Fermi system which have lost the series of symmetries appropriate to the normal state of ^{3}He. The order parameters of superfluid *A*- and *B*-phases are complicated multidimensional objects with nontrivial topological structures that generate rich properties of the Bose-condensate of Cooper pairs with spins $S=1$ and internal orbital moments $L=1$ (Ref. 1). Along with the amplitudes that characterize the amount of the Bose-condensation energy, the order parameters of the superfluid phases of ^{3}He depend on the Goldstone variables (overall phase and various angles specifying orientation of spin and orbital degrees of freedom of Cooper pairs).

The external magnetic field has a strong influence on the properties of superfluid phases. Especially susceptible in this respect is the initially isotropic *B*-phase, which is unable (in contrast to the *A*-phase) to adjust to the applied magnetic field at the expense of the reorientation of the Goldstone degrees of freedom, thereby saving the condensation energy. Instead, the *B*-phase exhibits strong distortion even at moderately high magnetic fields that lose part of the condensation energy (at a given temperature and pressure): its longitudinal $\langle\langle \text{gap}\rangle\rangle$ $\Delta_\parallel$ along the direction of the field is suppressed[2,3] and the superfluid state acquires magnetic anisotropy. It is important that because of the relative spin-orbit coherence of the *B*-phase, the appearance of the magnetic anisotropy axis $\hat{\mathbf{h}}$ (along the direction of the field $\mathbf{H}$) generates uniaxial anisotropy of the orbital properties of the magnetized ^{3}He-*B* along the axis $\hat{\mathbf{l}}_B=\hat{\mathbf{h}}\overleftrightarrow{R}$, where $\overleftrightarrow{R}$ is the matrix of $3D$ rotations of the spin space with respect to the orbital space. In particular, the energy spectrum of fermionic excitations becomes anisotropic so that the normal (as well as superfluid) component density exhibits tensor character.

At present, there is a considerable amount of experimental information concerning diverse properties of strongly magnetized *B*-phase. Acoustic measurements allowed us to observe directly the suppression of $\Delta_\parallel$ by the external magnetic field[4,5] and to investigate orbital anisotropy of the magnetized stationary and rotating ^{3}He-*B*.[6] The anisotropic nature of magnetically distorted *B*-phase was observed also by means of the NMR techniques[7,8] and by measuring the ion mobility.[9]

There is satisfactory understanding of the properties of ^{3}He-*B* in the case where the anisotropy parameter $\delta_B=(\Delta_\perp-\Delta_\parallel)/\Delta_\perp$ is small ($\delta_B\ll 1$). On the other hand, the magnetic distortion of the *B*-phase is very pronounced near the *B* to *A* transition (at low pressures), where $\Delta_\parallel\ll\Delta_\perp$ (when the transformation is close to a continuous transformation). In this region there is still a gap in the detailed theoretical description of the behavior of the ^{3}He-*B*. One of the goals of this study is the elaboration of the theoretical background for the interpretation of the properties of strongly distorted ($\delta_B \lesssim 1$) *B*-phase of superfluid ^{3}He. In Sec. 2 we consider the anisotropy of the superfluid density of the magnetized ^{3}He-*B* in the (T, H) plane. The results are used to construct T and H dependences of the dipolar velocity v_D in Sec. 3. The effect of the magnetic-field-dependent orbital anisotropy on the behavior of the freely rotating *B*-phase is analyzed in Sec. 4.

2. ANISOTROPY OF THE SUPERFLUID DENSITY OF MAGNETIZED ^{3}He-*B*

Uniaxial orbital anisotropy of ^{3}He-*B* in the flow effects manifests itself, in the first place, in the tensorial character of superfluid density (below we drop the subscript at $\hat{\mathbf{l}}_B$):

$$\rho_{ij}^{(S)}=\rho_\parallel^{(S)}\hat{l}_i\hat{l}_j+\rho_\perp^{(S)}(\delta_{ij}-\hat{l}_i\hat{l}_j), \tag{2.1}$$

so that in the presence of a superflow with the velocity $\mathbf{v}_S$ an $\hat{\mathbf{l}}$-dependent contribution in the kinetic energy density appears:

$$F_{\text{flow}}^{(\text{an})}=-\frac{1}{2}\,\delta\rho_{\text{an}}^{(S)}(\hat{\mathbf{l}}\mathbf{v}_s)^2,$$

$$\delta\rho_{(\text{an})}^{(S)}=\rho_\perp^{(S)}-\rho_\parallel^{(S)}. \tag{2.2}$$

Anisotropic contribution (2.2) was extensively used to interpret peculiar properties of the rotating magnetized ^{3}He-*B*.[7] In the vortex-free state, which can be easily achieved before the formation of an equilibrium vortex lattice, large counterflows of normal and superfluid components have a pronounced influence on the $\hat{\mathbf{l}}$-field texture through the anisotropic interaction (2.2). After the equilibrium vortex state is established large counterflows are eliminated but the anisotropic interaction still survives due to the presence of superflows that circulate around individual, quantized, singular vortices (see, for example, Ref. 10).

Anisotropic part of the superfluid density $\delta\rho_{\text{an}}^{(S)}(T,H)$ of magnetically distorted *B*-phase is an even function of the applied magnetic field and in the low field limit is propor-

tional to H^2. On the other hand, in the case where the magnetic field strongly deforms ^{3}He-B order parameter (especially near the $B\to A$ phase transition at low pressures) one should expect to observe a pronounced deviation of $\delta\rho_{\rm an}^{(S)}$ from linearity in H^2. At the same time, the temperature dependence of $\delta\rho_{\rm an}^{(S)}$ for the strong field case must be established.

Since $\delta\rho_{\rm an}^{(S)}$ is an equilibrium property of magnetized B-phase, its (T,H)-behavior is completely determined by the structure of the excitation spectrum $E_{k\sigma}$ of quasiparticles with momentum $\mathbf{k}$ and spin projection $(1/2)\sigma=\pm(1/2)$) (of course, the Fermi-liquid effects must be incorporated in a proper way).

We start with a standard expression for the normal component density tensor (disregarding for the moment the Fermi liquid corrections),

$$\rho_{ij}^{(n)}=\frac{1}{m}\sum_{k\sigma}\ k_ik_j(-\partial f/\partial E_{k\sigma})=\rho Y_{ij}(T), \tag{2.3}$$

where $f(E)$ is the Fermi distribution and

$$Y_{ij}(T)=3\langle\hat{k}_i\hat{k}_jY(\hat{k};T)\rangle \tag{2.4}$$

with the generalized Yosida function

$$Y(\hat{k};T)=\frac{1}{2}\sum_{\sigma}\ \int_{-\infty}^{\infty}d\xi_k(-\partial f/\partial E_{k\sigma})$$

$$=\frac{1}{8T}\sum_{\sigma}\ \int_{-\infty}^{\infty}\frac{d\xi_k}{\cosh^2(E_{k\sigma}/2T)}. \tag{2.5}$$

In (2.4) the angle brackets denote averaging over the position on the Fermi surface and in (2.5) $\xi_k=(k^2-k_F^2)/2m$.

Using (2.3), we conclude that

$$\delta\rho_{\rm (an)}^{(S)}/\rho=(\rho_{\parallel}^{(n)}-\rho_{\perp}^{(n)})/\rho$$

$$=\frac{3}{2}\frac{1}{8T}\sum_{\sigma}\ \int_{-\infty}^{\infty}d\xi_k\left\langle\frac{3(\hat{\mathbf{k}}\hat{\mathbf{l}})^2-1}{\cosh^2(E_{k\sigma}/2T)}\right\rangle. \tag{2.6}$$

We now must use the explicit form of $E_{k\sigma}$ for the magnetized ^{3}He-B. The order parameter of this superfluid state is described by the bivector $A_{\mu i}=\Delta_{\mu\upsilon}R_{\upsilon i}\exp(i\Phi)$, where the uniaxial ''gap'' tensor is

$$\Delta_{\mu\nu}=\Delta_{\parallel}\hat{h}_{\mu}\hat{h}_{\nu}+\Delta_{\perp}(\delta_{\mu\nu}-\hat{h}_{\mu}\hat{h}_{\nu}). \tag{2.7}$$

The (T,H)-dependence of $\Delta_{\parallel}$ and $\Delta_{\perp}$ was extensively studied theoretically[2,3] using the set of Gorkov equations for the spin-triplet p-wave superfluid. The fermions excitation spectrum of the magnetized B-phase is given by

$$E_{k\sigma}^2=\left(\sqrt{\xi_k^2+\Delta_{\parallel}^2(\hat{\mathbf{k}}\hat{\mathbf{l}})^2}+\frac{1}{2}\,\sigma\omega_0\right)^2+\Delta_{\perp}^2(\hat{\mathbf{k}}\times\hat{\mathbf{l}})^2$$

$$=\left(|\xi_k|+\frac{1}{2}\,\sigma\omega_0\right)^2+|\Delta(\hat{\mathbf{k}})|^2+\sigma\omega_0(\sqrt{\xi_k^2+\Delta_{\parallel}^2(\hat{\mathbf{k}}\hat{\mathbf{l}})^2}$$

$$-|\xi_k|), \tag{2.8}$$

where $\omega_0=gH$ is the Larmor frequency of ^{3}He nuclear magnetic moments, and

$$|\Delta(\hat{\mathbf{k}})|^2=\Delta_{\parallel}^2(\hat{\mathbf{k}}\hat{\mathbf{l}})^2+\Delta_{\perp}^2(\hat{\mathbf{k}}\times\hat{\mathbf{l}})^2=\Delta_{\perp}^2[1-\delta_B(2-\delta_B)$$

$$\times(\hat{\mathbf{k}}\hat{\mathbf{l}})^2]. \tag{2.9}$$

Inspection of the second and third lines in (2.8) shows that the influence of the Zeeman slitting on the quasiparticle spectrum is twofold: the presence of ω_0, renormalizes the Fermi energy (via the first term) and changes the character of the dispersion relation (via the last term). Of course, ω_0, appears implicitly in $|\Delta|^2$ through the anisotropy parameter $\delta_B=\delta_B(\omega_0)$. In the low field limit δ_B is proportional to ω_0^2/Δ_0^2 where $\Delta_0(T)$ denotes the energy gap in the excitation spectrum of the zero-field isotropic B-phase.

Since in all practical cases $\omega_0\ll\varepsilon_F$, the field renormalization of the Fermi energy is negligible. If in addition $\Delta_{\parallel}\ll T$, we can use a simple BCS-type dispersion relation,

$$E_{k\sigma}^2=\xi_k^2+|\Delta(\hat{k})|^2 \tag{2.10}$$

with an anisotropic gap given by (2.9).

In Ref. 7, $\delta\rho_{\rm an}^{(S)}$ was estimated in the low field limit ($\omega_0\ll\Delta_0$, $\delta_B\ll1$) using the approximate expression (2.10) for $E_{k\sigma}$. As we have seen above, this consideration is justifiable for the case with $\Delta_{\parallel}\ll T$. More generally, an exact dispersion relation (2.8) should be considered. For the low field case the expansion of $Y(\hat{k};T)$ to the lowest order in δ_B and ω_0^2 gives

$$Y(\hat{k};T)=Y(T)+a(T)(\hat{\mathbf{k}}\hat{\mathbf{l}})^2, \tag{2.11}$$

where the anisotropic contribution is described by

$$a(T)=\delta_BZ(T)+(\omega_0^2/\Delta_0^2)\widetilde{Z}(T) \tag{2.12}$$

with

$$Z(T)=(\Delta_0/2T)^2\int_{-\infty}^{\infty}\frac{\tanh(E_k^0/2T)d\xi_k}{\cosh^2(E_k^0/2T)E_k^0}, \tag{2.13}$$

$$\widetilde{Z}(T)=\frac{1}{4}\,(\Delta_0/2T)^4\int_{-\infty}^{\infty}\frac{3\tanh(E_k^0/2T)-1}{\cosh^2(E_k^0/2T)}\left(\frac{T}{E_k^0}\right)\frac{d\xi_k}{E_k^0},$$

and $E_k^0=\sqrt{\xi_k^2+\Delta_0^2}$. Finally, from (2.3) and (2.4) it follows that in the low magnetic fields

$$\delta\rho_{\rm an}^{(S)}/\rho=\frac{2}{5}\,[\,\delta_BZ(T)+(\omega_0^2/\Delta_0^2)\widetilde{Z}(T)]. \tag{2.14}$$

When using the dispersion relation (2.10) the $\widetilde{Z}$-contribution to $\delta\rho_{\rm an}^{(S)}$ is lost. Although near $T_c(\Delta_0\ll T)$ this term is negligible ($\widetilde{Z}\ll Z$), on lowering the temperature it becomes increasingly important. This fact was noticed in Ref. 8, where $\delta\rho_{\rm an}^{(S)}$ was calculated for the low field limit for the magnetic energy density

$$F_{\rm mag}^{(S)}=\frac{1}{2}\,\chi_{\mu\nu}^{(S)}H_{\mu}H_{\nu}, \tag{2.15}$$

where $\chi_{\mu\nu}^{(S)}$ is the tensor of the magnetic susceptibility of ^{3}He-B in the presence of superflow with velocity v_s. Because of above-mentioned spin-orbit coherence of ^{3}He-B, the presence of preferred direction in orbital space along $\hat{v}_s=v_s/v_s$ induces a uniaxial magnetic anisotropy:

$$\chi_{\mu\nu}^{(S)}=\chi_{\parallel}^{(S)}\hat{s}_\mu\hat{s}_\nu+\chi_{\perp}^{(S)}(\delta_{\mu\nu}-\hat{s}_\mu\hat{s}_\nu), \tag{2.16}$$

where $\hat{s}_\mu=R_{\mu i}\cdot\hat{v}_{si}$. As a result, an anisotropy contribution appears in (2.15):

$$F_{\rm mag}^{(S)}=-\frac{1}{2}\,\delta\chi_{\rm an}^{(S)}(\hat{s}\mathbf{H})^2=-\frac{1}{2}\,(\delta\chi_{\rm an}^{(S)}H^2)(\hat{h}_\mu R_{\mu i}\hat{v}_{si})^2, \tag{2.17}$$

with $\delta\chi_{\rm an}^{(S)}=\chi_{\perp}^{(S)}-\chi_{\parallel}^{(S)}$. One the other hand, conceptually the same contribution to the spin-orbit anisotropy energy density is contained in Eq. (2.2), from which

$$F_{\rm flow}^{(\rm an)}=-\frac{1}{2}\,(\delta\rho_{\rm an}^{(S)}v_s^2)(\hat{h}_\mu R_{\mu i}\hat{v}_{si})^2. \tag{2.18}$$

Equation (2.17) and (2.18), we find the relation

$$\delta\rho_{\rm an}^{(S)}=(H^2/v_s^2)\,\delta\chi_{\rm an}^{(S)}, \tag{2.19}$$

which is an alternative way to calculate $\delta\rho_{\rm an}^{(S)}$. Using (2.19), it can be shown (see Ref. 8) that in the lowest order in H^2

$$\delta\rho_{\rm an}^{(S)}/\rho=\frac{1}{2}\left(\frac{\omega_0^2}{\Delta_0^2}\right)\left[\left(1-\frac{3}{5}\frac{Z_5}{Z_3}\right)\left(Z_3-\frac{3}{2}\,Z_5\right)+\frac{6}{5}\left(Z_5-\frac{5}{4}\,Z_7\right)\right], \tag{2.20}$$

where

$$Z_n(T)=\pi T\sum_\omega\ \frac{\Delta_0^{n-1}}{(\omega^2+\Delta_0^2)^{n/2}}. \tag{2.21}$$

In (2.20) we have dropped the Fermi-liquid corrections for simplicity of presentation. The sum in (2.21) is taken over $\langle\langle$odd$\rangle\rangle$ Matsubara frequencies. It can be shown (see the Appendix) that Eq. (2.20) is completely equivalent to our expression (2.14). The result (2.20) can be obtained by using the expressions for $\rho_{\parallel}^{(S)}$ and $\rho_{\perp}^{(S)}$ given in Ref. 11.

Returning to the general expression (2.6) for $\delta\rho_{\rm an}^{(S)}$ and using $E_{k\sigma}$ from (2.8), we calculate numerically the (T,H)-dependence of $\delta\rho_{\rm an}^{(S)}$ for arbitrary magnetic fields and arbitrary temperatures.

In order to take into account the Fermi-liquid effects we must introduce the Landau molecular fields in a standard way. We will therefore use the following expression for $\delta\rho_{\rm an}^{(S)}(T,H)$:

$$\delta\rho_{\rm an}^{(S)}/\rho=\frac{(1+1/3F_1^S)(Y_\parallel-Y_\perp)}{(1+1/3F_1^SY_\parallel)(1+1/3F_1^SY_\perp)}, \tag{2.22}$$

where

$$Y_\parallel=\frac{1}{2}\sum_\sigma\ \frac{1}{4T}\int_{-\infty}^{\infty}d\xi_k\left\langle\frac{3(\hat{\mathbf{k}}\hat{\mathbf{l}})^2}{\cosh^2(E_{k\sigma}/2T)}\right\rangle,$$

$$Y_\perp=\frac{1}{2}\sum_\sigma\ \frac{1}{4T}\int_{-\infty}^{\infty}d\xi_k\left\langle\frac{3/2(1-(\hat{\mathbf{k}}\hat{\mathbf{l}})^2)}{\cosh^2(E_{k\sigma}/2T)}\right\rangle. \tag{2.23}$$

To take into account the Landau exchange parameter F_0^a it is enough to make a substitution $\omega_0\to\tilde{\omega}_0$, where the renormalized Larmor frequency $\tilde{\omega}_0$ is defined by the equation

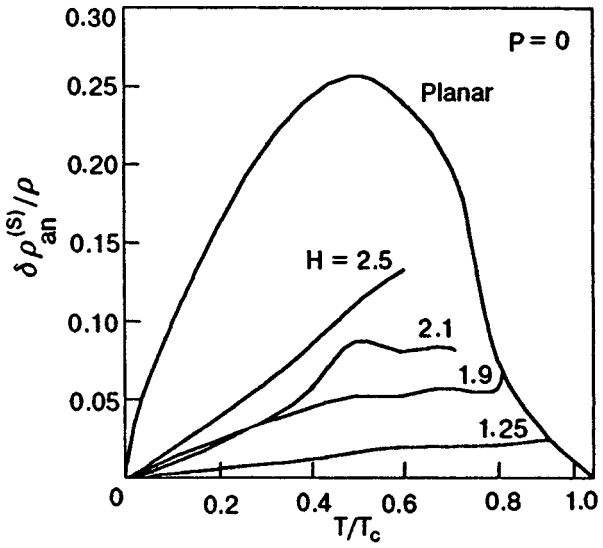

FIG. 1. Temperature dependence of $\delta\rho_{\rm an}^{(S)}$ at $P=0$ bar for various values of the magnetic field (in kGs).

$$\tilde{\omega}_0=\frac{\omega_0}{1+F_0^a\left[\frac{2}{3}+\frac{1}{3}\,Y(T,\tilde{\omega}_0)\right]}, \tag{2.24}$$

where $Y(T,\omega_0)$ is the field-dependent Yosida function (introduction of higher-order exchange parameter requires a more complicated procedure[2]).

In Figs. 1 and 2 some results for $\delta\rho_{\rm an}^{(S)}(T,H)$ are shown.

3. DIPOLAR VELOCITY OF THE MAGNETIZED ^{3}He-*B*

In addition to the anisotropic part of the flow energy (2.2), the dipole-dipole potential also contains terms which depend on the orbital anisotropy axis $\hat{l}$. Starting from the expression of the dipolar energy density

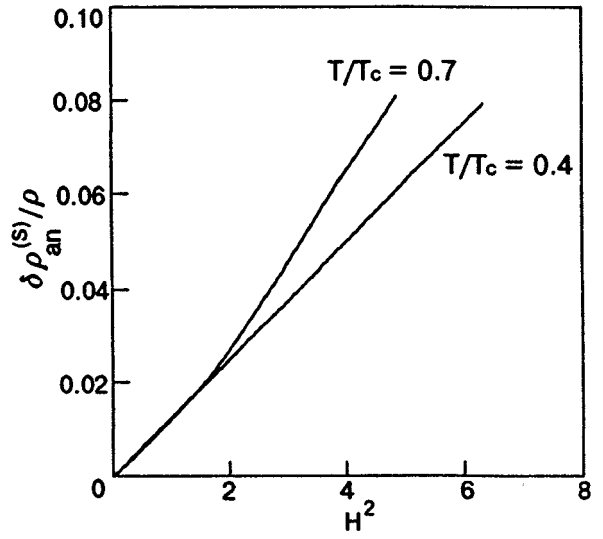

FIG. 2. Field dependence of $\delta\rho_{\rm an}^{(S)}$ at $P=0$ bar for various values of T/T_c. Deviation from linearity in H^2 is clearly seen at $T/T_c=0{,}7$.

$$F_D=\frac{1}{15}\,\chi_B(\Omega_B/g)^2\Delta_B^{-2}\{|\mathrm{Tr}\hat{A}|^2+\mathrm{Tr}(\hat{A}^+\hat{A})\} \tag{3.1}$$

and using an explicit form of the order parameter of the magnetized B-phase, it can be shown that (up to a constant term)

$$F_D=\frac{2}{15}\,\chi_B(\Omega_B/g)^2(\Delta_\perp/\Delta_B)^2\Big\{-\delta_B(2-\delta_B)\hat{\mathbf{l}}\hat{\mathbf{h}} + \Big[\Big(2\cos\theta+\frac{1}{2}\Big)+\delta_B\Big(\frac{1}{2}-\hat{\mathbf{l}}\hat{\mathbf{h}}\Big)\Big]^2\Big\}. \tag{3.2}$$

In (3.2) θ denotes the angle appearing in the matrix $\overleftrightarrow{R}=\overleftrightarrow{R}(\theta,\hat{\mathbf{n}})$ of the relative spin-orbit rotation about the axis n. At the fixed value of $\hat{\mathbf{l}}\hat{\mathbf{h}}=\cos\beta$ the minimum of the dipolar energy is realized at

$$\cos\theta_0=-\frac{1}{4}\,[1+\delta_B(1-2\cos\beta)]. \tag{3.3}$$

Combining (3.2) with the flow contribution (2.2), we obtain an expression for the anisotropic part of the bulk energy density of the magnetically distorted ^{3}He-B:

$$F_B^{(\mathrm{an})}=F_D(\theta=\theta_0)+F_{\mathrm{flow}}^{(\mathrm{an})}=-\frac{4}{5}\,A(H)\Big\{\hat{\mathbf{l}}\hat{\mathbf{h}} + \frac{1}{2}\,(v_s/v_D)^2(\hat{\mathbf{l}}\hat{\mathbf{v}}_s)^2\Big\}, \tag{3.4}$$

where

$$A(H)=\frac{1}{6}\,\delta_B(2-\delta_B)\chi_B(\Omega_B/g)^2(\Delta_\perp/\Delta_B)^2 \tag{3.5}$$

and the dipolar velocity v_D is defined by

$$v_D^{-2}=5\,\delta\rho_{\mathrm{an}}^{(S)}/4A. \tag{3.6}$$

At the low fields ($\delta_B\ll 1,\delta_B\propto H^2$) we conclude $A(H)\simeq aH^2$ and recalling that $\hat{h}\hat{l}=\cos\theta_0+(1-\cos\theta_0)(\hat{\mathbf{n}}\hat{\mathbf{h}})^2$, we can write the anisotropy energy density in a conventional form:

$$F_B\simeq -aH^2\Big\{(\hat{\mathbf{n}}\hat{\mathbf{h}})^2+\frac{2}{5}\,(v_s/v_D)^2(\hat{h}_\mu R_{\mu i}(\theta_0,\hat{n})\hat{v}_{si})^2\Big\} + \mathrm{const}. \tag{3.7}$$

In Ref. 6, an attempt to measure v_D at high fields was made using an ultrasonic probe. When the rotating vessel with strongly magnetized B-phase was slowly accelerated in the vortex-free Landau state, a critical angular velocity Ω_c signaling a textural transition was observed. Since v_D defines a characteristic velocity above which the superfluid counterflow takes over in the competition with the magnetic anisotropy (of the dipole-dipole origin), it was concluded that the experimentally observed critical velocity $v_c=\Omega_c R_0$ (where R_0 is the radius of the cylindrical container) is directly connected to v_D. Although an accurate interpretation of v_D in terms of v_c needs a detailed knowledge of the textural distribution, as a rough estimate we can set $v_D\simeq v_c$.

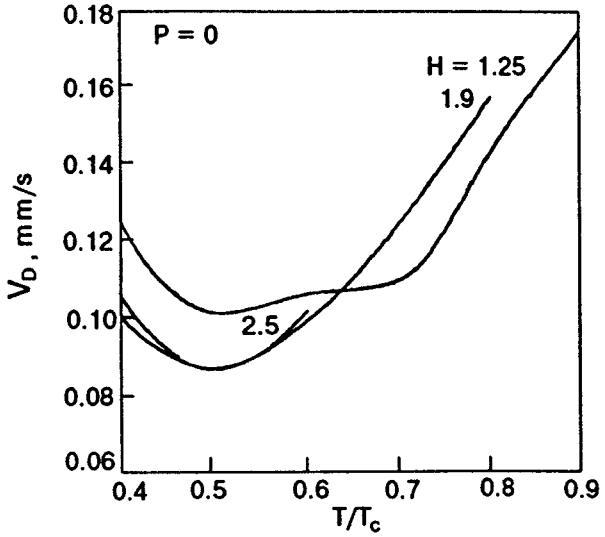

FIG. 3. Temperature dependence of the dipolar velocity at $P=0$ bar for various values of H (in kGs).

Using the definition (3.6), we have calculated numerically the dipolar velocity v_D for various fields and temperatures. Some of the results are presented in Fig. 3.

4. ANGULAR MOMENTUM OF THE ROTATING, MAGNETIZED, VORTEX-FREE ^{3}He-B

The amount of the orbital anisotropy of ^{3}He-B depends on the strength of the applied magnetic field. This can be explored, in particular, in experiments with a freely rotating vessel. Since the angular momentum $\mathbf{L}$ of the rotating magnetized B-phase in the vortex-free state strongly depends on the magnetic field (see below), it would be possible to observe the variation in the angular velocity Ω of the freely rotating sample when chanding H (due to the conservation of $\mathbf{L}$). In the case of the vortex-free rotation the angular momentum of a superfluid liquid is

$$\mathbf{L}=\mathbf{L}_n=\int(\mathbf{R}\times\mathbf{J}_n)d^3R, \tag{4.1}$$

where the mass current of the normal component is

$$\mathbf{J}_n=\overleftrightarrow{\rho}_n v_n, \tag{4.2}$$

where $v_n=\Omega\times\mathbf{R}=(\Omega r)\hat{\varphi}$. Here r is the radial coordinate in the plane perpendicular to the angular velocity Ω, and $\hat{\varphi}$ is the unit vector in the circular direction. It is clear that

$$\mathbf{J}_n=(\Omega r)[\rho_\perp^{(n)}\hat{\varphi}+(\rho_\parallel^{(n)}-\rho_\perp^{(n)})(\hat{\mathbf{l}}\hat{\varphi})\hat{\mathbf{l}}]. \tag{4.3}$$

Setting

$$\hat{\mathbf{l}}=\cos\beta\hat{\mathbf{z}}+\sin\beta(\cos\alpha\hat{\mathbf{r}}+\sin\alpha\hat{\varphi})=\cos\beta\hat{\mathbf{z}} + \sin\beta[\cos(\alpha+\varphi)\hat{\mathbf{x}}+\sin(\alpha+\varphi)\hat{y}] \tag{4.4}$$

and considering a circular cylindrical vessel in the magnetic field oriented along the symmetry axis, we easily see that in the case of an axially symmetric $\hat{l}$-texture [$\alpha=\alpha(r)$, $\beta=\beta(r)$] $L_x=L_y=0$ and

$$L_z/\Omega = 2\pi \int \{\rho_\perp^{(n)} + (\rho_\parallel^{(n)} - \rho_\perp^{(n)})\sin^2\alpha(r)\sin^2\beta(r)\} r^3 dr dz. \quad (4.5)$$

This result is quite transparent, L_z depends on the degree of the orbital anisotropy of the magnetized B-phase, but in the region where $\hat{\mathbf{l}}$ has no circular component ($\alpha = 0$) only the transverse part $\rho_\perp^{(n)}$ of the density tensor is probed.

Introducing the moment of inertia $I_{zz}^{(0)} = 1/2\rho R_0^2 V$ of the normal state ^{3}He liquid that fills a cylindrical container of radius R_0 (and of volume V), Eq. (4.5) can be rewritten as

$$L_z/\Omega = I_{zz}^{(0)} F, \quad (4.6)$$

where

$$F = 4\int_0^1 \{\rho_\perp^{(n)}/\rho + [(\rho_\parallel^{(n)} - \rho_\perp^{(n)})/\rho]\sin^2\alpha(x)\sin^2\beta(x)\} x^3 dx, \quad (4.7)$$

with $x = r/R_0$. For the isotropic B-phase (realized in zero magnetic field) $F = \rho_n(T)/\rho$, as it should be for the case of vortex-free rotation. For the magnetized ^{3}He-B $F = F(T,H,\Omega)$ and the Ω-dependence appears through the textural distribution which is sensitive to the superfluid counterflow orienting effects.

Using (4.6) and referring to the conservation of the angular momentum of an isolated system for the case of freely rotating magnetized ^{3}He-B, we conclude that due to the field-dependent orbital anisotropy one should observe the dependence of the angular velocity of rotation Ω on the strength of the applied field. In particular, if we start with a freely rotating state at $\Omega = \Omega_0$ and $H = 0$ and then apply the magnetic field H, the final state will be characterized by an angular velocity

$$\Omega(H) = \frac{1 + [\rho_n(T)/\rho]B}{1 + F(T,H,\Omega)B}\,\Omega_0, \quad (4.8)$$

where B is the ratio of moments of inertia of the normal ^{3}He liquid and of the container. It is to be remembered that the above-mentioned results refer to the case of a metastable, vortex-free rotation. When an equilibrium number of vortices fill the vessel, the anisotropy is washed out and the angular momentum in this case is $L_z = I_{zz}^{(0)}\Omega$ (on the average).

In order to calculate $F(T,H,\Omega)$ we must know the textural distribution across the rotating vessel. For a crude estimate of F it is instructive to use an approximate description with

$$\sin^2\alpha = 1,$$
$$\cos\beta \simeq \begin{cases} 1, & \Omega r < v_D, \\ (v_D/\Omega r)^2, & \Omega r > v_D. \end{cases} \quad (4.9)$$

Substituting (4.9) into (4.7), we easily find

$$F = \begin{cases} \rho_\perp^{(n)}, & \Omega < \Omega_c \\ \rho_\parallel^{(n)}/\rho - [(\rho_\parallel^{(n)} - \rho_\perp^{(n)})/\rho](\Omega_c/\Omega)^4(1 + 4\ln(\Omega/\Omega_c)), & \Omega > \Omega_c, \end{cases} \quad (4.10)$$

where $\Omega_c = v_D/R_0$, as in Sec. 3. Since we are dealing with a vortex-free rotation of ^{3}He-B, his consideration is valid for $\Omega < v_{cr}/R_0$, where v_{cr} is the critical velocity of the vortex nucleation.

ACKNOWLEDGMENTS

This work is a part of the ROTA Project. We are sincerely grateful to P. Hakonen, M. Krusius, E. Thuneberg, and G. Volovik for many useful discussions. The authors are greatly indebted to Prof. Olli Lounasmaa for continuous support and to the scientific staff of the Low-Temperature Laboratory of the Helsinki University of Technology for hospitality.

APPENDIX

Starting from the ω-sum representation of the Fermi distribution $f(E)$, which gives

$$\partial f/\partial E = T\sum_\omega \frac{E^2 - \omega^2}{(\omega^2 + E^2)^2}, \quad (A1)$$

and using the identity

$$\frac{1}{2}\left[\frac{E^2 - \omega^2}{(E^2 + \omega^2)^2} + \frac{d}{d\xi}\left(\frac{\xi}{\omega^2 + E^2}\right)\right] = \frac{E^2 - \xi E(\partial E/\partial\xi)}{(\omega^2 + E^2)^2}, \quad (A2)$$

we obtain the useful formula

$$\int_{-\infty}^{\infty}(-\partial f/\partial E)d\xi = 1 - 2T\sum_\omega \int_{-\infty}^{\infty} d\xi \frac{E^2 - \xi E(\partial E/\partial\xi)}{(\omega^2 + E^2)}. \quad (A3)$$

From (A3) follows the ω-sum representation for the Yosida function

$$Y(\hat{k};T) = 1 - T\sum_\sigma \sum_\omega \int_{-\infty}^{\infty} d\xi_k \frac{E_{k\sigma}^2 - \xi_k E_{k\sigma}(\partial E_{k\sigma}/\partial\xi_k)}{(\omega^2 + E_{k\sigma}^2)^2}. \quad (A4)$$

Taking into account that for the spectrum $E_{k\sigma}$ given by (2.8)

$$\partial E_{k\sigma}/\partial\xi_k = \frac{\xi_k}{E_{k\sigma}}\left(1 + \frac{1}{2}\frac{\sigma\omega_0}{(\xi_k^2 + \Delta_\parallel^2(\hat{k}\hat{l})^2)^{1/2}}\right) \quad (A5)$$

and explanding (A4) with respect to δ_B and ω_0^2/Δ_0^2, we conclude that in the low field limit

$$Y(\hat{k};T) \simeq Y(T) + a(T)(\hat{\mathbf{k}}\hat{\mathbf{l}})^2,$$

where

$$a(T) = 2\delta_B\left(Z_3 - \frac{3}{2}Z_5\right) + \frac{3}{2}\frac{\omega_0^2}{\Delta_0^2}\left(Z_5 - \frac{5}{4}Z_7\right). \quad (A6)$$

As a final step we must express the anisotropy parameter $\delta_B = (\Delta_\perp - \Delta_\parallel)/\Delta_\perp$ in terms of $Z_n(T)$. Using the equations for $\Delta_\perp$ and $\Delta_\parallel$, it can be shown that in the low field limit

$$\delta_B(T,H) \simeq \frac{5}{8}\frac{\omega_0^2}{\Delta_0^2}\left(1 - \frac{3}{5}\frac{Z_5}{Z_3}\right). \quad (A7)$$

Insertion of (A7) into (A6) restores the result (2.20) for $\delta\rho_{an}^{(S)}$.

[1)]E-mail: khar@physics.iberiapac.ge

[1] D. Vollhardt and P. Wölfle, *The Superfluid Phases of Helium-3*, Taylor and Francis (1990).
[2] N. Schopohl, J. Low Temp. Phys. **49**, 347 (1982).
[3] M. Ashida and K. Nagai, Prog. Theor. Phys. **74**, 949 (1985).
[4] R. Movshovich, N. Kim, and D. M. Lee, Phys. Rev. Lett. **64**, 431 (1990); R. Movshovich and D. M. Lee, J. Low Temp. Phys. **89**, 515 (1992).
[5] S. N. Fisher, A. M. Guenault, C. J. Kennedy and G. R. Pickett, Phys. Rev. Lett. **67**, 1270 (1991).
[6] J. M. Kyynarainen, J. P. Pekola, K. Torizuka, A. J. Manninen, and A. V. Babkin, J. Low Temp. Phys. **82**, 325 (1991).
[7] P. J. Hakonen, M. Krusius, M. M. Salomaa *et al.*, J. Low. Temp. Phys. **76**, 225 (1989).
[8] J. Korhonen, Yu. M. Bunkov, V. Dmitriev *et al.*, Phys. Rev. B**46**, 13983 (1992).
[9] K. K. Nummila, P. J. Hakonen, and J. Korhonen, Europhys. Lett. **11**, 651 (1990).
[10] G. A. Kharadze, *In Helium-3*, W. P. Halperin and L. P. Pitaevskli (Eds)., North-Holland, Amsterdam (1990).
[11] G. Baramidze, G. Kharadze, and G. Vachnadze, JETP Lett. **63**, 107 (1996).

This article was published in English in the original Russian journal. It was edited by S. J. Amoretty.

Zero-temperature relaxation in spin-polarized Fermi systems

A. E. Meyerovich,[a] J. H. Naish,[b] J. R. Owers-Bradley,[b] and A. Stepaniants[a]

[a]*Department of Physics, University of Rhode Island, Kingston, RI 02881, USA*
[b]*Department of Physics, University of Nottingham, Nottingham NG7 2RD, United Kingdom*
(Submitted October 31, 1996)
Fiz. Nizk. Temp. **23**, 553–563 (May–June 1997)

The effect of zero-temperature attenuation, which has been recently observed in spin dynamics of Fermi liquids, on various processes in helium and ferromagnetic systems is described. A brief review of theoretical and experimental data on zero-temperature attenuation in transverse spin dynamics of helium systems is followed by a discussion of coupling between longitudinal and transverse processes, the Castaing instability in ^{3}He and ^{3}He$-^4$He mixtures, and applications to pure ferromagnetic metals. © *1997 American Institute of Physics.* [S1063-777X(97)00805-0]

1. INTRODUCTION

One of the recent developments in physics of Fermi liquids was a discovery of peculiar zero-temperature attenuation in transverse spin dynamics of spin-polarized Fermi liquids. In contrast to all other dissipative processes in pure Fermi liquids, the transverse relaxation time $\tau_\perp$ and the coefficient of transverse spin diffusion $D_\perp$ do not increase with decreasing temperature as $1/T^2$, but saturate and remain finite even at $T\to 0$. By transverse dynamics we mean the dynamics of components of magnetization perpendicular to its equilibrium direction. The transverse processes are excited, for example, by inhomogeneous tipping of spins in NMR experiments. Longitudinal processes in exchange systems, i.e., processes which do not change the direction of polarization, do not exhibit any zero-temperature attenuation, irrespective of spin polarization.

The zero-temperature attenuation in transverse dynamics was predicted first on the basis of general conservation law and symmetry arguments.[1,2] This prediction was confirmed by direct transport calculations for degenerate Fermi gases[3–5] and, later, dense Fermi liquids.[6] The temperature saturation of transverse diffusion and relaxation has been observed in low-temperature spin dynamics experiments in spin-polarized liquid ^{3}He$\uparrow$ (Ref. 7) and ^{3}He$\uparrow-^4$He mixtures.[8]

The transverse zero-temperature relaxation time is $\tau_\perp(T=0)\sim(Nv_F\sigma)^{-1}(T_F/\beta H)^2$ for a system of fermions with Fermi velocity (temperature) $v_F(T_F)$, magnetic moment β, effective cross section σ, and density N in the external magnetic field H. Since the usual temperature-driven relaxation time is $\tau_\perp(H=0)\sim(Nv_F\sigma)^{-1}(T_F/T)^2$, the transition from the temperature-driven to polarization-driven transverse attenuation occurs at the temperature $T_a\sim\beta H$ when the phase space between the spin-up and spin-down Fermi spheres is comparable to the thermal smearing of the Fermi spheres.

The reason for such an unusual behavior is that the transverse relaxation and spin diffusion at low temperatures are determined by collisionless decay of magnons. Spin polarization of the Fermi liquid opens phase space between the spin-up and spin-down Fermi spheres necessary to allow these decay processes for magnons with finite $\mathbf{k}$ (inhomogeneously tipped spins) even at $T=0$. Mathematically, the zero-temperature attenuation can be described by a pole contribution in the transverse component of the interaction function, and is, in this sense, similar to the Landau damping in collisionless plasma.[5]

Below we will briefly describe theoretical and experimental aspects of this phenomenon, and discuss its consequences. We are interested in both helium and electron systems. In spin-polarized helium Fermi liquids, the zero-temperature transverse attenuation can affect other dynamic processes via the magnetic dipole-dipole interaction and nonlinear coupling. Electron Fermi liquids with large degree of spin polarization exist in ferromagnetic metals. In itinerant ferromagnets, the manifestations of the zero-temperature transverse attenuation are similar to those in helium systems (with spin-lattice coupling to longitudinal modes). In Heisenberg ferromagnetic metals, the analogy is less direct: the Fermi-liquid, zero-temperature, transverse attenuation affects ferromagnetic properties only via exchange coupling of localized ferromagnetic spins to spins of conduction electrons.

In the next section we give a simple theory of the zero-temperature transverse attenuation. In Sec. 3 we highlight experimental aspects of this phenomenon in helium systems. Then, in Sec. 4, we describe the transfer of the zero-temperature attenuation into longitudinal channels by means of magnetic dipole interaction. Sec. 5 deals with Castaing instability in spin dynamics in an inhomogeneous setting. The last section contains applications to pure ferromagnetic metals.

2. THEORY

Usually, the conservation laws restrict all low-energy relaxation processes in Fermi liquids to a thin layer (with a relative thickness T/T_F) near the Fermi sphere, where the occupation numbers n change gradually from 1 to 0. Everywhere else there are either no particles (no ''initial'' states $n_{\rm in}$, or all states are completely occupied (no space for ''final'' states $n_{\rm fin}$). The probability of relaxation scattering processes for the fermions, which is proportional to $n_{\rm in}(1-n_{\rm fin})$, acquires the factor $(T/T_F)^2$ and is very small. As a result, the relaxation time increases at low temperatures as

$(T_F/T)^2$. In spin-polarized Fermi systems the situation is different: if the collision flips the spin of spin-up particle in the region between spin-up and spin-down Fermi spheres, this particle can easily change its energy since all spin-down states in this area are unoccupied.

Mathematically, this means that the collision integral of the form

$$\int d^3p_1 d^3p_2 d^3p_3 d^3p_4 W \delta(\epsilon_1+\epsilon_2-\epsilon_3-\epsilon_4-\hbar\omega - 2\beta_1 H)\,\delta(\mathbf{p}_1+\mathbf{p}_2-\mathbf{p}_3-\mathbf{p}_4)[n_{1\uparrow}n_{2\uparrow}(1-n_{3\uparrow})(1-n_{4\downarrow})+n_{1\uparrow}n_{2\downarrow}(1-n_{3\downarrow})(1-n_{4\downarrow})] \quad (1)$$

does not go to zero at $T\to 0$ as $(T/T_F)^2$, but remains finite and is proportional, at small polarization $\beta H/T_F$, to $(\beta H/T_F)^2$.

This mechanism of zero-temperature attenuation requires a spin flip during collision and exists in exchange systems only in transverse spin channel, i.e., for processes with changes in direction of magnetization such as spin waves, spin echo, and other NMR effects. The attenuation for exchange longitudinal processes-processes without changes in direction of magnetization-involves similar collision integrals, but with equal numbers of up and down arrows, and vanishes at $T\to 0$ as $(T/T_F)^2$.

In general, there should be no dissipative collisions at $T=0$. In Fermi liquids at $T=0$ all incoherent processes, including the transverse ones, should disappear, and the interaction should be described by the Landau interaction function, i.e., coherent molecular field. This seems to contradict the existence of zero-temperature attenuation. This contradiction is resolved if one notes that the microscopic equation for the transverse component of the Landau interaction function contains the integrals of the form[5]

$$\boldsymbol{\sigma}\cdot\boldsymbol{\sigma}'\int\frac{d^3p'}{(2\pi)^3}\left[\frac{1-n'_\downarrow-n'_{1\uparrow}}{p^2+p_1^2-p'^2-p_1'^2-i0\,\mathrm{sign}(p'-p_{F\downarrow})} - P\,\frac{1}{p^2+p_1^2-p'^2-p_1'^2}\right].$$

The imaginary (pole) part of this interaction function reproduces the integral (1). Therefore, the zero-temperature transverse attenuation can be interpreted as the imaginary (pole) part of the interaction function. In this sense, the zero-temperature attenuation is a direct analog of the Landau damping in collisionless plasma. Needless to say, this pole part disappears in the absence of polarization or for longitudinal processes.

The above simple theory is directly applicable to low-density Fermi liquids such as the ^{3}He component of ^{3}He↑−^{4}He mixtures, or to dense Fermi liquids at low spin polarization. The situation in dense, highly polarized Fermi liquids is more complicated. Here the molecular fields acting on slightly tilted spin-ups and spin-downs are different because of the large distance between spin-up and spin-down Fermi surfaces. (This effect is analogous to the well-known particle-hole anisotropy away from the Fermi surface.) Then the microscopic equations of transverse spin dynamics, i.e., the equations for (small) transverse components of slightly tilted spins, have the form of two separate equations for tilted spin-ups and spin-downs with different molecular fields. It is not clear how these equations translate into macroscopic equations of spin dynamics, and what are the necessary modifications of the Leggett equation of macroscopic spin dynamics.

The Leggett equation of Fermi-liquid spin dynamics is a closed equation in macroscopic magnetic moment **M**. This equation in its original form cannot be applied to highly polarized Fermi liquids: the molecular field term in the effective magnetic field inevitably involves integration of the magnetization distribution **m** with the Fermi-liquid interaction function f between spin-up and spin-down Fermi spheres

$$\int f(\mathbf{p},\mathbf{p}')\mathbf{m}(\mathbf{p}')[n_\uparrow^{(0)}(\mathbf{p}')-n_\downarrow^{(0)}(\mathbf{p}')]d^3p'/(2\pi\hbar)^3. \quad (2)$$

Integral (2) can be written via the macroscopic magnetic moment

$$\mathbf{M}=\int\mathbf{m}(\mathbf{p}')[n_\uparrow^{(0)}(\mathbf{p}')-n_\downarrow^{(0)}(\mathbf{p}')]d^3p'/(2\pi\hbar)^3 \quad (3)$$

only if the interaction function is constant between the Fermi spheres. This is true either for dilute Fermi gases[2] or, as in the original Leggett derivation, at very low polarization when the Fermi spheres almost coincide.

3. EXPERIMENT

Recent experiments at Nottingham[8,9] have used the techniques of pulsed nuclear magnetic resonance to measure both transverse and longitudinal spin diffusion in a saturated ($x_3=6.4\%$) solution of ^{3}He in ^{4}He. The active region of the experimental cell consisted of a 1-mm-diameter Stycast tube, 20 mm in length, around which an rf coil (3-mm radius, two turns of 0.6-mm-diameter Cu wire) was positioned. A main field of 8.8 T and a uniform gradient of 80 mT/m were applied to the cell, in a direction normal to the axis of the tube. The polarization of the saturated solution in such a field was a few percent and the Leggett spin rotation parameter μM_0 had a value of about 4 at the lowest temperatures.

In order to measure the transverse spin diffusion coefficient a $\theta - t_1 - 180°$ rf pulse sequence was applied to the ^{3}He spin system resulting in a spin-echo at time $2t_1$. The presence of transverse spin diffusion causes this echo signal to decay with interpulse time t_1. The height h and phase φ of the spin-echo was fitted to the Leggett-Rice equations

$$(1+\mu^2M_0^2\cos^2\theta)\ln(h(t_1))+\frac{\mu^2M_0^2}{2}\sin^2\theta(h^2(t_1)-1) = -\frac{2}{3}\gamma^2G^2D_\perp t_1^3,$$

$$\varphi=-\mu M_0\cos\theta\ln(h(t_1))$$

to obtain values for the spin-rotation parameter, μM_0, and the transverse spin diffusion coefficient $D_\perp$.

Longitudinal spin diffusion was measured using a technique similar to that used by Nunes *et al.*[10] By applying a

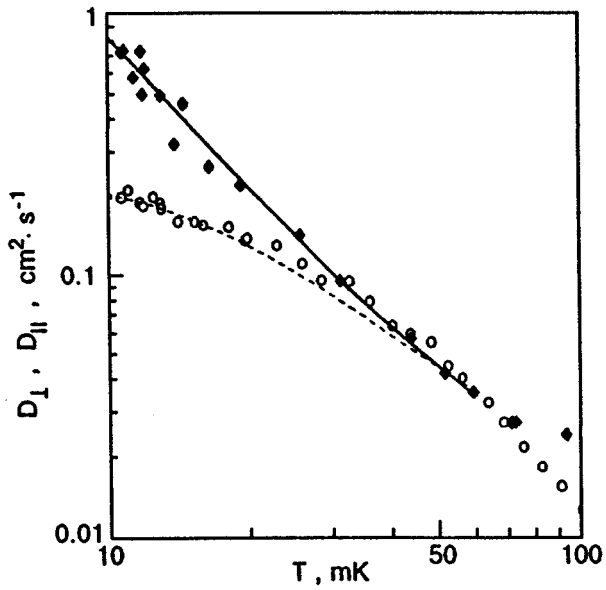

FIG. 1. Temperature dependence of transverse (circles) and longitudinal (diamonds) diffusion coefficients, $D_\perp$ and $D_\parallel$.

$\theta = 180°$ rf pulse we can invert the magnetization in the active region of the cell. A longitudinal magnetization gradient is thus set up between this region and the remainder of the cell, which results in the diffusion of spins into this region to recover equilibrium. The recovery of the magnetization can be characterized by harmonics in the wave number of the spin current, k, as

$$M_{\text{final}} - M_z(t) = \sum_k c_k e^{-D_\parallel k^2 t}.$$

The magnetization is sampled at times, t, after the application of the initial 180° pulse using a 21°−1 ms−180° pulse sequence. The resulting recovery profile can then be used to find the longitudinal spin diffusion current, $D_\parallel$.

The measured transverse and longitudinal spin diffusion coefficients are plotted on the same graph in Fig. 1. A clear deviation of $D_\perp$ from $D_\parallel$ can be seen at temperatures below about 30 mK. The longitudinal spin diffusion follows the expected T^{-2} dependence of a degenerate Fermi liquid (T_F=417 mK for a 6.4% solution of ^{3}He in ^{4}He), whereas the transverse spin diffusion approaches a constant value as $T \to 0$ K. The results for $D_\perp$ have been fitted to the theory[6] in the low spin polarization approximation. A value for the anisotropy temperature of $T_a = (19 \pm 3)$ mK was obtained. A fit of the theory to earlier measurements of the transverse spin diffusion coefficient in an $x_3 = 3.8\%$ mixture yields a value of $T_a = (13 \pm 2)$ mK for this concentration.

Similar results in pure ^{3}He have been obtained by Wei *et al.*[7] using the same pulsed NMR spin echo technique. In this case, the anisotropy temperature $T_a = 16$ mK.

4. DIPOLE EFFECTS AND LONGITUDINAL ATTENUATION

Since the transverse attenuation is the only zero-temperature relaxation mechanism in pure exchange Fermi liquids for low-frequency low-wave processes, it is interesting to inquire whether this dissipation mechanism is coupled to and affects longitudinal Fermi-liquid processes.

There are two general mechanisms that couple longitudinal and transverse processes in helium: the magnetic dipole-dipole interaction and the nonlinearity of equations of motion. We will look only at dipole coupling, which is quite strong in highly polarized systems,[12] although the nonlinear coupling also leads to interesting effects, especially near the spin-wave (Castaing) instability.

The dipole interaction transfers the zero-temperature transverse attenuation into the longitudinal channel by two different mechanisms.[11] First, in spin-polarized systems with magnetic dipole-dipole interaction the spin-flip processes of the type (1) with dipole vertex W are allowed in the longitudinal channel and enter the collision integral directly. Second, the dipole interaction couples the longitudinal modes to (attenuating) transverse spin waves. Then the collision integral (1) enters the longitudinal processes with transverse exchange vertex W and dipole interaction in the coupling constant.

As a result of direct and indirect dipole processes, the effective zero-temperature attenuation in the longitudinal channel $\tau_{\text{eff}}(T=0)$ should differ from $\tau_\perp(T=0)$ by an extra coupling factor $(E_d/T_F)^2$, where the characteristic dipole energy is $\beta^2 Z^2 m^{3/2} T_F^{3/2}/\hbar^3$, and Z is the microscopic parameter which describes the difference between the (pole terms for) Fermi liquids and gases. The transition from temperature-driven to polarization-driven zero-temperature sound attenuation should occur for longitudinal sound in sub-μK region, i.e., at considerably lower temperature than the recently observed anisotropy temperature T_a, at which the transverse attenuation loses its $1/T^2$ dependence. (For liquid ^{3}He ↑ this corresponds to the temperatures below the superfluid transition when the theory of normal Fermi liquids cannot be applied directly. Thus the unmodified results can only be applied to liquid ^{3}He↑ − ^{4}He mixtures.)

In order to avoid separate independent calculations of attenuation for different hydrodynamic and high-frequency longitudinal modes in ^{3}He↑ and ^{3}He↑−^{4}He mixtures, we calculated (zero-) sound attenuation in a generic polarized Fermi liquid. This allowed us to extract the effective, mode-independent, zero-temperature relaxation time $\tau_{\text{eff}}(T=0)$ and viscosity $n_{\text{eff}}(T=0) = \rho v_F^2 \tau_{\text{eff}}(1 + F_1^{(s)}/3)/5$. The effective relaxation time could be used in conjunction with standard hydrodynamic and hf equations[2,13] for polarized ^{3}He↑ and ^{3}He↑−^{4}He mixtures, giving the attenuation of all sound and hf modes in terms of effective η_{eff} and τ_{eff}.

Although the effective zero-temperature longitudinal relaxation parameters are quite small because of the weakness of dipole interaction, these parameters provide the real zero-temperature cutoffs for longitudinal relaxation and transport. Since liquid helium, in contrast to electron systems, does not have any impurities, one may expect to observe these limiting cut-offs at ultra-low temperatures in highly polarized ^{3}He↑ or ^{3}He↑−^{4}He mixtures.

A. Dipole collision integral and sound attenuation

Dipole interaction leads to spin-flip collisions even for longitudinal processes such as sound propagation. As a re-

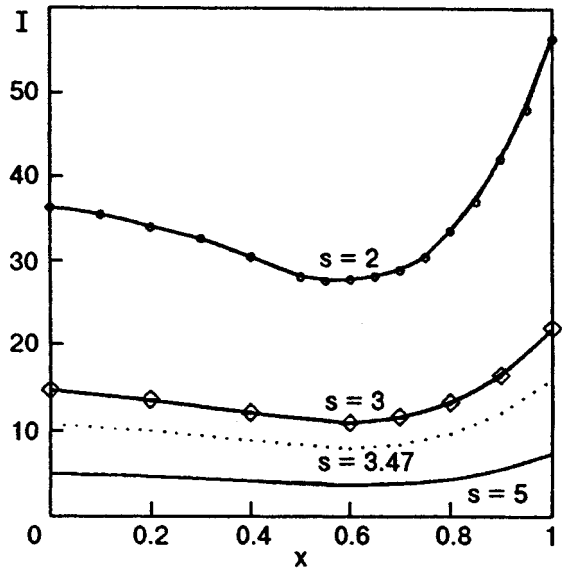

FIG. 2. $I(s,x)$ as a function of $x = \cos\theta$, Eq. (4), for four values of s, $s = 2; 3; 3.47; 5$.

sult, one can find zero-temperature terms with the spin structure (1) in the collision integral with the scattering probability

$$W(\mathbf{p}_1,\mathbf{p}_2,\mathbf{p}_3,\mathbf{p}_4)=\left(\frac{E_d}{T_F}\right)^2\left[\frac{(\mathbf{p}_1-\mathbf{p}_3)_z^3(\mathbf{p}_1-\mathbf{p}_3)_+}{(\mathbf{p}_1-\mathbf{p}_3)^4}-\frac{(\mathbf{p}_1-\mathbf{p}_4)_z^3(\mathbf{p}_1-\mathbf{p}_4)_+}{(\mathbf{p}_1-\mathbf{p}_4)^4}\right]^2,$$

where the z axis is chosen along the magnetic field (spin polarization), and the dipole energy is

$$E_d=\beta^2Z^2m^{3/2}T_F^{3/2}/\hbar^3.$$

The resulting sound attenuation is[11]

$$\mathrm{Im}\ \omega=\frac{E_d^2}{16\pi^5\hbar T_F}\left(\frac{\beta H}{T_F}\right)^2 I(s\cos\theta), \tag{4}$$

where $s = \omega/kv_F$ is the (dimensionless) sound velocity, and the function $I(s\cos\theta)$ is plotted in Fig. 2 for several values of s.

B. Coupling between sound and spin waves

Longitudinal and transverse processes are decoupled in Fermi liquids with exchange interaction between particles. Weak magnetic dipole-dipole interaction couples longitudinal and transverse processes. As a result, the zero-temperature attenuation in transverse channels can lead to zero-temperature dissipation even for ordinary longitudinal processes.

In spin-polarized Fermi liquids, sound propagation in the absence of dipole interaction is described by a set of two coupled equations for densities $n_\uparrow$ and $n_\downarrow$ of spin-up and spin-down particles. The coupling of longitudinal dynamic equations for $n_\uparrow$, $n_\downarrow$ to the transverse equation of motion for the mixed spin component of the density matrix $n_{\uparrow\downarrow}$ is provided by magnetic dipole-dipole interaction with the Hamiltonian[14,15]

$$\frac{4}{3}\pi\beta^2\left[\frac{3(\boldsymbol{\sigma}\cdot\mathbf{q})(\boldsymbol{\sigma}'\cdot\mathbf{q})}{q^2}-(\boldsymbol{\sigma}\cdot\boldsymbol{\sigma}')\right],\quad \mathbf{q}=\mathbf{p}-\mathbf{p}'. \tag{5}$$

This Hamiltonian is responsible for two effects. First, it causes demagnetizing factors which, in an elliptical sample, are equivalent to the demagnetizing field $\mathbf{H}_d$. The integration of dipolar interaction, necessary for the calculation of demagnetizing field, is not trivial because of the divergence at small wave vectors. It is possible to show[16–18] that the demagnetizing field in spherical samples is, with good accuracy,

$$\mathbf{H}_d=4\pi\left(\frac{\mathbf{H}(\mathbf{M}\cdot\mathbf{H})}{H^2}-\frac{\mathbf{M}}{3}\right)Z^2,$$

$$\mathbf{M}=(\beta/2)Tr_{\boldsymbol{\sigma}}\int\boldsymbol{\sigma}\hat{n}_{\boldsymbol{\sigma}}d\Gamma. \tag{6}$$

This equation for $\mathbf{H}_d$ includes both the equilibrium contribution with $\mathbf{M}_0$ and the non-equilibrium part with $\delta\mathbf{M}$.

Second, the dipole interaction changes the effective Landau interaction function (molecular field):

$$\delta f_{\alpha\beta,\gamma\delta}(\mathbf{p},\mathbf{p}')=\frac{4}{3}\pi Z^2\beta^2\left[\frac{3(\boldsymbol{\sigma}_{\beta\gamma}\cdot\mathbf{q})(\sigma_{\alpha\delta}\cdot\mathbf{q})}{q^2}-(\sigma_{\beta\gamma}\cdot\sigma_{\alpha\delta})\right], \tag{7}$$

where Z is the usual renormalization coefficient in the pole part of the single-particle Green's function for Fermi liquids. [Note, that Eq. (7) contains only one of the diagrams for the vertex Γ^ω. The other diagram is already included in the term with $\delta\mathbf{M}$ in the demagnetizing field $\mathbf{H}_d$ (6).] Substitution of the dipole terms (6) and (7) into the commutator in the equations of motion,

$$[\hat{n},\hat{\epsilon}],\quad \epsilon_{\alpha\gamma}=\epsilon_{\alpha\gamma}^{(0)}-\beta\sigma_{\alpha\gamma}\cdot\delta\mathbf{H}_d+\int f_{\alpha\beta,\gamma\delta}(\mathbf{p},\mathbf{p}')\,\delta n'_{\delta\beta}d\Gamma', \tag{8}$$

results in coupling of longitudinal and transverse equations.

As a result of this coupling, the sound waves acquire the zero-temperature attenuation[11]

$$\mathrm{Im}\ \omega=\frac{\hbar^2(kv_F)^2}{32\pi^2\tau_\perp}\left[\frac{F_0^{(s)}}{F_0^{(s)}-F_0^{(a)}}\right]^2\frac{E_d^2}{T_F^4}\left(\frac{k_z^2}{k^2}\frac{k^2-k_z^2}{k^2}\Gamma_1(s)+\frac{4k_z^4-3k^2k_z^2+k^4}{3k^4}\Gamma_2(s)\right), \tag{9}$$

where

$$\Gamma_1(s)=2s^2(s^2-1)\frac{w(s^2-3)-1/3}{w(s^2-1)-1}\left[2\frac{w(3s^2-1)-1}{1+F_0^{(a)}}+s^2-3w(s^2-1)^2-\frac{7}{5}\right],$$

$$\Gamma_2(s)=2s^2(s^2-1)\,\frac{w(s^2+3)-1/3}{w(s^2-1)-1}\left[w(s^4-1)-\frac{s^2}{3}-\frac{1}{5}\right], \tag{10}$$

$$w(s)=\frac{s}{2}\ln\frac{s+1}{s-1}-1,$$

and in the single-harmonic approximation $w(s) = 1/F_0^{(s)}$.

The most important difference from (4) is the k^2-dependence of the attenuation (9), which originates from the $\mathbf{k}\cdot\mathbf{v}$ factor in the coupling coefficient. The calculation was performed for low frequencies, $kv_F \ll \Omega_0$. At higher frequencies, the factor $(kv_F)^2$ should be substituted by the square of the Larmor frequency Ω_0.

C. Effective relaxation and viscosity

The above expressions for sound attenuation allow us to obtain the values of effective relaxation time and viscosity. Comparing Eqs. (4) and (9) with the standard expressions for (zero-) sound attenuation in Fermi liquids, we immediately obtain[11]

$$\frac{1}{\tau_{\rm eff}}=\frac{\mathrm{Im}\ \omega}{\xi(s)}=\frac{E_d^2}{16\pi^5\hbar T_F}\left(\frac{\beta H}{T_F}\right)^2\frac{I(s\ \cos\ \theta)}{\xi(s)}, \tag{11}$$

$$\xi(s)=s^2\,\frac{w^2(s^2-1)(3s^2+1)+2w(s^2-1)-1}{w(s^2-1)-1},$$

$$w(s)=\frac{s}{2}\ln\frac{s+1}{s-1}-1$$

for direct processes, and

$$\frac{1}{\tau_{\rm eff}}=\frac{\hbar^2(kv_F)^2}{32\pi^2\tau_\perp\xi(s)}\left[\frac{F_0^{(s)}}{F_0^{(s)}-F_0^{(a)}}\right]^2\frac{E_d^2}{T_F^4}\left(\frac{k_z^2}{k^2}\,\frac{k^2-k_z^2}{k^2}\,\Gamma_1(s)+\frac{4k_z^4-3k^2k_z^2+k^4}{3k^4}\,\Gamma_2(s)\right) \tag{12}$$

for indirect processes.

The high-frequency attenuation can be obtained by the method similar to that used in calculation of sound attenuation in Fermi liquids.[19] The analysis of the nonvanishing collision operator of the type (1), at $T = 0$ shows that this integral is similar to those studied in Refs. 3, 6, and 19 and that it should reduce to the form

$$\gamma_{lf}\left(1+\left(\frac{\omega}{\Omega_0/2}\right)^2\right) \tag{13}$$

(in dense Fermi liquids the Larmor frequency Ω_0 experiences the usual Fermi-liquid renormalization), where γ_{lf} determines the low-frequency sound attenuation in Fermi liquids,

$$\gamma_{lf}=\mathrm{Im}\ k=\frac{\xi(s)}{s\tau_{\rm eff}v_F}. \tag{14}$$

The effective field-driven viscosity at $T = 0$,

$$\eta_{\rm eff}=\frac{1}{5}\,\rho v_F^2\tau_{\rm eff}(1+F_1^{(s)}/3), \tag{15}$$

depends on the angle between the velocity gradient ($\mathbf{k}$) and the direction of polarization z. This anisotropy of the fluid dynamics in spin-polarized systems with dipole interaction is quite natural.

5. CASTAING INSTABILITY

A. Castaing instability in spin dynamics

Studies of instabilities and nonlinear effects help further understanding of spin dynamics in Fermi liquids. One of the most important spin-wave instabilities—the so-called Castaing instability—occurs in spin dynamics of spin-polarized Fermi liquids in the presence of a gradient of magnetic field and/or polarization.

At low spin polarization, the transverse spin dynamics in polarized Fermi liquids is governed by the Leggett equation (see, e.g., review article[2]):

$$\frac{\partial\mathbf{M}}{\partial t}+[\gamma\mathbf{B}\times\mathbf{M}]=\frac{\partial}{\partial x_k}\left[\frac{D_\perp}{1+\mu^2M_0^2}\left(\frac{\partial\mathbf{M}}{\partial x_k}+\mu\left[\mathbf{M}\times\frac{\partial\mathbf{M}}{\partial x_k}\right]\right)\right]. \tag{16}$$

If the magnetization gradients are small, the last term can be linearized in small deviations from equilibrium $\delta\mathbf{M}$ as $\mu[\mathbf{M}_0\times\partial\delta\mathbf{M}/\partial x_k]$, and the spin excitations are weakly attenuated by circularly polarized spin waves with the spectrum

$$\omega=\omega_0+\frac{D_\perp k^2}{1+\mu^2M_0^2}\,(i-\mu M_0). \tag{17}$$

Castaing[20] noticed that if the gradient in the magnetization ∇M is not negligible, the linearized last term in Eq. (16) is $\mu[\mathbf{M}_0\times\partial\delta\mathbf{M}/\partial x_k]+\mu[\delta\mathbf{M}\times\nabla\mathbf{M}_0]$, and the excitation spectrum changes from (17) to

$$\omega=\omega_0+\frac{D_\perp}{1+\mu^2M_0^2}\,(i-\mu M_0)(k^2-\mu\mathbf{k}\cdot\boldsymbol{\nabla}\mathbf{M}). \tag{18}$$

For a sufficiently large gradient (or sufficiently small $\mathbf{k}$), the last bracket and, therefore, the imaginary part of the spectrum change sign. Instead of attenuation, the perturbation increases with time resulting in instability starting from

$$k_c=\mu\mathbf{n}\cdot\nabla\mathbf{M},\quad \mathbf{n}=\mathbf{k}/k. \tag{19}$$

The nonlinearity of the Leggett equation of spin dynamics, which is responsible for the Castaing instability, leads to a highly inhomogeneous final stationary distribution of magnetization (magnetic domains) even in slightly inhomogeneous magnetic field.[21] Under certain conditions, the domain wall could become very wide.[22] The difference between longitudinal and transverse relaxation will then disappear, and the total relaxation is determined by the shortest of the two, i.e., by the field-driven, zero-temperature transverse attenuation.

B. Observation of the spin-wave instability

This instability is very general, and can be observed in helium systems in different configurations. We will illustrate it using the example of experiments[9] in saturated ^{3}He$-^4$He mixtures.

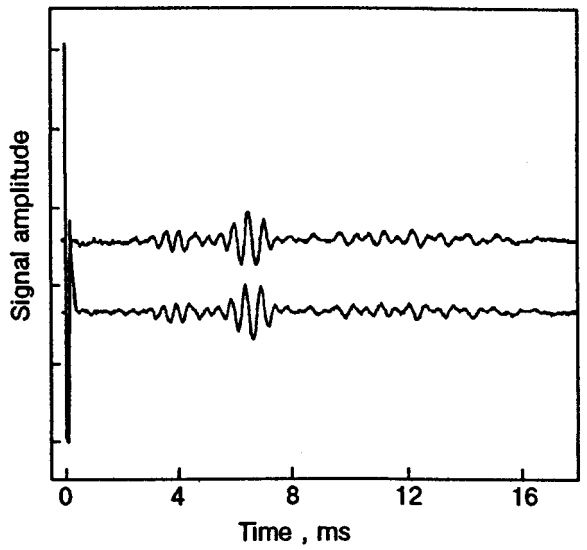

FIG. 3. The ringing signals observed after a $\theta = 105°$ pulse.

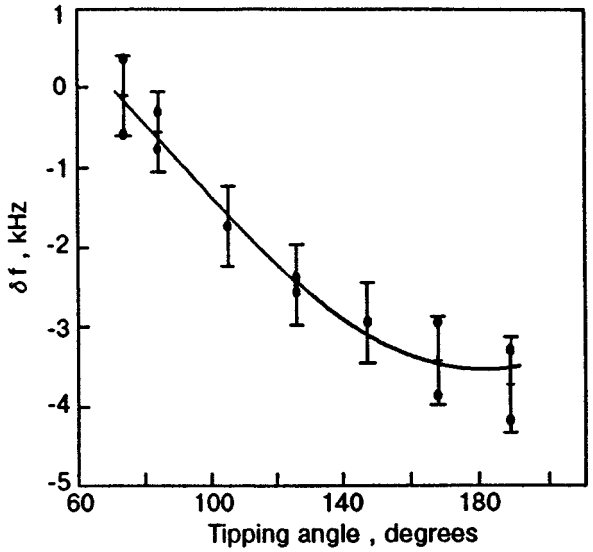

FIG. 4. The frequency shift as a function of the tipping angle. The line is a fit $\delta f = A(\cos\theta - \cos\theta_c)$.

We observed an oscillating signal that could be induced by the application of a single rf tipping pulse of angle θ applied to a small region of the helium in the middle of a 1-mm tube.[23] Large magnetization gradients were induced in the helium at the edges of this small region. We approximate these gradients as $|\nabla \mathbf{M}| \sim M_0(1 - \cos\theta)/\Delta x$, where Δx is the distance over which they extend. A typical NMR signal produced by a $\theta = 105°$ pulse is plotted in Fig. 3.

This long-lived ringing, which we interpret as a sign of instability, was observed only when the tipping angle exceeded some critical value $\theta_c \simeq 70°$. The frequencies of the oscillations were determined by Fourier transforming the signals; the frequency shift $\delta\omega$ away from the Larmor frequency increased with tipping angle. By substituting the expression for the magnetization gradient into the spectrum [Eq. (18)], we find that the frequency, $\delta\omega = \omega - \omega_0$, depends upon tipping angle as $\delta\omega \propto \cos\theta - \cos\theta_c$, where θ_c is the critical angle, i.e., the angle for which the last bracket of the spectrum is equal to zero (Fig. 4). Our estimate gives the value $k_c \sim 600\ \mathrm{cm}^{-1}$. This implies that the large magnetization gradient is over a distance of the order of 0.05 cm, consistent with the scale of our experimental setup.

These ringing signals possess several features which support an explanation in terms of an instability. There is a cutoff in tipping angle θ_c, below which no signals were observed. This circumstance, together with the fact that there was no ringing signal at higher temperatures when μM_0 is small, confirms the threshold nature of the phenomenon. The long-time scale of the signals and the initial increase in amplitude (Fig. 3) are also characteristic of an instability. The frequencies of the oscillations scale as the cosine of the tipping angle, $\cos\theta - \cos\theta_c$. The presence of two frequency peaks on the Fourier analysis of the spectrum suggests that the signals are coming from regions on either side of the rf coil where the magnetization gradients are slightly different. No such signals were observed during experiments on solutions with lower ^{3}He concentrations. Here μM_0 is of the same magnitude but negative, so that the instability propagates in the opposite direction, away from the receiving NMR coil.

Similar instabilities have been observed by Nunes[10] and Dmitriev *et al.*[24] The ringing continued for extremely long times, leading to conclusions about the existence of a metastable state (precessing spin domains)[21] after the instability develops. In our experiment we did not see such a long-time behavior due to the different setup. Only a small fraction of the spins in the lower chamber was tipped and the longitudinal spin diffusion coefficient $D_\parallel$ was large, so that the instability was quickly suppressed by diffusion of up-spins into the coil.

C. Dipole effects in Castaing instability

The nonlinear coupling between longitudinal and transverse channels is enhanced close to the instability in spin dynamics (see, e.g., Ref. 23 and the bibliography cited there). We analyzed[11] the dipole effects near the onset of Castaing instability. Without the dipole effects, the instability occurs at k_c [Eq. (19)]. The dipole interaction makes the instability anisotropic by adding terms of the form k_z^2, $\mu k_z \nabla_z M$, $(\mu\nabla M)^2$, and $(\mu\nabla_z M)^2$ to Eq. (19). However, these terms contain a small factor E_d/T_F (we will not give here the cumbersome coefficients). These anisotropic corrections do not have any fixed sign so that it is impossible to say whether the onset of instability occurs earlier in certain directions.

Although this instability exists in transverse spin dynamics, one of its features is that μ in Eq. (19) is proportional not to the transverse relaxation time $\tau_\perp$, but to the longitudinal time $\tau_\parallel$, $\mu = \Omega_i \tau_\parallel / M$. Since $\tau_\parallel \propto 1/T^2$, the onset of instability $k^2 = \mu k_i \nabla_i M$ occurs with decreasing temperature at larger and larger wave vectors. The usual derivation of the instability condition assumes that the gradient of the longitudinal magnetization leads to a large longitudinal diffusion current and not to longitudinal oscillations, i.e., that $1/\tau_\parallel \gg k v_F$.

These two conditions, taken together, limit the temperature range in which the instability can be observed to

$$T_F \gg T \gg T_F(\alpha a/L)^{1/4}/x^{1/3}, \tag{20}$$

where α is the degree of spin polarization, x is the molar density of the Fermi liquid, and L is the spatial scale of the polarization gradient.

The dipole coupling between longitudinal and transverse channels leads to a substitution of $\tau_{\|}$ by $\tau_{\rm eff}$ and lifts this temperature limitation. At zero temperature, the instability occurs at $k^2 = \mu_{\rm eff} k_i \nabla_i M$, $\mu_{\rm eff} = \Omega_i \tau_{\rm eff}/M$ under the condition $1/\tau_{\rm eff} \gg k v_F$. The compatibility of these equations requires high polarization with small gradient,

$$E_d \gg T_F(a/\alpha^3 L)^{1/4}.$$

As a result, the instability exists even at zero temperature, but occurs at extremely small values of k.

6. APPLICATION TO PURE FERROMAGNETIC METALS

Ferromagnetic metals can be roughly separated into two groups: itinerant ferromagnets with ferromagnetism of conduction electrons, and metals with ferromagnetic ordering of inner, localized electrons (with Heisenberg interaction). The zero-temperature transverse attenuation in the former systems seems similar to helium systems, while in the latter group such effects appear only as a result of exchange coupling between the localized ferromagnetic electrons and the Fermi liquid of conduction electrons. In addition, the spin-lattice relaxation, absent in helium, presents a strong coupling mechanism between longitudinal and transverse channels for both types of ferromagnetic systems.

A. Itinerant magnetism

The theory of transverse spin dynamics in electron Fermi liquid in itinerant ferromagnets should be similar to that in spin-polarized helium. To a large extent this is correct, especially well below the transition temperature. Close to the transition temperature the Fermi-liquid description is not applicable (see, e.g., Ref. 25). It is known[26] that the spin wave spectrum in ferromagnetic metals is similar to the spectrum of Silin spin waves in Fermi liquid. Careful analysis of the spectrum[26] shows that this spectrum contains the zero-temperature attenuation: the expression for the spectrum includes the integral between the spin-up and spin-down Fermi spheres,

$$\int \cdots [n_\uparrow - n_\downarrow] d\Gamma,$$

which, as any integral not localized near the Fermi surface, should contain a large imaginary part. However, this integration deep into the Fermi spheres makes the derivation[26] not self-consistent; a consistent-derivation should be based on the microscopic equations.[6]

Apart from the zero-temperature attenuation, these equations have another interesting feature, namely, the spin-up–spin-down asymmetry. This effect is similar to a well-known particle-hole asymmetry in Fermi liquids away from the Fermi sphere. In itinerant ferromagnets the radii of the Fermi spheres for spin-up and spin-down particles differ by a large margin resulting in different molecular fields (Landau–Fermi liquid functions) for quasiparticles near these Fermi surfaces. This means that the frequencies of inhomogeneous precession in the effective field for tipped spin-up and spin-down particles are different.

In general, the transfer of the microscopic equations[6] from Fermi liquids polarized by an external magnetic field to ferromagnetic Fermi liquids is rather straightforward, and we will not dwell on this matter here. Instead, we will mention another interesting aspect of microscopic equations. The spin-up–spin-down anisotropy of the effective field can give credence and microscopic justification[27] to the concept of reaction field suggested by Onsager[28] for ferroelectric systems (this concept for ferromagnetic systems was discussed in Ref. 29).

B. Heisenberg systems

The above zero-temperature dissipation mechanism is inherent to Fermi liquids and, in its original form, does not exist in a solid-state magnetic system of localized spins with Heisenberg interaction J. However, this unique Fermi-liquid dissipation mechanism should lead to some residual attenuation of magnons in pure ferromagnetic metals with Heisenberg interaction. We want to emphasize that in this section we are interested not in itinerant magnetism, for which the manifestation of Fermi-liquid effects is natural, but in an exchange magnetic system of localized electrons.

This fairly straightforward effect is based on exchange coupling of localized ferromagnetic spins (e.g., $3d$ electrons) to conduction (e.g., $4s$) electrons. This exchange coupling results in small polarization (not to exceed several percent) of conduction electrons of the order $J_1\langle S\rangle/T_F$, where J_1 is the exchange coupling constant between localized ferromagnetic electrons with spins $\mathbf{S}$ and spins of conduction electrons $\boldsymbol{\sigma}$. Polarization of spins of conduction electrons ensures the propagation of Silin spin waves in this system with finite zero-temperature attenuation, $\tau_\perp(T=0) \sim (N\tilde{v}_F\sigma)^{-1} \times (T_F/J_1\langle S\rangle)^2$. The exchange coupling between these attenuating Silin spin waves and ferromagnetic Heisenberg magnons transfers the zero-temperature attenuation to the magnon system resulting in the effective relaxation time $\tau_\perp^* \sim \tau_\perp (J_1/J)^2$. The competing processes that lead to the magnon attenuation are, obviously, scattering on impurities and spin-lattice processes studied long ago (see, e.g., Ref. 30). The former processes are small in pure metals, while the latter are suppressed at low temperatures.

The equilibrium energy of conduction electrons has the form

$$\varepsilon_i^e = \varepsilon_i^o - \beta_1^e \boldsymbol{\sigma}_i \cdot \mathbf{H} - J_1 \sigma_i \cdot \langle \mathbf{S}\rangle/2, \tag{21}$$

while the Hamiltonian of localized electrons is

$$\varepsilon_i^l = -\beta^l \mathbf{S}_i \cdot \mathbf{H} - \frac{1}{2} J_0 \langle \boldsymbol{\sigma}\rangle \cdot \mathbf{S}_i - J \sum_a (\mathbf{S}_{i+a_x} + \mathbf{S}_{i+a_y} + \mathbf{S}_{i+a_z}) \cdot \mathbf{S}_i. \tag{22}$$

The effective parameters for conduction electrons are already

renormalized by their Fermi-liquid interaction, $\beta_1^e = \beta^e/(1 + F_0^{(a)})$, $J_1 = J_0/(1 + F_0^{(a)})$, while the averages

$$\langle \mathbf{S} \rangle = \sum \mathbf{S}_i N_i ,$$

$$\langle \sigma \rangle = \sum \sigma_i n_i = p_F m(\beta_1^e H + 1/2\, J_1 \langle S_z \rangle)/\pi^2 \hbar^3 . \qquad (23)$$

The Fermi-liquid term in the energy of conduction electrons has the usual form,

$$\delta\varepsilon^e_{\alpha\beta} = -\frac{1}{2} J \sigma_{\alpha\beta} \cdot \delta \mathbf{S} + \int f_{\alpha\beta\alpha'\beta'}(\mathbf{p},\mathbf{p}')\, \delta n_{\beta'\alpha'}(\mathbf{p}')\, d\Gamma' , \qquad (24)$$

with the Landau Fermi-liquid function

$$\frac{p_F m}{\pi^2 \hbar^3} f_{\alpha\beta\alpha'\beta'}(\mathbf{p},\mathbf{p}') = F^{(s)}(\mathbf{p},\mathbf{p}')\, \delta_{\alpha\beta}\delta_{\alpha'\beta'} + F^{(a)} \times (\mathbf{p},\mathbf{p}')\, \boldsymbol{\sigma}_{\alpha\beta} \cdot \boldsymbol{\sigma}_{\alpha'\beta'} . \qquad (25)$$

Often, in ferromagnetic systems $J_0\langle S_z \rangle \gg J_0 \langle \sigma_z \rangle$, βH, and $\Omega_0 \gg \omega_0$. In this approximation, the analysis of the coupled equations of motion for localized and delocalized spins $\mathbf{S}$ and σ with the Hamiltonian (21)–(25) yields, after some algebra, the following expression for the attenuation of ferromagnetic magnons:[31]

$$\mathrm{Im}\ \omega = -\frac{\beta^l H}{6 J_0 \langle S_z \rangle} \frac{\langle \sigma_z \rangle}{\langle S_z \rangle} \frac{k^2 v_F^2 \tau_\perp (1 + F_0^{(a)})(1 + F_1^{(a)}/3)}{1 + [\tau_\perp \Omega_0 (1 + F_1^{(a)}/3)/(1 + F_0^{(a)})]^2} .$$

This equation is valid only for $\beta^l H \gg J\langle S_z \rangle k^2 a^2$ and formally yields zero at $H = 0$. In smaller fields the attenuation does not vanish, but becomes proportional to k^4, in accordance with the general result.[32]

The strength of the effect depends on the exchange interaction $J_0 \mathbf{S} \cdot \boldsymbol{\sigma}$ between spins of ferromagnetic and conduction electrons. In free atoms the $s-d$ exchange is of the scale of 1 eV. In metals, screening weakens this exchange by about one or two orders of magnitude. There is also an enhancement factor, which is related to the Kondo-like logarithmic divergence of the effective field. The localized electrons create the (transverse) coherent exchange field for conduction electrons:[33]

$$L_{\mathrm{coh}} = \frac{i\pi}{2\hbar V} [\delta S_+ (n_\uparrow - n_\downarrow) - \delta\sigma^+ \langle S_z \rangle N] \Bigg[4 t_2 + \int \frac{d^3 p'}{(2\pi\hbar)^3}\, P\, \frac{1}{\epsilon' - \epsilon} (2N t_1 t_2 + t_2^2 (n_\uparrow - n_\downarrow + N)) \Bigg] .$$

The exchange field for localized electrons is similar. Here t_1 and t_2 are the bare direct and exchange interaction constants, and N is the density of localized spins. If the polarization of conduction electrons is low, the direct interaction t_1 disappears from the results. The above integral, as other similar integrals in the theory of metals, diverges logarithmically. After introducing the usual cutoff, we obtain the following renormalization of the bare interaction:

$$J_0 = t_2 \left(1 + 8\pi t_2 \nu_F \ln \frac{T_F (1 + F_0^{(a)})}{\beta^e H + t_2 \langle S_z \rangle/2} \right) ,$$

where ν_F is the density of states on the Fermi surface. As a result of this large logarithmic enhancement of the interaction, J_0 can reach several hundred K and the polarization of conduction electrons can exceed one percent. Then the zero-temperature attenuation for conduction electrons $\tau_\perp$ can become shorter than 10^{-10} sec, and τ^* can reach 10^{-7} sec.

7. CONCLUSIONS

The zero-temperature transverse attenuation in spin-polarized Fermi liquids, which was observed recently in spin dynamics of ^{3}He↑ and ^{3}He↑-^{4}He mixtures, is the only low-frequency dissipative process in Fermi liquids at $T = 0$. This effect can have much broader implications than a simple low-temperature saturation of transverse transport parameters in polarized helium systems. We highlighted several of such effects.

The dipole coupling between longitudinal and transverse spin dynamics processes in spin-polarized Fermi liquids leads to the transfer of zero-temperature transverse attenuation into longitudinal channels. This transfer is responsible for the zero-temperature dipole contribution to the sound attenuation in a generic Fermi liquid described by the effective mode-independent longitudinal relaxation time and viscosity. These effective parameters provide the low-temperature limit for dissipation of various hydrodynamic and high-frequency modes in helium systems.

The zero-temperature attenuation processes have interesting implications for ferromagnetic metals. Of course, the direct manifestations of this Fermi-liquid anomaly can be observed in itinerant ferromagnets. Here the most interesting effect is, probably, not the zero-temperature attenuation itself, but a pronounced spin-up—spin-down asymmetry of the effective field which could manifest itself in the formation of a peculiar Onsager reaction field.

In metals with ferromagnetism of localized Heisenberg spins, the effects of the zero-temperature Fermi-liquid interaction are indirect. In this case, the exchange coupling of localized and conduction electrons results in low residual polarization of spins of conduction electrons. This, in turn, leads to the propagation of Silin spin waves with small zero-temperature attenuation in the system of conduction electrons. The coupling of these spin waves to the spin waves in the system of localized Heisenberg electrons transfers the zero-temperature attenuation to ferromagnetic magnons. This mechanism is responsible for the residual attenuation of ferromagnetic magnons in pure ferromagnetic metals.

Another important peculiarity of spin dynamics in spin-polarized Fermi liquids is the spin-wave instability in inhomogeneous setting (Castaing instability). We presented and analyzed experimental data confirming the existence of this instability, and discussed some further experimental options. As a result of dipole transfer of zero-temperature attenuation into longitudinal channels, the Castaing instability does not

disappear at ultralow temperatures, although its observation would require a relatively large experimental installation. In addition, the dipole interaction makes all the processes, including the instability in spin-polarized Fermi liquids, highly anisotropic.

The nonlinearity of the Leggett equation of spin dynamics, which is responsible for the Castaing instability, results in a highly inhomogeneous final distribution of magnetization even in almost homogeneous magnetic field. In these conditions, the difference between longitudinal and transverse relaxation disappears, and the overall relaxation is determined by the shortest of the two. Then the overall low-temperature relaxation is similar to the field-driven, zero-temperature, transverse attenuation in homogeneous systems.

The work was supported by NSF grant DMR-9412769 and EPSRC grant GR/K44008.

[1] A. E. Meyerovich, Phys. Lett. A **107**, 177 (1985).
[2] A. E. Meyerovich, *Spin-Polarized Phases of* ^3He, in Helium Three, Eds. W. P. Halperin and L. P. Pitaevski (Elsevier, Amsterdam) 1990, pp. 757–879.
[3] J. W. Jeon and W. J. Mullin, J. Phys. (Paris) **49**, 1691 (1988); Phys. Rev. Lett. **62**, 2691 (1989); J. Low Temp. Phys. **88**, 483 (1992).
[4] D. I. Golosov and A. E. Ruckenstein, Phys. Rev. Lett. **75** (1994).
[5] A. E. Meyerovich, S. Stepaniants, and F. Laloe, Phys. Rev. B (1995).
[6] A. E. Meyerovich and K. A. Musaelian, Phys. Rev. Lett. **72**, 1710 (1994); Phys. Rev. B **47**, 2897 (1993); J. Low Temp. Phys. **89**, 781 (1992); **94**, 249 (1994); **95**, 789 (1994).
[7] L.-J. Wei, N. Kalenchofsky, and D. Candela, Phys. Rev. Lett. **71**, 879 (1993).
[8] J. Owers-Bradley, A. Child, and R. M. Bowley, Phisica B **194–196**, 903 (1994) [Proc. LT-20]; J. H. Ager, A. Child, R. Konig, J. R. Owers-Bradley, and R. M. Bowley, J. Low Temp. Phys. **99**, 683 (1995).
[9] J. H. Ager, R. König, J. R. Owers-Bradley, and R. M. Bowley, Phys. Rev. B **50**, 13062 (1994); J. H. Ager, A. Child, R. König, J. R. Owers-Bradley, and R. M. Bowley, J. Low Temp. Phys. **99**, 693 (1995).
[10] G. Nunes, C. Jin, D. L. Hawthorne, A. M. Putnam, and D. M. Lee, Phys. Rev. B **46**, 9082 (1992).
[11] A. E. Meyerovich and A. Stepaniants, preprint #1 (1996).
[12] P.-J. Nacher and E. Stolz, J. Low Temp. Phys. **101**, 311 (1995); E. Stolz, J. Tannenhauser, and P.-J. Nacher, J. Low Temp. Phys. **101**, 839 (1995).
[13] E. P. Bashkin and A. E. Meyerovich, Adv. Phys. **30**, 1 (1981).
[14] D. Vollhardt and P. Wölfle, Phys. Rev. Lett. **47**, 190 (1981).
[15] K. S. Bedell and D. E. Meltzer, J. Low Temp. Phys. **63**, 215 (1986).
[16] M. H. Cohen and F. Keffer, Phys. Rev. **99**, 1128 (1955).
[17] G. Deville, M. Bernier, and J. M. Delrieux, Phys. Rev. B, **19**, 5666 (1979).
[18] E. D. Nelson and W. J. Mullin, J. Low Temp. Phys. **97**, 251 (1994); R. J. Ragan and W. J. Mullin, J. Low Temp. Phys. 5/6 (1996), in print.
[19] L. D. Landau [Zh. Éksp. Teor. Fiz. **32**, 59 (1957)] Sov. Phys. JETP **5**, 101 (1958).
[20] B. Castaing, Physica **126B**, 212 (1984).
[21] I. A. Fomin, Physica B **210** (1995).
[22] I. A. Fomin, private communication.
[23] R. Konig, J. H. Ager, R. M. Bowley, J. R. Owers-Bradley, and A. E. Meyerovich, J. Low Temp. Phys. **101**, 833 (1995).
[24] V. V. Dmitriev, V. V. Moroz, A. S. Visotskiy, and S. R. Zakazov, Physica B **210** (1995); V. V. Dimitriev, V. V. Moroz, and S. R. Zakazov, J. Low Temp. Phys. **100**, 141 (1995).
[25] T. Moriya, J. Mag. and Mag. Mat. **100**, 261 (1991).
[26] A. A. Abrikosov and I. E. Dzyaloshinski [Zh. Éksp. Teor. Fiz. **35**, 771 (1958)] Sov. Phys. JETP **8**, 535 (1958).
[27] K. A. Musaelian, Ph.D. Thesis, URI (1994).
[28] L. Onsager, J. Am. Chem. Soc. **58**, 1486 (1936).
[29] M. Cyrot, in *Electron Correlation and Magnetism in Narrow Band Systems*, Ed. T. Morya, Springer Ser. Sol. St. Sci., Vol. 29 (Springer, Berlin) 1981, p. 51.
[30] E. Abrahams, Phys. Rev. **98**, 387 (1955); A. H. Mitchell, Phys. Rev. **105**, 1439 (1957); C. W. Haas and H. B. Callen, in *Magnetism, Vol. 1. Magnetic Ions in Insulators*, Eds. G. T. Rado and N. Suhl (Academic Press, New York), 1963.
[31] A. E. Meyerovich and A. Stepaniants, preprint #2 (1996).
[32] B. I. Halperin and P. C. Hohenberg, Phys. Rev. **188**, 898 (1969).
[33] S. Stepaniants, Ph.D. Thesis, URI (1995).

This article was published in English in the original Russian journal. It was edited by S. J. Amoretty.

Finite temperature effects in the Fermi liquid theory of the diffusion of ^{4}He in ^{3}He

H. H. Hjort, T. G. Culman, D. O. Edwards, and Jizhong He

Physics Department, The Ohio State University, Columbus, Ohio, USA 43210
(Submitted October 24, 1996)
Fiz. Nizk. Temp. **23**, 564–573 (May–June 1997)

The diffusion coefficient D and the thermal diffusion ratio k_T for dilute ^{4}He in liquid ^{3}He are calculated from Fermi liquid theory. The collision integral assumes a scattering amplitude a^{34} expanded in scalar combinations of the quasiparticle momenta. As $T\to 0$, D varies as 1/T and k_T/c, where c is the concentration, approaches a constant. As shown previously, the limits for DT and k_T/c are determined by thermodynamic properties, the ^{4}He effective mass and partial volume, and properties of pure ^{3}He. We have decreased k_T/c by a few percent, by including the effect of ∇T on the ^{3}He distribution function. The temperature dependence of DT and k_T/c is linear and related to the coefficients in the expansion of a^{34}. Two coefficients can be found from thermodynamics. A conjecture about the remainder suggests that DT may have a maximum between 0 and 0.5 K. © *1997 American Institute of Physics.* [S1063-777X(97)00905-5]

1. INTRODUCTION

In this paper we calculate the diffusion coefficient D and the thermal diffusion ratio k_T for very dilute solutions of ^{4}He in normal (nonsuperfluid) liquid ^{3}He. The quantities D and k_T are defined[1] by the equation for the impurity mass current $\mathbf{i}$ in terms of the gradients of the ^{4}He mass concentration, $c=N_4m_4/(N_4m_4+N_3m_3)$, and the temperature T:

$$\mathbf{i}=-\rho D[\nabla c+(k_T/T)\nabla T]. \tag{1.1}$$

When the total mass current $\rho\mathbf{v}$ is zero, $\mathbf{i}$ is simply the ^{4}He mass current; otherwise,[1] the ^{4}He current is $\rho c\mathbf{v}+\mathbf{i}$ and the ^{3}He current is $(1-c)\rho\mathbf{v}-\mathbf{i}$. When there are no currents, $(\nabla c)/c=-k_T/c(\nabla T)/T$.

The low temperature behavior of D and k_T is determined by Fermi liquid theory from the Boltzmann transport equation of Zharkov and Silin.[2] In the dilute limit, the diffusion coefficient D is proportional[3] to 1/T and k_T/c tends to a constant when $T\to 0$. As shown in Ref. 4, k_T/c and DT tend to values determined solely by the $l=0$ forward scattering amplitude[5,6] a_0^{34}, which can be obtained from thermodynamic measurements. The limit for DT is[4]

$$DT=D_0\,\frac{\hbar}{m_4^*}\,\frac{m_3^*}{m_4^*}\left(\frac{v_3}{v_4^*}\right)^2 T_F;\quad D_0=0.4461\ldots\,. \tag{1.2}$$

Here m_4^* and m_3^* are the ^{4}He and ^{3}He quasiparticle effective masses, and T_F is the ^{3}He Fermi temperature, given by $k_BT_F=p_F^2/2m_3^*$. Equation (1.2) uses the relation between a_0^{34} and thermodynamic properties derived by Saam and Laheurte:[5,6]

$$a_0^{34}=(v_4^*/v_3)/\nu(0). \tag{1.3}$$

In (1.2) and (1.3), v_4^* is the partial volume of a ^{4}He atom dissolved in liquid ^{3}He. The ^{3}He atomic volume is v_3 and $\nu(0)=3/(2v_3k_BT_F)$ is the ^{3}He density of states.

The limit for k_T/c was given as 0.3823 in Ref. 4, but we find a value a few percent smaller. We include the effect of the temperature gradient on the ^{3}He distribution function which was neglected in Ref. 4. The correction, which depends on pressure, can be calculated from m_4^* and v_4^* and from known properties of pure liquid ^{3}He. The limit for DT is unchanged.

Equation (1.2) implies a ^{4}He collision time,[2] $t=3m_4D/(2k_BT)$, that varies as $1/T^2$. For Fermi liquid theory to be valid, the energies of the ^{4}He quasiparticle states must be well defined; this implies $\hbar/t\ll k_BT$, which is equivalent to $D\gg 2\hbar/(3m_4)$. This criterion is well satisfied provided $T\ll T_F$.

As noted in Ref. 4, a measurement of k_T/c or a comparison between measurements of the limit for DT and Eq. (1.2) would provide a stringent test of the underlying Fermi liquid theory. In this respect, ^{4}He in ^{3}He is qualitatively different from other applications of the theory. For example, to relate the kinetic coefficients to the thermodynamic properties in pure ^{3}He or ^{3}He in liquid ^{4}He, some assumptions about the dependence of the ^{3}He–^{3}He scattering amplitude on the momentum transfer are necessary.[7] For ^{4}He in ^{3}He at low T, because the ^{4}He is dilute, only ^{4}He–^{3}He collisions need to be considered. Since the ^{4}He obeys Boltzmann statistics, the ^{4}He momentum and energy are small compared to the Fermi momentum and energy. In addition, the Pauli principle excludes large energy or momentum transfer from the ^{3}He. Therefore, as $T\to 0$, the ^{3}He is restricted to forward scattering, which is determined by a_0^{34}.

Although measurements[8,9] of D and k_T/c have been made above 0.5 K, experiments to test the theory must be made at temperatures where pure ^{3}He obeys Fermi liquid theory, which is below 0.1 K and above the ^{3}He superfluid transition. Here the solubility $c^{\rm sat}(P,T)$ is very small,[10] less than 500 ppm below 0.1 K. The thermodynamic quantities in the expression for D, v_4^*, and m_4^* can be obtained by analyzing measurements of $c^{\rm sat}(P,T)$. Solubility data by Nakamura *et al.*[10] below 0.1 K and a preliminary measurement[11,12] of D indicate that such experimental tests are feasible.

In the present paper we find the solution of the ^{4}He Boltzmann equation with a momentum-dependent scattering amplitude. We prove the assertion, made in Ref. 4, that the

momentum dependence produces terms in DT and k_T/c which are of the order of T/T_F, so that only a_0^{34} appears in the limiting values of DT and k_T/c. Since the Fermi temperature T_F of liquid ^{3}He is approximately 1.77 K at zero pressure,[13] terms of order T/T_F are expected to be small below 0.1 K, where Fermi liquid theory is valid. However, in Sec. 7 we show that the temperature dependence of DT could be measurable. In Sec. 2 we deal with the symmetry and parametrization of the scattering amplitude; the solution to the Boltzmann equation is given in Secs. 3–6. In Secs. 6 and 7 we give the numerical results, and in Sec. 7 we summarize the paper.

As in Ref. 4, we assume that the ^{4}He quasiparticle spectrum has the conventional, particle-like form $E=-E_{43}+q^2/2m_4^*$, rather than the alternative, roton-like, ''bubble spectrum'' (Ref. 2) $E=-E_{43}+(q-q_0)^2/2m_4^*$. Here E_{43} is the binding energy of one ^{4}He atom in liquid ^{3}He in the ground state. A microscopic calculation[14] shows that the conventional spectrum is correct, with $m_4^*/m_4\approx 1.21$ at zero pressure. In Ref. 15, a fit to the $c^{\rm sat}(P,T)$ data of Nakamura *et al.*[10] gave $m_4^*/m_4=(1.1+0.4/-0.1)$.

2. MOMENTUM DEPENDENT SCATTERING AMPLITUDE

In general, the scattering amplitude depends on $\mathbf{p}$ and $\mathbf{q}$, the initial momenta of the ^{3}He and ^{4}He quasiparticles, and the momentum transfer $\mathbf{k}=\mathbf{p}'-\mathbf{p}=\mathbf{q}-\mathbf{q}'$. It is also true that the inverse collision must have the same amplitude to within a phase factor:[16]

$$|a^{34}(\mathbf{p},\mathbf{q},\mathbf{k})|=|a^{34}(\mathbf{p}',\mathbf{q}',-\mathbf{k})|. \tag{2.1}$$

This symmetry has a simpler form when a^{34} is written as a function of the mean momenta $\mathbf{q}_m=\mathbf{q}-\mathbf{k}/2$ and $\mathbf{p}_m=\mathbf{p}+\mathbf{k}/2$

$$|a^{34}(\mathbf{p}_m,\mathbf{q}_m,\mathbf{k})|=|a^{34}(\mathbf{p}_m,\mathbf{q}_m,-\mathbf{k})|. \tag{2.2}$$

We expand a^{34} in terms of the lowest-order scalar functions of $\mathbf{q}_m$, $\mathbf{p}_m$, and $\mathbf{k}$, using the symmetry in (2.2). Keeping terms up to and including the second power in the small momenta $\mathbf{q}_m$ and $\mathbf{k}$, the results are equivalent to expanding $|a^{34}|$:

$$|a^{34}|=a_0^{34}\left[1+\alpha_1\left(\frac{p_m^2}{p_F^2}-1\right)+\alpha_2\frac{\mathbf{p}_m\cdot\mathbf{q}_m}{p_F^2}+\alpha_3\frac{q_m^2}{p_F^2}+\alpha_4\frac{(\mathbf{p}_m\cdot\mathbf{q}_m)^2}{p_F^4}+\cdots+\alpha_5\frac{k^2}{p_F^2}+\alpha_6\frac{(\mathbf{p}_m\cdot\mathbf{k})^2}{p_F^4}+\cdots\right]. \tag{2.3}$$

The real coefficients α_i, like a_0^{34}, depend on the pressure. We shall find that α_6 only produces terms of higher order than T/T_F, so that it does not appear in our results for DT or k_T/c.

The forward scattering amplitude corresponds to a^{34} with zero momentum transfer $\mathbf{k}$. In this case, $\mathbf{p}_m=\mathbf{p}$ and $\mathbf{q}_m=\mathbf{q}$. Saam derived a relation[5] between the forward scattering amplitude and the thermodynamic Landau interaction function f^{34}. The forward scattering amplitude and the Landau function differ because the latter includes successive or multiple scattering events. Saam's equations, which are analogous to a similar set for the ^{3}He–^{3}He amplitude,[7] link the two functions through the coefficients of their expansions in Legendre polynomials of $\hat{\mathbf{p}}\cdot\hat{\mathbf{q}}$,

$$\{a^{34}(\mathbf{k}=0)\}_l=\{f^{34}\}_l/[1+F_l^s/(2l+1)]. \tag{2.4}$$

The F_l^s are the symmetric Fermi liquid factors[13] for pure liquid ^{3}He.

Using Galilean invariance[17] and invariance with respect to the reference system,[5,6,15] some properties of the Landau function f^{34} have been directly related to thermodynamic quantities such as v_4^* and m_4^*. As a result, we find the following relations between a_0^{34} and α_i and the corresponding known coefficients f_0^{34}, a_1', and a_1'' in a similar expansion for f^{34} in Ref. 15

$$\begin{aligned}
a_0^{34}&=\frac{f_0^{34}}{(1+F_0^s)}=\frac{v_4^*}{v_3\nu(0)}=\frac{2}{3}\,k_BT_Fv_4^*,\\
\alpha_2&=\frac{3a_1'}{(3+F_1^s)}\frac{p_F^2}{a_0^{34}}=3\frac{v_3}{v_4^*}\left(1-\frac{m_4}{m_4^*}\right),\\
\alpha_3&=\frac{a_1''}{(1+F_0^s)}\frac{p_F^2}{a_0^{34}}=\frac{3}{2}\frac{v_3}{v_4^*}\frac{m_3^*}{m_4^*}\frac{1}{(1+F_0^s)}\frac{d\,\log(m_4^*)}{d\,\log(v_3)}.
\end{aligned} \tag{2.5}$$

The first relation is the same as (1.3). Since $(1+F_0^s)\approx 10.6$ in liquid ^{3}He at zero pressure,[13] and since[14,15] $m_4\approx m_4^*$, both α_2 and α_3 are smaller than one. The rest of the α_i are undetermined. In Sec. 7 we find that the α_5k^2 term in a^{34} has the largest effect on the temperature dependence of DT and k_T/c.

3. THE ^{4}He BOLTZMANN EQUATION

In setting up and solving the Boltzmann equation, we follow the work of Zharkov and Silin,[2] Leggett and ter Haar,[3] Dandache *et al.*,[18] and Geilikman and Chechetkin.[19] The notation is nearly the same as in Ref. 4. According to Zharkov and Silin, the linearized ^{4}He Boltzmann equation in the dilute limit (negligible ^{4}He–^{4}He scattering) for small temperature and concentration gradients and $\mathbf{v}=0$ has the form

$$n_{i0}(\mathbf{q}/m_4^*)\cdot[(\boldsymbol{\nabla}c)/c+(q^2/2m_4^*k_BT-3/2)(\boldsymbol{\nabla}T)/T]=J_{if}(\mathbf{q}). \tag{3.1}$$

Here n_{i0} is the equilibrium ^{4}He quasiparticle occupation number:

$$n_{i0}=(\rho c/m_4)(2\pi\hbar/m_4^*k_BT)^{3/2}\exp(-q^2/2m_4^*k_BT), \tag{3.2}$$

where $\rho c/m_4$ is the ^{4}He number density. The collision integral is[2,18]

$$J_{if}(\mathbf{q})=(2\pi/\hbar)\int|a^{34}|^2n_{f0}(1-n_{f0}')n_{i0}(\boldsymbol{\psi}_i-\boldsymbol{\psi}_i'+\boldsymbol{\varphi}_f-\boldsymbol{\varphi}_f')\delta(\varepsilon+E-\varepsilon'-E')(2/h^6d\mathbf{p}d\mathbf{q}'). \tag{3.3}$$

The factor of 2 multiplying $d\mathbf{p}$ allows for the sum over the initial ^{3}He spin states. In Refs. 18 and 19 we have a factor of

4, which implies that the ^{3}He quasiparticle may change its spin orientation during a ^{4}He–^{3}He collision. As explained in Ref. 4, we think this is incorrect. Our equation agrees with the original formulation by Zharkov and Silin.

In the collision integral, $\mathbf{p}'$ is related to the other momenta by conservation of momentum:

$$\mathbf{p}'-\mathbf{p}=\mathbf{q}-\mathbf{q}'=\mathbf{k}. \tag{3.4}$$

The Fermi functions n_{f0} and n'_{f0} are the equilibrium occupation numbers for the initial and final ^{3}He states which have energies ε and ε'. The initial and final ^{4}He energies are E and E', so that the delta function $\delta(\varepsilon+E-\varepsilon'-E')$ enforces conservation of energy.

In (3.3), the quantities $\psi_i=-\delta n_i/n_{i0}$ and $\psi'_i=-\delta n'_i/n'_{i0}$ are the negatives of the small fractional deviations from the equilibrium ^{4}He distribution function. Because they are linear in the concentration and temperature gradients, ψ_i and ψ'_i depend on $\mathbf{q}$ and $\mathbf{q}'$ according to the equation[2]

$$\psi_i(\mathbf{q})=a_c(q)\mathbf{q}\cdot\nabla c+a_T(q)\mathbf{q}\cdot\nabla T. \tag{3.5}$$

The functions $a_c(q)$ and $a_T(q)$ are found by solving the ^{4}He Boltzmann equation (3.1).

The deviations from equilibrium of the ^{3}He occupation number are related to φ_f and φ'_f in (3.3) by $\delta n_f=-\varphi_f k_B T\partial n_{f0}/\partial\varepsilon$. They are determined from the known solution[7] of the Boltzmann equation for a temperature gradient in pure ^{3}He. The effect of the ^{4}He on φ_f is negligible, because in the dilute limit the number of ^{3}He at the Fermi surface and available for scattering is much larger than the number of ^{4}He. When $\nabla T=0$, as in the calculation of the diffusion coefficient, φ_f and φ'_f are negligible. In previous studies[2,18,19,4] φ_f and φ'_f were incorrectly omitted in the calculation of k_T.

We divide the collision integral (3.3) into two contributions. The first, $J_i(\mathbf{q})$, is from the term proportional to $(\psi_i-\psi'_i)$, the deviations from equilibrium in the ^{4}He distribution function. The second, $J_f(\mathbf{q})$, is from the term in $(\phi_f-\phi'_f)$.

4. CALCULATION OF THE COLLISION INTEGRAL $J_i(\mathbf{q})$

We first evaluate $J_i(\mathbf{q})$. This is all that is needed to calculate the diffusion coefficient D. We set $\nabla T=0$ and, using (3.5), $J_i(\mathbf{q})$ becomes

$$J_i(\mathbf{q})=\mathbf{C}\cdot\int[\mathbf{q}a_c(q)-\mathbf{q}'a_c(q')]J(\mathbf{q},\mathbf{q}')d\mathbf{q}', \tag{4.1}$$

where

$$J(\mathbf{q},\mathbf{q}')=\int|a^{34}|^2n_{f0}(1-n'_{f0})\,\delta(\varepsilon+E-\varepsilon'-E')d\mathbf{p} \tag{4.2}$$

and

$$\mathbf{C}=(8\pi^2/h^7)n_{i0}\nabla c. \tag{4.3}$$

To calculate k_T/c, we set $\nabla c=0$ and $J_i(\mathbf{q})$ has the same form as (4.1) except that a_c is replaced by a_T and the vector $\mathbf{C}$ has ∇T instead of ∇c.

In $J(\mathbf{q},\mathbf{q}')$ the energy transfer $E-E'=(q^2-q'^2)/2m_4^*$ and momentum transfer $\mathbf{k}=\mathbf{q}-\mathbf{q}'$ are fixed by $\mathbf{q}$ and $\mathbf{q}'$. Since $|a^{34}|$ in (2.3) is written in terms of $\mathbf{p}_m$, $\mathbf{q}_m$, and $\mathbf{k}$, we transform the integral in (4.2) by replacing $d\mathbf{p}$ by $d\mathbf{p}_m$. We choose an axis along $\mathbf{k}$ and write $d\mathbf{p}_m=p_m^2dp_m d\cos\theta_m d\varphi_m$. The $\varphi_m=0$ plane contains the vector $\mathbf{q}_m$.

The integration with respect to φ_m is elementary and performed first. Using

$$\varepsilon'=\varepsilon=kp_m\cos\theta_m/m_3^* \tag{4.4}$$

in the delta function, we integrate over $\cos\theta_m$:

$$J(\mathbf{q},\mathbf{q}')=2\pi m_3^*/k\int\langle|a^{34}|^2\rangle n_{f0}(s_m-\Delta/2)[1-n_{f0}(s_m+\Delta/2)]p_m dp_m. \tag{4.5}$$

Here $\langle|a^{34}|^2\rangle$ is $|a^{34}|^2$ averaged over all values of φ_m. The Fermi function $n_{f0}(s)$ is $(e^s+1)^{-1}$, and $s_m=\varepsilon_m/k_BT$. The mean energy $\varepsilon_m=(p_m^2+k^2/4-p_F^2)/2m_3^*$ is measured from the Fermi energy. To order T, the Fermi energy is the same as the ^{3}He chemical potential. Note that $\Delta=(E-E')/k_BT$ does not depend on p_m. The integration over the delta function gives $\cos\theta_m$ a definite value that depends on p_m:

$$\cos\theta_m=m_3^*(E-E')/(p_mk). \tag{4.6}$$

Thus, the factors of $p_m\cos\theta_m$ in $\langle|a^{34}|^2\rangle$ are simply functions of $\mathbf{q}$ and $\mathbf{q}'$.

The right-hand side of (4.6) is of the order of q/p or $(T/T_F)^{1/2}$. This means that the momentum transfer $\mathbf{k}$ usually is very nearly perpendicular to $\mathbf{p}$ and $\mathbf{p}_m$. From (4.6), the condition $-1\leqslant\cos\theta_m\leqslant1$ gives the lower limit for p_m in the integral (4.5):

$$p_m\geqslant|m_3^*(E-E')/k|=|(m_3^*/m_4^*)\mathbf{q}_m\cdot\hat{\mathbf{k}}|. \tag{4.7}$$

When $T\ll T_F$, so that q and k are small compared to p_F. Replacing this lower limit by zero has an exponentially small effect on the integral, of order $\exp(-T_F/T)$. Therefore, we evaluate $J(\mathbf{q},\mathbf{q}')$ using the relation

$$\int_{-\infty}^{\infty}n_{f0}(s_m-\Delta/2)[1-n_{f0}(s_m+\Delta/2)]ds_m=\Delta/(1-e^{-\Delta}). \tag{4.8}$$

As in Ref. 4, the replacement of the lower limit (4.7) by zero is the crucial approximation in finding the collision integral. Since the integrand in (4.5) is always positive, by using $p_m\geqslant0$ (or $s_m\geqslant-\infty$) instead of (4.7), we have overestimated the effect of collisions with large k. Because q is small at low T (due to the Boltzmann distribution), large k corresponds to large negative values of Δ, and therefore q' must be large if k is large. The collision rate, which is proportional to (4.8), is very small when $\Delta\ll-1$, so the approximation is self-consistent.

The final result for $J(\mathbf{q},\mathbf{q}')$, to second order in q and q', is

TABLE I. The functions $g_i(x,y)$ and $h_i(x,y)$ in Eq. (4.14), and the integral $\int_x^\infty (x-y)[1-e^{y-x}]g_i(x,y)dy$ for $P_i(x)$ in Eq. (5.4). The Riemann zeta function $\zeta(3)=1.2020\ldots$

	$y\leqslant x$		$y\geqslant x$		
i	$(x/y)^{1/2}g_i(x,y)$	$(x/y)^{1/2}h_i(x,y)$	$g_i(x,y)$	$h_i(x,y)$	$\int_x^\infty (x-y)[1-e^{y-x}]g_i(x,y)dy$
0	1	$y/3x$	1	1/3	$\pi^2/6$
1	$x+y/3$	$-y/3+y^2/15x$	$y+x/3$	$-y/3+x/15$	$2\zeta(3)+2\pi^2x/9$
2	$x+5y/3$	$y+3y^2/5x$	$y+5x/3$	$y+3x/5$	$2\zeta(3)+4\pi^2x/9$
3	$x-y$	$y-y^2/x$	$y-x$	$y-x$	$2\zeta(3)$

$$J(\mathbf{q},\mathbf{q}')=2\pi(m_3^*a_0^{34})^2k_BT\,\frac{\Delta}{k(1-e^{-\Delta})}\left[1+\gamma_1\frac{(\mathbf{q}-\mathbf{q}')^2}{p_F^2}+\gamma_2\frac{(\mathbf{q}+\mathbf{q}')^2}{p_F^2}+\gamma_3\frac{(\mathbf{q}^2-\mathbf{q}'^2)^2}{(\mathbf{q}-\mathbf{q}')^2p_F^2}\right], \tag{4.9}$$

where

$$\gamma_1=2\alpha_5-\alpha_1/2,$$

$$\gamma_2=\alpha_3/2+\alpha_4/4+\alpha_2^2/8,$$

$$\gamma_3=(m_3^*/m_4^*)\alpha_2/2-\alpha_4/4-\alpha_2^2/8. \tag{4.10}$$

As noted in Sec. 2, α_6 does not appear in (4.10); it does not affect DT or k_T/c to order T/T_F.

From symmetry, the vector integral in (4.1) is parallel to $\mathbf{q}$. Therefore, we choose a new axis along $\mathbf{q}$, so that the collision integral (4.1) becomes

$$J_i(\mathbf{q})=\mathbf{C}\cdot\hat{\mathbf{q}}\int[qa_c(q)-q'\cos\theta'a_c(q')]J(\mathbf{q},\mathbf{q}')q'^2dq'd\cos\theta'd\varphi', \tag{4.11}$$

where θ' is the angle between $\mathbf{q}$ and $\mathbf{q}'$.

After integrating over φ' and then $\cos\theta'$, and introducing the dimensionless variables $x\equiv q^2/(2m_4^*k_BT)$, $y\equiv q'^2/(2m_4^*k_BT)$, we obtain

$$J_i(\mathbf{q})=n_{i0}(\mathbf{q}/m_4^*)\cdot(\nabla c)/c\int_0^\infty F(x,y)dy, \tag{4.12}$$

where

$$F(x,y)=F_0(x,y)+(m_4^*/m_3^*)(T/T_F)\sum_{i=1}^{3}\gamma_iF_i(x,y), \tag{4.13}$$

$$F_i(x,y)\equiv(x-y)/(1-e^{y-x})[g_i(x,y)f(x)-h_i(x,y)f(y)];\quad i=0,\ldots,3. \tag{4.14}$$

The function $f(x)$ is a dimensionless form of $a_c(q)=f(x)/cC_1$, where the constant C_1 is

$$C_1=(m_3^*m_4^*k_BTa_0^{34})^2/(2\pi^3\hbar^7). \tag{4.15}$$

The quantities $g_i(x,y)$ and $h_i(x,y)$ are the simple algebraic functions of x and y, shown in Table I.

5. SOLUTION OF THE BOLTZMANN EQUATION

After substituting (4.12) in (3.1) we obtain a dimensionless form of the Boltzmann equation for the case in which $\nabla T=0$,

$$\int_0^\infty F(x,y)dy=1. \tag{5.1}$$

Equation (5.1) is a one-dimensional integral equation for $f(x)=cC_1a_c(q)$.

In the same way the integral equation for the situation where $\nabla c=0$ becomes

$$\int_0^\infty F(x,y)dy=x-3/2-b_3(x). \tag{5.2}$$

In this case, $f(x)=TC_1a_T(q)$. The ''driving'' terms, $x-3/2$ and 1 on the right-hand sides of (5.2) and (5.1) come from the left side of the Boltzmann equation. The additional driving term $b_3(x)$ in (5.2) is the dimensionless form of the collision integral $J_f(\mathbf{q})$. The calculation of $J_f(\mathbf{q})$ and the derivation of $b_3(x)$ are described in Sec. 6.

The numerical solution of the integral equations (5.1) and (5.2) at $T=0$, disregarding the term in $b_3(x)$, is given in Ref. 4. At $T=0$, substitution from (4.13) and (4.14) in (5.1) gives

$$f(x)P_0(x)-\int_0^\infty M_0(x,y)f(y)dy=1, \tag{5.3}$$

where we have defined the functions

$$P_i(x)\equiv\int_0^\infty\frac{x-y}{1-e^{y-x}}g_i(x,y)dy,\qquad M_i(x,y)\equiv\frac{x-y}{1-e^{y-x}}h_i(x,y).\qquad i=0,\ldots,3 \tag{5.4}$$

In Ref. 4, Eq. (5.3) and the similar one for $\nabla c=0$ were solved in terms of the variables t and t' defined by $t=\exp(-x/g)$, $t'=\exp(-y/g)$, where $g\sim3$ is a dimensionless scale factor. The equations were discretized over a one-dimensional lattice of N points evenly spaced in t. As a result, f and P_0 became vectors and M_0 a square matrix. The integral for P_0 from $y=0$ to x was evaluated numerically. The other part, from $y=x$ to infinity, is listed in Table I, with the companion formulas for P_1, P_2, and P_3. Rather than inverting M_0, the equations were more efficiently solved by iteration. An approximate form was used for $f(y)$, giving a new estimate for $f(x)$, and so on. Accurate solutions were obtained with $N=100$ or 200, iterating up to fifteen times.

At all temperatures, the impurity current **i**, and thus the diffusion coefficient D and thermal diffusion ratio k_T/c, are found from the appropriate integration over the ^{4}He occupation number. As explained in Ref. 4, we calculate **i** from the ^{4}He particle current:

$$\mathbf{i}=m_4\int \delta n_i(\mathbf{q}/m_4^*)d\mathbf{q}/h^3. \tag{5.5}$$

In this equation, $\mathbf{q}/m_4^*=\nabla_q E$ is the ^{4}He quasiparticle velocity. Previous authors[2,18] have used $\mathbf{i}=\int \delta n_{\mathbf{i}}\mathbf{q}d\mathbf{q}/h^3$, the momentum density associated with the ^{4}He. The two formulas differ by a factor of m_4/m_4^*. Using (5.5) and (3.2), the expression for D_0 in (1.2) in terms of the function $f(x)$ for $\nabla T=0$ is

$$D_0=16/(3\pi^{3/2})\int_0^\infty f(x)x^{3/2}\mathrm{e}^{-x}dx. \tag{5.6}$$

If the $f(x)$ for $\nabla c=0$ is called $f_T(x)$, then k_T/c is given by

$$k_T/c=\int_0^\infty f_T(x)x^{3/2}\mathrm{e}^{-x}dx \Big/ \int_0^\infty f(x)x^{3/2}\mathrm{e}^{-x}dx. \tag{5.7}$$

To obtain D_0 and k_T/c at finite temperature, we use the fact that $(m_4^*/m_3^*)(T/T_F)$ in (4.13) is a small quantity. Therefore, the solutions to the integral equations (5.1) and (5.2) may be expanded in the form

$$f(x)=f^0(x)+(m_4^*/m_3^*)(T/T_F)f^1(x)+\dots . \tag{5.8}$$

Here $f^0(x)$ is the solution of the integral equation at $T=0$. The term in f^1 gives the finite temperature correction to f^0 to order T/T_F. As a result of (5.8), we may write the F_i in (4.14) as

$$F_i(x,y)=F_i^0(x,y)+(m_4^*/m_3^*)(T/T_F)F_i^1(x,y)+\dots , \tag{5.9}$$

where $F_i^0(x,y)$ means $F_i^0(x,y)=(x-y)/(1-\mathrm{e}^{y-x})\times[g_i(x,y)f^0(x)-h_i(x,y)f^0(y)]$, etc. Substituting in (5.1) and retaining terms up to T/T_F gives the following expression for $\nabla T=0$:

$$\int_0^\infty \left\{F_0^0(x,y)+(m_4^*/m_3^*)(T/T_F)\left[F_0^1(x,y)+\sum_{i=1}^3 \gamma_i F_i^0(x,y)\right]\right\}dy=1. \tag{5.10}$$

The integral equation for the situation where $\nabla c=0$ is the same as (5.10), except that the driving function on the right side is $x-3/2-b_3(x)$.

When the solution for $T=0$ is subtracted from (5.10), the result is

$$\int_0^\infty \left[F_0^1(x,y)+\sum_{i=1}^3 \gamma_i F_i^0(x,y)\right]dy=0. \tag{5.11}$$

From this equation we see that $f^1(x)$ is the sum of three contributions, each linearly proportional to one of the γ_i:

$$f^1(x)=\sum_{i=1}^3 \gamma_i f_i^1(x). \tag{5.12}$$

Using the functions defined in (5.4), the $f_i^1(x)$ are the solutions of the three integral equations

$$f_i^1(x)P_0(x)-\int_0^\infty M_0(x,y)f_i^1(y)dy = -f^0(x)P_i(x)+\int_0^\infty M_i(x,y)f^0(y)dy; \quad i=1,2,3. \tag{5.13}$$

These equations differ from the $T=0$ equation [Eq. (5.3)] only in the driving term on the right side. This is obtained from the $T=0$ solution. We have solved (5.13) numerically by the method used for $T=0$ in Ref. 4. The results are given in Sec. 7.

6. CALCULATION OF THE COLLISION INTEGRAL $J_f(\mathbf{q})$

In this section we evaluate $J_f(\mathbf{q})$, the part of the collision integral produced by the temperature gradient in the solvent ^{3}He and equal to the term proportional to $(\varphi-\varphi')$ in (3.3). $J_f(q)$ is needed to calculate the driving term $-b_3(x)$ on the right side of the ^{4}He Boltzmann equation (5.2):

$$J_f(\mathbf{q})=(2\pi/\hbar)\int |a^{34}|^2 n_{f0}(1-n'_{f0})n_{i0}(\varphi_f-\varphi'_f)\delta(\varepsilon+E-\varepsilon'-E')2d\mathbf{p}d\mathbf{q}'/h^6. \tag{6.1}$$

Using the notation of the review paper by Baym and Pethick,[7] we find $\varphi_f=-\tau\Psi(s)(p\cdot\nabla T)/(m_3^*T)$, where s is the reduced energy ε/k_BT, and ε is measured from the ^{3}He chemical potential. The quantity τ is a characteristic relaxation time, defined more precisely below. The dimensionless function $\Psi(s)$ is odd[7] in s, $\Psi(s)=-\Psi(-s)$. Although it may be calculated exactly from an infinite series,[20,7] it is simpler to use the approximate expression due to Emery and Cheng:[7,21]

$$\Psi(s)=2s/(\pi^2+s^2)+15s\lambda_K/(3-\lambda_K)/(2\pi^2). \tag{6.2}$$

This formula is accurate enough[21] to give the ^{3}He thermal conductivity to about 1%. The pressure-dependent number λ_K in (6.2) is a measure of the angular dependence of the ^{3}He–^{3}He scattering amplitude.[7] For s-wave scattering, λ_K is unity:

$$\lambda_K=\langle W\rangle^{-1}\int d\cos\theta d\varphi W(\theta,\varphi)(1+2\cos\theta)/\cos(\theta/2),$$

$$\langle W\rangle=\int d\cos\theta d\varphi W(\theta,\varphi)/\cos(\theta/2). \tag{6.3}$$

Here $W(\theta,\varphi)$ is the ^{3}He–^{3}He scattering probability at the Fermi surface averaged over spin.[7] The angle θ is between the initial quasiparticle momenta and, because of conservation of momentum, between the final momenta as well. The collision rotates the plane containing the momenta by φ. The characteristic relaxation time τ is determined by the mean scattering probability $\langle W\rangle$:

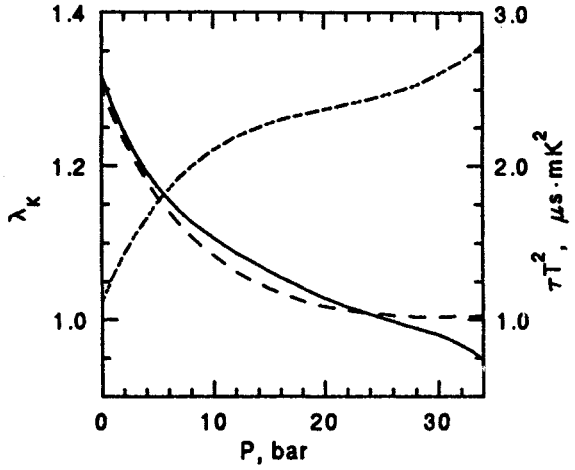

FIG. 1. Plot of the dimensionless factor λ_K and the product τT^2, where τ is the characteristic ^{3}He–^{3}He relaxation time, versus pressure in pure ^{3}He. The dot-dot-dashed curve is λ_K, the solid curve is τT^2 calculated from Greywall's thermal conductivity data and the dashed curve is from the s- and p-wave approximation.

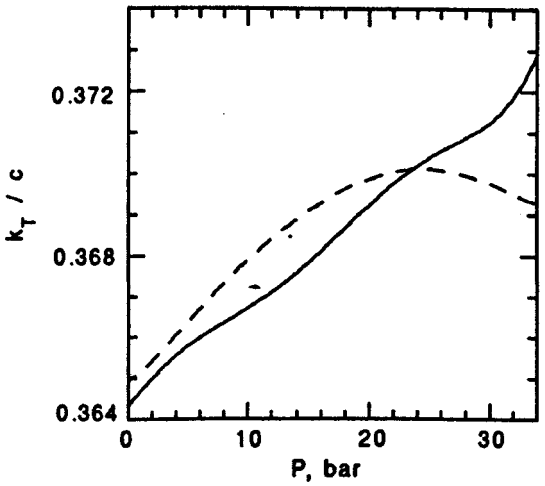

FIG. 2. Plot of the predicted thermal diffusion factor for ^{4}He in liquid ^{3}He, k_T/c, versus pressure as $T \to 0$. The solid curve is calculated using the ^{3}He–^{3}He relaxation time τ from the thermal conductivity data of Greywall, while the less accurate dashed curve uses τ from the s- and p-wave approximation.

$$\tau = \frac{8\pi^4/\hbar^6}{m_3^{*3}\langle W\rangle (k_B T)^2}. \tag{6.4}$$

The s- and p-wave approximation[22] gives λ_K in terms of the Landau parameters. The value of τ can also be found[22] from this model; however, the exact equations (1.2.113a) and (1.2.113c) in Baym and Pethick[7] relate τ to the thermal conductivity and λ_K. Figure 1 shows λ_K and the product τT^2 in the s- and p-wave approximation, as well as τT^2 calculated from Greywall's thermal conductivity data.[23] The τT^2 from the s- and p- wave approximation agrees quite well with the exact formula. The Landau parameters, m_3^*, v_3, and the specific heat, needed in these calculations were taken from the review article by Halperin and Varoquaux.[13]

In integrating (6.1) we neglected the momentum dependence of the ^{4}He–^{3}He scattering amplitude $|a^{34}|$ and replaced it with a_0^{34}. This simplification is justifiable because the effect of $b_3(x)$ on k_T/c turns out to be small, a decrease of about 0.01 or 2.5% of k_T/c. The momentum dependence of a^{34} would produce an effect of the order of T/T_F, which we consider negligible.

To integrate $J_f(\mathbf{q})$, we replace $d\mathbf{p}$ by $d\mathbf{p}_m$ and choose an axis along $\mathbf{k}$ with ∇T in the xz plane. The integral over φ_m is done first and then the integral over $\cos\theta_m$. The delta function causes $\cos\theta_m$ to be replaced by $m_3^*(E-E')/(p_m k)$, as in (4.6). Using the same arguments as in Sec. 4, the lower limit for $s_m = \varepsilon_m/k_B T$ is replaced by $-\infty$. The result is

$$J_f(\mathbf{q}) = (8\pi^2/\hbar h^6)|a_0^{34}|^2 n_{i0}\tau m_3^* \int (\nabla k_B T)\cdot \mathbf{k} n_{f0}(1 - n'_{f0})(\Psi' - \Psi)(E-E')/k^3 ds_m d\mathbf{q}'. \tag{6.5}$$

Defining a new axis along $\mathbf{q}$, and replacing $d\mathbf{q}'$ by $q'^2 dq' d\cos\theta' d\varphi'$, one can integrate over φ' and $\cos\theta'$ analytically. We write the final result in terms of $-b_3(x)$ on the right side of (5.2):

$$b_3(x) = c_3(P)\int_0^\infty \int_{\Delta=0}^{x} n_{f0}(1-n'_{f0})(\Psi' - \Psi)(1 - \Delta/x)^{1/2}(\Delta/x) d\Delta ds_m, \tag{6.6}$$

where

$$c_3(P) \equiv \frac{4\pi}{\hbar}\frac{m_4^*}{m_3^*}\frac{|a_0^{34}|^2}{\langle W\rangle}. \tag{6.7}$$

The ^{4}He–^{3}He scattering amplitude is weak compared to the ^{3}He–^{3}He amplitude. Consequently, $c_3(\mathbf{P})$ is much smaller than one. At zero pressure, $c_3(\mathbf{P}) \approx 0.03$.

To calculate $b_3(x)$, we integrated (6.6) numerically, using the Emery-Cheng $\Psi(s)$. The Emery-Cheng formula (6.2) is the sum of two terms; the first terms, which does not depend on λ_K, and the second term, which is linear in $\lambda_K/(3-\lambda_K)$. Since $f(x)$ in the integral equation (5.2) is linear in the driving terms, the effect of each term was evaluated separately. The results give the correction to the $T=0$ value of k_T/c as

$$(k_T/c)_{T=0} = 0.3823 - c_3(P)[0.1045 + 0.391\lambda_K/(3-\lambda_K)]. \tag{6.8}$$

The result of using (6.7) to calculate k_T/c at $T=0$ as a function of pressure is shown in Fig. 2. The function $c_3(P)$ is uncertain because it contains m_4^* and v_4^*, which are not accurately known, especially at high pressures. Based on an analysis[15] of the data of Nakamura *et al.*, we assumed in Fig. 2 that $m_4^* \approx m_4$. Laheurte's results[24] for v_4^* at $T=0$ were extrapolated above 15 atm.

7. RESULTS AND CONCLUSIONS

The finite temperature correction to $DT$was calculated by solving (5.13) for $f_1^1(x)$, $f_2^1(x)$ and $f_3^1(x)$. The results are shown in Fig. 3b as a function of the reduced ^{4}He momentum $x^{1/2}$. The physically important parts of these functions are in the region where the Maxwell distribution xe^{-x},

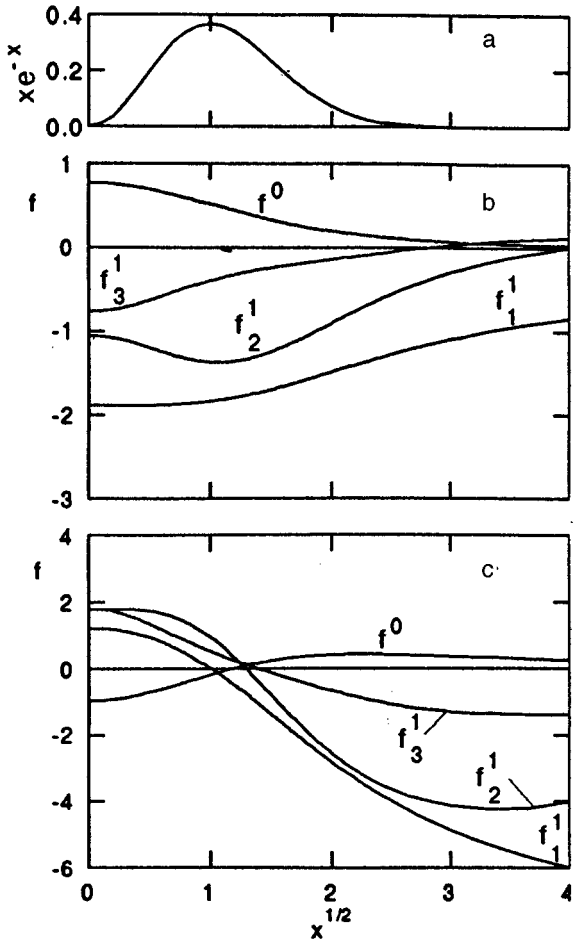

FIG. 3. (a) The equilibrium Maxwell-Boltzmann distribution, xe^{-x}, plotted against the reduced ^{4}He quasiparticle momentum, $x^{1/2}=q/(2m_4^*k_BT)^{1/2}$. (b) The solutions to the integral equations (5.3) and (5.13). The function $f^0(x)$ is the $T=0$ solution of the reduced ^{4}He Boltzmann equation (5.3) for an isothermal concentration gradient. The functions $f_1^1(x)$, $f_2^1(x)$, and $f_3^1(x)$ give the corrections to $f^0(x)$ at finite temperature. (c) The same as (b), but for a temperature gradient at constant concentration.

shown in Fig. 3a, is large. From the $f_i^1(x)$ and (5.6), (5.8), and (5.12), the diffusion coefficient in the Fermi liquid region below 0.1 K is given by

$$DT=(\hbar/m_4^*)T_F(v_3/v_4^*)^2\{0.4461(m_3^*/m_4^*)-(T/T_F)\times[2.127\gamma_1+1.479\gamma_2+0.337\gamma_3]\}, \tag{7.1}$$

where the γ_i are defined in terms of the α_i in (4.10). As noted in Sec. 2, α_2 and α_3 are smaller than 1. The α most likely to be important is α_5, the coefficient of k^2 in $|a^{34}|$. This also has by far the largest coefficient in (7.1): it appears as $2\alpha_5$ in γ_1.

If $|a^{34}|$ is regarded as the Fourier transform of a distance-dependent potential $v(r)$, a plausible length scale in $v(r)$ would be $\sim\hbar/p_F$. This implies an α_5 of ~ 1. Setting $\alpha_5=1$ in (7.1) gives a decrease in DT of about 15% between 0.05 and 0.1 K. Such a small variation would be quite difficult to measure. On the other hand, if the length scale were as large as $2\pi\hbar/p_F$, α_5 would be $4\pi^2$. The T dependence of DT below 0.1 K would then be so large as to require careful measurement in order to extrapolate DT to $T=0$. Moreover, terms higher than T/T_F would probably be appreciable at 0.1 K.

We note that a large positive value of α_5 is plausible because it would indicate that a^{34} increases at large momentum transfer k toward the much larger ^{3}He–^{3}He amplitude. With a positive α_5, DT decreases with temperature toward the measurements of DT by Vvedenski and Peshkov[8] at 0.5 K. They are ~ 5 times smaller than the $T=0$ Fermi liquid predictions.[4]

On the other hand, we may compare a^{34} to the ^{3}He–^{3}He interaction in dilute solutions of ^{3}He in superfluid ^{4}He. The original ''*BBP*'' interaction[25] has the form $V(k)=-V_0\cos(k\delta/\hbar)$ with the length $\delta\approx 3.16$ Å. The quantity V_0 is similar in magnitude to a_0^{34}, although the interactions are opposite in sign; $V_0\approx 60$ K cm^3/mol as compared to $a_0^{34}\approx 30$ K cm^3/mol, both at zero pressure. If a^{34} had the same dependence on k as $V(k)$, expanding the cosine would give $\alpha_5=-(p_F\delta/\hbar)^2/2\approx -3.1$. If α_5 were this negative, the T/T_F term would increase DT by 30% between 0.05 and 0.1 K. Since the measurements of DT by Vvedenski and Peshkov at 0.5 K are smaller than the $T=0$ Fermi liquid predictions, there would be a maximum in DT between 0 and 0.5 K. This effect would be measurable.

Similar conclusions apply to the temperature variation of k_T/c in the Fermi liquid region. The results for $f^0(x)$, $f_1^1(x)$, $f_2^1(x)$, and $f_3^1(x)$, when $\nabla c=0$ are shown in Fig. 3c. When used to calculate k_T/c, the result is

$$k_T/c=(k_T/c)_{T=0}-(m_3^*/m_4^*)(T/T_F)[2.194\gamma_1+1.057\gamma_2-0.055\gamma_3], \tag{7.2}$$

where the value at $T=0$ is given in (6.8) and illustrated in Fig. 2. The numerical coefficients in the T/T_F term were calculated without the $-b_3(x)$ term in the integral equation for $f^0(x)$. This means that they are subject to a small pressure-dependent error of $\sim 2.5\%$.

The dominant effect in the T/T_F term in (7.2) is, again, due to α_5 and γ_1. We expect a decrease in k_T/c with temperature if α_5 is positive. The thermal diffusion ratio has been measured by Dandache and Laheurte[9] between 0.6 to 2 K. This value is well outside the Fermi liquid region but k_T/c is negative, about -10 for $c\sim 2\%$, consistent with a positive α_5 or a maximum in k_T/c between 0 and 0.6 K. Using arguments from irreversible thermodynamics, Dandache and Laheurte have linked the negative k_T/c at high temperatures with the dependence of the thermal conductivity on the ^{4}He concentration.

In summary, solutions of ^{4}He in liquid ^{3}He have a simple relation between the low-temperature limits for the kinetic coefficients D and k_T and the thermodynamic properties v_4^* and m_4^*. The limit for DT and its finite temperature corrections are given in (7.1), while k_T is predicted in (6.8) and (7.2), and shown in Fig. 2. If one can overcome the experimental difficulties in making measurements at sufficiently low temperatures, where the solubility of ^{4}He approaches a few parts per million,[10,15,12,26] these results present a unique opportunity to test Fermi liquid theory.

ACKNOWLEDGMENTS

This work was supported by grants from the US National Science Foundation, DMR 9220400 and DMR 9630930. We are grateful to Prof. W. F. Saam, Dr. S. Mukherjee, Dr. M. S. Pettersen, and Dr. Y. Bazaliy for useful discussions and assistance.

[1] L. D. Landau and E. M. Lifshitz, Fluid Mechanics (Pergamon, London, 1959).
[2] V. N. Zharkov and V. P. Silin, Zh. Éksp. Teor. Fiz. **37**, 143 (1959); [Sov. Phys. JETP **10**, 102 (1960)].
[3] A. J. Leggett and D. ter Haar, Physics Lett. **11**, 129 (1964).
[4] T. G. Culman, D. O. Edwards, and Jizhong He, Phys. Rev. Lett. **74**, 948 (1995).
[5] W. F. Saam, Phys. Rev. A**4**, 1122 (1971).
[6] W. F. Saam and J. P. Laheurte, Phys. Rev. A**4**, 1170 (1971).
[7] See, for example, G. Baym and C. Pethick, Landau Fermi-Liquid Theory (John Wiley and Sons, New York, 1991).
[8] V. L. Vvedenskii and V. P. Peshkov, Pisma Zh. Éksp. Teor. Fiz. **23**, 643 (1976); [JETP Lett. **23**, 589 (1976)].
[9] H. Dandache and J. P. Laheurte, J. de Physique **34**, 635 (1973).
[10] M. Nakamura, Y. Fujii, T. Shigi, and K. Nagao, J. Phys. Soc. Japan **57**, 1676 (1988); M. Nakamura, G. Shirota, T. Shigematsu, K. Nagao, Y. Fujii, M. Yamaguchi, and T. Shigi, Physica B **165 & 166**, 517 (1990).
[11] T. G. Culman, Jizhong He, H. H. Hjort, and D. O. Edwards, Czech. J. of Phys. **46**, Suppl. S1, 105 (1996).
[12] Jizhong He, T. G. Culman, D. O. Edwards, and H. H. Hjort, J. Low Temp. Phys. **101**, 167 (1995).
[13] For current values of the Fermi liquid parameters, see W. P. Halperin and E. Varoquaux, in Helium Three, edited by W. P. Halperin and L. P. Pitaevskii, (North-Holland, Amsterdam 1990) p. 353.
[14] F. Arias de Saavedra, J. Boronat, A. Polls, and A. Fabrocini, Phys. Rev. B **50**, 4248 (1994).
[15] D. O. Edwards, M. S. Pettersen, and T. G. Culman, J. Low Temp. Phys. **89**, 831 (1992).
[16] E. M. Lifshitz and L. P. Pitaevskii, Physical Kinetics (Pergamon, London, 1981).
[17] There is an apparent discrepancy between Refs. 15 and 5 about the result for α_2 found from Galilean invariance. The discrepancy is due to some typographical and other errors in Ref. 5. The most important correction is in Eq. (42) of Ref. 5, which should contain an additional factor of q/p_F on the right. In addition, the expression for δn^l just below Eq. (38) should contain a delta function at the Fermi energy.
[18] H. Dandache, J. P. Laheurte, and M. Papoular, J. de Physique **34**, 643 (1973).
[19] B. T. Geilikman and V. R. Chechetkin, Zh. Éksp. Teor. Fiz. **69**, 1108 (1975); [Sov. Phys. JETP **42**, 564 (1976)].
[20] G. A. Brooker and J. Sykes, Phys. Rev. Lett. **21**, 279 (1968); H. Hojgard Jensen, H. Smith, and J. W. Wilkins, Physics Lett. **27B**, 532 (1968); J. Sykes and G. A. Brooker, Ann. of Phys. **56**, 1 (1970).
[21] V. J. Emery and D. Cheng, Phys. Rev. Lett. **21**, 533 (1968).
[22] P. Bhattacharyya, C. J. Pethick, and H. Smith, Phys. Rev. B**15**, 3367 (1977).
[23] D. S. Greywall, Phys. Rev. B**29**, 4933 (1984).
[24] J. P. Laheurte, J. Low Temp. Phys. **12**, 127 (1973).
[25] J. Bardeen, G. Baym, and D. Pines, Phys. Rev. **156**, 207 (1967).
[26] M. S. Pettersen, D. O. Edwards, and T. G. Culman, J. Low Temp. Phys. **89**, 473 (1992).

This article was published in English in the original Russian journal. It was edited by S. J. Amoretty.

Diffusion in liquid and solid solutions ^{3}He–^{4}He

I. N. Adamenko, A. V. Zhukov, and K. È. Nemchenko

*Kharkov State University, 310077 Kharkov, Ukraine**

T. F. George

*Office of the Chancellor, Department of Chemistry and Physics and Astronomy, University of Wisconsin–Stevens Point, Stevens Point, Wisconsin, 54481-3897, USA***

(Submitted November 15, 1996)
Fiz. Nizk. Temp. **23**, 574–585 (May–June 1997)

An exact expression for diffusion time, which depends on the interaction rates for particles of not only different, but also of the same species, has been derived from the system of kinetic equations. The result is valid for particles with arbitrary statistics and energy–momentum relations. The derived general relations are valid for investigating diffusion in liquid and solid ^{3}He–^{4}He mixtures. The contribution of interaction between quasiparticles of the same type to the diffusion coefficient and effective thermal conductivity of superfluid solutions is analyzed. The calculated values are compared with experimental data. The calculated diffusion coefficient of ^{3}He–^{4}He solid solutions differs from the previous theoretical results. A comparison of the obtained diffusion coefficient with experimental data makes it possible to determine the numerical value of the energy band width for impurity quasiparticles. © *1997 American Institute of Physics.* [S1063-777X(97)01005-0]

INTRODUCTION

The determination of diffusion coefficient is a traditional problem for mixture of classical gases and condensed media for which the quasiparticle description is applicable. In order to calculate the diffusion coefficient, we must solve the system of kinetic equations by using various approximations in view of the complexity of this system. As a result, the diffusion coefficient is usually a function of the time of interaction between particles of different species only and does not contain the equilibrium stabilization time in the solution components. The method developed here makes it possible to obtain a compact exact solution for the problem formulated above. The expressions for diffusion coefficient obtained by us depend on the time of interaction between particles of the same and different species. The inclusion of the latter particles affects significantly the value of diffusion coefficient in some cases. The obtained general expression is valid for particles with an arbitrary statistics and energy–momentum relation. This allows us to use the obtained results for mixtures of classical gases as well as for quantum-mechanical quasiparticle systems.

In this research, the general relations are used for an analysis of diffusion in liquid and solid solutions of helium isotopes. The theory of quantum diffusion in crystals was constructed by Andreev and Lifshits.[1] Quantum diffusion in ^{3}He–^{4}He solid solutions was observed for the first time by Esel'son *et al.*[2–4]

1. SOLUTION OF KINETIC EQUATIONS

Let us consider a stationary nonequilibrium state of two components α and β of a gas mixture in which the number densities of quasiparticles are functions of the coordinate z. For example, for a gas of thermal excitations whose chemical potential is zero, this situation is realized by creating a constant temperature gradient.

In the state under investigation, the existing steady-state gradients of partial pressures of the components lead to quasiparticle fluxes

$$\mathbf{j}_k = -\sum_{l=\alpha,\beta} \frac{\rho_k}{\rho} d_{kl} \nabla P_l, (k=\alpha,\beta), \tag{1}$$

where

$$\mathbf{j}_k = \int \mathbf{p}_k f_k d\Gamma_k \tag{2}$$

is the flux density for the kth component of the mixture,

$$P_l = \frac{1}{3} \int \mathbf{p}_l \cdot \mathbf{v}_l f_l d\Gamma_l \tag{3}$$

the partial pressure of quasiparticles,

$$\rho_k = -\frac{1}{3} \int \mathbf{p}_k^2 f_k' d\Gamma_k \tag{4}$$

the density of the kth component, $\rho = \rho_\alpha + \rho_\beta$, $f_k' = \partial f_k / \partial \varepsilon_k$ is the derivative of the energy distribution function, $d\Gamma_k$ the element of the phase volume, and $\mathbf{v}_l = \partial \varepsilon_l / \partial \mathbf{p}_l$ the velocity of quasiparticles of the l species. In the steady state, the sum $P_\alpha + P_\beta$ of the partial pressures is assumed to be constant. It should be noted that expressions (3) and (4) are universal for a gas of thermal excitations as well as for quasiparticles with a nonzero chemical potential. For quasiparticles with arbitrary energy–momentum relations and chemical potentials, formulas (3) and (4) lead to the generally accepted relations.

A relation between the matrix of diffusion times d_{kl} and diffusion coefficients D can be derived by comparing for-

mula (1) with definitions of diffusion coefficients. These definitions are different for different physical systems and will be considered below for various cases.

The diffusion coefficient for all existing physical systems can be written in the form

$$D = u_D^2 \tau_D, \tag{5}$$

where u_D is the characteristic velocity whose analytic expression is determined by the energy–momentum relation for particles in the mixture and by their statistics, and τ_D is the characteristic diffusion time. It will be shown below that the latter quantity can be written in the general form for gases with arbitrary statistics, energy-momentum relations, and chemical potentials.

According to formulas (1) and (2), the expression for a diffusion coefficient can be obtained from the solution of the system of kinetic equations, which can be written for a stationary state in the form

$$\mathbf{v}_k \frac{\partial f_k}{\partial \mathbf{r}} = \sum_{l=\alpha,\beta} J_{kl}(f_k, f_l), \tag{6}$$

where $J_{kl}(f_k, f_l)$ is the collision integral, which is a functional of the distribution function.

For definiteness, we consider below the diffusion in a system with a conserved number of particles. A generalization to the case of excitations will be made at the end of this section.

We seek the solution of system (6) in the form

$$f_k = f_{0k} + \delta f_k, \tag{7}$$

where f_{0k} is the locally equilibrium distribution function for the kth component whose chemical potential μ_k is a function of the coordinate z, and δf_k is a small correction which can be represented in the form

$$\delta f_k = -f'_{0k} g_k. \tag{8}$$

Linearizing the system of equations (6), we obtain the following system of linear integral equations in the sought quantities g_k:

$$\mathbf{v}_k \frac{\nabla P_k}{n_k} = J_{kk} g_k + J_{kl}(g_k + g_l),$$

$$k,l = \alpha,\beta; \quad k \neq l. \tag{9}$$

Here n_k is the number density of particles of the kth species and J_{kl} are the linearized collision operators for particles of the same component ($k=l$) and of different components ($k \neq l$). The action of these operators on the arbitrary function of momentum $\psi(\mathbf{p}_{k,l})$ is determined by the form of the collision integral. For a binary collision integral with the transition probability density $w_{kl}(\mathbf{p}_k, \mathbf{p}_l | \mathbf{p}'_k, \mathbf{p}'_l)$, for $k \neq l$ we have

$$J_{kl}\psi(\mathbf{p}_{k,l}) = \int w_{kl}(\mathbf{p}_k, \mathbf{p}_l | \mathbf{p}'_k, \mathbf{p}') f_{0l}(\mathbf{p}_l) \times \{1 \pm f_{0k}(\mathbf{p}_k)\}^{-1} \{1 \pm f_{0k}(\mathbf{p}'_k)\} \{1 \pm f_{0l}(\mathbf{p}'_l)\} \times \{\psi(\mathbf{p}'_{k,l}) - \psi(\mathbf{p}_{k,l})\} d\Gamma_l d\Gamma'_k d\Gamma'_l;$$

for $k=l$, we have

$$J_{kk}\psi(\mathbf{p}_k) = \int w_{kk}(\mathbf{p}_k, \mathbf{p} | \mathbf{p}'_k, \mathbf{p}') f_{0k}(\mathbf{p}) \{1 \pm f_{0k}(\mathbf{p}_k)\}^{-1} \times \{1 \pm f_{0k}(\mathbf{p}'_k)\} \{1 \pm f_{0k}(\mathbf{p}')\} \{\psi(\mathbf{p}'_k) + \psi(\mathbf{p}') - \psi(\mathbf{p}_k) - \psi(\mathbf{p})\} d\Gamma d\Gamma'_k d\Gamma'.$$

The plus and minus signs correspond to bosons and fermions, respectively. According to (3), the partial pressure gradient for quasiparticles with a nonzero chemical potential is given by

$$\nabla P_k = n_k \nabla \mu_k|_{T,\mu_l}. \tag{10}$$

It is convenient to write system (9) in a compact matrix form

$$\sum_{k=\alpha,\beta} |\varphi_k\rangle \frac{\partial P_k}{\partial z} = \hat{J}|g\rangle, \tag{11}$$

where

$$|\varphi_\alpha\rangle = \begin{vmatrix} v_{\alpha z} n_\alpha^{-1} \\ 0 \end{vmatrix}\rangle; \quad |\varphi_\beta\rangle = \begin{vmatrix} 0 \\ v_{\beta z} n_\beta^{-1} \end{vmatrix}\rangle;$$

$$g = \begin{vmatrix} g_1 \\ g_2 \end{vmatrix}\rangle. \tag{12}$$

are two-dimensional ket vectors, and

$$\hat{J} = \hat{S} + \hat{I} \tag{13}$$

is the operator matrix which can be conveniently presented as the sum of the matrix

$$\hat{S} = \begin{pmatrix} J_{\alpha\alpha} & 0 \\ 0 & J_{\beta\beta} \end{pmatrix} \tag{14}$$

of collision operators for particles of the same type and the matrix

$$\hat{I} = \begin{pmatrix} J_{\alpha\beta} & J_{\alpha\beta} \\ J_{\beta\alpha} & J_{\beta\alpha} \end{pmatrix}. \tag{15}$$

of collision operators for particles of different types.

The scalar product of arbitrary two-dimensional bra vector $\langle\psi| = \langle\psi_\alpha(\mathbf{p}_\alpha); \psi_\beta(\mathbf{p}_\beta)|$ and ket vectors $|\chi\rangle$ is defined as

$$\langle\psi|\chi\rangle = \sum_{k=\alpha,\beta} {}_1\langle\psi_k|\chi_k\rangle_1 = -\sum_{k=\alpha,\beta} \int \psi_k^* \chi_k f'_{0k} d\Gamma_k, \tag{16}$$

where the subscript ''1'' on the vector indicates that it has only one component.

System (11) is a system of nonhomogeneous linear integral equations. The sought solution $|g\rangle$ must be orthogonal to the solution of the system of corresponding homogeneous equations:

$$\hat{J}|\varphi_1\rangle = 0. \tag{17}$$

The solution of system (17) normalized to unity can be written in the form

$$|\varphi_1\rangle = \frac{1}{\sqrt{\rho}} \begin{vmatrix} p_{\alpha z} \\ p_{\beta z} \end{vmatrix}\rangle. \tag{18}$$

The vector $|\varphi_1\rangle$ corresponds to the momentum of a two-component system of quasiparticles. The physical meaning of solution (18) boils down to conservation of the total momentum of the two-component system of colliding quasiparticles. It should be noted that the role of a solution of Eq. (17) can be played by other vectors corresponding to laws of conservation: of the number of quasiparticles (with a nonzero chemical potential), of energy, and of the x- and y-components of the momentum. However, these vectors can be disregarded since, according to (11), the sought solution $|g\rangle$ contains only the z-components of the vector **p**.

It is convenient to write the formal solution of system (11) so that the orthogonality condition

$$\langle g|\varphi_1\rangle = 0 \tag{19}$$

be contained in the expression of the solution. For this purpose, we introduce the projector operator $\mathscr{P}_n$ to the subspace orthogonal to the vector $|\varphi_1\rangle$:

$$\mathscr{P}_n = 1 - \mathscr{P}_c, \quad \text{where} \quad \mathscr{P}_c = |\varphi_1\rangle\langle\varphi_1|. \tag{20}$$

Then the formal solution of Eq. (11) can be written in the form

$$|g\rangle = \mathscr{P}_n(\hat{J}^{-1})\mathscr{P}_n \sum_{k=\alpha,\beta} |\varphi_k\rangle \frac{\partial P_k}{\partial z}. \tag{21}$$

Substituting solution (21) into expression (2) for flux density, taking into account relations (7) and (8), and comparing the obtained result with definition (1), we obtain the following expression for the diffusion time matrix:

$$d_{\alpha\alpha} = \frac{\rho_\beta}{\rho_\alpha}\tau_D; \quad d_{\alpha\beta} = d_{\beta\alpha} = -\tau_D; \quad d_{\beta\beta} = \frac{\rho_\alpha}{\rho_\beta}\tau_D, \tag{22}$$

where

$$\tau_D = -\langle\varphi_2|\hat{J}^{-1}|\varphi_2\rangle \tag{23}$$

is the characteristic diffusion time and

$$|\varphi_2\rangle = \frac{1}{\sqrt{\rho\rho_\alpha\rho_\beta}} \begin{vmatrix} \rho_\beta & p_{\alpha z} \\ -\rho_\alpha & p_{\beta z} \end{vmatrix} \tag{24}$$

the diffusion vector orthogonal to the vector $|\varphi_1\rangle$.

For the sake of definiteness, all calculations were made for quasiparticles with a nonzero chemical potential μ. Similar calculations for the diffusion component of flux (1) for quasiparticles with an arbitrary chemical potential ($\mu = 0$ or $\mu \neq 0$) give the same results (22)–(24). Thus, formulas (1) and (22)–(24) for the diffusion component of flux are valid for quasiparticles with any statistics and any chemical potential.

2. EXACT AND LIMITING EXPRESSIONS FOR DIFFUSION TIME

In order to obtain an exact expression for the matrix element (23), we introduce the complete system of orthonormal two-dimensional vectors $|\varphi_n\rangle$ (here $n = 1,2,3,\ldots$). We take (18) as the first vector and (24) as the second vector. The remaining vectors can be constructed by using the standard procedure (see, for example, Ref. 5) taking into account the definition (16) of scalar product. In the complete system of vectors constructed in this way, the exact solution for

$$\tau_D = -\left\{ \begin{matrix} & -1 \\ (\hat{I}+\hat{S}) & \end{matrix} \right\}_{22} \tag{25}$$

can be reduced to the form

$$\tau_D = -\left\{ I_{22} - \sum_{n,n'=3}^{\infty} I_{2n}(\{\widetilde{I}+\widetilde{S}\}^{-1})_{nn'} I_{n'2} \right\}^{-1}. \tag{26}$$

Here the square matrices $\widetilde{I}$ and $\widetilde{S}$ contain the matrix elements

$$(\widetilde{I})_{nn'} = I_{nn'}; \quad (\widetilde{S})_{nn'} = S_{nn'}, \tag{27}$$

where

$$I_{nn'} = \langle\varphi_n|\hat{I}|\varphi_{n'}\rangle; \quad S_{nn'} = \langle\varphi_n|\hat{S}|\varphi_{n'}\rangle. \tag{28}$$

While deriving expression (26), we took into account relation (17).

Matrices (27) are infinite-dimensional and nondiagonal. Consequently, the exact solution (26) does not lead to an explicit analytic expression for τ_D. However, solution (26) makes it possible to analyze various limiting cases, to find the minimum ($\tau_{D\,\min}$) and maximum ($\tau_{D\,\max}$) values of τ_D, to obtain correct interpolation formulas, and to carry out computer calculations for specific physical problems.

For example, in the case of rapid stabilization of equilibrium between particles of the same species, when the inequalities

$$S_{nn'} \gg I_{nn'}, \tag{29}$$

are satisfied, from relation (26) we obtain

$$\tau_D \equiv \tau_{D\,\min} = -\frac{1}{I_{22}} = [\,\tau_{\alpha\beta}^{(0)^{-1}} + \tau_{\beta\alpha}^{(0)^{-1}}\,]^{-1}, \tag{30}$$

where

$$\tau_{kl}^{(0)} = -\langle J_{kl}\rangle_k^{-1}; \quad k,l = \alpha,\beta; \quad k \neq l. \tag{31}$$

Here and below, the normalized mean value of an arbitrary operator R is denoted by

$$\langle R\rangle_k = \frac{1}{\rho_k}\,{}_1\langle p_{kz}|R|p_{kz}\rangle_1; \quad k = \alpha,\beta.$$

According to the momentum conservation law, for collisions we can write

$$\tau_{\alpha\beta}^{(0)^{-1}} = \frac{\rho_\beta}{\rho_\alpha}\tau_{\beta\alpha}^{(0)^{-1}}. \tag{32}$$

Proceeding from the fact that the operators $\hat{S}$ and $\hat{I}$ are hermitian and negative definite, we can prove that

$$\tau_D \geqslant \tau_{D\,\min}. \tag{33}$$

In the opposite limiting case of slow stabilization of equilibrium between particles of the same species ($S_{nn'} \to 0$), τ_D attains its maximum value

$$\tau_{D\,\max} = \langle\varphi_2|\hat{I}^{-1}|\varphi_2\rangle. \tag{34}$$

In the case when the number density of the α component is relatively low ($\rho_\alpha \ll \rho_\beta$) and the time of interaction between particles α is large ($J_{\alpha\alpha} \to 0$), we obtain from (26)

$$\tau_D|_{0,\infty} = \tau_{\alpha\beta}^{(\infty)}, \tag{35}$$

where

$$\tau_{\alpha\beta}^{(\infty)} = -\langle J_{\alpha\beta}^{-1} \rangle_\alpha . \tag{36}$$

It should be noted that we average frequency in (31) and time in (36). According to the Cauchy–Buniakowski inequality, the time defined by (31) is always smaller than the time defined by (36) for any momentum dependence of $J_{\alpha,\beta}$. In the case when $J_{\alpha,\beta}$ does not depend on the momentum $\mathbf{p}_\alpha$, $\tau_{\alpha\beta}^{(\infty)} = \tau_{\alpha\beta}^{(0)}$, while $\tau_D = \tau_{D\,\min}$. If, however, the operator $J_{\alpha,\beta}$ depends on $\mathbf{p}_\alpha$, the stabilization of equilibrium between particles of different species depends on the rate of equilibrium stabilization between particles of the same species. In this case, the situation is similar to that in a phonon–impuriton system of superfluid solutions of helium isotopes[6] and in phonon systems of solids.[7]

In these systems, a two-stage mechanism of relaxation between particles of different species operates. At the first stage, particles β mainly interact only with those particles α for whose momenta the operator $J_{\alpha\beta}$ assumes the maximum value. At the second stage, the stabilization of equilibrium in the mixture is determined by the interaction between particles α. This is due to the fact that it is more advantageous for particles α for which the value of $J_{\alpha\beta}$ is minimal to interact not with particles β, but with those particles α which are already in equilibrium with the β-component.

As a rule, the calculation of $\tau_{\alpha\beta}^{(0)-1}$ does not involve any difficulties. As regards the evaluation of $\tau_{\alpha\beta}^{(\infty)}$, we must determine the operator inverse to the integral operator $J_{\alpha\beta}$, which can be done only by using certain approximations. For example, in the case of a Lorentz gas,[8] when particles β are stationary, and the scattering of particles α is elastic, the action of the operator $J_{\alpha\beta}$ is reduced to the multiplication by the expression

$$J_{\alpha\beta} = -|\mathbf{v}_\alpha| \sigma_t n_\beta , \tag{37}$$

where σ_t is the transport cross section of scattering of a particle α by a particle β. Approximation (37) makes subsequent calculations trivial.

3. RELAXATION TIME APPROXIMATION

The exact expression (26) makes it possible to propose a model form of the operator $\hat{J}$ leading to an interpolation formula for the diffusion time (23), which contains the results for all of the known limiting cases.

For the collision integral J_{kk} for particles of the same species, we propose the following model of a correct τ-approximation, taking into account the momentum dependence of the interaction time $t_{kk} = t_{kk}(\mathbf{p}_k)$ between the particles of type k:

$$J_{kk} = -t_{kk}^{-1} + t_{kk}^{-1} \rho_k^{-1/2} |p_{kz}\rangle_1 \tau_{kk}^{(0)}{}_1 \langle p_{kz}| \rho_k^{-1/2} t_{kk}^{-1}, \tag{38}$$

where

$$\tau_{kk}^{(0)^{-1}} = \langle t_{kk}^{-1} \rangle_k . \tag{39}$$

The correctness of the τ-approximation (38) ensures the fulfillment of the momentum conservation law in collisions, according to which

$$J_{kk}|p_{kz}\rangle_1 = 0.$$

Relation (38) contains only the z-component of the momentum since, according to (11), the sought solution $|g\rangle$ contains only the z-component of the vector $\mathbf{p}$.

The diagonal elements in matrix (15) can be replaced by the corresponding frequencies of collisions of particles k with particles l:

$$J_{kl} = -t_{kl}^{-1}(p_k); \quad k,l = \alpha,\beta; \quad k \neq l. \tag{40}$$

The functions $t_{kk}^{-1}(p_k)$ and $t_{kl}^{-1}(p_k)$ are defined by the operators J_{kk} and J_{kl}, respectively. The following definition of collision frequency for $k \neq l$ and $k = l$ is most convenient:

$$t_{kl}^{-1}(p_k) = \frac{\nu_{kl}(p_k)}{\langle \nu_{kl} \rangle_k} \tau_{kl}^{(0)^{-1}}, \tag{41}$$

where $\nu_{kl}(p_k)$ is the transport collision frequency which can be written in the standard way by using the collision integral. For example, for a binary collision we have

$$\nu_{kl}(p_k) = \int \left(1 - \frac{\mathbf{p}_k \cdot \mathbf{p}_k'}{p_k p_k'}\right) w_{kl} f_{0l}(\mathbf{p}_l)[1 \pm f_{0k}(\mathbf{p}_k)]^{-1}[1 \pm f_{0k}(\mathbf{p}_k')][1 \pm f_{0l}(\mathbf{p}_l')] d\Gamma_k' d\Gamma_l d\Gamma_l' . \tag{42}$$

It should be noted that the relaxation time approximation describes all the limiting cases (30), (34), (35), and (37) following from the general solution (26) only with such a choice of collision frequency (41).

The nondiagonal operators of matrix (15) acting on the functions of momenta of particles of the same species give functions of momenta of particles of the other type. In contrast to relation (40), this does not allow us to replace the nondiagonal operators of matrix (15) by multiplication operators.

We propose here the following model expression for nondiagonal collision operators:

$$J_{kl} = t_{kl}^{-1}(p_k)|p_{kz}\rangle_1 \rho_k^{-1} \tau_{kl}^{(0)}{}_1 \langle p_{lz}| t_{lk}^{-1}(p_l). \tag{43}$$

Relations (40) and (43) for the operator matrix (15) give

$$\hat{I} = \begin{pmatrix} -t_{\alpha\beta}^{-1} & t_{\alpha\beta}^{-1}|p_{\alpha z}\rangle_1 \rho_\alpha^{-1} \tau_{\alpha\beta 1}^{(0)} \langle p_{\beta z}| t_{\beta\alpha}^{-1} \\ t_{\beta\alpha}^{-1}|p_{\beta z 1} \rho_\beta^{-1} \tau_{\beta\alpha 1}^{(0)} \langle p_{\alpha z}| t_{\alpha\beta}^{-1} & -t_{\beta\alpha}^{-1} \end{pmatrix}. \tag{44}$$

It should be noted that expressions (38) and (44) for the operator matrix (13) satisfy the total momentum conservation law (17) for collisions of particles in the mixture.

The model expressions (38) and (44) for the operator matrix (13) allow us to obtain the diffusion time τ_D as a function of the times of interaction between quasiparticles in the mixture proceeding from definition (23). Carrying out calculations similar to those presented in Ref. 9, we obtain

$$\tau_D = \tau_{D\,\min} + \frac{\rho_\beta}{\rho}(\tau_{\alpha\beta} - \tau_{\alpha\beta}^{(0)}) + \frac{\rho_\alpha}{\rho}(\tau_{\beta\alpha} - \tau_{\beta\alpha}^{(0)}), \tag{45}$$

where

$$\tau_{kl}=\langle R_k\rangle_k+\langle R_k t_{kk}^{-1}\rangle_k^2\langle R_k t_{kk}^{-1}t_{kl}^{-1}\rangle_k^{-1};$$

$$R_k=(t_{kk}^{-1}+t_{kl}^{-1})^{-1}. \tag{46}$$

In contrast to $\tau_{kl}^{(0)}$, the time τ_{kl} depends on the frequency t_{kk}^{-1} of interaction between particles of type k. According to (45), such a dependence can only increase the diffusion time τ_D. This becomes obvious if we write relation (46) in the form

$$\tau_{kl}=\tau_{kl}^{(0)}+\langle(1-\tau_{kl}^{(0)}t_{kl}^{-1})^2R_k\rangle_k$$
$$+\langle(1-\tau_{kl}^{(0)}t_{kl}^{-1})R_k t_{kk}^{-1}\rangle_k^2\langle R_k t_{kk}^{-1}t_{kl}^{-1}\rangle_k^{-1}. \tag{47}$$

Expression (45) leads to all the limiting cases (30), (34) and (35) considered above. If the time $t_{\alpha\beta}$ is independent of momentum, relation (45), as well as (26), gives $\tau_D=\tau_{D\,\min}$.

In the limit of low density of one of the components (e.g., $\rho_\alpha\ll\rho_\beta$), formula (45) leads to the following expression corresponding to the approximation used in Ref. 7:

$$\tau_D=\langle R_\alpha\rangle_\alpha+\langle R_\alpha t_{\alpha\alpha}^{-1}\rangle_\alpha^2\langle R_\alpha t_{\alpha\alpha}^{-1}t_{\alpha\beta}^{-1}\rangle_\alpha^{-1}. \tag{48}$$

If $t_{\alpha\alpha}$ is independent of momentum, and $\tau_{\beta\beta}\to 0$, formula (45) leads to the result obtained in Ref. 6:

$$\tau_D=\frac{\langle R_\alpha\rangle_\alpha}{\langle R_\alpha t_{\alpha\beta}^{-1}\rangle_\alpha}. \tag{49}$$

Thus, formula (45) generalizes the result obtained in Refs. 6 and 7 and leads to the expression following from the exact solution (26) in all the limiting cases.

4. DIFFUSION AND EFFECTIVE THERMAL CONDUCTIVITY OF SUPERFLUID SOLUTIONS ^{3}He–^{4}He

According to the Landau–Pomeranchuk theory,[10] the kinetic properties of superfluid solutions ^{3}He–^{4}He are determined by a three-component gas of weakly interacting quasiparticles: phonons, rotons (thermal excitations), and impuritons (^{3}He quasiparticles in the solution).

Khalatnikov and Zharkov[11] formulated the fundamentals of the theory of solutions in 1957. At the time when the theory[11] was constructed, the required set of experimental data on superfluid solutions ^{3}He–^{4}He had not been accumulated, and some of the results available at that time proved to be incorrect. For example, the first results on the effective mass of a roton and the assumption concerning the nondecay nature of the phonon spectrum of solutions were erroneous. For this reason, the theory[11] did not provide, for example, the time of three-particle phonon processes ensuring rapid longitudinal relaxation in the phonon system, and the diffusion coefficient for a solution was determined in the Lorentz gas approximation (37). In this case, rotons were regarded as stationary particles. However, subsequent experiments devoted to an analysis of the roton spectrum[12] proved that the average thermal velocity of rotons is even higher than the thermal velocity of impuritons. For this reason, the agreement between the theoretical and experimental values in the first theory[11] constructed in analogy with the kinetics of rarefied gases was attained by introducing a number of fitting parameters. It should be emphasized that the basic concepts of the theory[11] and a number of its results remain valid even today. They formed the basis of subsequent theoretical publications.

For example, Baym and Ebner[13] developed a kinetic theory of ^{3}He–^{4}He solutions in the low temperature region, in which the roton contribution can be neglected. This theory did not take into account the interaction between phonons, and its results described experimental data only for concentrated solutions.

Subsequent experimental and theoretical investigations[6,14–16] made it possible to describe kinetic phenomena in the phonon–impuriton system of superfluid ^{3}He–^{4}He solutions to a high degree of accuracy. The kinetic theory of solutions was developed further in Refs. 9 and 17, where relaxation processes in a three-component gas of quasiparticles (phonons, rotons, and impuritons) were investigated.

In this section, we shall derive expressions for diffusion coefficients and effective thermal conductivity of superfluid ^{3}He–^{4}He solutions proceeding from the general relations (1), (22) and (45), compare the theoretical values with those observed in the entire experimental temperature range, and analyze the contributions from interaction of quasiparticles of the same type to the diffusion coefficients of superfluid ^{3}He–^{4}He solutions.

For further analysis, it is convenient to single out three temperature regions in which the physical processes determining diffusion in the solution are different. In the low-temperature region ($T<0.6$ K), in which the contribution of rotons can be neglected, the thermal conductivity of solutions is determined by diffusion in the phonon–impuriton system. According to the results obtained in Ref. 1, the effective thermal conductivity in this temperature range is given by

$$\kappa_{\rm eff}=D_{\rm iph}\left(S_{\rm ph}\frac{\rho_{\rm ph}+\rho_{\rm i}}{\rho_{\rm ph}}\right)^2\frac{1}{n_{\rm i}}+\kappa_{\rm i}. \tag{50}$$

Here $D_{\rm iph}$ is the diffusion coefficient of impuritons in the phonon gas, $S_{\rm ph}$ the entropy of the phonon gas, $\rho_{\rm ph}$ and $\rho_{\rm i}$ are the densities of the phonon and impuriton gases defined by (4), $n_{\rm i}$ the number density of ^{3}He atoms in the solution, and $\kappa_{\rm i}$ the thermal conductivity of the impuriton gas. The expression for $D_{\rm iph}$ follows from relations (1) and (22), and the definition of the diffusion coefficient for a superfluid solution (see, for example, Refs. 18 and 19):

$$D_{i\rm ph}=\frac{2}{3}\frac{1}{m_i}\frac{{}_1\langle\varepsilon_i|1\rangle_1}{{}_1\langle 1|1\rangle_1}\frac{\rho_{\rm ph}}{\rho_{\rm ph}+\rho_i}\,\tau_D^{({\rm ph}i)}, \tag{51}$$

where $\varepsilon_i=p_i^2/2m_i$ is the kinetic energy of an impuriton, and $\tau_D^{({\rm ph}i)}$ is defined by formula (45) in which the subscripts α and β must be replaced by the subscripts ''i'' (impuriton) and ''ph'' (phonon). For nondegenerate solutions, we have

$$\frac{2}{3}\frac{{}_1\langle\varepsilon_i|1\rangle_1}{{}_1\langle 1|1\rangle_1}=T.$$

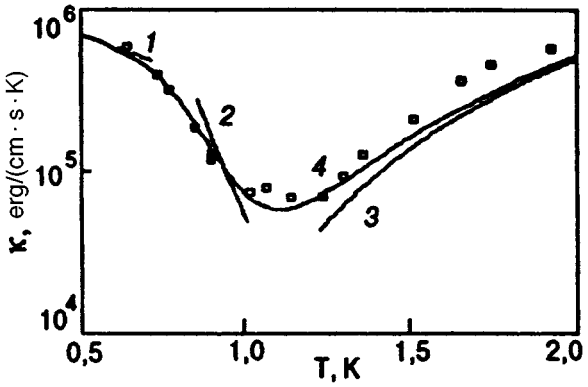

FIG. 1. Temperature dependence of the effective thermal conductivity of a solution with the concentration $x=1.39\cdot10^{-4}$. The contributions to the effective thermal conductivity from diffusion in the impuriton–phonon (curve *1*), roton–phonon (curve *2*), and impuriton–roton (curve *3*) systems. Curve *4* corresponds to the effective thermal conductivity values calculated by taking into account contributions from all quasiparticles; experimental data obtained in Ref. 22 are presented by □.

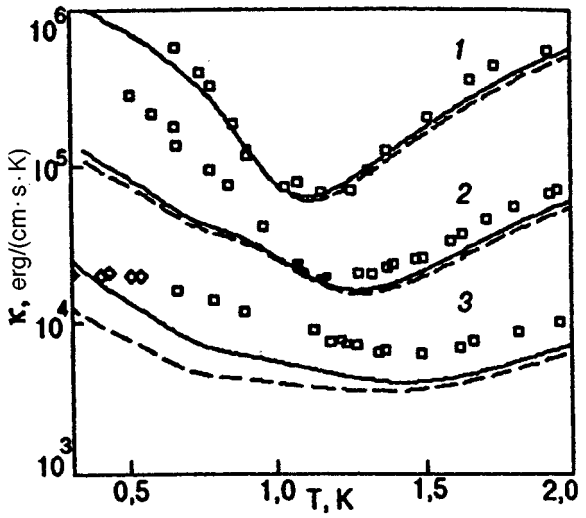

FIG. 2. Temperature dependence of the effective thermal conductivity of a solution with different concentrations $x=1.39\cdot10^{-4}$ (curve *1*), $1.32\cdot10^{-3}$ (curve *2*), and $1.36\cdot10^{-2}$ (curve *3*). The results of calculations taking into account the contributions from all types of quasiparticles are depicted by solid and dashed curves. The latter correspond to calculations in the instantaneous relaxation approximation in the solution components; experimental results obtained in Refs. 22 and 23 are presented by □ and ◇.

Let us consider the relation between the times appearing in (45). According to Refs. 13 and 20, the phonon–impuriton interaction time is defined as

$$t_{\mathrm{ph}i}=13.6n_4/cxp_{\mathrm{ph}}^4, \tag{52}$$

where $x=n_{\mathrm{i}}/(n_{\mathrm{i}}+n_4)$ is the solution concentration, and c and p_{ph} are the velocity and momentum of a phonon, respectively. A noticeable dependence of time (52) on the phonon momentum necessitates the inclusion of the time of interaction between quasiparticles of the same type. The impuriton–impuriton interaction time $t_{\mathrm{ii}}\sim x^{-1}$ and is much smaller than $\tau_{D\min}^{(i\,\mathrm{ph})}$.[21] For this reason, relaxation in the impuriton system can be regarded as instantaneous, and the second term in expression (45) can be omitted. The decay phonon spectrum permits three-particle phonon processes, ensuring relatively rapid stabilization of equilibrium for phonons moving in a given direction with the time[21]

$$t_{\mathrm{ph\,ph}}=15\rho_4c^4/\pi^3(u_1+1)^2T^4p_{\mathrm{ph}}, \tag{53}$$

where ρ_4 is the density of ^{4}He in the solution, and $u_1=\rho_4\partial c/c\partial\rho_4$.

The relation between the times (52) and (53) is determined by the solution concentration and temperature. Figure 1 shows the values of effective thermal conductivity of a solution with $x=1.39\cdot10^{-4}$ calculated by formula (50) and measured in Ref. 22. The contribution of κ_{i} for such a solution can be neglected. In this case, $\tau_D^{i\,\mathrm{ph}}$ virtually coincided with $\tau_{D\min}^{(i\,\mathrm{ph})}$, which indicates rapid relaxation in the phonon system of the solution. As the concentration increases, the time (52) decreases, and the finiteness of the time (53) becomes significant.

Figure 2 shows the observed and calculated values of effective thermal conductivity for solutions with different concentrations. It can be seen from Fig. 2 that as the concentration increases in the temperature range under investigation ($T<0.6$ K), the values of κ_{eff} with $\tau_D^{(i\,\mathrm{ph})}=\tau_{D\min}^{(i\,\mathrm{ph})}$ (dashed curves) deviate from the values calculated by formula (45) taking into account the finiteness of the relaxation time in the phonon system (solid curves). In this case, the solid curves are in better agreement with experimental data. It should be noted that the reduced results in the temperature range under investigation are in accord with the results of calculations and conclusions drawn in Refs. 6, 15, and 16.

In the region of intermediate temperatures ($0.7\ \mathrm{K}<T<1$ K), in which the impuriton contribution is small, the effective thermal conductivity is mainly determined by diffusion in the gas of thermal excitations. Diffusion in a two-component phonon–roton gas was investigated for the first time in Ref. 24. Subsequently, it was proved[19] that this process leads to heat transfer in view of the difference between the energy–momentum relations for phonons and rotons. An analysis based on formulas (1), (22) and (45) and similar to that in Ref. 19 gives

$$\kappa_{\mathrm{eff}}\approx\kappa_D^{(r\mathrm{ph})}=\frac{1}{T}\frac{\rho_{\mathrm{ph}}\rho_r}{\rho_{\mathrm{ph}}+\rho_r}\left\{\frac{S_{\mathrm{ph}}T}{\rho_{\mathrm{ph}}}-\frac{S_rT}{\rho_r}\right\}^2\tau_D^{(r\mathrm{ph})}. \tag{54}$$

Here S_r and ρ_r are the entropy and the density of the roton gas, and $\tau_D^{(\mathrm{r\,ph})}$ is defined by formula (45) in which the indices α and β should be replaced by ''r'' (roton) and 'ph'' (phonon). Expression (54) is transformed to the result obtained in Ref. 19 if we make the times $t_{\mathrm{ph\,ph}}$ and t_{rr} in (45) tend to zero.

In analogy with (52), the phonon–roton collision frequency $t_{\mathrm{ph}\,r}^{-1}$ depends strongly on the phonon momentum:[18]

$$t_{\mathrm{ph}r}^{-1}\sim p_{\mathrm{ph}}^4.$$

However, the characteristic phonon–phonon interaction time defined by (53) is considerably smaller than the phonon–roton interaction time in the given temperature range. Hence we can neglect the contribution from the second term in (45).

According to Khalatnikov,[18] the phonon–roton collision frequency $t_{\mathrm{ph}\,r}^{-1}$ is assumed to be independent of the roton momentum, which allows us to omit the last term in (45) also. As a result, the phonon–roton diffusion time $\tau_D^{(\mathrm{ph}\,r)}$ is determined by its minimum value

$$\tau_D^{(\mathrm{phr})}=\tau_{D\min}^{(\mathrm{phr})}=(\tau_{\mathrm{ph}r}^{(0)^{-1}}+\tau_{r\mathrm{ph}}^{(0)^{-1}})^{-1}. \tag{55}$$

Curve *2* in Fig. 1 is the result of calculations based on formula (54), which indicates the existence of a wide temperature region in which $\kappa_D^{(r\ \mathrm{ph})}$ must be taken into account. In this region, the value of $\kappa_D^{(r\ \mathrm{ph})}$ determines the effective thermal conductivity completely. This proves that diffusion between thermal excitations must be taken into consideration in an analysis of thermal conductivity of condensed media.

At high temperatures ($T>1$ K), the kinetic properties of superfluid solutions are mainly determined by rotons and impuritons. According to Khalatnikov,[18] the effective thermal conductivity in this region is given by

$$\kappa_{\mathrm{eff}}=D_{ir}\left(S_r\,\frac{\rho_r+\rho_i}{\rho_r}\right)^2\frac{1}{n_i}+\kappa_i+\kappa_r, \tag{56}$$

where κ_{r} is the thermal conductivity of the roton gas. Proceeding from relations (1) and (22), and the definition of the diffusion coefficient of a superfluid solution (see, for example, Ref. 19), for the diffusion coefficient of an impuriton in a roton gas we have

$$D_{ir}=\frac{\rho_r}{\rho_i+\rho_r}\,\frac{T}{m_i}\,\tau_D^{(ir)}, \tag{57}$$

where the time $\tau_D^{(ir)}$ is defined by (45) in which the indices α and β must be replaced by the indices ''i'' and ''r'', respectively.

Relation (57) is transformed into the result obtained in Ref. 19 if we make the times t_{ii} and t_{rr} in (45) tend to zero.

According to the results obtained in Ref. 25 and definition (41), the frequency of impuriton–roton collisions can be written in the form

$$t_{ir}^{-1}(p_i)=A^2n_r\left(\int_0^\infty\exp\left(-\frac{\mu v_r^2}{2T}\right)dv_r\right)^{-1}\times\int_0^\infty\exp\left(-\frac{\mu v_r^2}{2T}\right)\int_{-1}^1\frac{1}{2}\sin^2\theta\left(\frac{\mu}{2}(v_r-v_i)^2+\frac{p_i^2}{2m_i}\sin^2\theta\right)^{1/2}d\cos\theta dv_r, \tag{58}$$

where A is the amplitude of impuriton–roton scattering.

In the temperature and concentration ranges under investigation the relaxation time obeys limiting expressions which are determined by the absence of equilibrium in the impuriton gas[9,21] ($\tau_{ii}\gg t_{ir}$) and by rapid relaxation in the roton gas[9,18] ($\tau_{rr}\ll t_{ri}$). Under these conditions, the general expression (45) gives

$$\tau_D^{(ir)}=\tau_{D\max}^{(ir)}=\langle t_{ir}\rangle_i. \tag{59}$$

The results of calculations of effective thermal conductivity for solutions with $x=1.39\cdot10^{-4}$ on the basis of formula (57) are presented in Fig. 1 (curve *3*). In this case, the contributions of the second and third terms in (56) can be neglected. The inclusion of finiteness of the times t_{ii} and t_{rr} increases the calculated value by approximately 10%, thus improving the agreement between the theory and experimental results. It should be noted that a relatively small difference between $\tau_{\min}^{(ir)}$ and $\tau_{\max}^{(ir)}$ is due to a weak dependence of frequency (58) on momentum. Dashed curves in Fig. 2 correspond to the results of calculations with $\tau_D=\tau_{D\min}$, while solid curves correspond to the values of τ_D calculated by formula (45).

It would be undoubtedly interesting to measure the diffusion coefficient for superfluid ^{3}He–^{4}He solutions with different concentrations up to very high values for which the time τ_{ii} becomes comparable to τ_{ir}. A comparison of such experimental data with the results presented here would lead to the dependence of τ_{ir} on the relaxation rate in the impuriton gas.

5. DIFFUSION IN ^{3}He–^{4}He SOLID SOLUTIONS

A phenomenological theory of quantum diffusion of ^{3}He impurity atoms in solid solutions of helium isotopes was proposed for the first time by Andreev and Lifshits.[1] These authors regarded impurity atoms as delocalized quasiparticles which move virtually freely through the crystal. Thus, quantum diffusion of impuritons in ^{3}He–^{4}He solid solutions was predicted in Ref. 1. Subsequent theoretical investigations were carried out in Refs. 26–30, in which special attention was paid to an analysis of the phonon–impuriton interaction. This interaction leads to a strong temperature dependence (T^{-9}) of diffusion coefficient. Such a dependence was observed for the first time in Refs. 2–4 and made it possible to carry out a quantitative comparison with the theory.

In this section, we calculate the diffusion coefficient for solid solutions proceeding from the general technique described in Sec. 1. The expressions obtained for diffusion coefficient differ in form from the results of previous publications and contain parameters that can be determined from other experiments. The method proposed in Secs. 1–3 makes it possible to compare the parameters determined from different experiments.

Let us consider a stationary nonequilibrium state of a ^{3}He–^{4}He solid solution in which the number $n_\uparrow$ and $n_\downarrow$ of impuritons with different spin projections per unit volume are functions of the coordinate z. In this case, the total number density $n=n_\uparrow+n_\downarrow$ and temperature are constant.

By definition,[12] the diffusion coefficient D_s for impuritons with the given spin projection $\uparrow$ is defined by the relation

$$\mathbf{u}_\uparrow=-D_s\,\frac{\nabla n_\uparrow}{n_\uparrow}, \tag{60}$$

where

$$\mathbf{u}_\uparrow=j_\uparrow\rho_\uparrow^{-1} \tag{61}$$

is the average rate of diffusion flow of impuritons with the spin $\uparrow$, $j_\uparrow$ the diffusion flux density, whose function dependence on $f_\uparrow$ is defined by formula (2) with $k=\uparrow$, and $\rho_\uparrow$ the

normal density of impuritons with the spin ↑, which is defined by the general expression (4). The relation between D_s and the matrix of diffusion times is defined by formula (1) in which the indices α and β must be replaced by the indices ↑ and ↓, and we must take into account the fact that $\nabla n_\uparrow = -\nabla n_\downarrow$.

At a constant temperature and in the absence of a dependence of interaction of quasiparticles on the direction of spin, the phonon system is in the equilibrium state. Consequently, in order to find the diffusion coefficient D_s as a function of impuriton–impuriton and impuriton–phonon collision frequencies, we must solve the system of only two kinetic equations. This system can be obtained from equations (11) by introducing the terms describing collisions of impuritons with equilibrium phonons into the right-hand sides of equations (11). As a result of solution of this system of equations according to the algorithm proposed in Secs. 1 and 2, for the diffusion coefficient of an impuriton with the spin ↑, we have

$$D_s = \frac{2}{3}\frac{{}_1\langle \varepsilon_i|1\rangle_1}{{}_1\langle 1|1\rangle_1}\frac{1}{m_i}\,\tau_S . \tag{62}$$

Here $\varepsilon_i = p_i^2/2m_i$ is the kinetic energy of the impuriton, and τ_S is defined by relation (25) in which

$$\hat{I} = \begin{pmatrix} J_{\uparrow\downarrow} + J_{\uparrow \mathrm{ph}} & J_{\downarrow \mathrm{ph}} \\ J_{\uparrow \mathrm{ph}} & J_{\downarrow\uparrow} + J_{\downarrow \mathrm{ph}} \end{pmatrix}; \tag{63}$$

$$\hat{S} = \begin{pmatrix} J_{\uparrow\uparrow} & 0 \\ 0 & J_{\downarrow\downarrow} \end{pmatrix}. \tag{64}$$

Considering that phonons interact identically with impuritons having different spin projections and assuming that the momentum dependence of the frequency of collisions between impuritons is weak, we obtain

$$\tau_S = [\,\tau_{ii}^{-1} + \tau_{i\mathrm{ph}}^{(0)^{-1}}]^{-1}, \tag{65}$$

where

$$\tau_{ii}^{-1} = -\langle J_{\uparrow\downarrow}\rangle_\uparrow - \langle J_{\downarrow\uparrow}\rangle_\downarrow . \tag{66}$$

is the frequency of collisions between impuritons and

$$\tau_{i\mathrm{ph}}^{(0)^{-1}} = -\langle J_{\uparrow \mathrm{ph}}\rangle_\uparrow = -\langle J_{\downarrow \mathrm{ph}}\rangle_\downarrow : \tag{67}$$

the frequency of collisions of impuritons with phonons.

For dilute solutions in the region of relatively high temperatures, the impuriton–impuriton collision frequency τ_{ii}^{-1} in (65) can be neglected. In this case, D_s is mainly determined by the diffusion of impuritons in the gas of phonons with the coefficient

$$D_{i\mathrm{ph}}^{(s)} = \frac{2}{3}\frac{{}_1\langle \varepsilon_i|1\rangle_1}{{}_1\langle 1|1\rangle_1}\frac{1}{m_i}\,\tau_{i\mathrm{ph}}^{(0)}. \tag{68}$$

While calculating the scalar products appearing in (62) and (68), we evaluate the integrals within the impuriton band width $\Delta \ll T$. Ultimately, relation (68) gives

$$D_{i\mathrm{ph}}^{(s)} = \frac{2}{5}\frac{\Delta}{m_i}\,\tau_{i\mathrm{ph}}^{(0)}. \tag{69}$$

This result differs from the diffusion coefficient (51) for the phonon– impuriton system of liquid ^{3}He–^{4}He solutions.

First, the finite energy band width for impuritons in a solid solution leads to the replacement of T by Δ for $\Delta \ll T$.

Second, expression (51) contains the factor $\rho_{ph}/(\rho_{ph}+\rho_i)$, which determines the temperature dependence of $D_{i\ \mathrm{ph}}$ to a considerable extent. Such a factor can be due to dissipative flow of phonons directed towards the diffusion flow of impuritons so that the total momentum is equal to zero.

Third, in contrast to $\tau_{i\ \mathrm{ph}}^{(0)}$ in (69), the time $\tau_{D}^{(i\ \mathrm{ph})}$ in (45) is a function of the frequency of collisions between particles of the same type (t_{ii} and $t_{\mathrm{ph\,ph}}$). The difference in the contributions from the impuriton–phonon interaction to the mass and spin diffusion coefficients of liquid solutions ^{3}He–^{4}He was described for the first time in Ref. 19.

Let us consider the temperature dependence of the diffusion coefficient $D_{\mathrm{i}\ ph}^{(s)}$. For this purpose, using the momentum conservation law, we write $\tau_{i\ \mathrm{ph}}^{(0)}$ in the form

$$\tau_{i\mathrm{ph}}^{(0)} = \tau_{\mathrm{ph}i}^{(0)}\rho_i/\rho_{\mathrm{ph}}. \tag{70}$$

According to the general expression (4), we have here

$$\rho_i = \frac{2}{5}\frac{\Delta}{T}\,n_i m_i , \tag{71}$$

$$\rho_{\mathrm{ph}} = \frac{2\pi^2}{15}\frac{T^4}{u^5}, \tag{72}$$

where u is the averaged velocity of longitudinal and transverse sounds in solid helium. Substituting (70) and (71) into (69), we obtain

$$D_{i\mathrm{ph}}^{(s)} = \frac{4}{25}\frac{\Delta^2}{T}\frac{n_i}{\rho_{\mathrm{ph}}}\,\tau_{\mathrm{ph}i}^{(0)}. \tag{73}$$

The time $\tau_{\mathrm{ph}i}^{(0)}$ has the dependence T^{-4} typical of Rayleigh scattering, while ρ_{ph} is proportional to T^4 in accordance with (72). Ultimately, according to (73), we have $D_{i\ \mathrm{ph}}^{(s)} \sim T^{-9}$.

Such a strong temperature dependence was obtained for the first time in Ref. 1 proceeding from phenomenological considerations. According to (69), the temperature dependence of $D_{i\ \mathrm{ph}}^{(s)}$ is determined only by $\tau_{i\ \mathrm{ph}}^{(0)}$. It follows from (70)–(73) that in this case eight powers of temperature are associated with phonons (the normal phonon density $\rho_{\mathrm{ph}} \sim T^4$ and the frequency of collisions of phonons with impuritons $\tau_{\mathrm{ph}i}^{(0)^{-1}} \sim T^4$), and one power is associated with the normal density of impuritons (71).

Expressions (69) and (73) differ in the form of notation from the results presented in Ref. 1 and 26–30. Relation (73) contains parameters which can be determined experimentally.

For example, the time $\tau_{\mathrm{ph}i}^{(0)}$ appearing in (73) can be determined from the thermal conductivity data for solid solutions ^{3}He–^{4}He.[31] The contribution of the phonon–impuriton interaction to the effective thermal conductivity is determined by the first term on the right-hand side of equality (50). According to (45), for dilute solutions with $x \leqslant 10^{-3}$, the time $\tau_D = \tau_{\mathrm{ph}i}^{(0)}$ in (50). Using the experimental results obtained in Ref. 31, we have

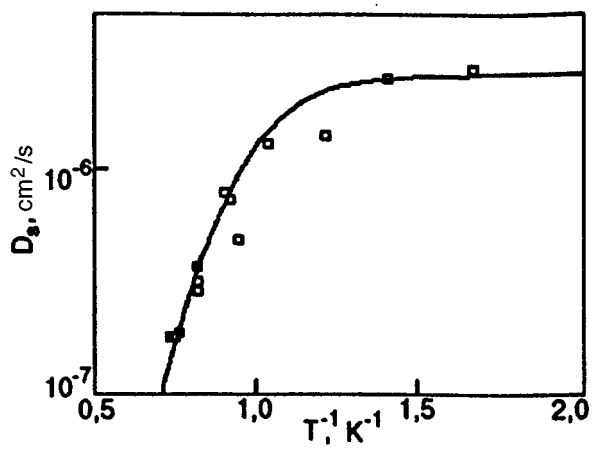

FIG. 3. Dependence of the diffusion coefficient D_s on reciprocal temperature for a solution with the concentration $x=6\cdot10^{-5}$; the experimental results obtained in Refs. 2–4 are represented by □; the solid curve is calculated on the basis of relations (72)–(77).

$$\tau_{\mathrm{ph}i}^{(0)}=8.96\cdot10^{-11}T^{-4}x^{-1}. \tag{74}$$

The normal phonon frequency can be calculated from the velocities of longitudinal and transverse sounds. Thus, the right-hand side of (73) contains only one unknown parameter Δ.

We can obtain the numerical value of Δ by using the experimental results obtained in Refs. 2–4 for the impuriton–phonon diffusion coefficient in solutions with $x=6\cdot10^{-5}$. Taking into account (65), we can write the expression for D_s in the form

$$D_s=(D_{i\mathrm{ph}}^{(s)^{-1}}+D_{ii}^{-1})^{-1}. \tag{75}$$

where D_{ii} is the temperature-independent contribution of impuriton–impuriton interaction to spin diffusion, which, according to Ref. 12, is given by

$$D_{ii}=2.67\cdot10^{-7}\ \mathrm{cm^2/s}. \tag{76}$$

Figure 3 shows the experimental[2] and theoretical values of the diffusion coefficient calculated by formulas (72)–(76). The agreement between the observed and theoretical values is attained for

$$\Delta=3.5\cdot10^{-4}\ \mathrm{K}. \tag{77}$$

The obtained value refines the results presented in Refs. 26 and 33 which give only order-of-magnitude estimates.

CONCLUSION

The exact solution (26) obtained for the diffusion time determines the diffusion coefficient for mixtures of particles with arbitrary statistics and energy–momentum relations. It follows from the limiting cases (30), (34), and (35) that diffusion coefficient can depend strongly on the interaction between particles of the same type. The correct approximation (44) of relaxation time proposed for a two-component system makes it possible to write the diffusion time (45) as a function of the times of interaction between particles. The obtained general results are used for investigating diffusion in superfluid ^{3}He–^{4}He solutions. The contribution of the diffusion coefficient to the effective thermal conductivity is determined by taking into account intrinsic times over in the entire temperature range for which experimental data are available. The theoretical results are compared with experimental data (see Figs. 1 and 2).

The general results obtained in Secs. 1–3 made it possible to calculate the diffusion coefficient for ^{3}He–^{4}He solid solutions. The obtained expression (73) differs in form from the results of previous theories and contains parameters that can be found from other experiments. A comparison of the theoretical results with experimental data[2–4] allowed us to determine the numerical value of the impuriton energy band.

The authors are grateful to V. N. Grigor'ev for fruitful discussions of a number of problems associated with diffusion in solid solutions of helium isotopes.

*E-mail: berezhnoy@pem.kharkov.ua
**E-mail: tgeorge@uwsp.edu

[1] A. F. Andreev and I. M. Lifshits, Zh. Éksp. Teor. Fiz. **56**, 2057 (1969) [Sov. Phys. JETP **29**, 1107 (1969)].
[2] V. N. Grigor'ev, B. N. Esel'son, and V. A. Mikheev, Pis'ma Zh. Éksp. Teor. Fiz. **18**, 289 (1973) [JETP Lett. **18**, 169 (1973)].
[3] V. N. Grigor'ev, B. N. Esel'son, V. A. Mikheev *et al.*, J. Low Temp. Phys. **13**, 65 (1973).
[4] V. N. Grigor'ev, B. N. Esel'son, and V. A. Mikheev, Zh. Éksp. Teor. Fiz. **66**, 321 (1974) [Sov. Phys. JETP **39**, 153 (1974)].
[5] J. Ferziger and H. Kaper, *Mathematical Theory of Transport Processes in Gases*, North Holland, Amsterdam (1972).
[6] I. N. Adamenko, È. Ya. Rudavskiĭ, V. I. Tsyganok, and V. K. Chagovets, Pis'ma Zh. Éksp. Teor. Fiz. **39**, 404 (1984) [JETP Lett. **39**, 487 (1984)].
[7] J. Callaway, Phys. Rev. **113**, 1046 (1959).
[8] E. M. Lifshitz and L. P. Pitaevskiĭ, *Physical Kinetics* [in Russian], Nauka, Moscow (1979).
[9] I. N. Adamenko, K. È. Nemchenko, and V. I. Tsyganok, Zh. Éksp. Teor. Fiz. **96**, 1286 (1989) [Sov. Phys. JETP **69**, 731 (1989)].
[10] L. D. Landau and I. Ya. Pomeranchuk, Dokl. Akad. Nauk SSSR **59**, 669 (1948).
[11] I. M. Khalatnikov and V. N. Zharkov, Zh. Éksp. Teor. Fiz. **32**, 1108 (1957) [Sov. Phys. JETP **5**, 905 (1957)].
[12] B. N. Esel'son, V. N. Grigor'ev, V. G. Ivantsov *et al.*, *Solutions of Quantum Liquids* ^{3}He–^{4}He Nauka, Moscow (1973).
[13] G. Baym and C. Ebner, Phys. Rev. **164**, 235 (1967).
[14] È. Ya. Rudavskiĭ and V. K. Chagovets, Fiz. Nizk. Temp. **9**, 234 (1983) [Sov. J. Low Temp. Phys. **9**, 116 (1983)].
[15] I. N. Adamenko and V. I. Tsyganok, Zh. Éksp. Teor. Fiz. **87**, 865 (1984) [Sov. Phys. JETP **60**, 441 (1984)].
[16] I. N. Adamenko and V. I. Tsyganok, Zh. Éksp. Teor. Fiz. **88**, 1641 (1985) [Sov. Phys. JETP **61**, 978 (1985)].
[17] I. N. Adamenko, K. E. Nemchenko, and V. I. Tsyganok, J. Low Temp. Phys. **81**, 233 (1990).
[18] I. M. Khalatnikov, *Theory of Superfluidity* [in Russian], Nauka, Moscow (1971).
[19] I. N. Adamenko and K. E. Nemchenko, Fiz. Nizk. Temp. **21**, 498 (1995) [Low Temp. Phys. **21**, 386 (1995)].
[20] G. McHale, M. A. Jones, and R. M. Bowley, J. Phys. **C21**, 5757 (1988).
[21] I. N. Adamenko and È. Ya. Rudavskiĭ, Fiz. Nizk. Temp. **13**, 3 (1987) [Sov. J. Low Temp. Phys. **13**, 1 (1987)].
[22] T. P. Ptukha, Zh. Eksp. Teor. Fiz. **40**, 1583 (1961) [Sov. Phys. JETP **13**, 1112 (1961)].
[23] W. R. Abel and J. C. Wheatley, Phys. Rev. Lett. **21**, 1231 (1968).
[24] Ch. Um, Ch. Jun, H. Shin, and T. F. George, J. Low Temp. Phys. **78**, 51 (1990).
[25] I. N. Adamenko, A. V. Zhukov, and K. E. Nemchenko, Fiz. Nizk. Temp. **22**, 1470 (1996) [Low Temp. Phys. **22**, 417 (1996)].
[26] I. Pushkarev, Pis'ma Zh. Éksp. Teor. Fiz. **19**, 751 (1974) [JETP Lett. **19**, 386 (1974)].
[27] Yu. Kagan and L. A. Maksimov, Zh. Éksp. Teor. Fiz. **65**, 751 (1973) [Sov. Phys. JETP **38**, 373 (1973)].

[28] Yu. Kagan and M. I. Klinger, J. Phys. **C7**, 279 (1974).
[29] V. A. Slyusarev, M. A. Strzhemechny, and I. A. Burakhovich, Fiz. Nizk. Temp. **3**, 1229 (1977) [Sov. J. Low Temp. Phys. **3**, 591 (1977)].
[30] V. A. Slyusarev, M. A. Strzhemechny, and I. A. Burakhovich, Fiz. Nizk. Temp. **4**, 698 (1978) [Sov. J. Low Temp. Phys. **4**, 373 (1978)].
[31] A. A. Golub and S. V. Svatko, Fiz. Nizk. Temp. **7**, 970 (1981) [Sov. J. Low Temp. Phys. **7**, 469 (1981)].

Translated by R. S. Wadhwa

The properties of vacancies in solid ^{4}He as studied by pressure measurements

P. Remeijer, S. C. Steel, R. Jochemsen, and G. Frossati

*Kamerlingh Onnes Laboratorium, Leiden University, P.O. Box 9506, 2300 RA Leiden, The Netherlands**

J. M. Goodkind

Physics Department 0319, University of California at San Diego, 9600 Gilman Drive, La Jolla, CA 92037, U.S.A.

(Submitted November 29, 1996)
Fiz. Nizk. Temp. **23**, 586–597 (May–June 1997)

The temperature dependence of the pressure at a constant volume in solid ^{4}He in the low-density hcp phase has been measured. The measurements are analyzed in terms of a localized vacancy model and the free Bose gas model of vacancies in solid helium. The results agree better with the free Bose gas model. On the basis of this model the effective mass of the vacancies was determined to be 3–5 times the bare mass of a ^{4}He atom, which corresponds to a bandwidth of 1.3–2.1 K. © *1997 American Institute of Physics.* [S1063-777X(97)01105-5]

1. INTRODUCTION

There has always been much interest in vacancies in both solid ^{3}He and ^{4}He. Because of the large zero point motion in helium, a vacancy or free lattice site will have a high probability of tunneling to adjacent lattice sites. This distinguishes helium from other solids in which the vacancies are localized at low temperature. When the energy of formation of a vacancy is positive, the vacancies are thermally activated and will vanish exponentially at low temperature.

Theoretical studies suggest the possibility that in quantum solids, vacancies may still exist at absolute zero temperature.[1] Because of the large mobility of the vacancies, they will not have a single energy of formation but occupy a band of energy states; the energy of formation is in the center of the band. The lower limit of the band can become negative, which results in a nonzero vacancy concentration at zero temperature. In ^{4}He, these so-called zero-point vacancies behave like bosons and are expected to Bose condense, thus giving the crystal superfluid-like properties.

Most experiments seeking evidence for Bose condensation of the zero-point vacancies concentrated on superfluid mass flow.[2–5] No positive proof of vacancy flow was found. This has mainly been attributed to an extremely low critical speed or a very low T_c.

Van de Haar *et al.*[6] made an attempt to find the zero-point vacancies without depending on the critical velocity by measuring the pressure between 1.5 mK and 120 mK. The vacancies, which are expected to behave as an interacting Bose gas will contribute to the pressure in the solid and reveal themselves by a finite $\partial P/\partial T$ value at very low temperatures. A superfluid transition would be observed by a kink in the pressure. An upper limit to the zero-point vacancy concentration, $x_{zpv} \leqslant 6\times10^{-7}$, was determined and no sharp kinks were found, indicating a T_c lower than 1.5 mK, the lowest temperature obtained during the experiment.

In this work we concentrate on the properties of thermally activated vacancies. Although the existence of these vacancies is clear, their properties are not. A large collection of experiments has been carried out, involving charge mobility,[7–11] X-ray scattering,[12] NMR,[13–15] heat capacity,[16] and sound attenuation[17] measurements. Large discrepancies exist between the vacancy densities and activation energies that are extracted from the various experiments, although Burns *et al.*[18] showed that better agreement can be found when the data are interpreted under the assumption that the vacancies occupy a wide energy band (free boson model) instead of a narrow band.

We have measured the pressure of solid ^{4}He as a function of temperature for samples with molar volumes in the range of 20.908 cm^3 and 20.981 cm^3 and temperatures between 0.3 K and the melting temperature of the crystals. From the data we were able to establish the existence of thermally activated vacancies and we could, within the framework of the free Bose gas model, extract the effective mass and the activation energy of the vacancies.

2. THEORETICAL MODELS ON VACANCIES IN ^{4}He

We will give an overview of two common models that have been proposed to describe the vacancies. The first model presented treats the vacancies as localized phenomena or classical lattice defects with an activation energy Φ. The second model describes the opposite case of completely delocalized vacancies. In this case, the vacancies will behave like a free Bose gas with effective mass M. Finally, the contribution of the phonons to the pressure will be discussed.

2.1. Localized vacancies

When looking at vacancies from a classical point of view, we can visualize them as being static crystal defects which are localized in the lattice. The (configurational) entropy will then be given by the possible configurations of putting n vacancies in a lattice of N ^{4}He atoms,

$$S_c = k_B \cdot \ln\left(\frac{(N+n)!}{N! \cdot n!}\right), \tag{1}$$

which can be simplified by using Stirling's formula

$$S_c = k_B \cdot \left[n \cdot \ln\left(\frac{N+n}{n}\right) + N \cdot \ln\left(\frac{N+n}{N}\right)\right]. \tag{2}$$

The equilibrium number of vacancies can be found by minimizing the free energy of this system.

$$F = F_0 + n \cdot f - T \cdot S_c, \tag{3}$$

where F_0 is the free energy of the lattice without vacancies, and f is the free energy of a single vacancy. Using the fact that N is of the order of Avogadro's constant and $n \ll N$, we find

$$x = \frac{1}{e^{f/k_B T} - 1} \approx e^{-f/k_B T}, \tag{4}$$

where $x = n/N$ is the vacancy concentration, and the last simplification is true only for temperatures which are low compared to the free energy of the vacancy. With further definition of

$$f = \Phi - T \cdot s \tag{5}$$

where s is the entropy change of the crystal due to the introduction of a single vacancy, the vacancy creation energy or activation energy Φ has been related to the vacancy concentration x. In practice, this nonconfigurational entropy s turns out to be rather small,[12] meaning that f and Φ are virtually equivalent.

Since in our experiments we measure pressure as a function of temperature, it is necessary to know the pressure contribution of the vacancies. The total pressure of a system is given by

$$P = -\left(\frac{\partial F}{\partial V}\right)_T. \tag{6}$$

In our case we can calculate the vacancy part of the pressure by using the vacancy free energy part of F, which yields

$$P_{\text{vacancies}} = -n \cdot \left(\frac{\partial f}{\partial V}\right)_T = -N \cdot \left(\frac{\partial \Phi}{\partial V} - T\,\frac{\partial s}{\partial V}\right) \cdot e^{-\Phi/k_B T} \times e^{s/k_B}. \tag{7}$$

The volume dependence of the activation energy has been studied by Lengua *et al.*[17] From their data one can calculate for the molar volumes of interest here that

$$N \cdot \left(\frac{\partial \Phi}{\partial V}\right) \approx -4.5 \times 10^8 \ \text{Pa}. \tag{8}$$

Consequently, this model provides a means of determining the activation energy and the vacancy formation entropy.

2.2. The free Bose gas model

The large quantum behavior of ^{4}He has the consequence that the tunneling probability for a vacancy to hop to an adjacent site is large. This mobility will lead to a band of energy states. In the case that the width of the band (Δ) is large compared to the temperature, the vacancies will behave like a free Bose gas. The great canonical partition function is given by

$$\Xi = \sum_{N=0}^{\infty} \sum_{\mathbf{k}} \frac{1}{N!}\, e^{(\mu N - E_{\mathbf{k}})/k_B T}. \tag{9}$$

The dispersion relation in the case $\Delta \gg T$ is equal to the dispersion relation of free bosons with an activation energy Φ and is given by

$$E_{\mathbf{k}} = \Phi + \frac{\hbar^2 \mathbf{k}^2}{2M}. \tag{10}$$

Here the vacancy activation energy Φ is sometimes called the gap of the energy band, and M is the effective mass of the vacancies. The sum over all $\mathbf{k}$ values in the great canonical partition function may be replaced by an integral over E. Using the density of states

$$\rho(E) = \frac{V}{(2\pi)^2}\left(\frac{2M}{\hbar^2}\right)^{3/2} (E - \Phi)^{1/2}, \tag{11}$$

we then find for the vacancy concentration

$$x = \frac{1}{N} k_B T \int_{\Phi}^{\infty} \frac{\rho(E)}{e^{E/k_B T} - 1}\, dE = \frac{V}{N}\left(\frac{M}{2\pi\hbar^2}\right)^{3/2} (k_B T)^{3/2} g_{3/2}(e^{-\Phi/k_B T}) \tag{12}$$

and for the pressure due to the vacancies

$$P = \frac{2}{3V} \int_{\Phi}^{\infty} \frac{E\rho(E)}{e^{E/k_B T} - 1}\, dE = \left(\frac{M}{2\pi\hbar^2}\right)^{3/2} (k_B T)^{5/2} g_{5/2}(e^{-\Phi/k_B T}), \tag{13}$$

where the polylog function g_σ is defined as

$$g_\sigma(z) = \frac{1}{\Gamma(\sigma)} \int_0^{\infty} \frac{x^{\sigma - 1}}{z^{-1} e^x - 1}\, dx. \tag{14}$$

As one can see, the model provides direct access to the effective mass M and the activation energy Φ. In the tight-binding approximation, the effective mass is directly correlated with the band width Δ of the energy spectrum by

$$M = \frac{6\hbar^2}{a^2 \Delta}, \tag{15}$$

where a is the atomic distance. If the activation energy is large compared to the temperature and the band width ($\Phi \gg k_B T, \Delta$), the free Bose gas model with the effective mass replaced by the band width, according to Eq. 15, becomes equivalent to a narrow band model, as described by various authors.[19,20]

2.3. The phonon contribution

In order to be able to study the vacancy contribution to the pressure, it is necessary to calculate the magnitude and temperature dependence of the phonon background pressure. The thermodynamic properties of solid ^{4}He have been exten-

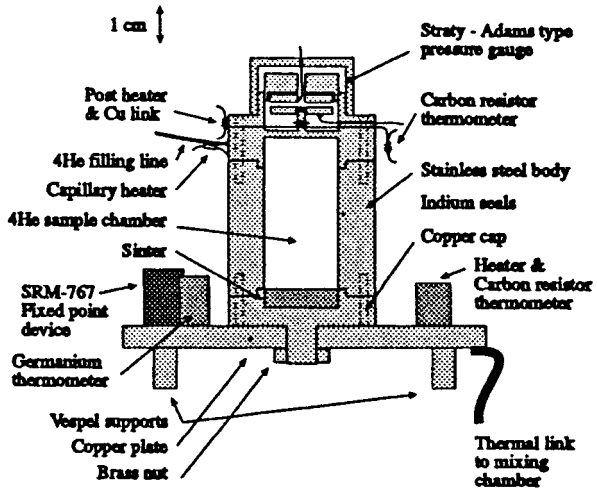

FIG. 1. The constant-volume cell placed on the copper platform. The post- and capillary heaters can be seen near the top.

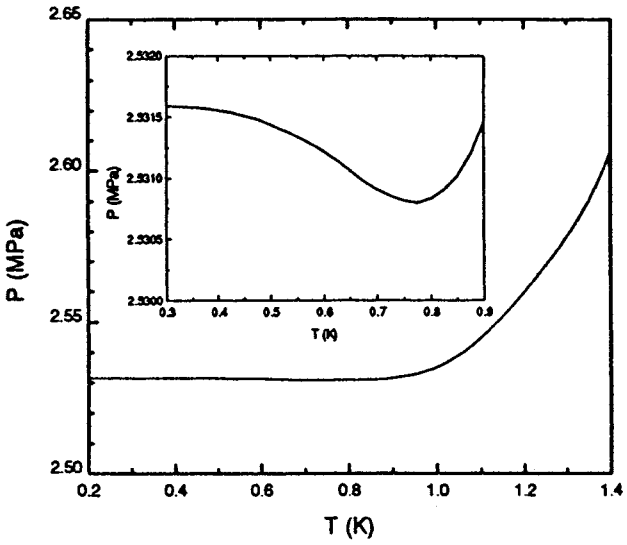

FIG. 2. The ^{4}He melting curve. The inset shows the region of the minimum. The temperature at which this minimum occurs is 780 mK and the depth is approximately 800 Pa.

sively studied by Gardner *et al.*[16] and we will use their results to make an estimate of the phonon contribution to the pressure. They found that the constant volume heat capacity C_v can be described with very good approximation by a Debye T^3 term supplemented by a T^7 term.

The Grüneisen parameter γ links the heat capacity to the pressure by

$$\frac{\alpha}{C_v}=\gamma\frac{B}{V}, \tag{16}$$

where α is the expansion coefficient, B is the bulk modulus, and V is the volume.

Using the reciprocity theorem, we obtain

$$\left(\frac{\partial P}{\partial T}\right)_V=-\left(\frac{\partial V}{\partial T}\right)_P\cdot\left(\frac{\partial V}{\partial P}\right)_T^{-1}=\frac{\alpha}{B}, \tag{17}$$

which in combination with Eq. 16 yields

$$\left(\frac{\partial P}{\partial T}\right)_V=\gamma\frac{C_v}{V}=\frac{\gamma}{V}\cdot(AT^3+CT^7+\ldots). \tag{18}$$

In the low-temperature limit ($T \ll \Theta_D$, where $\Theta_D \cong 27$ K for ^{4}He) the Grüneisen parameter is only slightly temperature dependent, which means that simple integration of the last expression yields a pressure term that depends only on T^4 and T^8 terms. Using the coefficients A and C of Gardner *et al.*,[16] converted to SI units, and $\gamma\cong 2.8$, we obtain

$$P=0.07\frac{A(V_m)}{V_m}T^4+0.035\frac{C(V_m)}{V_m}T^8. \tag{19}$$

3. EXPERIMENTAL SETUP

A copper platform (10 cm in diameter, thickness 0.6 cm) served as a single temperature mounting plate on which the cell, a germanium thermometer, a fixed point device, a heater, and a carbon resistor thermometer (CRT) were placed. This platform was attached to the mixing chamber cold plate using Vespel SP21 rods,[21] with a heat leak of less than 2.5 μW to the mixing chamber, with the platform held at a temperature of 1 K.

A thermal link was provided by means of a carefully calculated copper wire ($\varnothing$2.0 mm, length 45 mm, standard electrolytic quality) which was connected between the platform and the mixing chamber cold-plate. It was chosen in such a way that 5 mW of heating power would maintain a temperature of 1 K on the platform.

The constant-volume cell, shown in Fig. 1, was made as rigid as possible. To obtain this rigidity, the body was made of a 1-cm-thick stainless-steel cylinder. The low end was closed with a copper cap containing the silver sinter. The stainless-steel top cap contained the Straty-Adams pressure gauge. The ^{4}He volume formed in this manner measured $\varnothing 2$ cm $\times$ 4 cm, 12 cm^3. The cell was clamped onto the copper plate with a brass nut.

The sinter was made with 7.6 grams XRP-5 powder,[22] of which the surface area is estimated to be[23] 0.76 m^2.

A Straty–Adams[24] strain gauge was incorporated into the cell to measure pressure. The thin stainless-steel top wall of the cell served as the flexible membrane for the gauge. One of the capacitor electrodes of the gauge was glued to the post connected to this membrane using Stycast 2850FT.[25] The second electrode was glued in position while resting against the bottom plate, with the cell pressurized to 2.7 MPa. This procedure guarantees a very small spacing between the plates for pressures lower than 2.7 MPa, the ''gluing pressure,'' thereby giving a high sensitivity. Electrical connections to the electrodes were fed through small holes in the cell wall. Coaxial cables were used to minimize stray capacitance effects.

The gauge was calibrated at 1 K against a Degranges & Huot dead-weight tester.[26] The standard deviation of the fit to the calibration points was less than 50 Pa. The random error in the pressure, introduced through the capacitance measurement of the strain gauge, is smaller than 2 Pa when

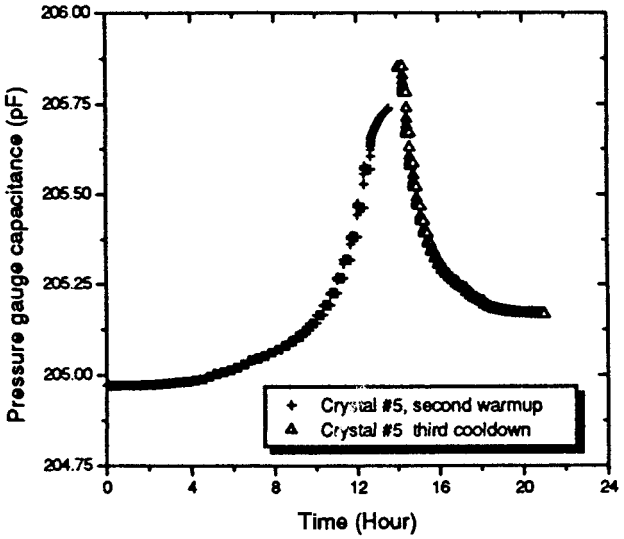

FIG. 3. The capacitance of the pressure gauge as a function of time before averaging, for crystal 5 during the second warmup and the third cooldown. The capacitance (pressure) increase between the two measurements is due to a shift of the plug.

using the Andeen Hagerling AH2500 capacitance bridge.[27] The pressure of the ^{4}He melting curve minimum, $P_{\min} = 2.53081$ MPa, was reproduced within 100 Pa.

To ensure a homogeneous growth of the crystals we needed to have a vertical temperature gradient in the cell, where the bottom was the coldest part. We therefore set up a system in which the post of the flexible membrane could be heated. Because of limited space near this post, the heater, a metal film resistor, was placed outside the cell, while the thermal contact between the post and the heater was provided by a copper wire.

Due to the shallow minimum in the ^{4}He melting curve, it is possible that the filling line could be blocked with a solid when its temperature is close to 780 mK. To overcome this undesirable effect, a second heater was connected to the ^{4}He filling line.

Another heater was placed on the platform. It consisted of 50-cm manganin wire wound on a copper cylinder (10 mm in diameter) on which a carbon resistor thermometer was placed.

Three thermometers were placed on the platform, the SRM-767 fixed-point device and a germanium and carbon resistor thermometers. Another carbon resistor thermometer was thermally anchored to the post that connects the top wall of the cell to the pressure gauge electrode. It was used to measure the temperature of the top of the cell (Fig. 1).

The germanium thermometer was calibrated against the SRM-767 fixed-point device.[28] The maximum deviation expected for this thermometer is 5 mK. A consistency check was made by carefully measuring the minimum of the ^{4}He melting curve. Our thermometers read 782 ± 3 mK at the minimum, which agrees quite well with earlier measurements by Grilly.[29]

For controlling the temperature we used the carbon resistor thermometer, which was located on the platform in combination with the platform heater, to form a PID (Proportional Integration Derivative) feedback loop. The brain of this regulator was a Hewlett Packard HP9000/300 Unix computer in combination with a DAC (Digital Analog Converter) to drive the heater and an ADC (Analog Digital Converter) to read the temperature. Both the ADC and the DAC were contained in a Hewlett Packard HP35650. The setup was able to maintain the temperature constant within 0.05% (programmable), which greatly simplified the slow process of working through the whole temperature region.

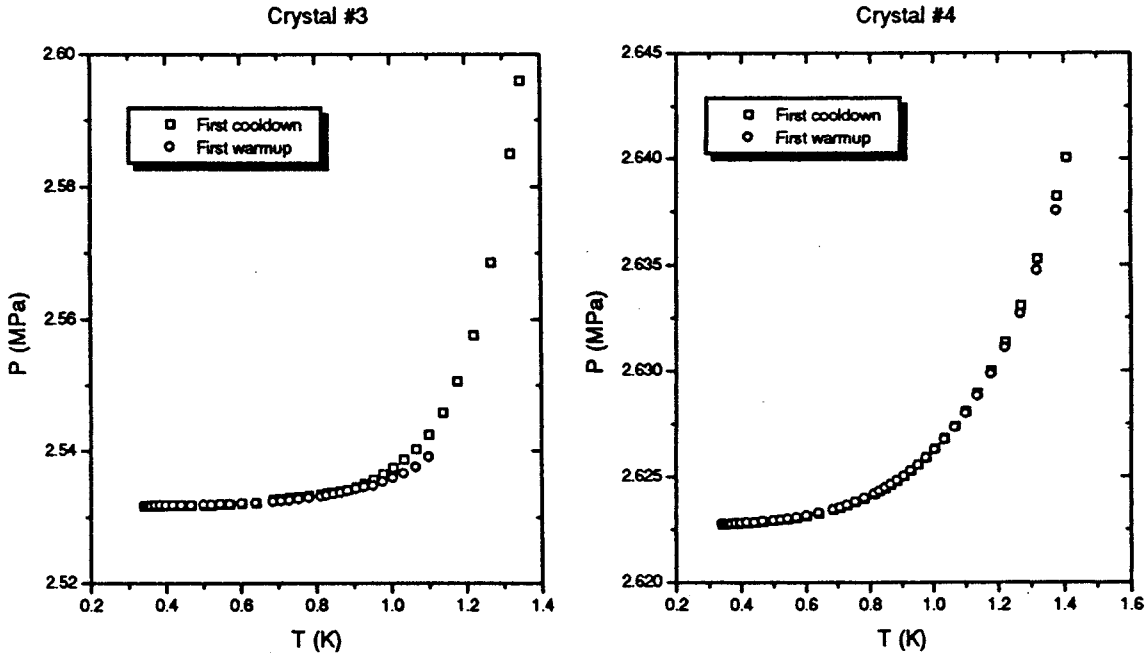

FIG. 4. The pressure of crystals 3 and 4 plotted as a function of temperature. The reproducibility between a cooldown and a subsequent warmup is good for crystal 4 but rather poor for crystal 3. The latter could be caused by inhomogeneities in the crystal which are introduced during its growth.

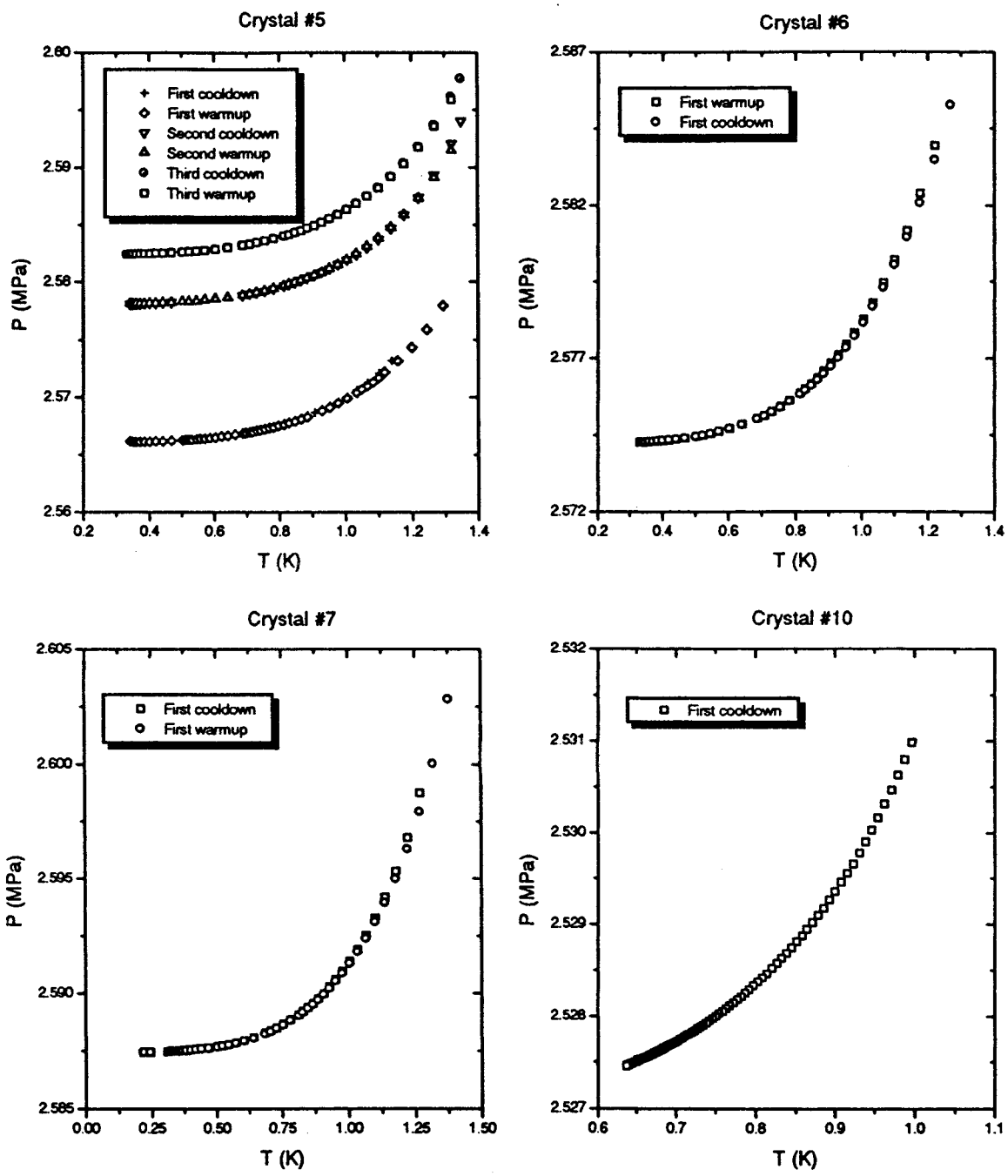

FIG. 5. Continuation of Fig. 4. The pressure as a function of temperature for crystals 5, 6, 7, and 10. All crystals show good reproducibility. The change in pressure for crystal 5 is due to a change in density at high temperatures.

Since vacancies have the tendency to bind to impurities and defects in the crystal, it is important to remove them as much as possible. Commercial ^{4}He is contaminated with ^{3}He, which is typically of the order of 1 ppm. We used the heat flush effect to purify the ^{4}He gas.[30,31] A mass spectrometer check showed that the ^{3}He impurity content is significantly below 1 ppm, but on the basis of the experience of other workers who used the same technique, it is more likely that the concentration is (far) below 1 ppb.

4. MEASUREMENTS OF THE *P–T* RELATION OF SOLID ^{4}He

All data presented here have been acquired during two cool-downs of the cell. Major improvements to the experimental setup, however, were made after the first run. The data from the first run are therefore included mainly for completeness.

4.1. Growing the crystals

All crystals were grown in the temperature range 1.2–1.4 K. As one can see from Fig. 2, the melting curve shows a positive slope in this temperature region. While growing the crystals, the temperature of the platform and the cell pressure were held constant. The cell pressure was chosen to coincide with the ^{4}He melting pressure which corresponded to the platform temperature. A vertical gradient was introduced by using a heater connected to the top of the cell

TABLE I. Summary of all good quality crystals that were used for fitting. Each item indicates a $P - T$ curve taken upon cooling or warming. Also shown are the crystal number and an index for future reference. The molar volumes were estimated from the limiting low-temperature pressure (see text).

Crystal No.	Warming / Cooling	Cycle No.	Index	V_m, cm^3
3	w	1	3w1	20.981
4	c	1	4c1	20.908
4	w	1	4w1	20.908
5	c	2	5c2	20.944
5	c	3	5c3	20.940
5	w	1	5w1	20.954
5	w	2	5w2	20.944
5	w	3	5w3	20.940
6	c	1	6c1	20.947
6	w	1	6w1	20.947
7	w	1	7w1	20.936

(post-heater). Slowly decreasing the vertical temperature gradient across the cell therefore caused the solid to grow from the bottom up, and the filling line, which was located at the peak of the cell, would block last.

After growing the crystal, the volume of the cell was closed by increasing the pressure a few bars above the growth pressure, thereby blocking the filling line. Subsequently, all crystals were annealed by leaving them slightly below their melting temperature during a period of 6 hours.

A total of eighteen crystals of very pure ^{4}He were prepared during the two runs. Several crystals proved to be badly grown, the telltale sign being anomalous superheating below the melting curve, sudden pressure shifts, or irreproducibility upon warming and cooling. We believe that the crystals were flowed mainly because of the lack of pressure stability during growth. After thermally cycling the crystals, the reproducibility of the P-T relation always improved significantly, indicating that this method, in fact, is a better annealing method than the one that was described before. This conclusion was also reached by Iwasa *et al.*[32] for solid ^{3}He crystals.

4.2. Results

The $P-T$ curves were measured by making small temperature steps ($\pm$ 40 steps over the whole temperature range 0.2 K–1.4 K) and allowing the crystal to equilibrate at each temperature. This procedure is shown in Fig. 3.

We used the stability of the pressure reading as the equilibrium condition. The time to reach equilibrium was typically 5 to 10 minutes, after which approximately 50 data readings were taken. Averaging reduced the noise contribution to the pressure reading by a factor 7 to 0.4 Pa. A single sweep through the temperature region would take approximately 7–10 hours. Also visible in Fig. 3 is the pressure shift occurring between a warmup measurement and a subsequent cooldown. This shift occurs due to a slow shift of the plug in the filling line, resulting in an increase of pressure and a decrease in molar volume. Therefore, only cooldowns with accompanying warmup measurements will be at equal molar volume. All useful samples along with their melting temperature and molar volume are summarized in Table I. The $P-T$ relations are shown in Figs. 4 and 5. Despite the smoothness of the $P-T$ relation of crystal #10, we could not use the curve for fitting because of its limited temperature span. The molar volumes of all samples were estimated from the limiting pressure at low temperature, using molar volume and compressibility data on HCP ^{4}He from Grilly.[29]

4.3. Analysis

The data were analyzed by fitting the functions representing one of the models described earlier. In addition, we compared the results with two ''phonons only'' fits to see

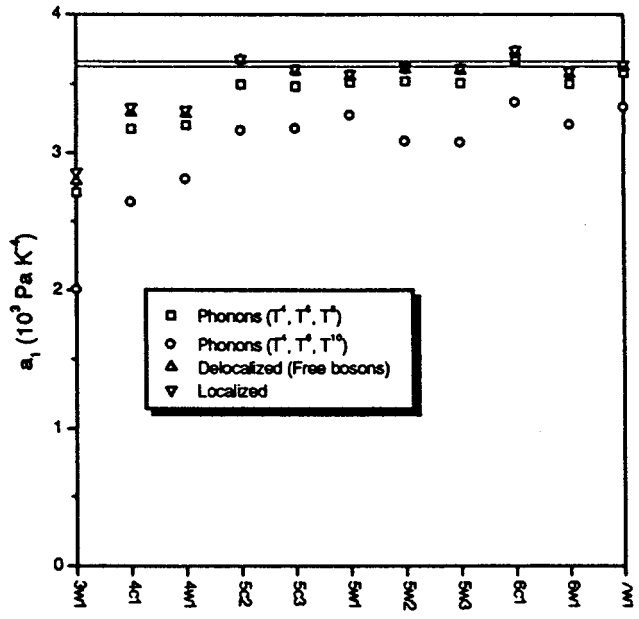

FIG. 6. The coefficient of the T^4 term for the various crystals and fits. We clearly see the improvement as a function of crystal number indicating better growth conditions. Also shown are the converted data (see text) by Gardner, indicated by the two solid lines.

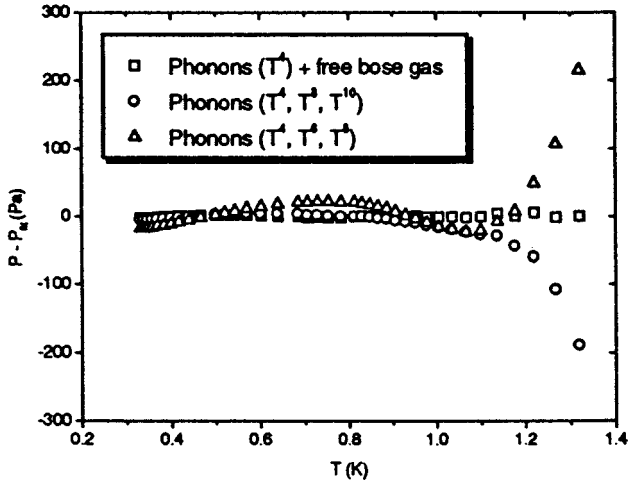

FIG. 7. The average data points of a P-T measurement, with phonon-fits and a Bose gas fit subtracted, are shown. The powers of T that are used in the phonon fits (see text) are also indicated.

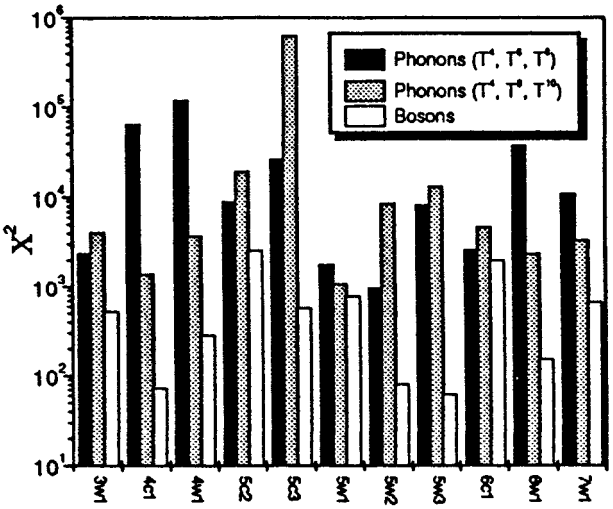

FIG. 8. The standard deviation of a vacancy (free boson) fit and different phonon fits are summarized in a bar graph. A large improvement gained from using vacancy fits is clearly seen. Note the logarithmic y scale.

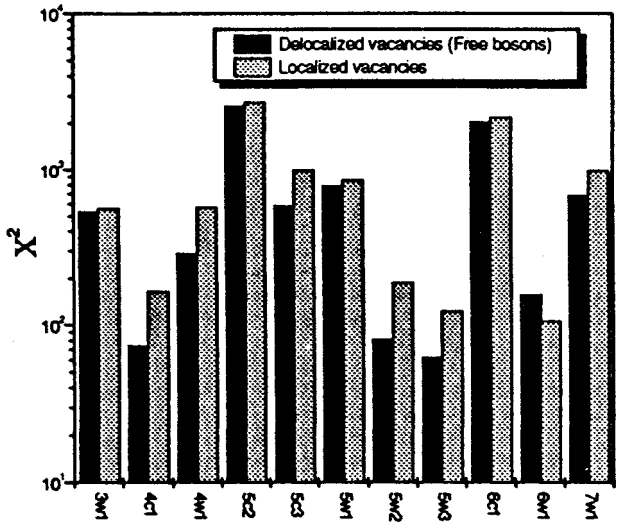

FIG. 9. A comparison between the standard deviation of localized and delocalized vacancy (free boson) fits. No clear difference can be seen, although the delocalized vacancy fit seems to be slightly better.

whether including a vacancy contribution would indeed improve the description of the data by phonons alone. The four fitting functions which we used are

$$P = P_0 + a_1 T^4 + a_2 T^6 + a_3 T^8, \quad \text{phonons}, \tag{20}$$

$$P = P_0 + a_1 T^4 + a_2 T^8 + a_3 T^{10}, \quad \text{phonons (Gardner)}, \tag{21}$$

$$P = P_0 + a_1 T^4 + a_2 e^{-a_3/T}, \quad \text{localized vacancies}, \tag{22}$$

$$P = P_0 + a_1 T^4 + a_2 T^{5/2} g_{5/2}(e^{-a_3/T}), \quad \text{free vacancies}. \tag{23}$$

As one can see, we chose to use the same number of fit parameters in all functions for the obvious reason that a greater number of parameters will increase the degrees of freedom and automatically lead to a better fit, which makes quantitative analysis of the fit deviations impossible.

4.3.1. Phonons

The first and second coefficient of all fits (P_0 and a_1) show basically the same values, regardless of the type of fit. This is indicative of the intrinsic meaning of these coefficients; here P_0 is the limiting zero-temperature pressure, and a_1 is the Debye-type phonon contribution. As a consistency check, we compared the T^4 phonon contribution to the specific heat measurements by Gardner *et al.*[16] Their coefficients for the heat capacity A (as seen in Table I of the article) can be converted to our T^4 coefficient a_1 by using Eq. (19)

$$a_1 = 7.0 \times 10^5 \frac{A(V_m)}{V_m} \, [\text{Pa}/K^4], \tag{24}$$

where A is given in J/mole K^4, and the molar volume V_m is given in cubic centimeters. The a_1 values for the various crystals and fits is shown in Fig. 6. The solid lines represent the A values by Gardner for the molar volumes of our crystals. The scatter in our a_1 coefficient is too large ($\simeq 5\%$) to determine a molar volume dependence, which only constitutes a 1% change in a_1.

The values for crystals 3 and 4 are much lower than the expected values, because of the poor growing conditions for these early crystals. The conditions for the later crystals improved as we became more skilled in controlling the pressure during growth.

For the remaining crystals the agreement with the heat capacity data is good, considering a scatter of 5%. An interesting observation is the fact that the fits which do not include a vacancy contribution are systematically below the two expected lines, while the fits, that do include a vacancy term, only show random scatter.

4.3.2. Vacancies

Besides the phonon contribution, we expect to find a vacancy term in the pressure. As we have already indicated,

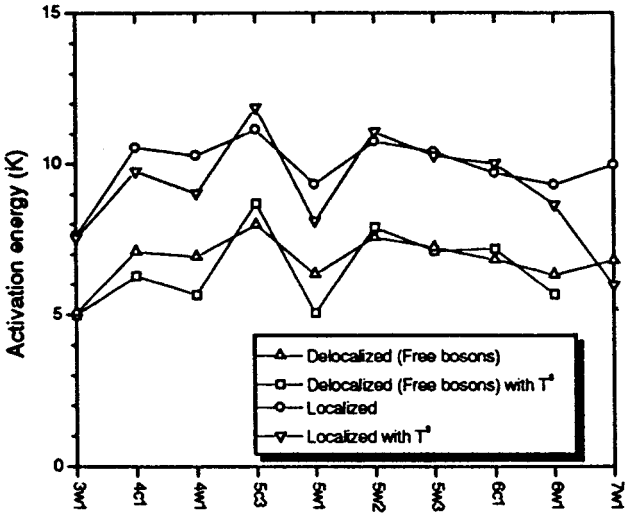

FIG. 10. Activation energy (a_3) as a function of crystal number for the localized and delocalized (free bosons) cases. The addition of the T^8 term decreases the coefficients by a small amount but increases the scatter significantly.

TABLE II. The fit parameters for the localized and delocalized models (Bose gas) from Eqs. (24) and (25). The lowest row shows the average values for the last two coefficients.

	Localized vacancies				Delocalized vacancies (free bosons)			
No.	P_0, MPa	a_1, MPa·K^{-4}	a_2, MPa	a_3, K	P_0, MPa	a_1, MPa·K^{-4}	a_2, MPa·K$^{-5/2}$	a_3, K
3w1	2.5316	2.853×10^3	2.731	7.608	2.5316	2.788×10^3	0.2217	5.056
4c1	2.6227	3.326×10^3	7.467	10.54	2.6227	3.287×10^3	0.2830	7.090
4w1	2.6227	3.309×10^3	4.957	10.27	2.6227	3.281×10^3	0.2005	6.912
5c2	2.5780	3.673×10^3	125.4	14.15	2.5780	3.667×10^3	5.838	11.000
5c3	2.5824	3.603×10^3	12.87	11.14	2.5824	3.588×10^3	0.5914	7.972
5w1	2.5660	3.568×10^3	2.306	9.334	2.5660	3.551×10^3	0.1251	6.341
5w2	2.5780	3.620×10^3	81.17	10.74	2.5780	3.603×10^3	0.3720	7.558
5w3	2.5824	3.611×10^3	6.561	10.39	2.5824	3.590×10^3	0.3036	7.218
6c1	2.5742	3.789×10^3	3.562	9.685	2.5742	3.726×10^3	0.2141	6.821
6w1	2.5742	3.585×10^3	2.676	9.308	2.5742	3.566×10^3	0.1459	6.326
7w1	2.5874	3.633×10^3	3.025	9.971	2.5874	3.618×10^3	0.1389	6.787
Avg.	–	–	7.355	9.83	–	–	0.246	6.77

it is possible that the phonon contribution, which can have T^6, T^8, and even T^{10} terms, in addition to the usual T^4 term, is indistinguishable from the exponential-like vacancy contribution. It is for this reason that we first compared fits with four free parameters containing only phonon terms (T^4, T^6, T^8, and T^4, T^8, T^{10}) and the limiting zero temperature pressure term (P_0) with other fourth-order fits combining the lower-order pressure and phonon terms (P_0, T^4) with a vacancy contribution (free bosons).

It was found that for all crystals the standard deviation would be at least a factor of 2, but mostly an order of magnitude smaller when fitting vacancies to the experimental data. This means that our experimental precision clearly decides in favor of vacancies. More important, the deviation for the phonon fits from the data proved to be systematic, while the deviation of the vacancy fits showed only random scatter.

This can be clearly seen in Figs. 7 and 8. Figure 7 shows deviations up to 200 Pa for the phonon fits, with a pressure resolution of $\simeq$ 0.4 Pa. The largest deviations are seen at the highest temperatures, where the vacancy contribution is largest. Figure 8 shows the standard deviation for several fits.

Having established the presence of vacancies, a comparison was made between the localized model and the free Bose gas model. The standard deviation from the data is shown in Fig. 9. The models fit the data well, but within the experimental precision it is difficult to make a selection.

We must also bear in mind that, although a combination of a T^4 phonon term with a vacancy contribution fits the data better than a T^4, T^8 phonon term, the data of Gardner *et al.* suggest the presence of higher-order phonon terms, which they proved by showing that the heat capacity followed a universal function of T/Θ for all molar volumes. It is possible, however, that a small part of the T^7 term is still due to vacancies. This could be within the experimental error, which is especially close to the melting temperature of his samples, where the data deviate considerably from the universal function. This implies that a fit containing both $\mathbf{T}^4$, T^8 phonon and vacancy terms should be used, and that the magnitude of the higher-order terms need not be as large as found by Gardner *et al.*[16]

TABLE III. The same table as before, but now the T^8 phonon term has been included. This term lowers the vacancy terms and increases the scatter. The lower row contains average values for the vacancy coefficients.

	Localized vacancies				Delocalized vacancies (free bosons)			
No.	P_0, MPa	a_1, MPa·K^{-4}	a_2, MPa	a_3, K	P_0, MPa	a_1, MPa·K^{-4}	a_2, MPa·K$^{-5/2}$	a_3, K
3w1	2.5316	2.829×10^3	2.292	7.525	2.5316	2.768×10^3	0.1873	4.976
4c1	2.6227	3.242×10^3	2.046	9.747	2.6227	3.216×10^3	0.0788	6.283
4w1	2.6227	3.233×10^3	7.385	9.042	2.6227	3.215×10^3	0.0305	5.658
5c2	2.5780	3.584×10^3	5349	19.89	–	–	–	–
5c3	2.5824	3.541×10^3	10.72	11.87	2.5824	3.535×10^3	0.4943	8.703
5w1	2.5660	3.512×10^3	0.2751	8.106	2.5660	3.501×10^3	0.0149	5.065
5w2	2.5780	3.554×10^3	4.091	11.06	2.5780	3.549×10^3	0.1900	7.891
5w3	2.5824	3.546×10^3	2.529	10.25	2.5824	3.538×10^3	0.1198	7.101
6c1	2.5742	3.692×10^3	1.827	10.02	2.5742	3.688×10^3	0.1124	7.180
6w1	2.5742	3.533×10^3	0.6505	8.634	2.5742	3.524×10^3	0.0367	5.680
7w1	2.5874	3.558×10^3	0.0151	5.971			–	–
Avg.	–	–	4.467	9.54	–	–	0.126	6.49

TABLE IV. The average physical properties as derived from the fit coefficients for localized and delocalized models.

	Localized		Delocalized (free bosons)		
	s/k_B, K	Φ/k_B, K	$M/M_{^4\mathrm{He}}$	Δ, K	Φ/k_B, K
T^4	-4.11 ± 0.18	9.83 ± 0.32	5.19 ± 0.7	1.31 ± 0.17	6.77 ± 0.25
T^4, T^8	-4.61 ± 0.33	9.54 ± 0.55	3.58 ± 0.9	2.05 ± 0.47	6.49 ± 0.43

4.4. Discussion

We will now discuss the merits of each model and the validity of the parameters that can be distilled from the fit coefficients. Because it is evident that the phonon part includes a T^8 term, we extended the vacancy fits to incorporate this term as well. In order to restrict the number of free fit parameters, we determined the ratio of the T^4 and the T^8 coefficients from Gardner's data, thereby giving an upper limit on the phonon contribution.

The effect of introducing this additional term is illustrated in Fig. 10, where the activation energy is plotted for all crystals. Including the T^8 term decreases the magnitude of the energies but increases the scatter.

The fit coefficients for the two models are summarized in Table II and Table III. The first and second coefficients $\mathbf{P}_0$ and $\mathbf{a}_1$ were discussed before. For the localized model the third and the last coefficients represent

$$a_2 = N\left(\frac{\partial\Phi}{\partial V} - T\,\frac{\partial s}{\partial V}\right)\mathbf{e}^{s/k_B}, \tag{25}$$

a measure of the nonconfigurational entropy, and

$$a_3 = \Phi/k_B, \tag{26}$$

the activation energy, respectively. Using the calculated values as shown in Table II, in combination with the data of Lengua and Goodkind[17] for $N\cdot\partial\Phi/\partial V$, we find for the nonconfigurational entropy $s = -4.11k_B$. In that case, the vacancy concentration at the melting temperature of the crystals will be approximately 9×10^{-6}. Compared to the phonon entropy, which is $\simeq 3\times10^{-3}k_B$ per atom, such a large negative entropy per vacancy seems rather unphysical. In addition, the extremely low concentration is in clear disagreement with other work in which concentrations as high as 0.1 to 1 percent were found.[12,17] This leads us to conclude that the localized model does not seem to be appropriate for the description of our results.

For the free Bose gas model the third coefficient can be interpreted as

$$a_2 = k_B^{5/2}\left(\frac{M}{2\pi\hbar^2}\right)^{3/2}, \tag{27}$$

from which we can calculate the effective mass M of the vacancies by

$$\frac{M}{M_{^4\mathrm{He}}} = 1.32425\times10^{-3}\cdot a_2^{2/3}. \tag{28}$$

The last coefficient

$$a_3 = \Phi/k_B \tag{29}$$

will again yield the activation energy. Table IV summarizes the averaged results for both models.

The calculated values for the effective masses are larger than those of a bare ^{4}He atom. This is to be expected since the vacancy will not be able to move freely but will feel some interaction with the surrounding atoms. This interaction will reveal itself by the larger mass.

In the tight binding approximation ($\Delta \gg T$), the band width can be determined from the effective mass with Eq. 15. From Table IV it can be seen that the band width is on the order of 1.3–2.1 K, which again indicates that the vacancies are only partly delocalized. This also means that a description in terms of free bosons is not completely valid, since the condition $\Delta \gg T$ has not been quite met.

In the limit where the activation energy is much larger than the temperature and the band width ($\Phi \gg \Delta, T$), a condition which is satisfied in our case, the free Bose gas model, with the effective mass replaced by the band width, according to 15, is equivalent to a band model.[19,20] The values for the band width given in the table for the tight binding approximation are therefore equal to the values that would have been obtained using this band width model.

Lengua and Goodkind[17] determined the molar volume dependence of the activation energy. On the basis of their data we expect $\Phi=4$ K for the molar volumes investigated by us, which is much lower than the values we actually found. The discrepancy can be explained by the fact that the crystals grown by Lengua and Goodkind may have contained a much lower concentration of dislocations than ours. Since dislocations or strains in the crystals will have a localizing effect on the vacancies, this will yield an increase of the effective mass and the energy of formation.

Another source of error could be the assumptions we have to make on the phonon contribution. This might seem worse than it actually is because we only assumed a certain functional behavior (T^4 and T^8). The magnitude of the phonon contribution is still fitted and determined within our experiment. For this reason, we expect these errors to be of minor importance.

5. CONCLUSIONS

We have shown that it is possible to detect the presence of vacancies by measuring the $P-T$ relation of a crystal. It was found that the phonon contribution to the pressure is in good agreement with heat capacity measurements by Gardner *et al.*[16] The additional vacancy term proved to be quite small and its magnitude depends on the assumptions one has to make on the phonon contribution. Within the framework of the free Bose gas model we have determined the effective

mass of the vacancies, which was 3–5 times the bare mass of a ^{4}He atom, corresponding to a band width of 1.3 – 2.1 K.

It was found that the crystal quality can be improved more by thermal cycling than by isothermal annealing. Higher activation energies than those measured by other authors indicate that our samples may contain a high concentration of dislocations. Improved measurements of, for example, the heat capacity combined with simultaneous pressure measurements, and ultrasound measurements to consider crystal quality, would clarify these conflicting results.

This investigation was financially supported by Stichting FOM, which is part of the NWO in The Netherlands.

*E-mail: reyer@rulkol.leidenuniv.nl

[1] A. F. Andreev, Sov. Phys. JETP **29**, 1107 (1969).
[2] D. S. Greywall, Phys. Rev. B **18**, 2127 (1978); Phys. Rev. B **21**, 1329 (1978).
[3] D. J. Bishop, M. A. Paalanen, and J. D. Reppy, Phys. Rev. B **24**, 2844 (1981).
[4] G. Bonfait, H. Godfrin, and B. Castaing, Proc. of the Quantum Fluids and Solids, AIP Conf. Proc. No. **194**, 294 (1989).
[5] M. W. Meisel, Physica B **178**, 121 (1992).
[6] P. G. van de Haar, C. M. C. M. van Woerkens, M. W. Meisel, and G. Frossati, J. Low Temp. Phys. **86**, 349 (1992).
[7] A. I. Shalnikov, Sov. Phys. JETP **20**, 1161 (1965).
[8] K. O. Keshishev, L. P. Mezhov-Deglin, and A. I. Shal'nikov, Sov. Phys. JETP Lett. **12**, 160 (1970).
[9] G. A. Sai-Halasz and A. J. Dahm, Phys. Rev. Lett. **28**, 124 (1972).
[10] D. Marty and F. I. B. Williams, J. Physique **34**, 989 (1973).
[11] K. O. Keshishev, Sov. Phys. JETP **45**, 273 (1977).
[12] B. A. Fraass, P. R. Granfors, and R. O. Simmons, Phys. Rev. B **39**, 124 (1989).
[13] A. R. Allen, M. G. Richards, and J. Schratter, J. Low Temp. Phys. **47**, 289 (1982).
[14] V. N. Grigor'ev, B. N. Esel'son, and V. A. Mikheev, Sov. J. Low. Temp. Phys. **1**, 1 (1975).
[15] T. Mizusaki, Y. Hirayoshi, S. Maekawa, and A. Hirai, Phys. Lett. **50A**, 160 (1974).
[16] W. R. Gardner, J. K. Hoffer, and N. E. Phillips, Phys. Rev. **A7**, 1029 (1973).
[17] G. A. Lengua and J. M. Goodkind, J. Low Temp. Phys. **79**, 251 (1990).
[18] C. A. Burns and J. M. Goodkind, J. Low Temp. Phys. **95**, 695 (1994).
[19] N. Sullivan, G. Deville, and A. Landesman, Phys. Rev. B **11**, 1858 (1975).
[20] C. A. Burns and J. M. Goodkind, Physica B **194–196**, 949 (1994).
[21] Vespel, graphite-filled polyimide, Dupont de Nemours.
[22] XRP-5, 10-mm powder, manufactured by Comptoir Lyon Allemand Lonyot, 13 Rue Montmorency, Paris, France.
[23] G. Frossati, Ph.D. Thesis Grenoble (1978).
[24] G. C. Straty and E. D. Adams, Rev. Sci. Instr. **40**, 1393 (1969).
[25] 2850FT, manufactured by Emerson and Cummings, Canton, Massachusetts 02021, U.S.A.
[26] Degranges et Huot France, 10, rue Bernard-et-Mazoyer, 93300 Aubervilliers, France.
[27] Andeen Hagerling, Inc. 31200 BainBridge Road, Cleveland Ohio 44139–2231, U.S.A.
[28] J. F. Schooley, R. J. Soulen, and G. A. Evans, *Preparation and Use of Superconductive Fixed-point Devices, SRM 767*, Issued by the National Bureau of Standards (1972)
[29] E. R. Grilly, J. Low Temp. Phys. **11**, 33 (1973).
[30] F. E. Moss, A. F. G. Wyatt, and M. J. Baird, Cryogenics **21**, 114 (1981).
[31] P. V. E. McClintock, Cryogenics **18**, 201 (1978).
[32] I. Iwasa and H. Suzuki, J. Low Temp. Phys. **62**, 1 (1986).

This article was published in English in the original Russian journal. It was edited by S. J. Amoretty.

Exchange and spin relaxation in solid ^{3}He

B. Cowan and M. Fardis[1)]

Royal Holloway University of London, Egham Hill, Egham, Surrey TW20 0EX, UK[2)]
(Submitted November 26, 1996)
Fiz. Nizk. Temp. **23** 598–606 (May–June 1997)

Spin relaxation measurements in solid ^{3}He in the temperature region where exchange dominates the behavior are reviewed and reanalyzed. A model which brings together the complex exchange modulation of the dipolar interaction into a single correlation time is adopted. This may be regarded as introducing an effective pairwise exchange Hamiltonian. On the basis of this model new procedures are proposed for obtaining mathematical expressions for the dipolar autocorrelation function and the spectral density functions, which determine the relaxation times. By the appropriate treatment of short-time and long-time asymptotic behavior, together with a method for taking into account the mid-range behavior, it is possible to fit the experimental data extremely well. The success of this procedure seems surprising in the light of multiple spin exchange in solid ^{3}He. It is an indication that the dominant exchange processes scale with density in a similar way. This conclusion is supported by path-integral Monte Carlo calculations. Some consequences and implications of this conclusion are discussed.
 [S1063-777X(97)01205-X]

1. INTRODUCTION

Although Thouless[1] pointed out the importance of multiple spin exchange in solid ^{3}He some time ago, it was only with the discovery of low-temperature, spin-ordered phases that its real significance was appreciated.[2] Certainly, thermal capacity and magnetization measurements in the paramagnetic phase exhibited some deviations, but the existence of the uudd phase was simply incompatible with pairwise Heisenberg exchange. In retrospect, it is surprising that the pairwise exchange model was found to be so successful in the explanation of the higher-temperature NMR behavior of solid ^{3}He. This question is addressed in the present paper.

Traditionally, NMR proved to be a particularly useful tool for the study of exchange in solid ^{3}He. The use of NMR provides a fairly direct probe of spin behavior through the measurement of spin susceptibility, spin relaxation times, and spin diffusion. In the temperature region of about 1 K the spin relaxation is determined solely by internuclear exchange. Here the temperature is high enough for the exchange ''bath'' to be tightly coupled to the lattice, while it is low enough to account for thermal excitation of the vacancies. Historically, this was seen in spin relaxation times which were found to be independent of temperature, but which varied rapidly with density.[3]

2. SPIN RELAXATION–THE FORMALISM

Spin relaxation in solid ^{3}He in the vicinity of 1 K is caused by the exchange modulation of the internuclear dipolar interaction. The relaxation times T_1 and T_2 for this system are given by

$$\frac{1}{T_1}=J_1(\omega)+4J_2(2\omega), \tag{1a}$$

$$\frac{1}{T_2}=\frac{3}{2}J_0(0)+\frac{5}{2}J_1(\omega)+J_2(2\omega), \tag{1b}$$

where the spectral density functions $J_m(\omega)$ are the Fourier transform of the corresponding dipolar correlation functions $G_m(t)$:

$$G_m(t)=\frac{\mathrm{Tr}\{D_m(t)D_m(0)\}}{\hbar^2\,\mathrm{Tr}\{I_z^2\}} \tag{2}$$

and D_m are the components of the dipolar Hamiltonian

$$D_m=\frac{\mu_0\hbar^2\gamma^2}{4\pi\sqrt{5}}\sum_{i,j}(-1)^m\frac{Y_2^{-m}(\Omega_{ij})}{r_{ij}^3}T_{ij}^m.$$

The spin part of the interaction is contained in the second-order spin tensor operators T_{ij}^m:

$$T_{ij}^0=\mathbf{I}^i\mathbf{I}^j-3I_z^iI_z^j,$$

$$T_{ij}^1=\sqrt{\frac{3}{2}}\{I_z^iI_+^j+I_+^iI_z^j\}=-(T_{ij}^{-1})^+,$$

$$T_{ij}^2=-\sqrt{\frac{3}{2}}I_+^iI_+^j=(T_{ij}^{-2})^+,$$

where the index m denotes the total induced spin flip.

The exchange interaction originates in the large zero-point motion of the ^{3}He atoms, which results in the movement of atoms among the lattice sites. The crucial point for multiple spin exchange is that the hard cores of the atoms can favor the coherent exchange of more than two particles.[1] However, since ^{3}He is a spin 1/2 fermion, an equivalent description of this motion is possible in terms of a spin exchange Hamiltonian. This may be written as

$$H_x=-\sum_n(-1)^nJ_nP_n^\sigma, \tag{3}$$

where n labels the number of particles in each cycle, J_n is the exchange frequency for n particle exchange, and P_n^σ is the generator of the permutation of n spins.

In the bcc phase the dominant 2-, 3-, and 4-spin exchange frequencies are of similar order of magnitude ($\sim 10^7$ Hz). However, since the exchange of an odd number of particles is ferromagnetic, while the exchange of an even number is antiferromagnetic, the resultant exchange can be small: a consequence of inexact cancellation of the ferromagnetic and antiferromagnetic tendencies. Thus we have a frustrated system and there is no *a priori* reason to expect the observed behavior to be ferromagnetic or antiferromagnetic. Indeed, different properties of such a system can exhibit different characteristics. This is particularly striking in two-dimensional solid ^{3}He films, which will be discussed for comparison in Sec. 11.

The lattice structure of the bcc solid means that next-nearest-neighbor exchanges should also be considered. This, together with the variety of multiple spin-exchange cycles, leads to a complex dynamical system, although there is a simplification which follows since three spin exchanges can be expressed as a superposition of pairwise exchanges. Notwithstanding these complexities, we shall start by considering a simplified and idealized model. In this paper we will analyze initially, in detail, the consequences of the pairwise Heisenberg exchange Hamiltonian. We will show that this model is consistent with spin relaxation measurements! Having done this, we will then attempt to explain the reasons for this apparent success in the light of the current understanding of multiple spin exchange. For now, therefore, the exchange Hamiltonian to be considered is

$$H_x = -2J\sum_{i<j}^{nn} \mathbf{I}^i\mathbf{I}^j, \tag{4}$$

where i and j label the spin sites, and the sum is taken over nearest neighbors.

We now have a well-defined problem for solution. Using the expression for the exchange Hamiltonian, we can write the time evolution of the dipolar components as follows:

$$D_m(t) = \exp\left(\frac{iH_x t}{\hbar}\right) D_m \exp\left(-\frac{iH_x t}{\hbar}\right),$$

which, from Eq. (2), gives the dipolar autocorrelation function. Fourier transformation then gives the spectral density functions and we can find the relaxation times from Eq. (1). Unfortunately, as is common in systems of this complexity, the problem does not have an analytic solution. Thus effort must be made to approximate methods. In the following sections we will review the traditional approaches, before describing an improved treatment in Sec. 7.

3. MOMENT EXPANSIONS

At short times, the dipolar autocorrelation function may be expanded in powers of time as

$$G(t) = \frac{1}{3}\left\{M_2 - \frac{1}{2}M_4 t^2 + \ldots\right\}. \tag{5}$$

The coefficients expressed in this way correspond to the conventional moments of the absorption lineshape. The important point about such an expansion, as first noted by Waller,[4] is that such moments can be calculated exactly without requiring a complete solution of the problem. Admittedly, evaluation of higher-order moments becomes increasingly difficult, but by diligent application and/or with the aid of a computer meaningful results may be obtained. For our system, the second and fourth moments have been evaluated. The second moment is

$$M_2 = \frac{9C}{20}\frac{\gamma^2\hbar^2}{a^6},$$

where a is the lattice spacing, and C is a constant which depends on the crystal lattice:

$C = 12.25$ for a bcc lattice,

$C = 14.45$ for a hcp lattice.

And the fourth moments are evaluated to be

$M_4 = 22.8 M_2 J^2$ for a bcc lattice,

$M_4 = 42.0 M_2 J^2$ for a hcp lattice.

Note that, as expected, the second moment is independent of motion, here parametrized by J, while the fourth moment is strongly dependent on J. Armed with very little else, the conventional approach at this point is to choose an appropriate functional form for $G(t)$, which is consistent with these values of M_2 and M_4.

4. TRADITIONAL TREATMENT

Experimentally it can be seen from T_1 measurements on solid ^{3}He that the spectral density function $J(\omega)$ is reasonably approximated by a Gaussian in the hcp phase and by a decaying exponential in the bcc phase. Thus, the hcp correlation function $G(t)$ should be approximately Gaussian, while that for the bcc phase should have a Lorentzian profile. In the conventional treatment of exchange-induced relaxation in solid ^{3}He the calculated M_2 and M_4 are fitted to these functions. Using the Fourier transform then yields expressions for the spectral density functions, from which the relaxation times may be found as a function of J:

$$G(t) = \frac{\overset{\text{bcc}}{M_2}}{3}\frac{1}{1+M_4 t^2/2M_2}, \quad G(t) = \frac{\overset{\text{hcp}}{M_2}}{3}\exp\left(-\frac{M_4}{2M_2}t^2\right).$$

But since M_4 is known in terms of M_2 and J, we have

$$G(t) = \frac{M_2}{3}\frac{1}{1+11.4J^2t^2}, \quad G(t) = \frac{M_2}{3}\exp(-21J^2t^2).$$

Using the Fourier transform yields

$$J(\omega) = \frac{0.31M_2}{J}\exp\left(-\frac{\omega}{3.38J}\right),$$

$$J(\omega) = \frac{0.05M_2}{J}\exp\left(-\frac{\omega^2}{84J^2}\right),$$

from which may be found the relaxation times as a function of exchange frequency J and Larmor frequency ω.

These spectral density functions make definite predictions about the frequency dependence of the relaxation times, in particular, that of T_1. In practice, these are not quite con-

sistent with the extensive experimental data available. Since these expressions have a single frequency parameter J and since the coefficient of ω/J is fixed by the short time expansion, while the functional form of the high-frequency behavior might be correct, it is not possible to ensure precise numerical agreement, because there is no free parameter with which to scale the frequency. This casts doubt on the values of J inferred from these analyses. A previous attempt to improve these functional expressions has been made by Guyer *et al.*[5]

The problem is to obtain a plausible approximation of the spectral function on the basis of limited information. Put another way, this means making the best possible use of all information available. Thus far, we have considered knowledge of the short-time behavior of the autocorrelation function. In the next section we see that information is available about its long-time behavior. In Sec. 6, we see that something may even be said about intermediate behavior as well. All information is drawn together in Sec. 7, where ''improved'' expressions for the spectral density/correlation function are obtained.

5. SPIN DIFFUSION

The flip-flip nature of the exchange interaction means that any excess magnetization in a part of the specimen will gradually become distributed uniformly. This diffusive process is very much slower than that found in fluids, but it may still be observed by the technique of spin echoes in a field gradient.[6]

Since J is the rate at which the $|\uparrow\downarrow\rangle$ spin configuration changes to the $|\uparrow\downarrow\rangle$ configuration, a simple counting argument implies that the order of magnitude of the diffusion coefficient for the magnetization will be $\approx Ja^2$. Once again, exact calculation of this relation, to find the numerical coefficient is impossible. However, a moment method of approximation[7] may be used, and it is actually possible to place bounds on the value of the coefficient.[8] The best estimates are found for the two lattices:

$$D = 0.655\ Ja^2 \quad \text{for a bcc lattice,}$$

$$D = 0.860\ Ja^2 \quad \text{for a hcp lattice.}$$

These relations are well-supported by spin echo measurements.[8,9,10]

Diffusion is a hydrodynamic process whose validity is limited to the long wavelength, long time limit. At shorter times and distances the precise details of the atomic motion become important. So far as spin relaxation in solid ^{3}He is concerned, this has the implication that both the long-time behavior of $G(t)$ and the low-frequency behavior of $J(\omega)$ are determined by the spin diffusion.[12] We therefore have the asymptotic expansion

$$G(t) \sim \frac{\hbar^2\gamma^4\alpha\sqrt{\pi}}{60\sqrt{2}D^{3/2}}\, t^{-3/2} + \ldots, \tag{6}$$

where a is the spin density. This diffusive hydrodynamic behavior has its corresponding effect in the frequency domain. We therefore have

$$J(\omega) = J(0) - \frac{1}{30}\frac{\pi a\hbar^2\gamma^4}{D^{3/2}}\,\omega^{1/2} + \ldots\,. \tag{7}$$

In both these expressions D may be eliminated in favor of J. From Eq. (7) the behavior of $J(\omega)$ at short frequencies provides another means of measuring the spin diffusion coefficient.[12] This makes it possible to observe smaller values of D, which may be further extended through $T_{1\rho}$ measurements. Note that $J(\omega)$ is not analytic at the origin, in contrast to the exponential and Gaussian functions discussed in the previous section.

In Sec. 3 we obtained an expression for the short-time behavior of the dipolar autocorrelation function $G(t)$. In this section we have obtained an expression for its long-time behavior. Any approximation function should satisfy both these conditions.

6. UNIVERSALITY AND THE T_1 MINIMUM

It is well-known that a minimum in T_1 occurs as the correlation time of the motion varies at a given Larmor frequency. The frequency at which the minimum is observed gives an order-of-magnitude estimate of the velocity. The minimum in T_1 is related to the behavior of the spectral density function in the middle range. In this section we shall formalize these ideas.[13] This will allow us to augment the long- and short-time behavior of $G(t)$ with further information which any approximation function would accept.

Within the framework of the Heisenberg pairwise exchange model there is a single microscopic time $\tau \sim J^{-1}$, which characterizes the dynamical behavior of the spins. From it a number of general interferences can be made about the relaxation in such cases. This can be illustrated as follows. Let us write the autocorrelation function $G(t)$ as the product of its initial value $G(0)$ and a normalized shape function g:

$$G(t) = G(0)g(t/\tau).$$

The shape function $g(t/\tau)$ is unity at $t = 0$ and its dimensionless argument t/τ indicates that τ is the characteristic time of this system; it is the natural time unit in terms of which the dynamical behavior of the system scales. Note that for simplicity we are considering a rotationally invariant system so that $G(t)$ need not be encumbered by a spin-flip subscript.

The spectral density function $J(\omega)$ is found from the Fourier transform of $G(t)$:

$$J(\omega) = \int_{-\infty}^{\infty} G(0)g(t/\tau)\exp(i\omega t)\,dt,$$

which, after changing the integration variables through $x = t/\tau$, can be written

$$J(\omega) = G(0)\tau j(\omega\tau),$$

where $j(z)$ is the Fourier transform of the shape function $g(x)$.

For simplicity let us start with a simplified expression for T_1

$$\frac{1}{T_1} = J(\omega),$$

where the double frequency term is disregarded. It is a straightforward matter to show that the use of this expression does not detract from the validity of our general conclusions[13] by subsuming the double frequency term into a composite $J(\omega)$ function. The simplified expression for T_1 is now

$$\frac{1}{T_1} = G(0)\tau j(\omega\tau).$$

If we divide this expression by τ or multiply it by ω, then the resulting expressions $1/(T_1\tau)$ and ω/T_1 will depend on ω and τ only through the product $\omega\tau$:

$$\frac{1}{T_1\tau} = G(0)j(\omega\tau), \tag{8}$$

$$\frac{\omega}{T_1} = G(0)\omega\tau j(\omega\tau). \tag{9}$$

This means that T_1, which is measured at a fixed τ by varying ω, and T_1, which is measured at a fixed ω by varying τ, will be universal functions of $\omega\tau$ for a given system.[14] The data plotted in this manner will therefore fall on single curves. This will be seen in Sec. 8. For now, our concern is to discuss the T_1 minimum.

In general, [except in very unusual circumstances where $j(0)$ diverges] $j(z)$ starts from $j(0)$ and initially is a slowly decreasing function of its argument, as in Eq. (7). The product $zj(z)$ starts from zero, when z is zero, and initially grows linearly. However, for large values of z the decay of $j(z)$ outweighs the linear growth of the z prefactor and the product decreases. Somewhere in between, when z is of the order of unity, say, at $z = z'$, $zj(z)$ must accordingly have a maximum.

Looking at the expression for T_1 as a function of τ (at a fixed frequency) [Eq. (9)], we see that the existence of a maximum in $zj(z)$ tells us that there must necessarily be a minimum in T_1 as the characteristic time is varied. The ''position'' of the T_1 minimum is given by $\omega_0\tau = z'$ or

$$\tau_{\min} = z'/\omega_0.$$

Thus, when a minimum is observed, within a constant of the order of unity, the characteristic time of the motion may be estimated by the Larmor period. The value of T_1 at the minimum may be written, from Eq. (9) as

$$\frac{1}{T_1^{\min}} = \frac{G(0)z'j(z')}{\omega_0}$$

or, since $G(0) = M_2/3$, and denoting the number $z'j(z')$ by K^{-1}, we can write

$$T_1^{\min} = 3K\,\frac{\omega_0}{M_2}.$$

We see that at the minimum the value of T_1 is proportional to the Larmor frequency. The number K depends on the shape of the autocorrelation function or the spectral density function. Thus, for example, for a Gaussian correlation function $K = 0.657$, while for an exponential $K = 1$. The value of K for a given system may be found from observations of T_1 minima over a range of frequencies. This information may be used in the approximation of the spectral density and autocorrelation functions.

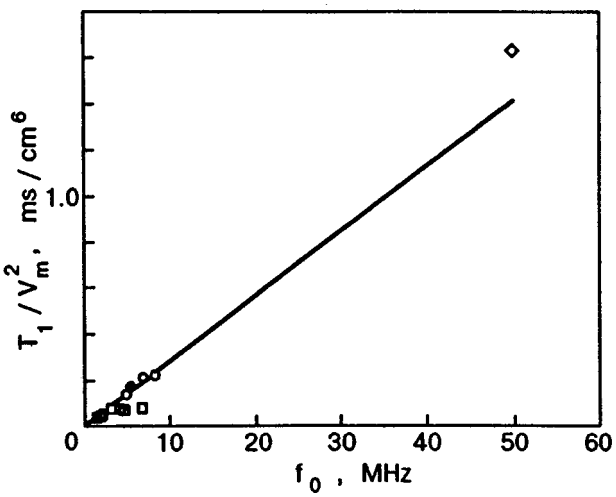

FIG. 1. T_1 minima at different Larmor frequencies for bcc ^{3}He. ○ Richardson, Hunt, and Meyer (1965), □ Richards, Hatton, and Giffard (1965), ● Reich (1963), ◇ Chapellier, Bassou, Devoret, Delrieu, and Sullivan (1985).

7. APPROXIMATING $G(t)$ AND $J(\omega)$

Let us now consider specifically the bcc phase of solid ^{3}He. We proceed to the construction of an approximate spectral density function, which is consistent with i) the short-time microscopic moment expansion of $G(t)$, ii) the spin diffusion in the hydrodynamic limit, and iii) the K value characterizing the mid-range region of the T_1 minima. In order to find the value of K we have collected T_1 minimum observations which we have plotted against Larmor frequency in Fig. 1. The T_1 data were divided by the square of the molar volume to remove the small dependence on M_2, which is present when the characteristic time is varied by changing the density. The straight line through the data is given by

$$\frac{T_1^{\min}\ (\text{in ms})}{V_m^2\ (\text{in cm}^6)} = 2.826\times10^{-2}\,\frac{\omega_0}{2\pi}\,(\text{in MHz}).$$

This ''fit'' to the data takes into account the larger experimental error in the data points at 50 MHz.

The functional form adopted to approximate $G(t)$ is given by

$$\frac{G(t)}{G(0)} = \frac{a_1}{(1+b_1^2J^2t^2)^4} + \frac{a_2}{(1+b_2^2J^2t^2)^{3/4}},$$

where the parameters a_1, a_2, b_1, and b_2 were chosen in such a way as to satisfy the above-mentioned criteria. The second term of this expression gives the correct long-time behavior, while its Fourier transform leads to the corresponding short-frequency form. The expression for the spectral density function can be written in analytic form as

$$\frac{J(\omega)}{G(0)} = \frac{a_1\pi}{96b_1J}\left\{\left(\frac{\omega}{b_1J}\right)^3 + 6\left(\frac{\omega}{b_1J}\right)^2 + 15\left(\frac{\omega}{b_1J}\right)\right.$$

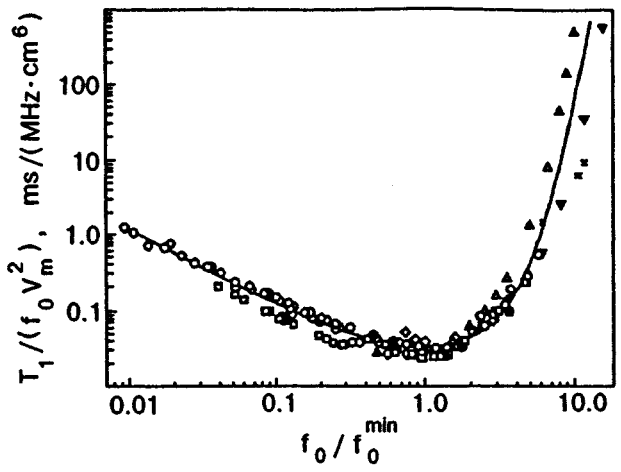

FIG. 2. Reduced plot of T_1 data for bcc ^{3}He together with the ''theoretical'' curve. ○ Richardson, Hunt, and Meyer (1965), □ Richards, Hatton, and Giffard (1965), △ Thomlinson, Kelley, and Richardson (1972), ▽ Bernier and Guerrier (1983), ◇ Chapellier, Bassou, Devoret, Delrieu, and Sullivan (1985), ● Reich (1963), × Kirk and Adams (1972), + Beal, Giffard, Hatton, Richards, and Richards (1964).

$$+15\Big\}\exp\left(-\frac{\omega}{b_1 J}\right)$$
$$+\frac{a_2}{2^{1/4}}\sqrt{\frac{2}{\pi}}\,\Gamma\left(\frac{1}{4}\right)\frac{1}{b_2 J}\left(\frac{\omega}{b_2 J}\right)^{1/4} K_{1/4}\left(\frac{\omega}{b_2 J}\right). \tag{10}$$

The parameter values are

$$a_1 = 0.840, \quad a_2 = 0.160,$$
$$b_1 = 1.768, \quad b_2 = 2.736,$$

Γ is the gamma function, and K is a Bessel function. We have also included a factor ξ by which the lattice sum value of M_2 is renormalized as a result of the zero-point motion that averages the interparticle spacing a.[14] We find a value of $\xi = 0.787$; further discussion of this matter is deferred to Sec. 9.

The adiabatic part of T_2 is given in terms of the zero frequency value of $J(\omega)$:

$$\frac{1}{T_2} = 0.270\,\frac{M_2}{J},$$

which is the quantitative manifestation of the qualitative result $T_2^{-1} = M_2\tau_c$. In other words, $\tau_c = 0.270/J$; we see that J^{-1} is a measure of the characteristic time for the exchange, but now with a precise numerical multiplier.

8. UNIVERSAL PLOT OF RELAXATION DATA

In Fig. 2 we show a plot of all published T_1 measurements on ^{3}He in the bcc phase presented in ''reduced'' form.

We know, in general, from the discussions in Sec. 6 that for a given system T_1/J is a single-valued function of ω_0/J. Since the exchange frequency J is proportional to the frequency at which the T_1 minimum is observed, it follows that the same universal behavior will be displayed when plotting T_1 divided by the frequency of the minimum against Larmor frequency divided by the minimum frequency. This curve we have plotted in Fig. 2, where the T_1 values were also divided by the square of the molar volume to account for the variation of M_2 [and thus $G(0)$] with density.

The experimental points, as we can see, fall very well on a single curve. At higher frequencies there is some discernible deviation from the universal behavior, which we attribute to different crystal orientations; in the analysis we make the assumption that we have a polycrystalline sample, taking averages over the crystal orientation. In the low-frequency region we see that the data of Richards *et al.* fall consistently below the other points. It is believed that this is a consequence of inaccuracies in the determination of the molar volume of the crystals.

Presenting the relaxation data in this manner facilitates the testing of proposed ''theoretical'' forms for the spectral density function $J(\omega)$. We have the proposed function in Eq. (10). For this function the relation between the exchange frequency and the frequency of the minimum is found to be

$$\omega_0^{\min} = 2.42J.$$

Use of this expression enables Eq. (10) to be plotted on the graph of experimental data. The solid line in Fig. 2 shows this plot. We conclude that Eq. (10) does indeed provide a good approximation of the functional form of the spectral density function.

The result of all these considerations is that the exchange frequency can be deduced in a consistent manner from the measurements made at each molar volume. The best fit to our analysis yields

$$\frac{J}{2\pi} = 14.08\left(\frac{V_m(\mathrm{cm}^3)}{24}\right)^{\eta}\ \mathrm{MHz}, \tag{11}$$

where the exponent $\eta = 18.3$. This compares favorably with the results obtained by other mean.[16]

9. T_1 SUM RULES AND MOMENTS

Moments were introduced originally in the study of transverse relaxation. However, since there is a close connection between the moments and the autocorrelation function $G(t)$, as we have seen in Eq. (5), and since the spin lattice relaxation is related to $J(\omega)$, which is the Fourier transform of $G(t)$, it follows that T_1 and the moments must be related. We shall investigate such relationships in this section.

Starting from the expression for the dipolar T_1, Eq. (1a), after changing the variables in the Fourier integral for the double frequency term, we can write

$$\frac{1}{T_1} = \int_{-\infty}^{\infty}\left\{G(t) + 2G\left(\frac{t}{2}\right)\right\}\exp(i\omega t)\,dt.$$

Again we have assumed rotational invariance for simplicity but the generalization to distinct $G_1(t)$ and $G_2(t)$ functions is straightforward. Inverting this Fourier integral, we obtain

$$G(t) + 2G(t/2) = \frac{1}{2\pi}\int_{-\infty}^{\infty}\frac{\exp(-i\omega t)}{T_1}\,d\omega,$$

and then expanding in powers of time leads to

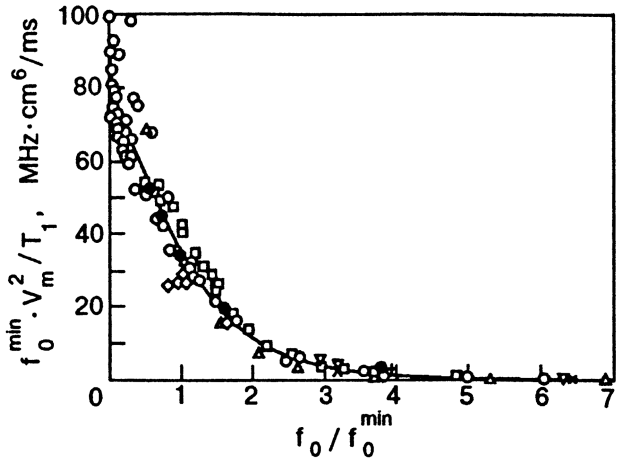

FIG. 3. Second moment sum rule for bcc ^{3}He.

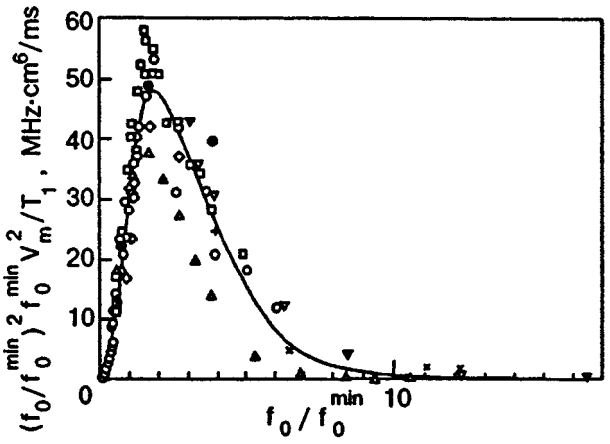

FIG. 4. Fourth moment sum rule for bcc ^{3}He.

$$\sum_{n=0}^{\infty} \frac{G^{(n)}(0)}{n!} t^n + 2\sum_{n=0}^{\infty} \frac{G^{(n)}(0)}{n!} \left(\frac{t}{2}\right)^n = \frac{1}{2\pi} \int_{-\infty}^{\infty} \sum_{n=0}^{\infty} \frac{(-1)^n \omega^n t^n}{n! T_1} d\omega.$$

Equating the powers of time then gives, since for even n the integral is symmetric,

$$\int_0^{\infty} \frac{\omega^n}{T_1} d\omega = (-1)^n \pi \left(1 + \frac{1}{2^{n-1}}\right) G^{(n)}(0),$$

which leads to a set of frequency sum rule expressions for T_1 for increasing n. The sum rules can be expressed in terms of moments, using the relations established in Eq. (5). In this way, for $n = 0,2,4,$ for example, we obtain

$$\int_0^{\infty} \frac{d\omega}{T_1} = \pi M_2,$$

$$\int_0^{\infty} \frac{\omega^2 d\omega}{T_1} = \frac{\pi}{2} M_4,$$

$$\int_0^{\infty} \frac{\omega^4 d\omega}{T_1} = \frac{3\pi}{8} M_6$$

in the case of rapid motion.

If one has a set of T_1 data taken over a range of Larmor frequencies, then the natural inclination is to interpolate smoothly between the points while extrapolating in an intelligent way beyond the end points. Relations such as the sum rules above provide a test of the validity of such procedures. One can immediately tell if all the area of $J(\omega)$ has been exhausted or if there is some unforseen behavior hiding between or beyond the experimental points.

In the present context the M_2 sum rule may be used for a determination of the renormalization factor ξ alluded to in Sec. 7. The area under the ''universal'' plot of T_1 data in Fig. 3 gives the renormalized value for M_2 and the line shown corresponds to our spectral density function of Eq. (10), with $\xi = 0.787$.

Since $M_4 = \text{const} \times M_2 J^2$, it follows that M_4 will be renormalized by the same factor. The area under the ''universal'' plot of T_1 data in Fig. 4 gives the renormalized value for M_4 and the line corresponds to the spectral density function of Eq. (10), with the chosen $\xi = 0.787$. The fit of the line through the experimental data is not so good in this case, particularly when $f_0/f_0^{\min} > 1$. This plot enhances the high-frequency discrepancies in T_1; what we are seeing here is a magnified version of the high-frequency deviations in Fig. 2.

10. MULTIPLE-SPIN EXCHANGE

The reality of the situation is that pairwise Heisenberg exchange is not adequate to describe the zero point motion in the bcc phase of ^{3}He. This becomes evident at lower temperatures. Thermal capacity and magnetic susceptibility may be analyzed on the basis of pairwise exchange, and theoretical expressions for these properties may be obtained as power series in inverse temperature. At lower temperatures, where higher-order terms are important, the experimental data are not consistent with the simple Heisenberg model. Even lower temperatures there is a phase transition to a complex, antiferromagnetic, spin-ordered phase, which definitely requires multiple spin exchange for its explanation.

This being the case, it seems then paradoxical that the scaling treatment of relaxation works so well and, in particular, that the data can be ''reduced'' so as to fall so well on the universal curve in Fig. 2. The high quality of this reduced data plot implies that so far as NMR relaxation is concerned, the system can be understood in terms of a single correlation time that characterizes the motion. In the context of the above discussion, the system may be regarded, equivalently, as having an effective pairwise exchange interaction. The effective pairwise exchange frequency will be some functional combination of the frequencies of the various interchange processes. Matsumoto *et al.*[17] have calculated the fourth moment for a restricted subset of two-, three-, and four-particle exchanges. We thus find the effective pairwise exchange frequency determining the NMR relaxation times to be the combination

$$J_{\text{eff}}^2 = J_{nn}^2 - 14 J_{nn} J_t + 6.7 J_{nn} K_p + 61 J_t^2 - 54 J_t K_p + 18 K_p^2,$$

where J_{nn} is the pairwise exchange frequency, J_t is the frequency of the three-particle exchange, and K_p is the four-particle exchange frequency for interchanges in a plane.

The reduced data plots incorporate measurements made over a range of molar volumes, where the exchange varies over some two orders of magnitude. The quality of the reduced data plot then indicates that the interchange frequencies of the various exchange cycles scale with density in a similar manner, as Eq. (11). Ceperley and Jacucci have investigated this[18] using path-integral Monte Carlo calculations. They obtained the frequencies for a variety of two-, three-, four-, and six-spin exchanges (planar 5-spin exchange has also been calculated[19]). They found that the largest exchange frequencies scale with density in a similar manner; the exponents are $\eta_{nn} = 19.0$, $\eta_t = 19.8$, and $\eta_p = 17.6$. There is, however, no *a priori* reason to expect these dominant exchange processes to vary with density in the same way; indeed, it is a surprise that they do. One is led to wonder, with Cross,[20] if multiple spin exchange might be no more than a descriptive construction rather like the planetary epicycles of Ptolemy, and that there may be a more elementary physical origin of the atomic motion. Currently there is no satisfactory, first-principles, theoretical explanation, but it is likely that vacancy-interstitial formation is the fundamental process out of which all exchange cycles are built.[19] The different trajectories taken by the vacancy before reuniting with its interstitial would then correspond to different multiple-spin exchange cycles, the exponent η reflecting the probability for the creation of the pair. The elucidation of this problem remains one of the unsolved problems in the theory of solid helium.

11. SOLID ^{3}He FILMS

Further insights into the nature of exchange in bulk solid ^{3}He may be found from a consideration of two-dimensional films of ^{3}He. In submonolayer films the observed spin relaxation behavior is similar to that in three dimensions. The relaxation data may be analyzed[21] in a manner similar to that described above. Again, the data may be scaled onto a single curve, implying that here also the various exchange frequencies scale with density in the same way. When expressed as a function of interparticle spacing, the variation in two and three dimensions is similar.

The situation is very different, however, when considering multilayer films of ^{3}He. Here the main experimental tools have been measurements of spin susceptibility and thermal capacity. Starting with a submonolayer film, as the adsorbate density increases, a 2D triangular close-packed solid is formed. Increasing the density further, upon completion of the monolayer, there is promotion of atoms to the second layer. It is initially a fluid, but as the density is increased, the second layer solidifies. The first paramagnetic layer plays a very small part in the observed spin behavior; this has been confirmed by analyzing the two-component NMR line profiles and by replacing the first layer with a monolayer of ^{4}He.[22]

When it forms, the second solid layer exhibits antiferromagnetic exchange. However, when the density is increased further, the third fluid layer is formed. This fluid overlayer has a dramatic effect on the second layer, changing it from the antiferromagnetic to the ferromagnetic state. Simultaneous thermal capacity and magnetization measurements have been made.[23] These measurements indicate that the changeover becomes manifest in these two properties at different densities. A ferromagnetic thermal capacity can coexist with an antiferromagnetic spin susceptibility! This can be understood in terms of the different combinations of exchange frequencies which enter into the expressions for thermal capacity and spin susceptibility. The fluid overlayer shifts the balance of the different exchange processes. In contrast with the bulk solid, in 2D the various exchange frequencies can be varied in different ways; here one has the facility to continuously tune the frustrated spin exchange.[24,25] The rich variety of phenomena in bulk solid ^{3}He is therefore likely to be exceeded dramatically in solid ^{3}He films.

[1)]Present address: National Center for Scientific Research ''Demokritos,'' Athens, Greece.
[2)]E-mail: b.cowan@vms.rhbnc.ac.uv

[1] D. J. Thouless, Proc. Phys. Soc. **86**, 893 (1965).
[2] M. Roger, J. H. Hetherington, and J. M. Delrieu, Rev. Mod. Phys. **55**, 1 (1983).
[3] M. G. Richards, J. Hatton, and R. P. Giffard, Phys, Rev. **139**, A91 (1965).
[4] I. Waller, Z. Phys. **79**, 370 (1932)
[5] R. A. Guyer, R. C. Richardson, and L. I. Zane, Rev. Mod. Phys. **43**, 532 (1971).
[6] H. C. Torrey, Phys. Rev. **104**, 563 (1956).
[7] A. G. Redfield, Phys. Rev. **116**, 315 (1959).
[8] B. P. Cowan, W. J. Mullin, and E. Nelson, J. Low Temp. Phys. **77**, 181 (1989).
[9] H. A. Reich, Phys. Rev. **129**, 630 (1963).
[10] J. R. Thompson, E. R. Hunt, and H. Meyer, Phys. Lett. 25A, 313 (1967).
[11] B. Eselson, V. Mikheev, and V. Grigor'ev, Sov. J. Low Temp. Phys. **2**, 599 (1976).
[12] B. P. Cowan and M. Fardis, Phys. Rev. B. **44**, 4304 (1991).
[13] B. P. Cowan, L. A. El-Nasr, M. Fardis, and A. Hussain, Phys. Rev. Lett. **58**, 2308 (1987).
[14] B. P. Cowan, *Nuclear Magnetic Resonance and Relaxation*, Cambridge University Press, (1997).
[15] A. Landesman, Ann. de Phys. **8**, 53 (1973).
[16] M. F. Panczyk and E. D. Adams, Phys. Rev. **A1**, 1356 (1970).
[17] K. Matsumoto, T. Abe, and T. Izuyama, J. Phys. Soc. Jpn. **58**, 1149 (1989).
[18] D. M. Ceperley and G. Jacucci, Phys. Rev. Lett. **58**, 1648 (1988).
[19] D. M. Ceperley, Rev. Mod. Phys. **67**, 279 (1995).
[20] M. Cross, Jpn. J. App. Phys. **26**, 1855 (1987).
[21] B. P. Cowan, L. A. El-Nasr, M. Fardis, and A. Hussain, Phys. Rev. Lett. **58**, 2308 (1987).
[22] C. P. Lusher, J. Saunders, and B. P. Cowan, Europhys. Lett. **14**, 809 (1991).
[23] M. Siqueira, J. Nyéki, B. Cowan, and J. Saunders, Phys. Rev. Lett. **76**, 1884 (1996).
[24] M. Siqueira, J. Nyéki, B. Cowan, and J. Saunders, Czech J. Phys. **46**, ??, (1996).
[25] M. Siqueira, J. Nyéki, B. Cowan and J. Saunders, Phys. Rev. Lett. (1996).

This article is published in English in the original Russian journal. It was edited by S. J. Amoretty.

Spin–lattice relaxation in phase-separated ^{3}He–^{4}He solid solution

N. P. Mikhin, A. V. Polev, È. Ya. Rudavskii, and V. A. Shvarts

*B. Verkin Institute for Low Temperature Physics and Engineering, National Academy of Sciences of the Ukraine, 310164 Kharkov, Ukraine**

(Submitted November 14, 1996)
Fiz. Nizk. Temp. **23**, 607–614, May–June (1997)

The spin–lattice relaxation time in a ^{3}He–^{4}He solid solution with the initial concentration 3.18% ^{3}He is measured during phase separation by using the pulsed NMR technique. The relaxation time in a concentrated bbc phase formed as a result of phase separation is found to be independent of temperature over the entire range of its existence and is determined by the Zeeman-exchange interaction mechanism. In the dilute hcp daughter phase, the spin–lattice relaxation time increases on cooling according to the law $T_1 \sim x^{-n}$, where $n = 0.88 \pm 0.12$, and x is the ^{3}He concentration. The values of T_1 in this phase coincide with the values corresponding to a homogeneous (nonseparated) solution of the same concentration.
 [S1063-777X(97)01305-4]

INTRODUCTION

B. N. Esel'son was one of the first scientists who started in the fifties the systematic experimental investigations[1] of ^{3}He–^{4}He solid solutions which proved to be a very rich and interesting quantum system. At the beginning of seventies, a new fundamental phenomenon, viz., quantum diffusion of ^{3}He impurities, was discovered in this system. At low temperatures, these impurities are not localized, but form a gas of quasiparticles moving over a ^{4}He crystal.[2]

Large amplitudes of zero-point atomic vibrations in crystals of helium isotopes lead to overlapping of wave functions. In the case of ^{3}He, exchange processes associated with tunneling of neighboring atoms take place. Exchange processes determine not only spin diffusion, but also the magnetic properties of the system, and above all, the spin–lattice relaxation.

Spin–lattice relaxation processes in pure solid ^{3}He were studied in detail experimentally and theoretically (see, for example, Refs. 3–5). It was found that the temperature dependence of spin–lattice relaxation time T_1 is complex and nonmonotonic. This is due to the face that, according to the Garvin–Landesman model, solid ^{3}He can be regarded as a system consisting of three (Zeeman, exchange, and lattice) subsystems, and the energy between individual subsystems is transferred in diverse ways.

At high temperatures, the Zeeman subsystem associated with interaction between nuclear spins and the applied magnetic field transfers its energy to the lattice due to fluctuations of the local dipole field induced by thermally activated vacancion diffusion of atoms. Thus, the Zeeman subsystem relaxes directly to the lattice, and the function $T_1(T)$ passes through a minimum when the characteristic diffusion time becomes of the order of the reciprocal Larmor frequency.

The thermally activated diffusion flow of ^{3}He atoms is suppressed upon cooling and ultimately stops affecting the dipole–dipole interaction of nuclear spins. Under these conditions, the interaction between the Zeeman subsystem and the lattice occurs through the exchange subsystem as long as the latter has the lattice temperature. All this leads to one of the most interesting features of magnetic relaxation in solid ^{3}He, i.e., the existence of a wide region in which the time T_1 does not depend on temperature (the region of exchange plateau).

As the crystal is cooled further, the number of vacancies in it becomes insufficient not only for a direct thermal contact between the Zeeman subsystem and the lattice, but also for interaction between the exchange subsystem and the lattice. In this region, the relaxation of nuclear magnetization is determined by the exchange–vacancion interaction. An analysis of T_1 proved that the spin–lattice relaxation time in this case increases with decreasing temperature, which is in accord with experimental data.[3–5]

In this temperature range, ^{4}He impurities in a ^{3}He crystal can affect the spin–lattice relaxation processes significantly.[6] Such impurities behave as mobile point defects (delocalized atoms) moving with the tunnel frequency J_{43} which is of the same order of magnitude as the tunnel frequency J_{33} characterizing the ^{3}He–^{3}He exchange. In the region of the exchange plateau, ^{4}He impurities virtually do not change the time T_1, while at lower temperatures their influence becomes significant. In this region, the processes of phonon scattering by ^{4}He atoms can also make a contribution to the temperature dependence of T_1.[3–5]

Another temperature-independent relaxation process controlled by the concentration x_4 of ^{4}He impurities was observed by Bernier and Deville[6] in the low-temperature region. It was found that the corresponding spin–lattice relaxation time T_{1D} varies with x_4 as $T_{1D} \sim x_4^{-3}$. In the frame of the proposed phenomenological model, these authors explained the process by diffusive energy transfer from the Zeeman and exchange subsystems to relaxation centers consisting of ^{4}He clusters. This region on the temperature dependence of T_1 is often referred to as the diffusion plateau. Later, Bernier and Guerrier[5] also considered a possible role of dislocations in spin–lattice relaxation in the region of the low- temperature (diffusion) plateau and obtained an agreement with experimental data under the assumption that the energy is transferred from the Zeeman and exchange sub-

systems to the walls of dislocations which are coupled with the lattice strongly.

Magnetic relaxation in ^{3}He–^{4}He solid solutions was studied in Refs. 7–10 over a wide temperature range, but was not completed as in the case of pure ^{3}He. Miyoshi *et al.*,[7] who studied solutions with the concentration $x = 1.94–32.1\%$ ^{3}He, observed a Zeeman–exchange plateau both for the bcc and for the hcp phase as in the case of pure ^{3}He. They believed that the exchange interaction in the solution does not depend on the ^{3}He concentration, and the concentration dependence of the spectral density function is only due to the dependence $\omega_E \sim x^{1/2}$, where ω_E is the exchange frequency.

The experiments[7] were subsequently extended to the region of more dilute solutions of ^{3}He in ^{4}He (down to 0.2% ^{3}He),[8] and the obtained results were interpreted by the authors under the assumption that the main tunnel motion is the mutual exchange between neighboring ^{3}He and ^{4}He atoms. This temperature independent process is determined by the ^{3}He concentration and the molar volume of the crystal. If a ^{3}He atom is surrounded by z ^{4}He atoms, the characteristic time

$$\tau_{34} = (zJ_{34})^{-1} \tag{1}$$

of the process is determined by the tunnel frequency J_{34} of exchange for the ^{3}He–^{4}He pair. In this case, the experimental data could be described by using a single fitting parameter τ_{34}, and the concentration dependence of the spin–lattice relaxation time corresponded to the x^{-1} law. The same concentration dependence was also recorded by Richards *et al.*,[9] where the time T_1 was measured in the concentration range $0.01–0.24\%$ ^{3}He.

Hirayoshi *et al.*[10] studied magnetic relaxation in solutions containing from 0.22 to 7.2% ^{3}He in the region of the tunnel ''plateau.'' In contrast to the previous model, they assumed that the contribution to the spectral density function comes from both tunnel motions ^{3}He–^{3}He and ^{3}He–^{4}He. They also succeeded in explaining the obtained results on the basis of the proposed model with a single fitting parameter.

Thus, a single approach to the description of spin–lattice relaxation in ^{3}He–^{4}He solid solutions has not been worked out. Magnetic relaxation in phase-separated solutions, in which disperse inclusions of the concentrated phase are formed as a result of isotopic phase separation in the matrix of the dilute phase has also been studied insufficiently. This phenomenon was mentioned only in Ref. 8 in connection with the measurements of relaxation time.

This research mainly aims at an analysis of spin–lattice relaxation in a solution containing 3.18% ^{3}He over a wide temperature range. The main attention is paid to magnetic relaxation in daughter phases formed as a result of isotopic phase separation. Thus, the solid solution under investigation was transformed from the initial hcp phase to the mixture of a concentrated bcc phase and dilute hcp phase, which allowed us to study relaxation in such a complex and interesting system.

EXPERIMENTAL TECHNIQUE

We studied several samples of ^{3}He–^{4}He solid solutions grown from the initial mixture with the concentration $(3.18 \pm 0.02)\%$ ^{3}He during 0.5 h by the capillary blocking technique. In order to eliminate possible gradients of pressure and concentration, the samples were annealed near the melting point for 24 h. We used the experimental setup described in Ref. 11 and containing a cylindrical NMR cell prepared from the epoxy composite Stycast 1266 and connected with the nuclear stage through a thermal switch.

The samples were in the form of cylinders of diameter 4 mm and length 20 mm, and measurements were made under a pressure of 3.7 MPa which was recorded by a capacitive pickup in situ. The sample in the cell was cooled through a silver stem with a silver heat exchanger. Measurements were made in the temperature range from 700 mK down to 1 mK, i.e., included the range of the homogeneous solution as well as the range of isotopic phase separation. Cooling to the region of decomposition was carried out in steps ($\sim$10 mK) followed by temperature stabilization lasting for many hours. Such a technique was used earlier to obtain information on the equilibrium phase-separation curve for solutions[12] and on the kinetics of isotopic phase separation.[13]

The spin–lattice relaxation time T_1 was measured by using the pulsed NMR technique at a frequency $\omega_0/2\pi = 250$ kHz. The system was subjected to the action of a sequence of pulses $90–\tau–90$, and the longitudinal magnetization $M(\tau)$ of the system returned to its equilibrium value M_0 according to the law

$$M(\tau) = M_0(1 - e^{-\tau/T_1}). \tag{2}$$

After each pulse, the amplitude U of the experimentally observed free induction signal is proportional to magnetization. Consequently, in the general case when the solution contains two phases in equilibrium after decomposition, we have

$$\frac{U(\tau)}{U_0} = \frac{U_0^b}{U_0}(1 - e^{-\tau/T_1^b}) + \frac{U_0^h}{U_0}(1 - e^{-\tau/T_1^h}), \tag{3}$$

where the indices b and h correspond to the bcc and hcp phases, respectively.

The obtained experimental results were processed by the least-squares method with an approximating function of the form (3); typical results for several temperatures are presented in Fig. 1. Each point in the figure is the result of five-fold averaging. It can be seen from the figure that reconstruction of magnetization undergoes evolution: the curve has a one-exponential form with a spin–lattice relaxation time typical of the initial homogeneous solution at high temperatures (above the phase-separation temperature), while at low temperatures the curves can be approximated by two exponentials indicating a heterophase structure of the solution. The values T_1^h and T_1^b of spin–lattice relaxation time determined in this way are characterized by an error not exceeding 10%.

TEMPERATURE DEPENDENCE OF SPIN–LATTICE RELAXATION TIME

Figure 2 shows the values of spin–lattice relaxation time obtained during cooling of the solution. It should be noted that each point was obtained after a long temperature stabilization and corresponds to thermodynamic equilibrium. This

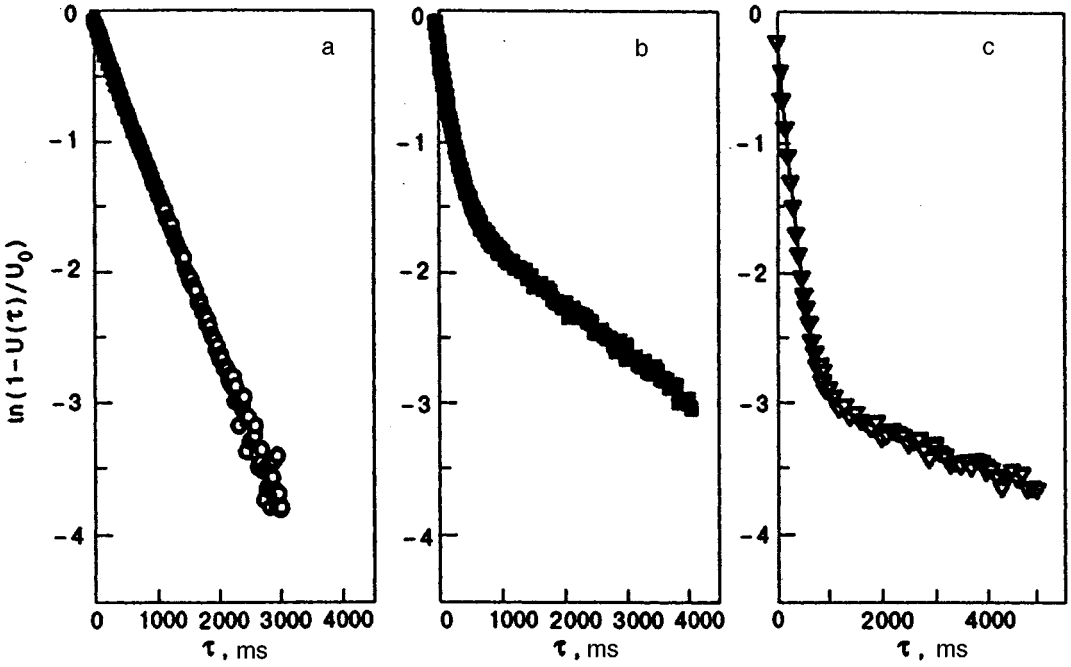

FIG. 1. Reconstruction of the longitudinal magnetization of the sample after the application of a 90° pulse at a constant temperature T. Before phase separation: $T=221$ mK, (a) after phase separation: $T=179$ mK (b) and $T=139$ mK (c).

is confirmed by the fact that the data on the phase-separation curve in the same experiment are in accord with the results obtained during sample heating without any noticeable hysteresis effects.

The temperature dependence of the time T_1 presented in Fig. 2 has three branches corresponding to the initial solution with the hcp structure (T_1^0) and two daughter phases, viz., the concentrated bcc phase (T_1^b) and dilute hcp phase (T_1^h). The branching temperature T_{ps} on this dependence corresponds to the beginning of phase separation of the initial solution (marked by arrow).

It should be noted that a qualitatively similar behavior of spin–lattice relaxation time during isotopic phase separation was also recorded by Greenberg *et al.*[8] who investigated a solution with the initial concentration 2% ^{3}He. They presented only the values of T_1 for concentrated phase, and a strong decrease in the value of T_1 near the phase-transition temperature was recorded in a wider temperature range than in Fig. 2. This can be due to incomplete thermodynamic equilibrium under the conditions of measurements of the spin–lattice relaxation time in Ref. 8.

The time T_1 in the concentrated phase is virtually independent of temperature, while in the dilute phase the value of T_1 increases with decreasing temperature significantly. Reliable values of T_1 for the dilute phase were obtained only in the temperature range above ~ 100 mK since the hcp phase at lower temperatures contains a very small amount of ^{3}He, which makes the NMR signal from the dilute phase comparable to the noise level.

The different forms of the temperature dependence of spin–lattice relaxation time for different phases of the solution under investigation illustrated in Fig. 2 correspond to different physical processes responsible for magnetic relaxation. We shall carry out an analysis of possible relaxation mechanisms separately for each phase.

MAGNETIC RELAXATION IN THE CONCENTRATED PHASE

The independence of the spin–lattice relaxation time T_1^b of temperature in the concentrated phase suggests that the main mechanism of magnetic relaxation in this case is connected with the Zeeman–exchange interaction. It is well known that exchange processes in ^{3}He cause the motion of neighboring atoms with antiparallel spins, which is equivalent to rotation of atoms around the center of mass of a pair of atoms with the angular frequency ω_E. Under these conditions, the relaxation mechanism is determined by the connection of the Zeeman system with the motion of ^{3}He atoms

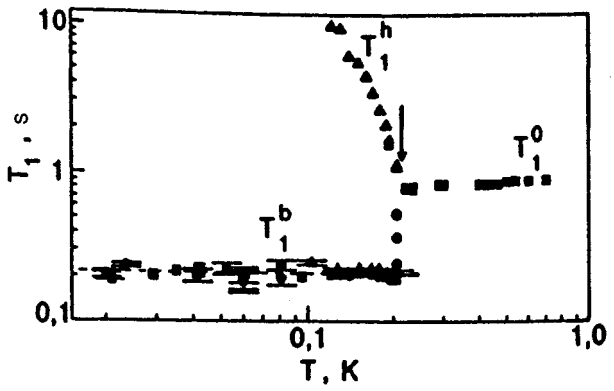

FIG. 2. Temperature dependence of the spin–lattice relaxation time in the initial solution (T_1^0) and in two daughter phases: concentrated (T_1^b) and dilute (T_1^h). The arrow corresponds to the phase-separation temperature.

during their tunneling due to dipole interaction, and the corresponding pair correlation function for the Gaussian approximation is taken in the form[14]

$$g(t) \sim \exp(-0.5\omega_E^2 t^2). \tag{4}$$

In this case, the spectral density function $J_1(\omega/\omega_E)$ describing the spin–lattice relaxation under modulation of the dipole interaction by the exchange of two ^{3}He atoms and being the Fourier transform of the correlation function $g(t)$ has the form

$$J_1(\omega/\omega_E) = \frac{(2\pi)^{1/2} M_2}{3\omega_E} \exp(-\omega^2/2\omega_E^2), \tag{5}$$

where ω is the Larmor frequency and M_2 the second van Vlek moment, which is connected with the molar volume V of the crystal through the following relation:[4]

$$M_2 = \frac{22.8 \cdot 10^{10}}{V^2} \ (\mathrm{s}^1). \tag{6}$$

It should be noted that along with the Gaussian correlation function (4), magnetic relaxation is sometimes analyzed by using the Lorentz correlation function leading to the following expression for the spectral density function:[4]

$$J_1(\omega/\omega_E) = \frac{(2\pi)^{1/2} M_2}{3\omega_E} \exp(-\omega/\omega_E). \tag{7}$$

The quantity ω_E appearing in (5) and (7) is proportional to the exchange integral J_{33}:

$$\omega_E = bJ_{33}, \tag{8}$$

where the constant $b = 3.36$ if $g(t)$ is approximated by the Lorentzian function and $b = 4.76$ if the approximation is carried out by using the Gaussian function.

In the approximation of pair exchange between nearest neighbors, the rate of energy relaxation from the Zeeman system to tunnel excitation is determined by the expression[3–5]

$$(T_1^b)^{-1} = J_1(\omega/\omega_E) + 4J_1(2\omega/\omega_e). \tag{9}$$

Since $\omega \ll \omega_E$ under the given experimental conditions, the exponents appearing in expressions (5) and (7) for the spectral density function are equal to unity to a high degree of accuracy. In this case, formula (9) for spin–lattice relaxation time does not depend on the type of approximation and acquires the form

$$(T_1^b)^{-1} = \frac{9.5 \cdot 10^{11}}{\omega_E V^2}. \tag{10}$$

Since the concentrated bcc phase contains almost pure ^{3}He, we can use for the molar volume $V = 23.95$ cm^3/mole the value of the parameter $J_{33} = 0.7 \cdot 10^{-3}$ K corresponding to the bcc of ^{3}He.[4] In this case, formula (10) gives $T_1^b = 0.27 \pm 0.1$ s, which is in good agreement with the experimental results (see Fig. 2).

Thus, the experimental values of spin–lattice relaxation time obtained for the concentrated phase of the decomposed solution in the entire temperature range under investigation are in quantitative agreement with the time of relaxation between the Zeeman and the tunnel system for pure bcc ^{3}He. It should be noted, however, that this relaxation mechanism in pure ^{3}He is manifested at not too low temperatures (above 0.4–0.5 K), while the region of the temperature dependence of T_1 characteristic of the exchange ''plateau'' for the concentrated phase under given experimental conditions corresponds to the temperature interval from 0.2 K down to the lowest temperatures investigated by us.

Although the reason behind such a difference remains unclear, we note some factors which can influence spin–lattice relaxation in a phase- separated solution. First, the concentrated phase formed in the process of isotopic phase separation contains a large amount of ^{4}He which can strongly affect magnetic relaxation at temperatures below the region of the exchange plateau typical of pure ^{3}He. In this region, the coupling between the exchange system and the lattice becomes weaker than between the Zeeman and exchange systems, and the value of T_1 must first increase abruptly upon cooling, and then attain a new (diffusion) ''plateau'' (see above).

It was proved by Bernier and Deville[6] that the energy transfer from the Zeeman subsystem to the lattice occurs through diffusion to clusters formed by ^{4}He impurity atoms. Since the value of T_{1D} is inversely proportional to the cube of the concentration x_4 of ^{4}He in ^{3}He (see above), we can expect that for a certain value of x_4, the diffusion plateau is ''lowered'' to the values of T_1 corresponding to exchange plateau. According to estimates based on the results obtained in Ref. 6, such an effect is possible under the given experimental conditions for ^{4}He concentrations amounting to only a few tens of percent.

Another possibility associated with the difference of the concentrated phase of the phase-separated solution from pure bcc ^{3}He is also worth noting. The concentrated phase can be presented as dispersive inclusions of ^{3}He in the hcp matrix formed by the dilute solution of ^{3}He in ^{4}He. In this case, relaxation of the Zeeman system at low temperatures occurs at the boundary of bcc phase inclusions. The spin–lattice relaxation time is proportional to the square of the radius R of inclusions (under the assumption that they are spherical) and inversely proportional to the spin diffusion coefficient within inclusions. According to estimates, the values of T_1 in the region of diffusion plateau and the exchange plateau can have the same order of magnitude for $R \sim 10^{-4}$ cm owing to such a ''size'' effect. Although the shape and size of ^{3}He inclusions in the ^{4}He matrix as well as possible low dimensionality of this structure remain disputable, all these factors can noticeably affect the processes of spin–lattice relaxation.

It should be noted that the boundaries of inclusions play a significant role in this process. At these boundaries, rapid relaxation due to coupling of the tunnel motion of ^{3}He atoms with the vibrational motion of dislocation lines occurs in view of a large number of edge dislocations.[5]

RELAXATION IN DILUTE SOLUTIONS OF ^{3}He IN ^{4}He

It was noted above that the temperature dependence of spin–lattice relaxation time presented in Fig. 2 has two regions corresponding to dilute hcp solutions of ^{3}He in ^{4}He.

Let us first consider the region corresponding to the initial solution with the concentration 3.18% ^{3}He. The value of T_1 in this region is independent of temperature within the experimental error. Hence it is natural to assume that spin–lattice relaxation occurs through a direct interaction between the Zeeman and exchange systems in this case also.

According to Miyoshi *et al.*,[7] we can estimate the value of T_1 expected for a solution of ^{3}He in ^{4}He by using relations (5)–(10). It was assumed in Ref. 7 that the concentration dependence of the spectral density function $J_1(\omega/\omega_E)$ is connected with ω_E, where $\omega_E \sim x^{1/2}$. Moreover, it was assumed that $M_2(x)=xM_2(1)$. If we also take into account the fact that the quantities appearing in (5)–(10) for the hcp phase under investigation with the molar volume $V=20.3$ cm^3/mole have the values $M_2 = 22.6 \cdot 10^{10}/V^2$ s^{-1}; $b = 6.48$; $J_{33} = 1.5 \cdot 10^{-5}$ K, the spin–lattice relaxation rate calculated in this way must be almost two orders of magnitude smaller than the observed values. In such an approach, the predicted concentration dependence has the form $T_1 \sim x^{-1/2}$, which also contradicts the experimental results (see below).

Another approach to the analysis of magnetic relaxation processes in ^{3}He–^{4}He solutions was used by Greenberg *et al.*[8] on the basis of the Torrey theory.[15] It is well known that ^{3}He impurities in a ^{4}He quantum crystal form quasiparticles (impuritons) which have the band width $\Delta E = z\hbar J_{34}$. In this case, ^{3}He and ^{4}He atoms can change places through tunneling with the frequency J_{34} and the exchange rate τ_{34}^{-1} which depends on the number of ^{4}He atoms surrounding a ^{3}He atom in accordance with formula (1). According to the theory,[15] the spin–lattice relaxation time in a ^{3}He–^{4}He solution with the concentration x in the exchange ''plateau'' region is described by the formula

$$T_1^{-1} = 2.29 M_2/(\omega^2 \tau_{34}). \tag{11}$$

The quantity τ_{34} was defined in Ref. 8 as a fitting parameter to the theory[15] describing the spin–lattice relaxation time in solutions with $x=1\%$ and 2% ^{3}He. It was proved that the time τ_{34} depends on molar volume and is virtually independent of concentration. If we use the value of τ_{34} obtained in Ref. 8 for the given experimental conditions ($\tau_{34}^{-1}/2\pi = 3 \cdot 10^3$ s^{-1}), the calculations based on formula (12) give $T_1 \sim 0.8$ s, which is in accord with the experimental data. In this model, the concentration dependence of T_1 has the form $T_1 \sim x^{-1}$.

It should be noted that the value of T_1 measured for the initial solution is also in agreement with the experimental results obtained in Ref. 10 if we normalize them to the frequency used by the formula $T_1 \sim \omega^2$. Such an agreement indicates that the spin–lattice relaxation processes in an hcp solution can be also described by taking into account both tunnel movements of ^{3}He–^{3}He and ^{3}He–^{4}He as it was done in Ref. 10. A fitting parameter is used in this case also.

The concentration dependence of the spin–lattice relaxation time in hcp ^{3}He–^{4}He solutions can be investigated from an analysis of the third branch in Fig. 2 corresponding to the dilute phase of the phase-separated solution. Since the measurements in this case were made along the equilibrium phase-separation line, the temperature dependence of T_1 can be reconstructed into the concentration dependence shown in Fig. 3 by taking into account the phase diagram obtained in Ref. 12. An analysis shows that $T_1^h \sim x^{-n}$, where $n = 0.88 \pm 0.12$, which speaks in favor of the approach developed in Refs. 8 and 14.

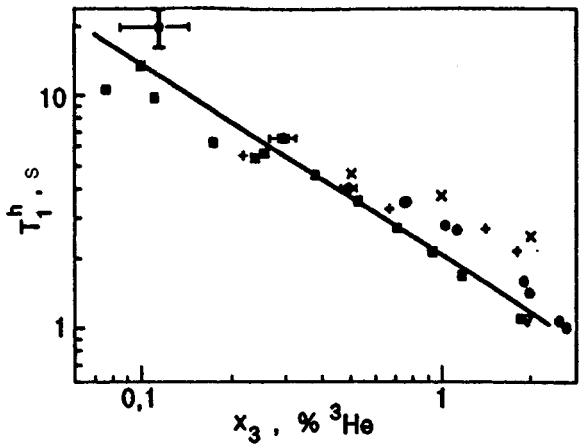

FIG. 3. Concentration dependence of the spin–lattice relaxation time in the dilute hcp phase. The symbols ■ and ● correspond to different crystals investigated by us. The experimental results obtained in Ref. 7 (▽), 8 (×), 9 (∗), and 10 (+) were normalized to our experimental conditions. The solid line corresponds to the dependence $T_1 \sim x^{-0.88}$.

In addition to experimental data obtained by us, Fig. 3 also presents the results of measurements[7–10] made for a homogeneous (single-phase) dilute hcp solution of ^{3}He in ^{4}He. According to Fig. 3, these results are in accord with the values of T_1 obtained by us for the dilute phase formed as a result of phase separation to within the overall experimental errors. This means that spin–lattice relaxation processes in homogeneous and phase-separated solutions of the same concentration are similar.

CONCLUSION

The experimental investigation indicates that the Zeeman–exchange interaction is the dominating process determining the spin–lattice relaxation time in a phase-separated ^{3}He–^{4}He solid solution.

Spin–lattice relaxation in the dilute phase of a phase-separated solution occurs in the same way as in a homogeneous solution of ^{3}He in ^{4}He. The spin–lattice relaxation time in the concentrated phase in the exchange region of the phase-separated solution coincides with the corresponding time for pure ^{3}He, but in contrast to ^{3}He, the region of the exchange plateau embraces almost the entire temperature region of existence of the concentrated phase.

The authors are grateful to Prof. V. N. Grigor'ev for fruitful discussions.

This research was partly supported by the European program INTAS (Project No. 94-3416).

*E-mail: rudavskii@ilt.kharkov.ua

[1] B. N. Esel'son, D.Sc. thesis, Kharkov (1957).
[2] V. N. Grigor'ev, B. N. Esel'son, V. A. Mikheev, and Yu. E. Shul'man, Pis'ma Zh. Éksp. Teor. Fiz. **17**, 25 (1973) [JETP Lett. **17**, 16 (1973)].

[3] A. Abragam and M. Goldman, *Nuclear Magnetism. Order and Disorder*, Clarendon Press, Oxford (UK) (1982).
[4] R. A. Guyer, R. C. Richardson, and L. I. Zane, Rev. Mod. Phys. **43**, 532 (1971).
[5] M. Bernier and G. Guerrier, Physica **121D**, 202 (1983); M. Bernier, J. Low Temp. Phys. **56**, 205 (1984).
[6] M. Bernier and G. Deville, J. Low Temp. Phys. **16**, 349 (1974).
[7] D. S. Miyoshi, R. M. Cotts, A. S. Grinberg, and R. C. Richardson, Phys. Rev. **A2**, 870 (1970).
[8] A. S. Grinberg, W. C. Thomlinson, and R. C. Richardson, J. Low Temp. Phys. **8**, 3 (1972).
[9] M. G. Richards, J. Pope, P. S. Tofts, and J. H. Smith, J. Low Temp. Phys. **24**, 1 (1976).
[10] Y. Hirayoshi, T. Mizusaki, S. Maekawa, and A. Hirai, J. Low Temp. Phys. **30**, 137 (1978).
[11] A. A. Golub, V. A. Goncharov, V. P. Litvinov *et al.*, Fiz. Nizk. Temp. **21**, 974 (1995) [Low Temp. Phys. **21**, 757 (1995)].
[12] V. A. Shvarts, N. P. Mikhin, È. Ya. Rudavskii *et al.*, Fiz. Nizk. Temp. **20**, 645 (1994) [Low Temp. Phys. **20**, 505 (1994)].
[13] V. A. Shvarts, N. P. Mikhin, È. Ya. Rudavskii, *et al.*, Fiz. Nizk. Temp. **21**, 717 (1995) [Low Temp. Phys. **21**, 556 (1995)].
[14] S. R. Hartman, Phys. Rev. **133**, 17 (1964).
[15] H. C. Torrey, Phys. Rev. **92**, 962 (1953); *ibid*. **96**, 690 (1954).

Translated by R. S. Wadhwa

Melting of ^{3}He in a phase-separated solid ^{3}He–^{4}He mixture

R. P. Haley and E. D. Adams

*Department of Physics, University of Florida, Gainesville, FL 32611-8440, USA**
(Submitted November 19, 1996)
Fiz. Nizk. Temp. **23**, 615–618 (May–June 1997)

The melting pressure of the ^{3}He-rich phase, which is formed after phase separation of a mixture of 0.6% ^{3}He in ^{4}He, has been studied in the temperature range 1–150 mK, below the phase-separation temperature T_{ps}, at pressures between 2.78 and 3.56 MPa. Measurements were made with the mixture confined in a silver sinter, and also in an open volume for comparison. An elevation of the melting pressure relative to pure ^{3}He of up to 60 kPa in the sinter cell and 20 kPa in the open-volume cell was observed. Hysteresis between the freezing and melting temperatures was found for both cells, similar to that observed for pure ^{3}He in small pores. The results of Schrenk *et al.* for heat capacity measurements on a similar system are discussed.
 [S1063-777X(97)01405-9]

1. INTRODUCTION

A homogeneous solid mixture of ^{3}He–^{4}He decomposes into separate phases when cooled to the phase-separation temperature T_{ps}. For low ^{3}He concentrations, at temperatures well below T_{ps}, the ^{4}He-rich hcp matrix contains clusters or droplets of almost pure ^{3}He (see Refs. 1 and 2 and the bibliography cited there). Schrenk *et al.*[1] have reported a depression of the melting pressure of the ^{3}He droplets relative to that of pure bulk ^{3}He. Furthermore, they have observed a history-dependent magnetic ordering in the droplets at pressures as low as 700 kPa below the melting pressure of pure[2] ^{3}He. A possible explanation for these results might be the confined-geometry effect of the small droplets. Pure ^{3}He in small glass pores has an elevated melting pressure,[3] while a depression of the melting pressure has been reported for ^{3}He on a MgO substrate.[4]

We have studied melting and freezing in a 0.6% ^{3}He mixture confined in a silver sinter cooled below T_{ps} (approximately 200 mK) at pressures from 2.78 to 3.56 MPa in order to determine the melting curve of the ^{3}He droplets.[5] We have also made measurements on the same mixture contained in an open volume in order to assess whether the silver sinter plays any role other than providing an effective means of cooling. Hysteresis and the effect of thermal history on the transition were investigated in both cells. The implications of our observations on the results of Schrenk *et al.*[2] are discussed, and possible explanations are given for some of the effects that they reported.

2. EXPERIMENTAL METHOD

The sinter cell contains a thin disk of silver sinter of particle size 500–1000 Å and packing fraction 50%. The disk of radius 25 mm and thickness 2.5 mm was packed in a silver cell with one wall forming the flexible diaphragm of a capacitive pressure transducer.[6] The open volume cell is similar in design, with the sample forming as a solid disk of radius 17 mm and thickness 1.3 mm. These geometries provide a short path for pressure transmission, thereby minimizing pressure gradients in the sample. The resolution of each cell is better than 1 Pa. The two cells were connected to the same fill-line, with a junction in the line at the experimental stage on which the cells were mounted.

Samples were formed at various pressures by the capillary-blocking technique, and it was intended that both the open-volume and sinter cells would contain samples at the same pressure, since they were connected to the same fill-line. However, the sinter cell samples consistently solidified at higher pressures than the open cell (by approximately 0.3 MPa). We attribute this to a larger degree of disorder in the sinter cell since there is a larger surface area on which a few atomic layers of amorphous solid ^{4}He form. After formation the samples were either quenched or annealed just below the solidification point. Phase separation in the sinter and open-volume cells was observed as an increase in sample pressure of approximately 15 kPa with a time constant on the order of 10 hours for the sinter cell and 20 hours for the open-volume cell. The absence of a sinter in the open-volume cell did not significantly affect the cooling/warming rate of the sample. After the phase separation and further cooling, samples were then warmed through the freezing transition and cooled back through melting, taking care to keep $T < T_{ps}$. In some cases, several such cycles were performed. Temperatures were measured precisely with a ^{3}He melting pressure thermometer[7] mounted on the same experimental platform as the cells. The temperature was regulated by using the signal from the thermometer bridge to control the current to a heater on the experimental stage. All three strain gauges were calibrated with the same Paroscientific quartz transducer.

In order to ensure that the data were taken at equilibrium, the desired thermometer bridge value was set on the temperature control system, the samples cooled/warmed to the new temperature, and then held at that temperature until the pressure in the cells reached equilibrium. In the freezing transition of the open-volume cell, equilibration could take up to 20 hours.

3. RESULTS AND DISCUSSION

In both the sinter and open-volume cells, melting of the ^{3}He droplets was observed at sample pressures from 3.13 to

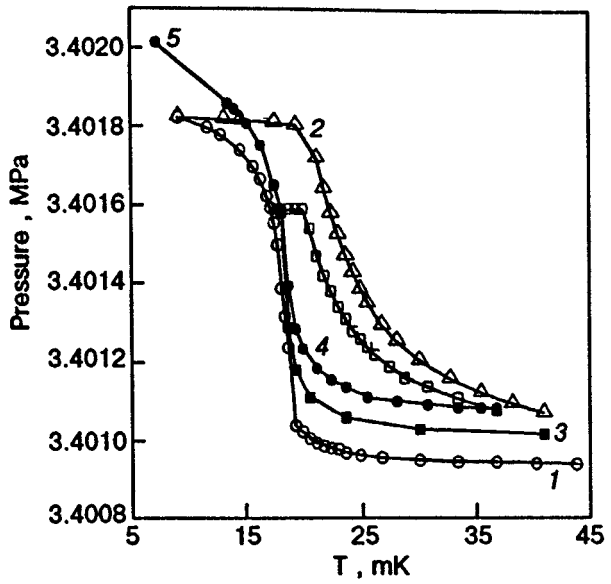

FIG. 1. Typical cooling (curves *1*, *3* and *5*) and warming (curves *2* and *4*) cycles for the melting/freezing of ^{3}He in the droplets in the sinter cell (see text).

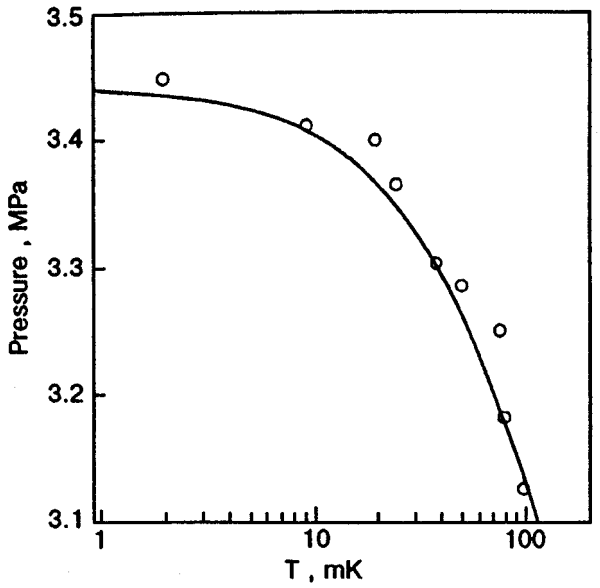

FIG. 3. The bulk ^{3}He melting curve (solid line) and the melting points of ^{3}He droplets, taken from sinter cell data.

3.45 MPa. At 3.48 MPa the ^{3}He remained solid down to the lowest temperature (1 mK), and at 2.96 MPa melting was not observed, presumably because the droplets formed as a liquid. Upon melting, the pressure of the sample in the sinter cell increased on the order of 1 kPa, and on the order of 5 kPa in the open-volume cell.

Figure 1 shows typical cooling/warming cycles displaying the hysteresis seen in every sample in which melting occurred in the sinter cell. The numbers by the curves indicate the time sequence; curves *4* and *5* illustrate the effect of reversing the direction of temperature changes in mid-cycle. Figure 2 shows a typical warming/cooling cycle in the open-volume cell, which also shows hysteretic behavior. In this figure the pressure in the cell is plotted relative to the pressure in the melting curve thermometer. Since the cells were calibrated against the same pressure standard, this eliminates uncertainty in the temperature and shows precisely the position of the transition relative to the bulk melting curve. Previously hysteresis was observed for pure helium in porous glasses and appears to be a characteristic of melting and freezing in confined geometries.[3] In that experiment the transitions occurred at pressures above that of the bulk melting curve, as one would expect for homogeneous nucleation of a new phase in a confined geometry.

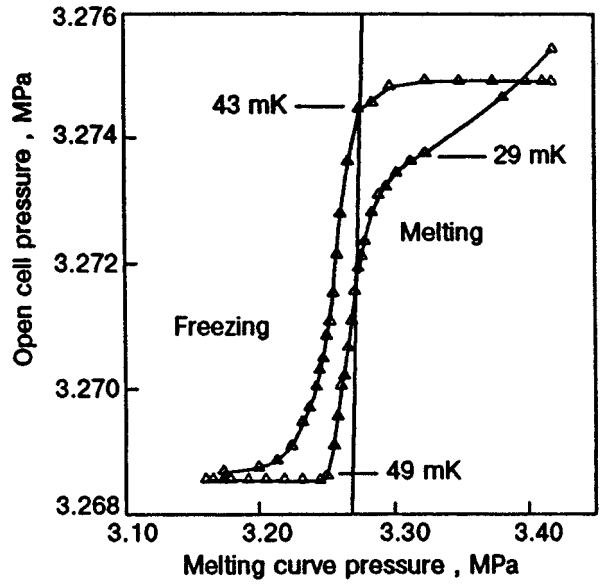

FIG. 2. Typical warming and cooling cycles for the freezing/melting of ^{3}He in the open-volume cell. The solid line shows the melting pressure of bulk ^{3}He. Temperatures are given for the points indicated.

The temperatures for the sharp kinks in the cooling and warming curves such as in Fig. 1 are almost the same and the pressure differences are small. These are shown in Fig. 3 as single points for samples formed at different pressures along with the pressure indicated by the pure ^{3}He melting pressure thermometer. For the sinter cell we found all melting transitions to be on or above the bulk melting pressure, elevated by as much as 60 kPa. The precision of the points in Fig. 3 is much better than would be indicated by the ''scatter'', which is possibly related to the thermal history of the sample and the droplet size.[8] However, we have not been able to correlate the size of the pressure elevation with the thermal history.

We have measured the pressure minimum of essentially pure ^{3}He in the sinter plated with 1% ^{4}He as a substrate and found an elevation of the melting pressure in the sinter of 63.9 kPa.

For the open-volume cell, it is clear from Fig. 2 that the onset of melting in the droplets is elevated above the bulk melting curve (by 20 kPa), and that the melting/freezing transition is broadened relative to a bulk ^{3}He isochore. We attribute this behavior to differences in droplet size between the sinter cell and the open cell. In the open volume cell, we suggest that the ^{3}He forms in a range of different-sized clus-

ters, up to a size on the order of 1 μm.[8] In the sinter cell, the pore size of approximately 100 nm limits the size of a cluster which can grow from the ^{3}He contained inside the pore. Thus, the larger droplets in the open-volume cell contain ^{3}He which is less confined and one would, therefore, expect a smaller elevation of the melting pressure. This accounts for the broadening of the melting transition for the open cell with the onset of smaller droplets at a high elevation. In comparison, the sinter cell melting transitions are sharper and more elevated, suggesting that a high percentage of the ^{3}He in a pore is contained in a single cluster, which is limited in size only by the ^{3}He available within that pore. The cluster size would be approximately 20 nm if it contained all the ^{3}He within a pore.

The fractional change in volume in the droplets on melting $\Delta v/v$ can be calculated from the change in pressure on melting such as that shown in Figs. 1 and 2, (assuming that the molar volume change of ^{3}He in the droplets in the same as in bulk). We find this to be only about 8% of that for pure ^{3}He in a typical sinter cell measurement, and 40% in the open-volume cell. This indicates that a large fraction of the ^{3}He remains solid at pressures well below the bulk melting curve. A volume change less than that for bulk ^{3}He would be expected if surface layers of the ^{3}He droplets do not melt because of the influence of the adjacent higher-density hcp ^{4}He. As a result of the van der Waals attraction to the ^{4}He surface, the density of the solid in the droplet would be higher at the interface than in the interior. The higher-density ^{3}He solid layers will melt at progressively colder temperatures. Evidence for these density gradients can be found in data such as those shown in Fig. 1, curve *5*, where the pressure continues to increase upon cooling well below the sharp melting transition. The initial pronounced increase in pressure would then be due to the material in the center of the droplets, indicating that the high-density hcp ^{4}He affects only the outer layers of the ^{3}He in the cluster. The larger fractional volume change in the open-volume cell reinforces the assertion that it contains larger droplets, so that a lower proportion of the ^{3}He is directly affected by its proximity to the ^{4}He matrix. It should be emphasized that this continued pressure increase is not attributable to the continued phase separation since the sample was held at a temperature below T_{ps} and above the melting transition temperature until the pressure remained constant with further lowering of temperature, before the onset of melting (Fig. 1, curve *1*).

The existence of density gradients in the outer layers of the droplets can account for effects reported by Schrenk *et al.*[2] relating to magnetic ordering of ^{3}He droplets in solid ^{4}He contained in a silver sinter. Their observations, based on the heat capacity, include higher magnetic ordering temperatures, T_N, at pressures as low as 2.8 MPa, 700 kPa below the melting pressure of pure ^{3}He, and a history-dependent transition temperature. As discussed above, the existence of solid ^{3}He at pressures below the bulk melting curve appears to be a consequence of confining the droplets within a higher density ^{4}He matrix. The history dependence of T_N they report is that samples cooled to lower minimum starting temperatures, $T_{\min}$, appear to give lower transition temperatures in the heat capacity data taken during warming. The transitions that they observed show no latent heat and are much broader than those measured by Greywall and Busch[9] in bulk ^{3}He. These are well-known effects of density gradients in the sample. The peak that they observed does indeed appear at a higher temperature if $T_{\min}$ is higher, although it is not clear that this peak actually indicates T_N. In fact, the broadening of the peak due to the density gradients means that the samples with higher values of $T_{\min}$ are not cooled all the way through the ordering transition, so that for successively higher values of $T_{\min}$, less of the solid ^{3}He contributes to the heat capacity. If the droplets were cooled all the way through the ordering temperature, then there would be a decrease in entropy (extrapolated to $T = 0$) of $R \ln 2$, where R is the gas constant. Their data for a sample at 3.4 MPa with $T_N = 0.92$ mK actually shows a greater contribution to the entropy reduction in cooling from 2 mK to just above T_N than that found by Greywall and Busch in bulk, probably indicative of a broadening of the transition in the droplets. Greywall and Busch report an entropy reduction of 0.41 $R \ln 2$ in going through the transition alone. However, even including contributions from 2 mK down to $T_{\min}$, the entropy reduction of Schrenk *et al.* is only 0.32 $R \ln 2$ for $T_{\min} = 783$ μK and 0.22 $R \ln 2$ for $T_{\min} = 837$ μK. This suggests strongly that all of the solid in the droplets was not cooled through T_N, as would occur for a transition broadened by density gradients.

4. CONCLUSIONS

Melting of ^{3}He droplets contained in a matrix of ^{4}He occurs at higher pressures than bulk ^{3}He and has a hysteresis characteristic of melting in confined geometries. The small volume change on melting indicates that much of the ^{3}He in the droplets does not undergo melting, and remains solid at pressures below the bulk melting curve due to interaction with the surrounding hcp solid ^{4}He. Comparison with a mixture in an open-volume indicates that containing the solid in a sinter has the effect of limiting the size of the ^{3}He clusters, and the smaller droplets give rise to a larger elevation of the melting pressure. We intend to use NMR to measure the droplet size, the relative amounts of liquid and solid, and to study solid ordering.

*E-mail: adams@phys.ufl.edu

[1] R. Schrenk, O. Friz, Y. Fujii, E. Syskakis, and F. Pobell, J. Low Temp. Phys. **84**, 133 (1991); and unpublished results.
[2] R. Schrenk, R. König, and F. Pobell, Phys. Rev. Lett. **76**, 2945 (1996).
[3] D. N. Bittner and E. D. Adams, J. Low Temp. Phys. **97**, 519 (1994).
[4] Y. Eckstein, J. Landau, S. G. Lipson, and Z. Olami, Phys. Rev. Lett. **45**, 1805 (1980).
[5] R. P. Haley, W. Ni, and E. D. Adams, Czech. J. Phys. **46-S1**, 477 (1996).
[6] E. D. Adams, Rev. Sci. Instrum. **64**(3), 601 (1993).
[7] W. Ni, J. S. Xia, E. D. Adams, P. S. Haskins, and J. E. McKisson, J. Low Temp. Phys. **99**, 167 (1995).
[8] V. A. Mikheev, V. A. Maidanov, N. P. Mikhin, S. E. Kal'noi, and N. F. Omelaenko, Sov. J. Low Temp. Phys. **14**(6), 309 (1988).
[9] D. S. Greywall and P. A. Busch, Phys. Rev. B **99**, 6853 (1987).

This article was published in English in the original Russian journal. It was edited by S. J. Amoretty.

Growth kinetics of ^{4}He crystal with a low ^{3}He impurity concentration

V. L. Tsymbalenko

*Russian Science Center ''Kurchatov Institute,'' Institute of Superconductivity and Solid State Physics, 123182 Moscow, Russia**

(Submitted November 12, 1996; revised February 12, 1997)
Fiz. Nizk. Temp. **23**, 619–623 (May–June 1997)

The kinetic growth coefficient is measured for an atomically rough surface of a helium crystal grown from a solution with a low ^{3}He impurity concentration ($x=8\cdot10^{-5}$ and $2\cdot10^{-4}$). The impurity does not affect the growth rate of the surface in the temperature range from 1.2 to 1.4 K. A comparison of the experimental results with the theory leads to the conclusion that the additional contribution of impurity diffusion to the growth kinetics is equal to zero.
 [S1063-777X(97)01505-3]

1. INTRODUCTION

The growth kinetics for ^{4}He crystals was studied intensely during the last fifteen ears following the theoretical prediction[1] and experimental observation[2] of the quantum nature of this process (see the review in Ref. 3). According to the model considered by Andreev and Parshin,[1] the growth rate for the crystal–liquid interface is determined by the mobility of elementary defects (steps) of the surface structure. In turn, the mobility of steps in pure helium is limited by scattering at quasiparticles, leading to an exponential temperature dependence of the growth rate in the region dominated by rotons and to a power dependence at lower temperatures. The introduction of ^{3}He impurity leads to an additional scattering of steps at ^{3}He atoms and, as a result, to a decrease in the growth rate. Analyzing this mechanism, Parshin[4] determined an additional contribution to the growth coefficient K associated with impurity: $K_3\sim1/(xv_3)\sim1/\sqrt{T}$, where x is the solution concentration and v_3 the thermal velocity of ^{3}He atoms. A similar estimate was obtained by Castaing *et al.*[5] A numerical comparison of the magnitude of this contribution for a concentration $x\sim10^{-4}$ with experimental values of the kinetic growth coefficient for pure helium indicates that impurities start playing a significant role below ~0.6 K.

The model considered by Parshin presumes that the impurity concentration near the surface remains unchanged during the growth. The experimental phase-equilibrium curves[6] show that the equilibrium concentrations of impurity in the crystal and in the liquid are different in the general case. During the crystal growth, the solution near the interface will be depleted or enriched, leading to the emergence of diffusion flows and additional dissipation in the solution, which reduces the growth rate. Considering this mechanism, Burmistrov and Dubovskiĭ[7] proved that the presence of an even small amount of impurity at the level of $x_3\sim10^{-4}$ reduces significantly the kinetic growth coefficient at high temperatures ~1.4 K.

In this communication, the results of measurements of the growth coefficient for two impurity concentrations are presented with a view to determine the contribution from the diffusion mechanism of the growth.

2. TEMPERATURE DEPENDENCE OF IMPURITY CONCENTRATION IN CRYSTAL AND IN LIQUID AT EQUILIBRIUM

For a low concentration of the solution, when the effect of impurity is weak, as well as at a high temperature, when the role of quantum effects is insignificant, the change in the chemical potential μ_4 of the solvent is proportional to the impurity concentration[8]:

$$\mu_4(T,x)=\mu_4(T,0)-Tx. \tag{1}$$

Equating the chemical potentials of the liquid and solid phases, we obtain the following expression for the displacement of the phase-equilibrium point on the pressure scale: $\Delta p=T(x_l-x_s)/(v_l-v_s)$, where $x_{l,s}$ is the impurity concentration in the liquid and in the crystal and $v_{l,s}$ the volume per atom.[8] Transforming this expression, we obtain the relation defining the ratio of the impurity concentrations in the crystal and in the liquid in terms of the shift in the phase-equilibrium point:

$$\frac{x_s}{x_l}=1-\frac{\Delta V_m\Delta p}{RTx_l}, \tag{2}$$

where ΔV_m is the difference in the molar volumes of the crystal and the liquid and R the gas constant.

Phase-equilibrium curves for low concentrations x were not measured directly. Figure 1 shows the temperature dependencies of impurity distribution, plotted for solutions with a high impurity concentration (0.99–8.9%).[6] It can be seen that the results obtained in the temperature range 1.2–1.4 K in which our experiments were made coincide to a high degree of accuracy for all concentrations. Therefore, we can assume that the same impurity distribution among phases is also preserved at lower concentrations. It should be noted that the impurity concentrations in the phases at $T=1.4$ K are identical. This means that the effect considered by Burmistrov and Dubovskiĭ[7] is absent at this temperature, and the crystal growth rate in the solution must coincide with the growth rate for pure helium. According to the theory,[7] the growth rate in the solution at a lower and at a higher temperature must be lower than the growth rate in pure helium since the additional dissipation is proportional to the square of the difference in concentrations.

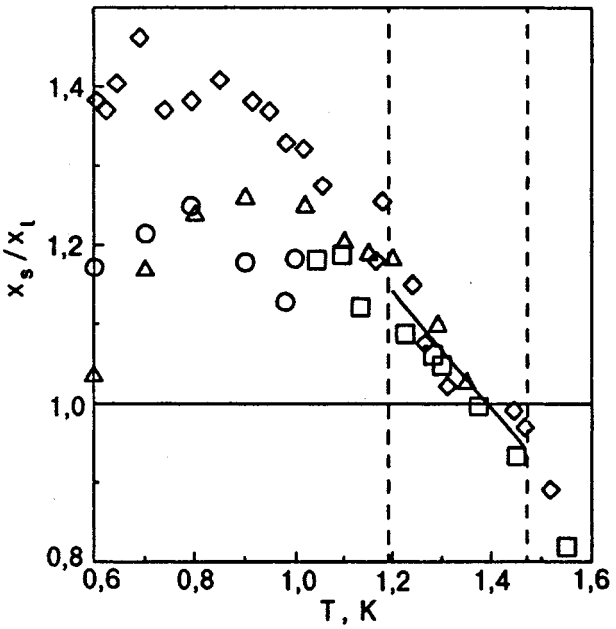

FIG. 1. Impurity distribution between the liquid and solid phases, calculated according to phase-equilibrium curves for solution[6] by using formula (2) for various concentrations x, % 0.99 (○), 2.77 (△), 5.03 (□), and 8.9 (◇). Dashed lines indicate the temperature region presented in Fig. 2. The solid line is plotted by processing the entire body of experimental data in this range using the least square method.

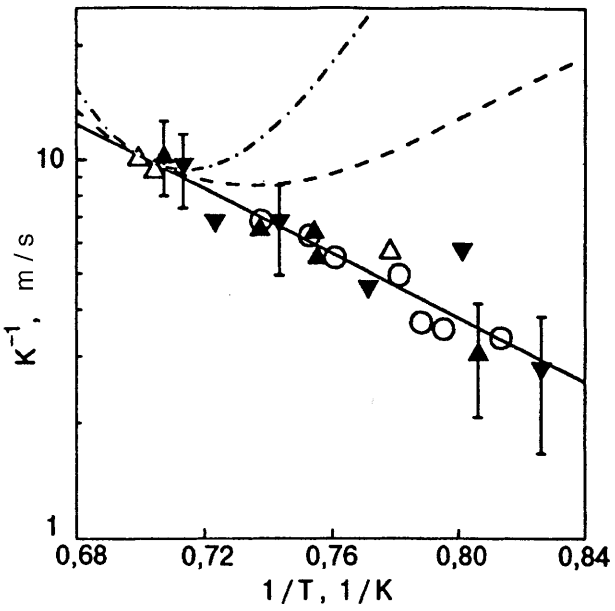

FIG. 2. Temperature dependence of the kinetic growth coefficient. Pure helium: the data obtained in Ref. 11 (○) and our results (△). Growth coefficients for solution with $x=8\cdot10^{-5}$ (dark triangles) and $2\cdot10^{-4}$ (dark nablas). The dashed and dot-and-dash curves correspond to the growth coefficient calculated by the formulas from Ref. 7 for the concentrations 0.008 and 0.02%, respectively.

Let us estimate the contribution from the diffusion mechanism numerically. In Ref. 7, a simplified situation of a steady-state growth of the plane surface of a crystal was considered without taking into account the difference in the densities of the liquid and solid phases. In this case, the value of the diffusion kinetic growth coefficient K_D is defined as

$$K_D=\frac{2D}{((c-c')^2\partial Z/\partial c)^2}\frac{\Delta\Phi}{L},$$

where D is the diffusion coefficient, c and c' are the concentrations of impurity per unit mass in the liquid and solid phases, $Z=\mu_3/m_3-\mu_4/m_4$, $\partial Z/\partial c\approx T/(m_3c)$ for dilute solutions, $\Delta\Phi$ is the difference between the chemical potentials of the liquid and solid phases, and L the characteristic growth length. It will be shown below that the crystal in this experiments grows nonuniformly, relaxing to the equilibrium position under the action of hydrostatic pressure gradient. For this reason, and also due to the simplifications mentioned above, this expression should be regarded as an order-of-magnitude estimate of the effect. In our experiments, $\Delta\Phi=\Delta\rho/\rho_l\rho_s\Delta p=\Delta p/\rho_s gL$, where $\rho_{l,s}$ is the density of solid and liquid helium, $\Delta\rho=\rho_s-\rho_l$, and g is the acceleration due to gravity. Substituting these expressions into the formula from Ref. 7, we obtain the following expression for the reciprocal growth coefficient:

$$1/K_D=\frac{1}{2}\left(\frac{\Delta x}{x}\right)^4\frac{\rho_s}{\Delta\rho}\frac{1}{Dg}\left(\frac{RT}{M_3}c\right)^2.$$

Here M_3 is the mass of a gram-atom of ^{3}He. The concentration per unit mass is connected with the atomic concentration through the relation $c\approx3x/4$. The observed growth coefficient K is now given by the formula $1/K=1/K_0+1/K_D$, where K_0 is the growth coefficient for pure helium.

The obtained expression shows that the temperature dependence of the kinetic growth coefficient is mainly determined by the temperature variation of the concentration difference $\Delta x/x$. In the narrow temperature range 1.2–1.4 K under investigation, the remaining parameters change insignificantly. For example, the diffusion coefficient increases upon a decrease in temperature approximately twofold. Figure 2 shows the theoretical dependencies of the total growth coefficient for two concentrations ($x=0.02$ and 0.008%) and for the following values of parameters: $\rho/\Delta\rho\approx10$, $g=10$ m/s, $D=8\cdot10^{-4}$ cm^2/s, $\Delta x/x\approx0.53(1.4-T)$. It can be seen that, if the effect under consideration exists, the growth coefficient must change insignificantly.

3. EXPERIMENTAL TECHNIQUE

The crystal was grown in an optical container[9] whose photograph at the moment of measurement is shown in Fig. 3. A tip emitting electrons is located at the center of the field of vision with diameter 10 mm. Under the action of electrostatic pressure exerted by electrons, the surface of the helium crystal ''sagged'' by 0.5–1 mm. Then the voltage at the tip was switched from the negative value of ~1 kV to a positive value of the order of several hundreds volts. The crystal surface relaxed to its equilibrium position at a rate determined by the hydrostatic pressure gradient and the kinetic growth coefficient K. The relaxation process was photographed, and the number of the shot was printed in the frame.[10] A mathematical analysis of the indentation contours distinctly visible on the photographs led to the function $y=f(x,t)$ for the

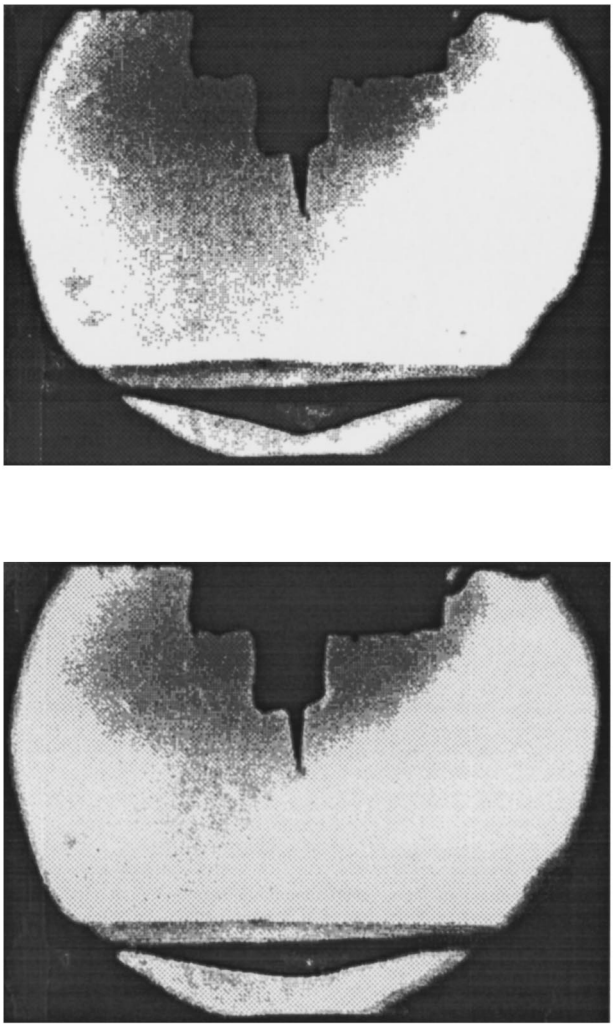

FIG. 3. Photograph of the crystal in the process of relaxation of the surface to the equilibrium value at $T=1.414$ K. The time interval between the shots is 2.8 s. The crystal occupies the lower part of the container. The crystal–liquid interface in transmitted light can be seen from the difference in the brightness of the image. The grey spot at the center of the field of vision is formed as a result of nonuniform illumination.

family of such contours. The electron pressure on the surface was used earlier by Leiderer *et al.*[11] for measuring the kinetic growth coefficient for pure helium crystal.

We describe the time variation of crystal contour by using the equation for the evolution of crystal contour of an arbitrary shape,[12] introduced by us earlier and defined by the implicit function $F(x,y,t)=0$:

$$\frac{\partial F}{\partial t}+v\left[\left(\frac{\partial F}{\partial x}\right)^2+\left(\frac{\partial F}{\partial y}\right)^2\right]^{1/2}=0, \tag{3}$$

where v is the crystal growth rate. This rate is connected with the kinetic growth coefficient and the difference in chemical potentials through the following expression:

$$v=K\Delta\mu=K\,\frac{\Delta\rho}{\rho_l\rho_s}\left[-\rho_l g y-\frac{\rho_l}{\Delta\rho}\left(\frac{\tilde{\alpha}_1}{R_1}+\frac{\tilde{\alpha}_2}{R_2}\right)\right], \tag{4}$$

where $\rho_{l,s}$ is the density of liquid and solid helium, $\Delta\rho=\rho_s-\rho_l$, $\tilde{\alpha}_{1,2}$ is the surface rigidity, and $R_{1,2}$ are the main radii of curvature. Putting $F(x,y,t)=y-f(x,t)$, we obtain the equation for the vertical displacement of the contour:

$$\frac{\partial f}{\partial t}+v\left[1+\left(\frac{\partial f}{\partial x}\right)^2\right]^{1/2}=0. \tag{5}$$

Using the experimental dependence $f(x,t)$, we can determine only one radius of curvature. For this reason, we make an assumption which is justified by visual observations of the crystal surface, according to which the shape of the indentation is almost axially symmetric. In this case, we assume that $R_1\approx R_2$, $\tilde{\alpha}_1\approx\tilde{\alpha}_2$, and $\partial f/\partial x=0$ at the lower point of the contour and obtain the equation of motion of the central point of the indentation:

$$\frac{\partial f}{\partial t}=K\,\frac{\Delta\rho}{\rho_s}\,g\left(-f+2a^2\,\frac{\partial^2 f}{\partial x^2}\right),\quad a=\left(\frac{\tilde{a}}{g\Delta\rho}\right)^{1/2}, \tag{6}$$

where a is the capillary constant, $a\approx 1.1$ mm. The surface rigidity was assumed to be the same as for pure helium, i.e., $\tilde{\alpha}\approx 0.2$ erg/cm^2, since the adsorption of impurity at the surface is small in the given temperature range and changes the surface energy insignificantly.[13] It should also be noted that surface relaxation took place in the constant volume of the crystal in the container so that the edges of the indentation were lowered slightly (by Δy) as the central part rose. This sets a limit on the applicability of Eq. (6): $|f|\gg\Delta y$. The overall error in determining the kinetic growth coefficient is rather large (of the order of 50%). Nevertheless, it will be shown below that this accuracy is sufficient for determining the contribution of impurities to the surface growth kinetics.

4. RESULTS

Figure 2 presents the results of measurements of kinetic growth coefficient for two impurity concentrations. The dashed curves in the figure correspond to the total kinetic growth coefficients calculated by using the formulas from Ref. 7. It can be seen that even for such low concentrations, the theoretical kinetic growth coefficient must change radically, decreasing by a factor of 10–30 at $T=1.2$ K. This effect can be observed even for the low accuracy of our experiments. The curves show, however, that the crystal growth rate in the solution coincides (to within the experimental error) with the growth rate of a pure crystal, i.e., the correction to the kinetic growth coefficient due to dissipation associated with the diffusion of impurity is small.

It should be noted that such a low impurity concentration nevertheless affects the kinetic growth coefficient at lower temperatures. For example, crystallization waves which can be easily generated by shaking the cryostat at a temperature ~ 0.45 K in pure helium were not excited in the solution at the same temperature. This leads to the estimate $K^{-1}>0.01$ m/s for the kinetic growth coefficient at this temperature, which is in accord with the estimate obtained by Parshin.[4]

The absence of the effect of impurities on the growth kinetics indicates that additional dissipation associated with diffusion does not take place in the liquid. This is possible if the impurity concentration in the crystal is close to the con-

centration in the liquid, i.e., the crystal grows under nonequilibrium conditions. This situation differs from that considered in Ref. 7, in which it was assumed that the concentrations in both phases are close to the equilibrium concentration. Another possibility is connected with the simplifications made in Ref. 7. It can be seen from Fig. 1 that the impurity concentration in the crystal below 1.4 K at which the measurements were made is higher than in the liquid, i.e., diffusion flows must be directed towards the crystal surface. Burmistrov and Dubovskii[7] disregarded the difference between the densities of the liquid and solid phases, although the density of the crystal is actually higher than the density of the liquid, and its growth is accompanied by liquid flow to the crystal boundary. This flow coincides in direction with the diffusion flow, facilitating the transport of impurity to the crystal and suppressing diffusion, dissipation, and the effect of impurity on the growth kinetics. However, the opposite effect associated with the transport of impurity by the crystallization heat flow from the crystal surface also exists. The conclusions concerning the absence of a diffusion contribution to the growth kinetics cannot be made reliably before the creation of a theory which would take into account all these factors.

Another circumstance is also important in the interpretation of the obtained results. The theoretical calculations whose results are presented in Fig. 2 were made on the basis of the data on the impurity distribution between the liquid and the crystal, which are discussed in Sec. 2 (see Fig. 1). However, the theory of dilute ideal solutions[8] implies that the derivative dp/dT of the phase-equilibrium curve for the solution coincides with the slope of the phase diagram for the pure substance, i.e., the phase-equilibrium curve is displaced without a change in shape along the pressure scale by Δp which does not depend on temperature. In this case, the impurity distribution between the phases is also independent of temperature. This conclusion does not agree with experimental results of measurements of phase-equilibrium curves for solutions,[6] which were investigated starting from the concentration $\sim 1\%$. Thus, the applicability of the extrapolation of the results on the impurity distribution between the phases, presented in Sec. 2, to lower concentrations $\sim 10^{-4}$ used by us remains disputable.

A decrease in the kinetic growth coefficient under the action of impurity was observed earlier at a very low concentration $(5-50)\cdot 10^{-9}$ below 0.5 K by using the method of crystallization waves.[14,15] Leiderer *et al.*[16] reported recently on the measurements of the growth rate of an atomically rough surface of helium crystal in a solution with the concentration $(5-10)\cdot 10^{-6}$ in a narrow temperature range ~ 0.8 K by the same method as that used in Ref. 11 for pure helium. In this temperature range, the impurity reduces the growth rate by a factor of 2–3, i.e., the temperature dependence does not change after the introduction of impurities. In these experiments, an anomalously strong effect of impurity on the growth rate was not observed either.

Thus, the introduction of an impurity with a concentration $10^{-5}-10^{-4}$ does not lead to a significant change in the kinetic growth coefficient in the temperature range 1.2–1.4 K and becomes noticeable only at lower temperatures.

The author is grateful to S. N. Burmistrov and L. B. Dubovskii for numerous fruitful discussions in the course of research work and to A. Ya. Parshin for valuable discussion of the results.

This research was carried out under the support of the Russian Foundation of Fundamental Studies, Grant No. 96-02-18511a.

*E-mail: vlt@rau.kiae.su

[1] A. F. Andreev and A. Ya. Parshin, Zh. Éksp. Teor. Fiz. **75**, 1511 (1978) [Sov. Phys. JETP **48**, 763 (1978)].
[2] K. O. Keshishev, A. Ya. Parshin, and A. V. Babkin, Pis'ma Zh. Éksp. Teor. Phys. **30**, 63 (1979) [JETP Lett. **30**, 56 (1979)].
[3] S. G. Lipson and E. Polturak, *Progress in Low Temperature Physics*, Vol. XI (1987).
[4] A. Ya. Parshin, Physica **B109–110**, 1819 (1982).
[5] B. Castaing, A. S. Greenberg, and M. Papoular, J. Low Temp. Phys. **47**, 191 (1982).
[6] B. N. Esel'son, V. G. Ivantsov, V. A. Koval' *et al.*, in *Properties of Liquid and Solid Helium. He3–He4 Solutions* [in Russian], Naukova Dumka, Kiev (1982).
[7] S. N. Burmistrov and L. B. Dubovskii, Europhys. Lett. **24**, 749 (1993).
[8] L. D. Landau and E. M. Lifshitz, *Statistical Physics*, Pergamon, 1980.
[9] V. L. Tsymbalenko, Cryogenics **36**, 65 (1996).
[10] V. L. Tsymbalenko, Pribory Tekhn. Éksp. No. 2, 67 (1993).
[11] J. Bodensohn, K. Nicolai, and P. Leiderer, Z. Phys. **B64**, 55 (1986).
[12] V. L. Tsymbalenko, Fiz. Nizk. Temp. **21**, 162 (1995) [Low Temp. Phys. **21**, 120 (1995)].
[13] V. L. Tsymbalenko, Zh. Éksp. Teor. Fiz. **108**, 686 (1995) [JETP **81**, 373 (1995)].
[14] Ch. L. Wang and G. Agnolet, J. Low Temp. Phys. **89**, 759 (1992).
[15] Ch. L. Wang and G. Agnolet, Physica **B194–196**, 935 (1994).
[16] M. Suzuki, M. Thiel, and P. Leiderer, Proc. LT-21, **S1**, 459 (1996).

Translated by R. S. Wadhwa

Reconstruction of a charged helium film on a metallic substrate

V. Shikin

*Institute of Solid State Physics, Russian Academy of Sciences, 142432 Chernogolovka, Russia**

P. Leiderer

Universitat Konstanz, Postfach 5560 M 675, D-78434 Konstanz, Germany[1)]

(Submitted July 1, 1996; revised November 20, 1996)
Fiz. Nizk. Temp. **23**, 624–628 (May–June 1997)

Peculiarities of the reconstruction of a charged helium film surface on a metallic substrate are considered. Instability evolution in this case resembles the generation of a solitary wave in hydrodynamics of a free liquid surface and leads to the formation of charged solitons under certain conditions. Basic characteristics of such solitons are obtained in the one-dimensional approximation under the conditions of weak nonlinearity of the problem. © *1997 American Institute of Physics.* [S1063-777X(97)01605-8]

A charged liquid surface (the type of the liquid and the methods of introduction of charges into it are immaterial) possesses peculiar deformation properties. In the linear approximation, we are dealing with a considerable (''Coulomb'') rearrangement of the vibration spectrum of the free surface of such liquids. Ultimately, the spectrum of surface vibrations of the liquid loses its stability upon a monotonic increase in the surface charge. This phenomenon, which has become known mainly in connection with the decay of heavy nuclei, was studied by many authors (see, for example, Ref. 1). Most successful experiments were carried out with a liquid helium surface charged with electrons or ions,[2] for which the loss of stability by the surface can be traced in detail, and the main predictions of the theory can be confirmed.

The problem on the behavior of a charged liquid surface is important in the supercritical region also. For example, the reconstruction of the helium surface takes place for semi-infinite helium, for which the loss of stability is observed for the first time for finite wave numbers of ripplon spectrum (at the so-called capillary wave length) in the supercritical region. Instead of a plane boundary of the liquid, a periodically deformed structure is obtained with a period close to the capillary wave length and the modulation amplitude which is a complex function of supercritical parameters. The theory of this effect is presented in Refs. 3–5, while experimental investigations were carried out by the authors of Refs. 6–8.

As we go over to a liquid film of thickness smaller than the capillary length, the form of instability changes qualitatively. The most ''vulnerable'' mode in this case is that with zero wave vector. This circumstance, which had been reliably established theoretically,[9–11] was not proved in direct experiments in view of technological difficulties in operation with thick liquid films. Only indirect evidences[12] of the correctness of theoretical predictions are available, e. g., the observed decrease (as compared to the bulk value) in the critical charge density leading to the loss of stability. The evolution of instability of a charged liquid film surface in the supercritical region also remains unclear. Formally, the problem is that the ripplon spectrum has no preferred finite wave vector in the case of stability loss. As a result, it remains unclear which nonlinear reconstruction (periodic or nonperiodic) of the liquid boundary should be sought.

In this communication, we prove that the evolution of instability of the charged surface of a thick helium film (or other conducting liquid) can follow a scenario resembling the formation of a solitary wave in hydrodynamics of the free surface of a neutral liquid.[13] As in the case of a semi-infinite liquid, the transition to the instability region is accompanied by the emergence of periodic solutions of the deformation equilibrium equation. The period of this structure increases as we move further in the supercritical region, tending asymptotically to infinity. The deformation state of the charged helium film surface formed in this case is similar to an isolated soliton. The formulas describing the shape of a one-dimensional soliton will be derived in the weak nonlinearity approximation introduced below.

In addition to these original results, we shall refine some details of definition of critical conditions for the loss of stability in a charged helium film, which is important in view of the ambiguity of these definitions in Refs. 9–11.

1. Let us consider a charged helium film on a metallic substrate under the conditions of complete compensation of the electric field over the film. The relative position of the upper electrode, which is always present in problems on a charged helium surface, is immaterial (the separation between the electrode and the surface must only be larger than the film thickness). For simplicity, we assume that the possible deformation of the film surface is a function of the coordinate x alone. Thus, the initial equilibrium equation has the following structure:

$$\rho g \xi - \alpha \frac{\xi''}{[1+(\xi')^2]^{3/2}} + \frac{V^2}{8\pi(d+\xi)^2} = \text{const}, \quad -L \leqslant x \leqslant +L, \tag{1}$$

$$\xi'|_{x=0} = 0, \tag{2}$$

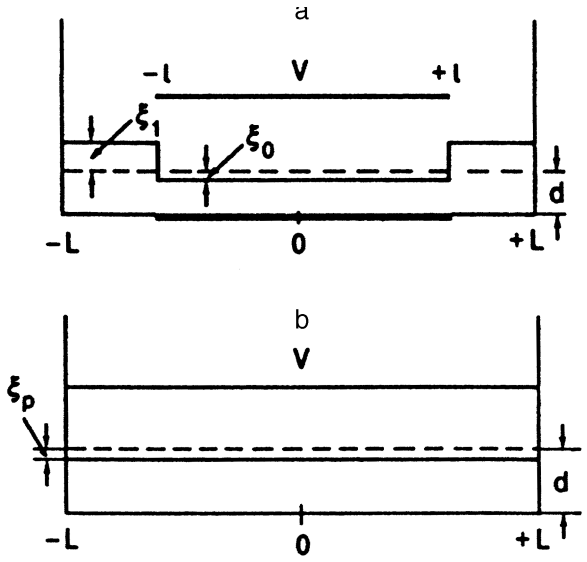

FIG. 1. Schematic diagram of experimental cell with incomplete coverage of the film surface with metallic electrodes (a) and with the film surface covered completely with metallic electrodes (b): $2l$ is the size of the electrodes, $2L$ the size of the cell, d the film thickness, ξ_0 the film strain under the electrodes, ξ_1 the film strain outside the electrodes, and ξ_p is the helium film strain.

$$V=\text{const}, \quad -l\leqslant x\leqslant +l, \tag{3}$$

$$\xi''=d^2\xi/dx^2, \quad \xi'=d\xi/dx.$$

Here $\xi(x)$ is the strain of the helium surface in the region $-L\leqslant x\leqslant +L$ in the presence of various forces acting on the film surface: gravity, surface tension, and the forces of electric origin, which are proportional to the potential difference V between the charged helium surface and the metallic substrate [$\xi(x)\to 0$ as $V\to 0$], ρ and g are the density of helium and the acceleration due to gravity, α is the surface tension, d the equilibrium thickness of the helium film for $V\to 0$, and $2l$ the size of the control electrode in the x-direction. The meaning of the constant on the right-hand side of Eq. (1) depends on the relation between l and L. The corresponding versions are given below. Requirement (2) is conditional and indicates in the long run that the solutions of Eq. (1) we are interested in have the form of standing waves. For the sake of definiteness, the origin of coordinates coincides with an extremum of one of such waves.

The electric component of Eq. (1) is written under the assumption that the solid substrate possesses perfect metallic properties. In addition, we assume that the total number of electrons on the helium film is not fixed (the potential difference V is preset). The origin of the coordinates lies on the metallic substrate. The z-axis is directed vertically upwards. The schematic diagram of the experimental cell is shown in Fig. 1.

Returning to the definition of the constant in Eq. (1), we consider first the case when $l<L$. In this case, a piecewise-smooth solution can be obtained for $\xi(x)$. Indeed, we neglect in Eq. (1) the gradients (in the general case, the reasoning remains asymptotically correct if $L>l\gg\kappa^{-1}$, where κ is the capillary constant for helium). Only the gravitational term competes with the electric term of the problem. The total volume of the liquid on free regions of the film beyond the interval $2l$ will be conserved if the strain ξ_1 of the film thickness changes sign relative to ξ_0 within this interval.This process is shown schematically in Fig. 1a. The value of the constant in Eq. (1) must be equal to $\rho g\xi_1$ so that

$$\rho g\xi_0+\frac{V^2}{8\pi(d+\xi_0)^2}=\rho g\xi_1; \quad \xi_0 l+\xi_1(L-l)=0. \tag{4a}$$

From the condition of conservation of the total volume of the liquid, we obtain

$$\xi_1=-\xi_0\,\frac{l}{L-l}. \tag{4b}$$

Here L is the total length of helium film in the x-direction.

Introducing the definition (4b) of ξ_1 into (4a), we obtain

$$\rho g^*\xi_0+\frac{V^2}{8\pi(d+\xi_0)^2}=0, \quad -l\leqslant x\leqslant +l,$$

$$g^*=g\left(1+\frac{l}{L-l}\right). \tag{4c}$$

In the limit $L\gg l$, the renormalization of g^* becomes insignificant, i.e.,

$$g^*\to g, \ \text{ if } \ L\gg l. \tag{4d}$$

The situation changes when $l\geqslant L$. The uniform electric pressure in the interval $-L\leqslant x\leqslant +L$ leads to bulk compression of helium. Naturally, we have the strain ξ_p of helium in this case also, but now its magnitude is controlled not by the gravitational term as in (4a), but by the helium compressibility $\partial P/\partial v$. Neglecting gravitation in (1) and assuming, on the contrary, that the constant is equal to the term containing $\partial P/\partial v$, we have (see also Fig. 1b)

$$\frac{V^2}{8\pi(d+\xi_p)^2}=-\frac{\partial P}{\partial v}\,L_xL_y\xi_p\,. \tag{5}$$

Here L_x and L_y are the dimensions of the helium film in the x- and y-directions. Naturally, the value of ξ_p is much smaller than ξ_0 from (4a).

2. Having analyzed expressions (4a) and (5) for static strain, we consider the existing criteria of the loss of stability in a charged helium film.

The conventional formulation of the problem on stability of a charged helium surface presumes that the size of the film in the x-direction is unlimited. Obviously, the lengths L and l cannot be varied in this case so that we can speak only of the version (5) of static strain. The equation for the small correction $\delta\xi(x)$ to static strain, which contains information on stability, can be written, according to (1) and (5), in the form

$$\xi(x)=\xi_p+\delta\xi(x), \quad \int_{-\infty}^{+\infty}\delta\xi(s)ds=0, \tag{6a}$$

$$\left[\rho g-\frac{V^2}{4\pi(d+\xi_p)^3}\right]\delta\xi$$

$$-\alpha\delta\xi''+\frac{3V^2}{8\pi(d+\xi_p)^4}\,\delta\xi^2=0. \tag{6b}$$

The combination of the terms in the brackets on the right-hand side of Eq. (6b) changes sign at the point

$$4\pi\rho g(d+\xi_p)^3 = V_{\rm cr}^2 . \tag{7}$$

This criterion corresponds to the loss of stability of the homogeneous state of a charged helium film. Neglecting the quantity ξ_p in this expression as compared to d, we arrive at the definition of the stability boundaries given in Refs 9 and 10.

If $l \neq L$, the situation changes:

$$4\pi\rho g^*(1+\xi_0)^3 = U_{\rm cr}^2. \tag{8a}$$

Here g^* and ξ are taken from (4c), and we cannot neglect the quantity ξ_0 in (8a) since $\xi_0 \gg \xi_p$. Let us suppose, for example, that the following relation is satisfied exactly:

$$V = U_{\rm cr}. \tag{8b}$$

Moreover, using relations (4c), (8a), and (8b), we obtain

$$\xi_0^{\rm cr} = -d/3. \tag{9}$$

In other words, the uniform strain from (4a)–(4c) at the critical point is comparable to the initial film thickness, and its disregard in the definition of $U_{\rm cr}$ is not justified. The correct expression for $U_{\rm cr}$ taking into account (8a) has the form

$$U_{\rm cr}^2 = 2V_{\rm cr}^2 g^*/3g, \quad V_{\rm cr}^2 = 4\pi\rho\ g d^3. \tag{10}$$

Here g^* is taken from (4c), and $V_{\rm cr}$ is the critical potential (7) from Refs. 9 and 10.

The possible effect of static deformation on the critical field of a thin film was noted for the first time in Ref. 11. The result obtained in Ref. 11 coincides with (10) if $g^*/g = 1$. However, an analysis of the conditions under which such a renormalization appears was not carried out in Ref. 11. For this reason, it was erroneously assumed in Ref. 11 that the definition (7) of the critical potential is not correct. In actual practice, both definitions of the critical potential ((7) and (10)) are justified under appropriate conditions.

3. Let us describe the reconstruction of a charged helium film. This problem is formulated in the simplest form for the version with $l = L$ to which our analysis will be confined. In this case, we proceed from Eq. (6b) with the boundary conditions

$$\delta\xi'(x=0) = 0, \tag{11}$$

$$\int_{-\infty}^{+\infty} \delta\xi(s)\,ds = 0. \tag{12}$$

The reconstruction of the film is naturally possible only in the region

$$V > V_{\rm cr}. \tag{13}$$

Under these conditions, the first integral in Eq. (6b) has the form

$$[d\xi(x)/dx]^2 = q^3[-\gamma\delta\xi^2 + \delta\xi^3 + c], \tag{14a}$$

where

$$p^2 = \kappa^2\left[\frac{V^2}{4\pi(d+\xi_p)^3\rho g} - 1\right], \quad q^3 = \frac{V^2}{4\pi(d+\xi_p)^4\alpha},$$

$$\gamma = p^2/q^3, \quad \kappa^2 = \rho g/\alpha, \tag{14b}$$

κ being the capillary constant for liquid helium.

Let us assume, in accordance with (11), that $\delta\xi'(x) = 0$ at a certain point $\delta\xi_0$, and

$$\delta\xi_0 > 0. \tag{15a}$$

These requirements lead to the following value of the constant c in Eq. (14a):

$$c = \gamma\delta\xi_0^2 - \delta\xi_0^3. \tag{15b}$$

A periodic (or soliton) solution of Eq. (14a) exists if, in addition to the point $\delta\xi_0$, there exist some additional points with $d\xi(x)/dx = 0$. Thus, the problem on reconstruction boils down to an analysis of the properties of the roots of the equation

$$\delta\xi^3 - \delta\xi_0^3 - \gamma(\delta\xi^2 - \delta\xi_0^2) = 0. \tag{16}$$

This equation has only one root $\delta\xi = \delta\xi_0$. Consequently, for the roots $\delta\xi \neq \delta\xi_0$, expression (16) is simplified:

$$\delta\xi^2 + \delta\xi(\delta\xi_0 - \gamma) + \delta\xi_0(\delta\xi_0 - \gamma) = 0. \tag{17}$$

The solution of Eq. (17) has the form

$$2\delta\xi_\pm = -(\delta\xi_0 - \gamma) \pm \sqrt{(\delta\xi_0 - \gamma)^2 - 4\delta\xi_0(\delta\xi_0 - \gamma)}. \tag{18}$$

For the roots $\delta\xi_\pm$ to be real-valued, the following condition must be satisfied:

$$(\delta\xi_0 - \gamma)^2 - 4\delta\xi_0(\delta\xi_0 - \gamma) \geqslant 0 \quad \text{or}$$

$$(3\delta\xi_0 + \gamma)(\gamma - \delta\xi_0) \geqslant 0. \tag{19}$$

Using (14a), we can draw the conclusion that the solutions $\delta\xi_\pm$ exist if

$$\delta\xi_0 \leqslant \gamma. \tag{20}$$

From the two versions of $\delta\xi_\pm$, we must use only the root $\delta\xi_-$ for the condition (12) to be satisfied.

In the limit $\delta\xi_0 \ll \gamma$, we have

$$\delta\xi_- \simeq -\delta\xi_0. \tag{21a}$$

If, however, $\delta\xi_0 \to \gamma$, we have

$$\delta\xi_- \simeq -2\sqrt{\delta\xi_0(\gamma - \delta\xi_0)}. \tag{21b}$$

The period T of the deformation structure formed can be determined from the relation

$$\frac{T}{2} = \frac{1}{q\sqrt{q}} \int_{\delta\xi_-}^{\delta\xi_0} \frac{d\,\delta\xi}{\sqrt{c + \delta\xi^3 - \gamma\delta\xi^2}}. \tag{22}$$

Together with (12) and (17), this expression defines the relation between T and γ. In the limit $\delta\xi_0 \ll \gamma$, when relation (21a) is valid, and hence condition (12) is satisfied automatically, relations (17) and (22) lead to

$$T = 2\pi/p. \tag{23}$$

In the opposite limiting case of the maximum amplitude $\delta\xi_0 \to \gamma$, the period $T \to \infty$, and the periodic solution is transformed into a soliton solution. The soliton profile can be obtained from the equation

$$\int_{\delta\xi}^{\gamma} \frac{d\,\delta\xi}{\delta\xi\sqrt{\gamma-\delta\xi}} = q\sqrt{q}x \tag{24}$$

or

$$\delta\xi(x) = \gamma[1-\tanh^2(px/2)], \tag{25}$$

where p and γ are taken from (14a).

The root $\delta\xi_-$ in this limit has the form (21b), while for $\delta\xi_0 \to \gamma$ it tends to zero.

Analyzing the results (21)–(25), we note that the period T is a nonmonotonic function of the supercritical parameter. According to (23), $T \to \infty$ as $p \to 0$. The behavior of T for $\delta\xi_0 \to \gamma$ is similar. This nonmonotonicity probably has a physical meaning. However, it is more natural to deal with the monotonic dependence $T(p)$, the more so that the amplitude of $\xi(x)$ does not depend on the supercritical parameter for small p (condition (12) is satisfied automatically). The nonmonotonicity in the behavior of $T(p)$ can be removed by introducing the procedure of subtraction

$$\frac{T^*}{2} = \frac{1}{q\sqrt{q}}\left[\int_{\delta\xi_-}^{\delta\xi_0} \frac{d\,\delta\xi}{\sqrt{c+\delta\xi^3-\gamma\delta\xi^2}} - \frac{\pi}{p}\right].$$

In this definition, T^* tends to zero as $p \to 0$ and increases monotonically with p, approaching the value of T defined by (22) in the region $\delta\xi_0 \to \gamma$.

Thus, a transition of a charged helium film to the supercritical state leads to the formation of solitons of the form (25) on its surface.

This research was carried out under the financial support of INTAS Grant No. 93 0933 and the NASA RKA program.

*E-mail: shikin@issp.ac.ru
1)E-mail paul.leiderer@uni-konstanz.de

[1] L. D. Landau and E. M. Lifshitz, *Electrodynamics of Continuous Media*, Pergamon, Oxford 1960.
[2] V. B. Shikin and Yu. P. Monarkha, *Two-Dimensional Charge Systems in Helium* [in Russian], Nauka, Moscow (1989).
[3] V. M. Zaitsev and M. I. Shliomis, Dokl. Akad. Nauk. SSSR **188**, 1261 (1969) [Sov. Phy. Doklady **14**, 1001 (1970)].
[4] L. P. Gor'kov and D. M. Chernikova, Dokl. Akad. Nauk. SSSR **228**, 829 (1976) [Sov. Phys. Doklady **21**, 328 (1976)].
[5] V. I. Mel'nikov and S. V. Meshkov, Pis'ma Zh. Éksp. Teor. Fiz. **33**, 222 (1981) [JETP Lett. **33**, 211 (1981)].
[6] M. Wanner and P. Leiderer, Phys. Rev. Lett. **42**, 315 (1979).
[7] P. Leiderer and M. Wanner, Phys. Lett. **A73**, 1869 (1979).
[8] R. W. Giannetta and H. Ikezi, Surf. Sci. **113**, 412 (1982).
[9] L. P. Gor'kov and D. M. Chernikova, Pis'ma Zh. Éksp. Teor. Fiz. **18**, 119 (1979) [JETP Lett. **18**, 109 (1979)].
[10] D. M. Chernikova, Fiz. Nizk. Temp. **2**, 1374 (1976) [Sov. J. Low Temp. Phys. **2**, 668 (1976)].
[11] V. V. Tatarskiĭ, Fiz. Nizk. Temp. **10**, 435 (1984) [Sov. J. Low Temp. Phys. **10**, 227 (1984)].
[12] A. P. Volodin, M. S. Khaikin, and V. S. Edel'man, Pis'ma Zh. Éksp. Teor. Fiz. **26**, 707 (1977) [JETP Lett. **26**, 543 (1977)].
[13] M. A. Lavrent'ev and B. V. Shabat, *Methods of the theory of functions of Complex Variables* [in Russian], Fizmatgiz, Moscow (1958).

Translated by R. S. Wadhwa

Quantum magnetotransport in a highly correlated two-dimensional electron liquid on a superfluid helium surface

Yu. P. Monarkha

B. Verkin Institute for Low Temperature Physics and Engineering, 47 Lenin Av. 310164, Kharkov, Ukraine
Institute for Solid State Physics, University of Tokyo, Roppongi 7-22-1, Minato-ku, Tokyo 106, Japan[*]

K. Shirahama and K. Kono

Institute for Solid State Physics, University of Tokyo, Roppongi 7-22-1, Minato-ku, Tokyo 106, Japan
(Submitted November 14, 1996)
Fiz. Nizk. Temp. **23**, 629–638 (May–June 1997)

The theoretical concept of the inelastic quantum magnetotransport of highly correlated surface electrons on superfluid helium is presented. The low-temperature magnetoconductivity data are obtained from the damping of the edge magnetoplasmons. It is shown that the temperature and magnetic field dependences of the magnetoconductivity can be perfectly described by the inelastic many-electron theory as the interplay of two kinds of Landau level broadening produced by scatterers and by mutual Coulomb interaction. © *1997 American Institute of Physics.* [S1063-777X(97)01705-2]

INTRODUCTION

In the presence of a strong magnetic field B oriented normally the surface electrons (SE) on superfluid helium provide a unique possibility for studying quantum transport phenomena in a highly correlated, two-dimensional ($2D$) electron liquid. At typical electron densities $n \sim 10^8$ cm^{-2} and temperatures $T < 0.5$ K the Coulomb coupling parameter (the mean Coulomb energy over the mean kinetic energy) $G = e^2\sqrt{\pi n}/(k_B T)$ attains unusually large values ($G \sim 100$). Since the Fermi energy of the SE is much less than $k_B T$, the ultra-quantum limit ($\hbar\omega_c \gg k_B T$ where ω_c is the cyclotron frequency) is easily achieved and at typical helium temperatures nearly all electrons populate the ground Landau level.

A $2D$ electron gas in a magnetic field is a singular system—the electron energy spectrum becomes discrete; therefore, the usual Born approximation fails to describe the quantum magnetotransport. The conventional way to treat this system is the self-consistent Born approximation (SCBA),[1] in which the effects of level broadening caused by scatterers are taken into account. For SE on the superfluid helium the level broadening is the smallest energy parameter: $\Gamma \ll k_B T$. Therefore, at $\hbar\omega_c \gg k_B T$ the SE are confined to a very narrow energy space of the ground level. In the limit $\Gamma \to 0$, the elastic and inelastic scattering processes result in the different analytical behavior of the magnetoconductivity: $\sigma_{xx} \propto 1/\Gamma \to \infty$ for the elastic scattering from impurities, whereas $\sigma_{xx} \to 0$ for the inelastic scattering within the ground level. It means that the correct result for σ_{xx} should be crucially dependent on the relationship between the two small parameters, the energy exchanged at a collision $\Delta\omega$, and the Landau level broadening Γ. It may be far away from the result of the usually used elastic approximation (the nonlinear breakage of the elastic approximation was recently discussed in Ref. 2).

The first zero-field conductivity measurements,[3–5] have shown that in spite of the high Coulomb correlations, in the low temperature (LT) range down to the Wigner solid transition the SE mobility behaves mostly like the mobility of an ideal $2D$ electron gas. The cause of this behavior is that the wavelength of thermal electrons is much shorter than the Coulomb correlation length.[6] In a magnetic field the energy scale of the SE density of states (Γ) is usually much less than thermal energy and the many-electron effect can be more pronounced.

The SE scattering arises from capillary wave quanta (ripplons) and helium vapor atoms. In the vapor atom scattering regime ($T > 1$ K) the quantization of the electron motion caused by the magnetic field leads to unexpected Hall effect: the Hall angle decreases with the magnetic field B in the ultra quantum limit, since the effective collision frequency $\nu(B)$ increases faster with B than the cyclotron frequency.[7,8] It was shown that the effect and the experimental data can be perfectly described by the extended SCBA theory[7] up to 20 T. In this regime the many-electron effect is usually small with the exception of the narrow temperature range around 1 K, where the magnetoconductivity becomes density dependent if the magnetic field is weak.[9,10] It should be pointed out that under such conditions the energy exchanged at a collision is of the same order of magnitude as Γ and the inelastic effect of the electron-atom scattering which is neglected in Refs. 9 and 10, should be additionally analyzed.

In the ripplon scattering regime ($T < 0.7$ K) the experimental and theoretical situations are much more complicated. The experimental magnetoconductivity data performed by different experimental groups contradict each other. According to Ref. 11 and 12, the SE magnetoconductivity σ_{xx} has a minimum at $T \approx 1$ K and increases slowly down to $T \simeq 0.5$ K, while in Ref. 13 the SE resistivity ρ_{xx} and, consequently, σ_{xx} decrease with decreasing temperature to 0.4 K. Therefore, any alternative experimental method of studying the quantum magnetotransport at LT is welcome.

At LT small deviations from the axial symmetry of the experimental cell spoils, in our view, the conventional analysis of the data due to the excitation of low frequency edge magnetoplasmons (EMP). At the same time, the EMP exci-

tation technique can be a tool for studying the quantum magnetotransport.[14] As was shown in a rather general way,[15,16] at strong magnetic fields the damping of the EMP is proportional to the longitudinal conductivity. Therefore, the EMP damping measurement can be an alternative way of determining the SE magnetoconductivity.

The electron-ripplon scattering is analogous to the electron scattering by acoustic phonons in solids. There is, however, a substantial difference in the SCBA treatment of SE due to the unusual ripplon dispersion, $\omega_q=(\alpha/\rho)^{1/2}q^{3/2}$ (here α is the surface tension and ρ is the liquid helium mass density). In the semiconductor $2D$ electron systems the acoustic phonon scattering is usually treated as quasi-elastic[17] since the typical phonon energies are much smaller than Γ. Previous theories of the ripplon-induced quantum magnetotransport, the single-electron theory (Saitoh[18]), and the many-electron theory (Dykman and Khazan (DK)[19]), which were organized in a much more complex way than the conventional SCBA theory, were based on the quasi-elastic approximation. It can be shown that for the electron-ripplon scattering the inelastic parameter $\delta=\hbar\omega_q/\Gamma$ increases with the magnetic field due to $\omega_q\propto q^{3/2}\propto B^{3/4}$ (usually $\Gamma\propto\sqrt{B}$). Additionally, δ increases with decreasing T and soon becomes larger than unity. Therefore, the theory of the LT quantum magnetotransport of SE should be initially formulated as an inelastic quantum transport theory.

In this paper we report the theoretical concept of the inelastic quantum magnetotransport of the SE on superfluid helium for electron-atom and electron-ripplon scattering, and the LT magnetoconductivity data obtained from the damping coefficient of the EMP. The many-electron effect which is important at rather weak magnetic fields is taken into account by means of the Coulomb correction to the broadening of the single-electron density of states, Γ_C. The theory based on the extended SCBA reproduces the results of the previous approaches as the opposite limiting cases, if the inelastic effect is ignored and if the Landau level broadening is successively reduced to the ripplon-induced broadening $\Gamma\to\Gamma_r$ ($\Gamma_C=0$; the single electron Saitoh's theory) and to the Coulomb broadening $\Gamma\to\Gamma_C$ ($\Gamma_r=0$; the DK theory). Under real experimental conditions, Γ transforms continuously from Γ_C to Γ_r with the increase of the magnetic field B and the inelastic effect substantially affects the quantum magnetotransport of SE, reducing both Γ and σ_{xx}. The new LT data of the SE magnetoconductivity as a function of T and B are in good agreement (without any adjusting parameter) with the presented theory of inelastic quantum magnetotransport. The same approach applied as a test to the electron-atom scattering describes previously measured σ_{xx} data, including the effects caused by the electron-electron interaction.

THEORETICAL CONCEPT

Our intention is to describe the quantum magnetotransport of an electron liquid of which the mean potential energy is approximately one hundred times larger than the mean kinetic energy. Under such condition the conventional approaches developed for electrons with weak mutual interaction can scarcely be used. As was shown in Ref. 7, it is natural to assume that the highly correlated electron liquid is in equilibrium in the center-of-mass frame moving along the surface with a drift velocity $\mathbf{u}_d$ in crossed magnetic $\mathbf{B}$ and electric $\mathbf{E}$ fields. In this case the substantial simplification of the mathematical formalism appears to be possible, since the conductivity of SE can be expressed in terms of the equilibrium dynamic structure factor of the $2D$ electron liquid.[7,8]

Effective collision frequency

We start with the interaction Hamiltonian which allows one to describe the inelastic magnetotransport induced by vapor atoms and ripplons in a similar way:

$$H_{\rm int}=\sum_{j=a,r}\sum_{\mathbf{q}} U_j n^{(\rm el)}_{-\mathbf{q}}A_{j,\mathbf{q}},$$

$$n^{(\rm el)}_{\mathbf{q}}=\sum_e \exp(-i\mathbf{q}\mathbf{r}_e). \tag{1}$$

Here we use j to distinguish the electron-atom interaction ($j=a$) from the electron-ripplon interaction ($j=r$) and introduce the notation

$$A_{r,\mathbf{q}}=b_{\mathbf{q}}+b^+_{-\mathbf{q}},\quad A_{a,\mathbf{q}}=\sum_k \eta_k\sum_{\mathbf{K}'} a^+_{\mathbf{K}'-\mathbf{K}}a_{\mathbf{K}},$$

$$U_r=V_q\sqrt{\frac{\hbar q}{2\rho\omega_q}},\quad U_a=\frac{2\pi\hbar^2 s}{m},\quad \eta_k=\langle 1|e^{ikz}|1\rangle, \tag{2}$$

$n^{(\rm el)}_{\mathbf{q}}$ is a $2D$ Fourier transform of the electron density; $b^+_{\mathbf{q}}$ and $a^+_{\mathbf{q}}$ are the creation operators of ripplons and ^{4}He atoms; $(1\|1)$ means the average over the ground surface level; $\mathbf{R}=\{\mathbf{r},z\}$; $\mathbf{K}=\{\mathbf{q},k\}$; V_q is the electron-ripplon coupling;[20] s is the electron-atom scattering length, and m is the free electron mass.

According to Refs. 7 and 8, the quantum magnetotransport can be described by the elementary expressions for the conductivity tensor with the field- and density-dependent effective collision frequency $\nu(B,n)$. For a highly correlated $2D$ electron liquid we have

$$\nu=\frac{1}{2mk_BT}\sum_{\mathbf{q}} q^2\Bigg\{U_r^2N_q^{(r)}S_0(q,\omega_q) + \frac{1}{2}U_a^2\sum_k|\eta_k|^2\sum_{\mathbf{K}'}N^{(a)}_{\mathbf{K}'},S_0(q,\Delta\omega_a)\Bigg\}, \tag{3}$$

where $N_q^{(r)}$ and $N^{(a)}_{\mathbf{K}'}$ are the distribution functions of ripplons and vapor atoms;

$$S_0(q,\omega)=N_e^{-1}\int e^{i\omega t}\langle n^{(\rm el)}_{\mathbf{q}}(t)n^{(\rm el)}_{-\mathbf{q}}(0)\rangle dt$$

is the equilibrium dynamic structure factor; $\hbar\Delta\omega_a=\varepsilon^{(a)}_{\mathbf{K}'}-\varepsilon^{(a)}_{\mathbf{K}'-\mathbf{K}}$ is the energy exchanged as a result of the electron-atom collisions, and N_e is the total number of electrons. In this treatment, the main problem is to find the appropriate approximation for $S_0(q,\omega)$.

It should be pointed out that Eq. (3) would still contain the many-electron effect even if we would use the single-electron approximation for the dynamic structure factor

$$S_0(q,\omega)=\frac{2\hbar}{\pi^2 N_e l^2}\int dE f(E)[1-f(E+\hbar\omega)]$$

$$\times\sum_{N,N'} J_{N,N'}\ \mathrm{Im}\ G_N(E)\mathrm{Im}\ G_{N'}(E+\hbar\omega). \tag{4}$$

Here l is the magnetic length $(=\sqrt{\hbar c/eB})$; $f(E)$ is the Fermi-distribution function; $J_{N,N'}=|\langle N,X|\exp(i\mathbf{qr}_e)\times|N',X-q_y l^2\rangle|^2$, and $G_N(E)$ is the single-electron Green's function. In this approximation the theory is the quantum analog of the semi-classical treatment of highly correlated electrons by means of the drift-velocity-shifted distribution function $f_{\mathbf{k}}=f(E-\hbar\mathbf{ku}_d)$.[6,21]

Following the general idea of Ref. 22, we take additionally into account the many-electron effect as a Coulomb correction to broadening of the single-electron density of states Γ_C. In this picture an electron feels the fluctuation field of others electrons as a random potential, since the density fluctuation has spectral intensities at very low frequencies. Im $G_N(E)$ is therefore assumed to have a semielliptic shape:

$$\mathrm{Im}\ G_N(E)=-\frac{2}{\Gamma_N}\sqrt{1-[(E-E_N^*)/\Gamma_N]^2}, \tag{5}$$

where E_N^* is the central position of the Landau level. The level broadening Γ_N is formed by all the present interactions, including the mutual interaction of the SE. Thus, here the many-electron effect is finally taken into account in two major respects: first, high Coulomb correlations form the equilibrium dynamic structure factor included in Eq. (3); secondly, the mutual interaction affects the single electron density of states.

Equation (3)–(5) establish the relationship between the effective collision frequency and the level broadening. In the ultraquantum limit ($N=0$, $\Gamma_0\equiv\Gamma$) we have

$$S_0(q,\omega)=\frac{32\hbar}{3\pi\Gamma}\exp\left(-\frac{q^2l^2}{2}\right)\chi\left(\frac{\hbar\omega}{\Gamma}\right),$$

$$\chi(\delta)=\frac{3}{4}\int_{-1}^{1-\delta}\sqrt{1-x^2}\sqrt{1-(x+\delta)^2}dx. \tag{6}$$

The function $\chi(\delta)$ describes the inelastic effect. For small values of the energy exchanged as a result of a collision, $\hbar\omega\ll\Gamma$, the quantum magnetotransport can be considered as quasielastic, $\chi\to 1$. At $\hbar\omega\sim\Gamma$, as it is shown in Fig. 1, the inelastic effect substantially reduces $S_0(q,\omega)$ and consequently $\nu(B,n)$.

In general, the inelastic effect is difficult to describe for the electron-vapor atom scattering because of additional integrations over k and $\mathbf{K}'$ which appear in Eq. (3) if $\Delta\omega_a\neq 0$. In this case we can therefore substantially simplify the problem as follows. Usually, $q',k'\gg q,k$, and $\Delta\omega_a\simeq\hbar(\mathbf{qq}'+kk')/M$ (here M is the helium atom mass). First, we disregard the term proportional to $\mathbf{q}$, since it is important only in the range of strong magnetic fields where the inelastic effect can be ignored. Taking into account that at $B<10$ T there is nearly no difference between σ_{xx} calculated for the Gaussian and semielliptic shapes of the density of states,[8] we use the more simple Gaussian shape for describing the inelastic effect of the electron-atom scattering:

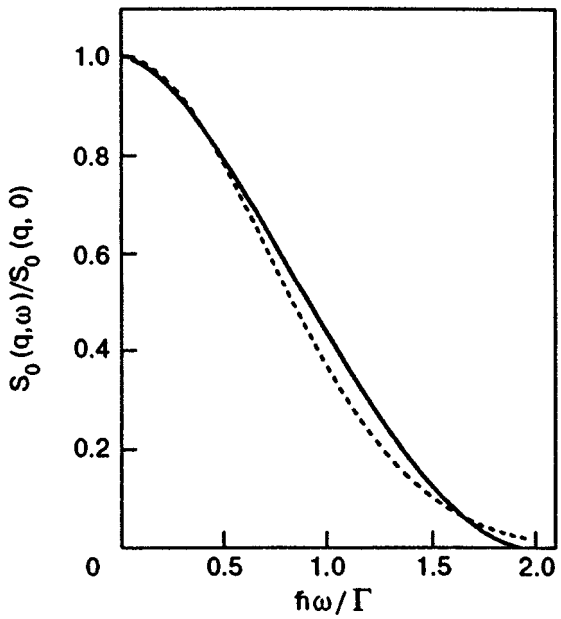

FIG. 1. The dynamic structure factor vs. the inelastic parameter for the semielliptic (solid) and Gaussian (dashed) shapes of the density of states in the ultraquantum limit.

$$\nu^{(a)}=\nu_0^{(a)}\frac{16}{3\pi}\int_0^\infty\frac{dy}{(1+y^2)^3\sqrt{1+\delta_a^2y^2/2}},$$

$$\delta_a=\frac{4\hbar\gamma}{\Gamma}\sqrt{\frac{k_BT}{M}}. \tag{7}$$

Here δ_a is the inelastic parameter for the electron-atom scattering,

$$\nu_0^{(a)}=\frac{\sqrt{\pi}\omega_c\Gamma_{a,0}^2}{4\Gamma k_BT}\exp\left[-\left(\frac{\Gamma}{4k_BT}\right)^2\right]\coth\left(\frac{\hbar\omega_c}{2k_BT}\right), \tag{8}$$

γ is the parameter of the SE wave function $\langle 1|z\rangle\propto z\times\exp(-\gamma z)$, which increases with the holding electric field $E_\perp$. As usual, we combined the interaction parameters into $\Gamma_{a,0}$, which is equal to the Landau level broadening caused by the electron-atom interactions only, $\Gamma_{a,0}=\hbar\sqrt{(2/\pi)\omega_c\nu(0)}$. It should be pointed out, however, that here $\Gamma_{a,0}$ does not originate from the density of states, and differs from Γ due to other interactions. In this form, the effective collision frequency has the required analytical behavior at $\Gamma\to 0$ ($\nu\propto 1/\Gamma\to\infty$), which proves additionally the importance of the self-consistent broadening of the Landau levels.

In the case of the electron-ripplon scattering, the inelastic parameter is of a very simple form, $\delta_r=\hbar\omega_0/\Gamma$ [here $\omega_0^2=2^{3/2}\alpha/(\rho l^3)$] and $\nu^{(r)}$ has no additional integrations typical of the electron-atom scattering. Therefore, Eq. (6) can be directly insert into

$$\nu^{(r)}(B,n)=\frac{1}{8\pi m\alpha}\int_0^\infty qV_q^2S_0(q,\omega_q)dq. \tag{9}$$

Landau level broadening

According to general rules of the many-particle physics,[23] if the Coulomb interaction is neglected, the SE self-energy can be written as

$$\Sigma_N(E)=i\sum_{\mathbf{q}}\sum_{N'}J_{N,N'}\int\frac{d\omega}{2\pi}G_{N'}(E-\hbar\omega)\sum_{j=a,r}U_j^2D_j(q,\omega). \tag{10}$$

Here we introduced the correlators

$$D_i(q,t-t')=-i\langle T[A_{j,\mathbf{q}}(t)A_{j,-\mathbf{q}}(t')]\rangle,$$

which are similar for the two kinds of electron scattering $(j=a,r)$.

It is easy to see that in the limit $\hbar\omega\ll E$, Eq. (10) reduces to $\Sigma_N=1/4\Gamma_N^2G_N(E)$ and the broadening can be found self-consistently by using Dyson's equation. In this case Im $G_N(E)$ has a semielliptic shape, with the level broadening $\Gamma=(\Gamma_{a,0}^2+\Gamma_{r,0}^2)^{1/2}$. Here $\Gamma_{a,0}$ is the usual vapor-atom-induced broadening, and $\Gamma_{r,0}$ is the ripplon-induced, quasielastic broadening, which is twice as large as a result of the qualitative analysis of Ref. 24:

$$\Gamma_{r,0}^2=\frac{\Lambda_0^2k_BT}{\pi\alpha l^4}I^*,\quad I^*=\int_0^\infty W^2(x)e^{-x}dx/x. \tag{11}$$

Here we use the notation

$$W(x)=x\omega\left(\frac{x}{2\gamma^2l^2}\right)+\frac{eE_\perp l^2}{\Lambda_0};\quad \Lambda_0=\frac{e^2(\varepsilon-1)}{4(\varepsilon+1)};$$

$$w(y)=-\frac{1}{1-y}+\frac{1}{(1-y)^{3/2}}\ln\left[\frac{(1+\sqrt{1-y}}{\sqrt{y}}\right];$$

ε is the dielectric constant. Since the elastic broadening is caused by ripplons $\Gamma_{r,0}\propto\sqrt{T}$, the effective collision frequency $\nu\propto 1/\Gamma_{r,0}$ reproduces the result of the previous single-electron theory:[18] $\sigma_{xx}\propto 1/\sqrt{T}$.

In Eq. (8) the term proportional to $E_\perp^2$ has a logarithmic divergence for small q. We should cut it off at wave vectors, for which the approximations made above fails (for instance, it can be $q\approx\sqrt{\pi n}$). Still, in the LT limit which we are considering the only low electron densities, $n<5\cdot10^7$ cm^{-2}, are important and this term can be neglected at $B>1$ T.

In the inelastic theory the situation is much more complicated. Im $G_N(E)$ is nonetheless assumed to be of a sharp semielliptic shape with the level broadening defined as $\Gamma_N=-2\,\mathrm{Im}\,\Sigma_N(E_N^*)$. Usually, $N_q^{(r)}\gg 1$; in this case the ripplon Green's function $D_r(q,\omega)$ and $D_a(q,\omega)$ have similar structures:

$$D_r(q,\omega)=-2\pi iN_q^{(r)}[\delta(\omega-\omega_q)+\delta(\omega+\omega_q)],$$

$$D_a(q,\omega)=-2\pi i\sum_k|\eta_k|^2\sum_{\mathbf{K}'}N_{\mathbf{K}'}^{(a)}\delta(\omega+\Delta\omega_a). \tag{12}$$

Therefore, the self-consistent equation for the level broadening can be written as

$$\Gamma_N=2\sum_{\mathbf{q}}\sum_{N'}J_{N,N'}\int\frac{d\omega}{2\pi}\,\mathrm{Im}\,G_{N'}(E-\hbar\omega)\sum_{j=a,r}U_j^2\,\mathrm{Im}\,D_j(q,\omega). \tag{13}$$

From this equation it can be seen that the mixing of the Landau levels can be ignored $(N'=N)$ if $\Gamma_N\ll\hbar\omega_c$ (which we assume). At the same time, it follows that the inelastic effect changes the level broadening if $\hbar\omega\sim\Gamma_N$.

In the presence of the Coulomb correction to the broadening of the single-electron density of states Γ_C, the self-consistent equation for the total level broadening Γ can be written as

$$\Gamma^2=\Gamma_C^2+\Gamma_{a,0}^2Y_a(\delta_a)+\Gamma_{r,0}^2Y_r(\delta_r). \tag{14}$$

Here δ_a and δ_r are the inelastic parameters for the two kinds of electron scattering;

$$Y_a(\delta)=\frac{16}{3\pi}\int_0^\infty\frac{dy}{[1+y^2]^3\sqrt{1+\delta^2y^2}};$$

$$Y_r(\delta)=\frac{1}{I^*}\int_0^\infty e^{-x}\sqrt{1-\delta^2x^{3/2}}W^2(x)\,\theta(1-\delta^2x^{3/2})\,\frac{dx}{x};$$

and $\theta(x)$ is the unit step function. Since the parameters δ_r and δ_a depend on Γ, Eq. (14) is a transcendental equation whose solution as a function of basic parameters T, B, and n should be found numerically.

Regarding the Coulomb broadening, we will use the results of Refs. 9 and 19 ($\Gamma_C=\hbar/\tau_e=eE_fl$), where the fluctuating electric fields were calculated

$$E_f\simeq 0.84\left(\frac{4\pi k_BTn^{3/2}}{\varepsilon}\right)^{1/2}.$$

Since the ripplon or vapor-atom-induced broadening increases with the magnetic field (which is approximately proportional to $\sqrt{B}$) while $\Gamma_C\propto 1/\sqrt{B}$, the Coulomb correlations affect the quantum magnetotransport only at weak magnetic fields and high electron densities.

It is instructive to plot the inelastic parameters as functions of T for different values of the magnetic field, as it is done in Fig. 2. For the electron-atom scattering it follows (Fig. 2,a) that at temperatures of about 1 K, where the many-electron effect is usually studied,[9,10] the Coulomb correlations substantially reduce the inelastic parameter. Still, the single-electron approximation (dashed curves) and many-electron theory (solid curves) give $\delta_a\sim 1$. According to Fig. 1, at such δ_a we could expect a large decrease in Γ and $\nu^{(a)}$. Regarding the level broadening and effective collision frequency induced by the electron-atom interactions, the inelastic effect nonetheless turns out to be less important due to the additional integrations over k and $\mathbf{K}'$ in Eqs. (3) and (12). As it is shown in Figs. 3 and 4, the many-electron effect and the contribution of ripplons to the level broadening prevent a strong decrease in Γ and $\nu^{(a)}$ at weak magnetic fields and $T<1$ K.

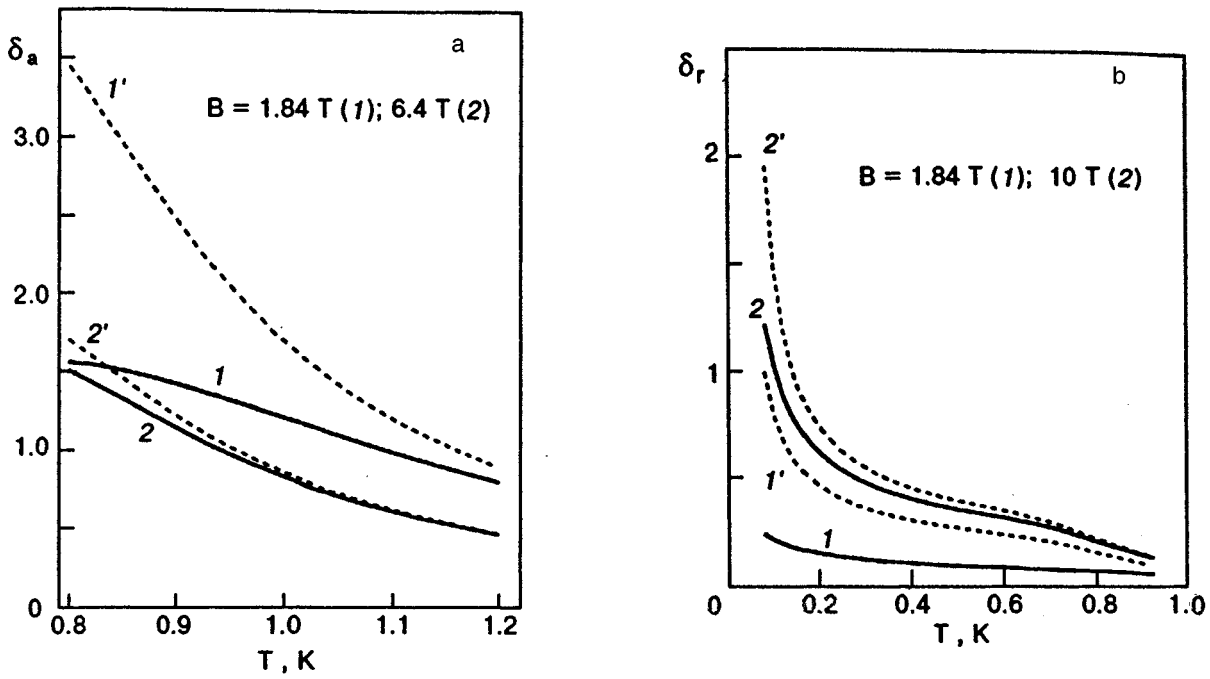

FIG. 2. The inelastic parameters δ_a (a) and δ_r (b) vs. temperature for $n=3.5\cdot 10^7$ cm^{-2} and the two values of the magnetic field: the many-electron theory (solid); the single-electron theory (dashed).

The situation is different for the electron-ripplon scattering where Γ_C and $\Gamma_{r,0}$ have the same T-dependences: Γ_C, $\Gamma_{r,0}\propto\sqrt{T}$. The inelastic parameter δ_r increases with decreasing temperature and the many-electron effect cannot suppress the increase at strong magnetic fields, as is clearly seen in Fig. 2,b. In this case there is no additional integration except for the integration over q [Eq. (9)]. Therefore, the inelastic effect should crucially affect the quantum cially affect the quantum magnetotransport of SE, which changes the T-dependences of Γ and σ_{xx} at LT.

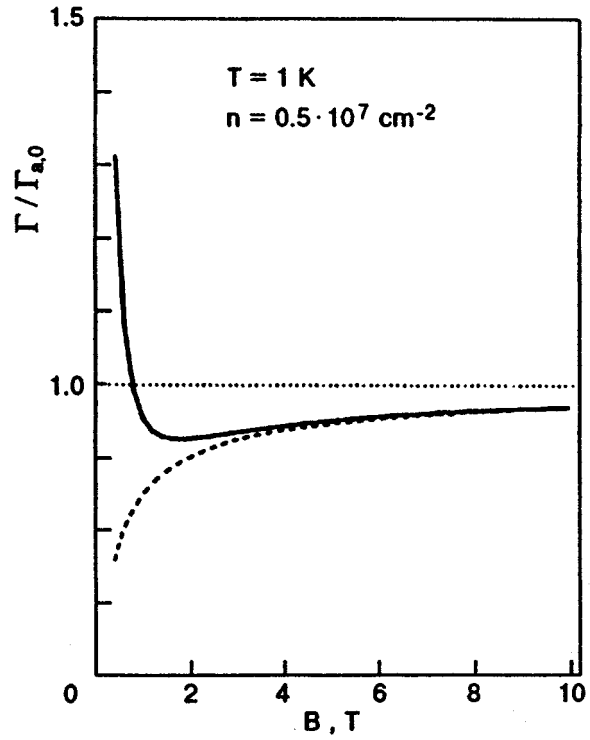

FIG. 3. The Landau level broadening Γ as a function of the magnetic field: the many-electron theory (solid); the single-electron theory (dashed).

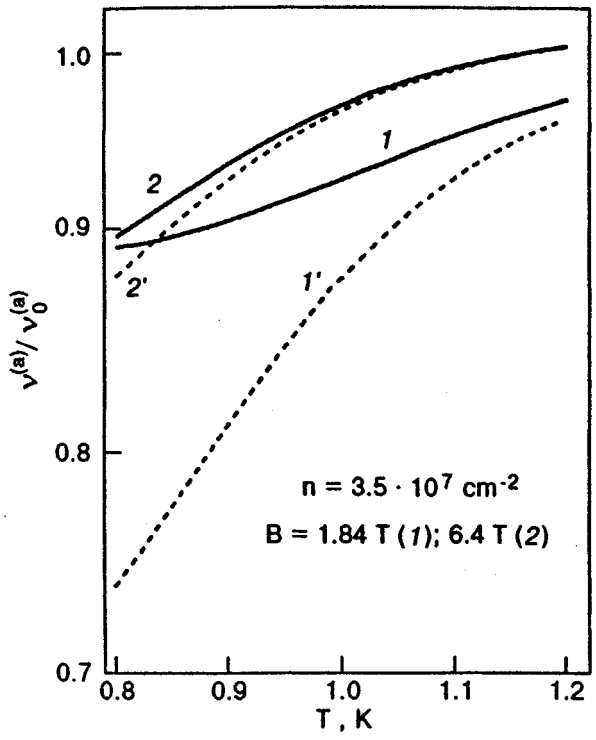

FIG. 4. The temperature dependence of the inelastic factor $\nu^{(a)}/\nu_0^{(a)}$ for two values of the magnetic field: the many-electron theory (solid); the single-electron theory (dashed).

EXPERIMENTAL METHOD

As was stated in the introduction, our experimental method of determining σ_{xx} is based on the general theoretical conclusions of Refs. 15 and 16 that at strong enough magnetic fields the damping coefficient of EMP is proportional to the longitudinal conductivity (usually it is valid at $B>0.5$ T). In this case the proportionality constant can be considered as a geometrical factor which is independent of B and T. Therefore, at fixed n the EMP damping can be used for determining temperature and magnetic field dependences of the SE magnetoconductivity. The edge phenomena for SE are smoothed over large distances, which assures that the data correspond to the real SE conductivity.

To study EMP damping we will use the conventional experimental technique which is similar to the one described in Ref. 25. The electron sheet employed in the present work has a circular geometry with a diameter of 30 mm, which is shaped by an electrode assembly. The electron assembly consists of a circular disk of 10 mm in diameter and four surrounding arc-shaped outer electrodes. The total diameter of the assembly is 30 mm. The electrodes were immersed in liquid helium, 1.0 mm under the surface. The width of the edge of the electron disk was estimated to be 0.3 mm. The resonance curve was obtained by sweeping the frequency of an ac excitation voltage, which was applied to one of the four surrounding electrodes. The output signal from the opposite electrode was analyzed by a two-phase lock-in. The magnetic field and temperature were held constant during the measurement of each resonance curve. The electron density was fixed at $n=3.5\cdot 10^7$ cm^{-2}.

Since the first mode was contaminated with a low-frequency tail and unfavorable noise, the second mode with a higher wave number was used to obtain the damping coefficient by fitting to the Lorentzian. Above 1 K the magnetic field dependence of the damping coefficient was found to be the same as the B-dependence of the previously studied longitudinal conductivity of SE. Therefore, we have determined the geometrical factor which gives the relationship between the damping coefficient and σ_{xx} at $T=1.1$ K, where the magnetoconductivity is well understood, both theoretically and experimentally, while the ripplon contribution and inelastic effect (according to Fig. 4) can be disregarded. This factor was then used in the ripplon scattering regime.

It should be noted that the driving amplitude had to be kept low in order to avoid the nonlinear distortion of the EMP line shape.

RESULTS AND DISCUSSION

To check that the many-electron effect is taken into account correctly in the theory presented above, we must first apply the theory to the high-temperature regime, $T=1.2$ K. The many-electron theory (solid curve) and the single-electron theory (dashed curve) results are shown in Fig. 5 for two electron densities. It can be seen that the many-electron effect can be ignored at low densities ($n<0.5\cdot 10^8$ cm^{-2}). At substantially higher density $n=3.2\cdot 10^8$ cm^{-2} and $B\leqslant 5$ T, the Coulomb correction to the Landau level broadening affects the field dependence of σ_{xx}. The experimental

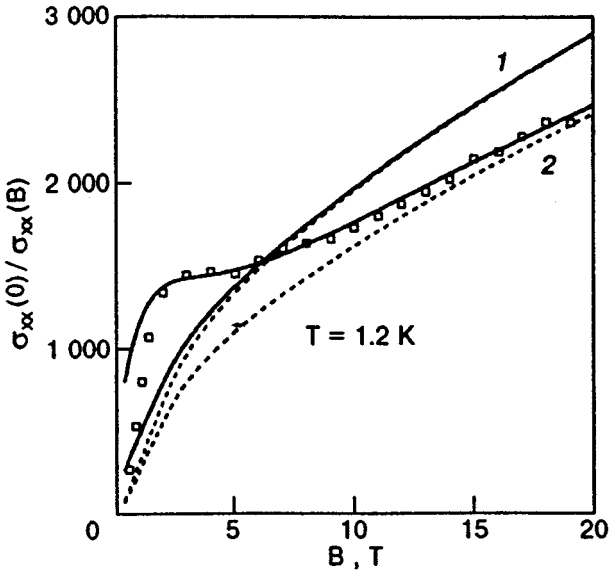

FIG. 5. $\sigma_{xx}(0)/\sigma_{xx}(B)$ vs. B for $n=0.5\cdot 10^8$ cm^{-2} (*1*) and $n=3.2\times 10^8$ cm^{-2} (*2*) at $T=1.2$ K. The lines show the many-electron theory (solid) and single-electron theory (dashed). Data (open squares) are taken from Ref. 26.

data of Ref. 26 for the SE conductance measured for $n=3.2\cdot 10^8$ cm^{-2} at $T=1.2$ K are plotted in Fig. 5. The conductance is proportional to σ_{xx} with the numerical factor of the order of unity unknown for the experiment. We have chosen the proportionality constant to fit the experimental data at extremely high magnetic fields ($B=20$ T), where the many-electron effect can be neglected. The data and the theory will then still in good agreement in the magnetic field range where the many-electron effect validity of the approximation made for the dynamic structure factor $S_0(q,\omega)$ of a highly correlated $2D$ electron liquid. It is instructive to note that in the high temperature range and $B\geqslant 1$ T, the quantum magnetotransport of SE can be described by using the simple many-electron correction to the level broadening $\Gamma=(\Gamma_{a,0}^2+\Gamma_C^2)^{1/2}$ in a single-electron expression for $\nu(B)$ presented in the form of Eq. (8).

In the ripplon scattering regime, the magnetic field dependence of σ_{xx} is shown in Fig. 6 for different approaches. It follows that the single-electron approximation ($\Gamma_C=0$) fails to describe the field dependence of σ_{xx} obtained from the damping coefficient of EMP (solid squares). At the same time, the many-electron DK theory results (curve *3*) cannot be fitted to the data. The theory presented here reproduces the B-dependence of the DK theory, if the ripplon contribution to the level broadening and inelastic effect are ignored: $\Gamma\to\Gamma_C$, $\delta_r\to 0$. Still, in this case, our theory gives σ_{xx} values which are approximately 2.6 times higher than the result of the DK theory. This is attributable to another way of treatment of the magnetoconductivity of the highly correlated electron liquid used here. It should be pointed out that the factor 2.6 is very important for describing the experimental data. Indeed, it is impossible to fit the data and the DK theory by just replacing $\Gamma_C\equiv\hbar/\tau_e$ by $\Gamma=(\Gamma_{r,0}^2+\Gamma_C^2)^{1/2}$ in the final conductivity equation, since it would reduce $\sigma_{xx}\propto 1/\Gamma_C$ from the data. Therefore, we conclude that the

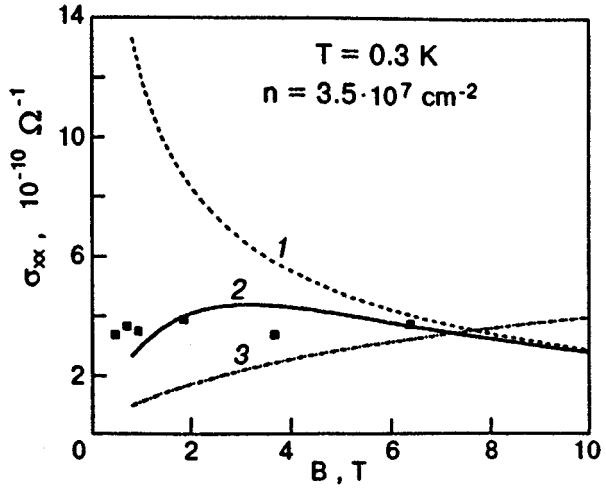

FIG. 6. The magnetoconductivity of SE vs. B at $T=0.3$ K: the single-electron approximation (*1*); the many-electron theory reported (*2*); the DK many-electron theory (*3*). Solid squares are the experimental data found from the EMP damping.

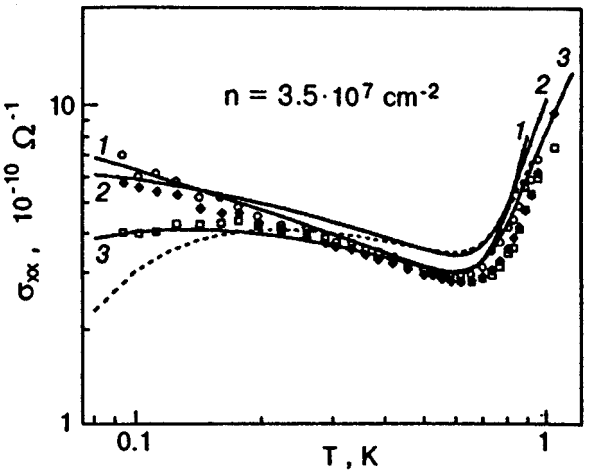

FIG. 7. σ_{xx} vs. T for three values of the magnetic field: $B=1.84$ T [curve *1*, ○]; $B=3.67$ T [curve *2*, ◆]; $B=6.4$ T [curve *3*, □]. The many-electron theory (solid) and the single electron theory (dashed; $B=6.4$ T) have no fitting parameters.

method proposed by us is a more adequate way of treating the conductivity of highly correlated $2D$ electron liquid.

The solid curve in Fig. 6 calculated on the basis of theory of this paper without a fitting parameter is in good agreement with the new experimental data. In the wide range of magnetic fields σ_{xx} has a very weak B-dependence because of the interplay of the different contributions (Γ_C and $\Gamma_{r,0}$) to the level broadening. The deviation from the data seen at $B\leqslant 1$ T is beyond the validity of the approximations used by us (at such fields the mixing of the Landau levels becomes important). The curve approaches the single-electron curve (curve 1) in the limit of strong magnetic field, since $\Gamma_C \propto 1/\sqrt{B}\to 0$. This is reasonable despite the large value of the Coulomb coupling parameter $G\approx 60$, since the typical wave vectors in the dynamic structure factor $q\propto\sqrt{B}$ are much larger than $\sqrt{\pi n}$ [according to Ref. 27, in this limit $S_0(q,\omega)$ is nearly the same as that of an ideal electron gas].

The agreement between the theory and the σ_{xx} data looks even more convincing in Fig. 7, where the results are plotted as a function of temperature for three different values of the magnetic field used in the experiment. The increase of σ_{xx} with decreasing temperature to 0.2 K is consistent with the prediction of the quassielastic theory (Saitoh[18]): $\sigma_{xx}\propto 1/\sqrt{T}$. At lower temperatures $T\leqslant 0.2$ K, the many-electron theory curves (solid) and the data deviate from the result of the quasielastic approximation—the stronger the magnetic field, the more SE magnetoconductivity deviates due to the inelastic effect. With the increase of the magnetic field, the curves and the data gradually approach the single-electron curve (dashed) plotted for the strongest magnetic field used in the experiment. The high-temperature deviation of the weak-field curves from the data might be caused by the increase of the population of higher Landau levels, which was disregarded in the electron-ripplon scattering.

The temperature dependence of σ_{xx} is the most decisive factor for the electron-ripplon scattering regime. Therefore, it is important to compare the previously measured $\sigma_{xx}(T)$ data with the data reported here. It should be noted that the temperature dependence observed in Ref. 12 at $T>0.5$ K is similar to the one shown in Fig. 7. Still, the minimum of σ_{xx} was situated at higher $T\approx 1$ K, and it was necessary to substantially reduce the level broadening $\Gamma\to\Gamma_{a,0}$ to fit the data. Regarding the $\rho_{xx}(T)$ data reported in Ref. 13 (ρ_{xx} and consequently σ_{xx} decrease with decreasing T), they are in contradiction with available theories of ripplon-induced magnetoconductivity including the DK theory.

CONCLUSIONS

We have investigated the inelastic quantum magnetotransport in a highly correlated $2D$ electron liquid of SE on superfluid helium. The theoretical concept presented and the magnetoconductivity data obtained from the damping of the EMP show that the usually used quasielastic approximation is valid only in a limited temperature range which narrows with increasing magnetic field. The inelastic effect which is important at LT drastically reduces the Landau level broadening and magneto-conductivity. The many-electron theory reported here reproduces the results of previous quasielastic theories[18,19] as the opposite limiting cases which cannot be separately applied to the real experimental situation.

We have shown that the EMP damping method of measuring the SE magnetoconductivity at LT can be an alternative to the conventional methods based on measuring the electron response to the ac voltage by means of the capacitive coupling techniques.

The perfect agreement achieved between the theory and experiment in the wide range of temperatures (including the vapor atom scattering regime) and magnetic fields supports the idea of the Coulomb correction to the broadening of the single-electron density of states and provides important clues about the behavior of highly correlated ($G\sim 100$) $2D$ electron liquids in quantizing magnetic fields.

ACKNOWLEDGMENTS

This work was partly supported by Grant in Aid for Scientific Research from the Japan Ministry of Education, Science, Sports and Culture, and Toray Science Foundation.

*E-mail: monarkha@lt.issp.u-tokyo.ac.jp

[1] T. Ando and Y. Uemura, J. Phys. Soc. Jpn. **36**, 959 (1974).
[2] Yu. P. Monarkha and F. M. Peeters, Europhys. Lett. **34**, 611 (1996).
[3] A. S. Rybalko, Yu. Z. Kovdrya, and B. N. Esel'son, JETP Lett. **22**, 280 (1976).
[4] C. C. Grimes and G. Adams, Phys. Rev. Lett. **36**, 145 (1976).
[5] R. Mehrotra, C. J. Guo, Y. Z. Ruan, D. B. Mast, and A. J. Dahm, Phys. Rev. **B29**, 5239 (1984).
[6] Yu. M. Vil'k and Yu. P. Monarkha, Sov. J. Low Temp. Phys. **15**, 131 (1989).
[7] Yu. P. Monarkha, Low Temp. Phys. **19**, 530 (1993).
[8] P. J. M. Peters, P. Scheuzger, M. J. Lea, Yu. P. Monarkha, P. K. H. Sommerfeld, and R. W. van der Heijden, Phys. Rev. **B50**, 11570 (1994).
[9] M. I. Dykman, M. J. Lea, P. Fozooni, and J. Frost, Phys. Rev. Lett. **70**, 3975 (1993).
[10] M. J. Lea, P. Fozooni, P. J. Richardson, and A. Blackburn, Phys. Rev. Lett. **73**, 1142 (1994).
[11] V. N. Grigor'ev, O. I. Kirichek, Yu. Z. Kovdrya, and Yu. P. Monarkha, Sov. J. Low Temp. Phys. **46**, 219 (1990).
[12] Yu. Z. Kovdrya, V. A. Nikolayenko, O. I. Kirichek, S. S. Sokolov, and V. N. Grigor'ev, J. Low Temp. Phys. **91**, 371 (1993).
[13] J. Frost, P. Fozooni, M. J. Lea, and M. I. Dykman, Europhys. Lett. **16**, 575 (1991).
[14] Yu. P. Monarkha, S-I. Ito, K. Shirahama, and K. Kono, Phys. Rev. Lett. **78**, 2445 (1997); S-I. Ito, K. Shirahama, and K. Kono, J. Phys. Soc. Jpn. **66**, (1997) (to by published).
[15] V. A. Volkov and S. A. Mikhailov, in *Modern Problems in Condensed Matter Sciences*, V. M. Agranovich and A. A. Maradudin (eds.) North-Holland, Amsterdam (1991), Vol. 27.2, Ch. 15, p. 855.
[16] I. L. Aleiner and L. I. Glasman, Phys. Rev. Lett. **72**, 2935 (1994).
[17] D. R. Leadley, R. J. Nicholas, W. Xu, F. M. Peeters, J. T. Devreese, J. Singleton, J. A. A. J. Perenboom, L. van Bockstal, F. Herlach, C. T. Foxon, and J. J. Harris, Phys. Rev. **B48**, 5457 (1993).
[18] M. Saltoh, Solid State Commun. **52**, 63 (1984).
[19] M. I. Dykman and L. S. Khazan, Sov. Phys. JETP **50**, 747 (1979).
[20] Yu. P. Monarkha and V. B. Shikin, Sov. J. Low Temp. Phys. **8**, 279 (1982).
[21] V. A. Buntar, Yu. Z. Kovdrya, V. N. Grigor'ev, Yu. P, Monarkha, and S. S. Sokolov, Sov. J. Low Temp. Phys. **13**, 451 (1987).
[22] H. Fukuyama, Y. Kuramoto, and P. M. Platzman, Phys. Rev. **B19**, 4980 (1979).
[23] G. D. Mahan, *Many-Particle Physics*, Plenum, New York (1981), p. 166.
[24] Yu. P. Monarkha, Sov. J. Low Temp. Phys. **17**, 76 (1991).
[25] P. J. M. Peters, M. J. Lea, A. M. L. Janssen, A. O. Stone, W. P. N. M. Jacobs, P. Fozooni, and R. W. van der Heijden, Phys. Rev. Lett. **67**, 2199 (1991).
[26] P. Scheuzger, J. Neuenschwander, W. Joss, and P. Wyder, Physica **B194–196**, 1231 (1994).
[27] H. Totsuji, Phys. Rev. **B22**, 187 (1980).

This article was published in English in the original Russian journal. It was edited by S. J. Amoretty.

Possibility of ripplon-induced weak localization

A. J. Dahm

Department of Physics, Case Western Reserve University, Cleveland, OH 44108
(Submitted December 24, 1996)
Fiz. Nizk. Temp. **23**, 639–641 (May–June 1997)

Ripplon-induced weak localization is proposed for electrons on a liquid-helium surface. Ripplon scattering is quasi-elastic, the ripplons are quasi-static relative to the electron velocity, and the relative change in occupation number of the ripplon state in a scattering event is small. Conditions for the observation of ripplon-induced weak localization are calculated.
 [S1063-777X(97)01805-7]

Electrons bound to a liquid-helium surface form an ideal two-dimensional system. Electron motion along the surface in a weak perpendicular field, $E_\perp$, is metallic with scattering occurring only from ripplons at temperatures below 0.5 K. The formation of a ripplonic polaron, consisting of an electron self-trapped in a dimple in the helium surface, is predicted[1] to occur in the presence of a sufficiently strong perpendicular field. A recent claim has been made for the observation of this state.[2]

Localization effects for electrons on helium films have been discussed only in terms of this ripplonic polaron. We present an alternate route to localization of electrons on helium films. Our suggestion is that electrons are weakly localized, and possibly strongly localized on a short time scale, by quasi-elastic ripplon scattering. When temporal strong localization occurs, a dimple or a precursor will form beneath the electron even if the polaronic state is not bound. We propose that as the holding field is increased to enhance electron-ripplon scattering, the system will traverse the regimes, weak localization to strong localization to the bound polaron state.

WEAK LOCALIZATION

Weak localization is the term applied to the coherent backscattering of electrons by elastic scattering from a random set of potentials. It is a precursor to strong localization. Excellent reviews on this topic exist.[3–5] Let us consider a set of fixed random potentials. Electrons can backscatter by traversing a circuit of scatters in clockwise (forward) or counterclockwise (time reversed) directions. A diagram is shown in Fig. 1a. In zero magnetic field with only elastic scattering the difference in phase shift along the two paths, $\Delta\varphi$, vanishes. The amplitudes for forward, A_f, and time-reversed, A_r, paths are additive. The probability of returning to the origin is

$$P=|A_f+A_r|^2=|A[1+\cos(\Delta\varphi)]|^2=4|A|^2 \qquad (1)$$

compared to $2|A|^2$ for scattering in other directions. This enhancement of back scattering leads to an increase in resistivity. In a magnetic field the additional phase shift $[(e/\hbar)\int A d\mathbf{l}]$ differs for the two paths and coherence is destroyed at fields $\sim\Phi_0/l^2$. Here Φ_0 is a flux quantum and l is the elastic mean free path. This leads to a negative magnetoresistance at low fields.

WEAK LOCALIZATION BY RIPPLONS

We argue that weak localization should occur from ripplon scattering. Ripplon scattering differs from scattering from fixed random potentials in the following ways.

1) Scattering is quasi-elastic. The dominant electron-ripplon scattering events involve the absorption or emission of ripplons with wave vectors, q, $\sim$the thermal wave vector of the electron, k_T. For 1-K electrons the energy of ripplons which dominate the scattering is $\hbar\omega_q\sim 10^{-2}$ K. Thus, the change in the electron wave vector, k, in a single scattering event is $<1\%$. The total phase change $\sim 5kl$ for $l\sim 100$ nm is ~ 20 radians, and $\Delta\varphi$ is ~ 0.2 radians.

2) Ripplons are quasi-static in the reference frame of the electrons. The velocity of ripplons with $q=k_T$ is $\sim 3\times 10^{-3}$ of the electron velocity. The positions at which scattering occurs on the two paths are nearly the same. This is illustrated in Fig. 1b. The total change in phase is nearly unaffected by the motion of slow ripplons.

3) The percentage change in the occupation number of ripplons in a scattering event involving the absorption or emission of a ripplon of one quantum is small. The occupation number is $\sim T/\hbar\omega_q\sim 100$ at 1 K. Electrons on the forward and time-reversed paths scatter from ripplons of the same amplitude to within 1%.

We conclude that the total phase change for electrons which traverse the two paths is nearly the same, and the loss in coherence for back scattering is very small. The reader may be inclined to make an analogy with phonon scattering which dephases the electrons in other two-dimensional systems. This analogy is incorrect. Phonon scattering occurs at energies $\hbar\omega\sim\hbar s k_F\sim 1$ K, where s is the sound velocity and k_F is $\sim 10^8$ m^{-1}. Electron-phonon scattering is not quasi-elastic, and the occupation number is approximately unity. Thus, a phonon of one quantum absorbed on one path will not exist for the time-reversed path. A good analogy of ripplon-induced weak localization is weak localization by quasi-elastic scattering from helium atoms which has been observed.[6,7]

STRONG LOCALIZATION BY RIPPLONS

Electron localization by ripplons or substrate scattering is complicated by the formation of a dimple under the electron. This dimple forms if an electron is temporarily localized even though no bound polaron state exists. The dimple

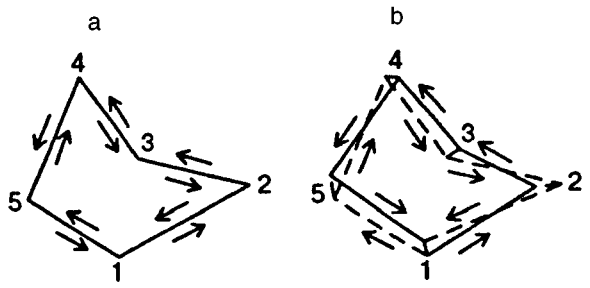

FIG. 1. Diagram illustrating forward and reversed paths. (a) fixed scatterers; (b) quasistatic scatterers.

impedes the motion of the electron. Nevertheless, we examine the possibility of strong localization by ripplons.

Strong localization occurs for short elastic mean free paths. The amplitude of the electronic wave function from successive scatterings will add constructively in some region of space where the electron becomes localized, and destructive interference will occur in other regions of space. The wave function decays as $\exp(-r/\xi)$, where $\xi > l$ is the localization length. In fixed random potentials, conduction occurs via variable-range tunneling from one localized state to another with the absorption or emission of a thermal excitation.[8] There is interference between different tunneling paths. A magnetic field suppresses destructive interference along critical links in the hopping network. This results in a giant negative magnetoresistance.[9]

The situation is much more complicated for the case of electrons on helium. Consider a mean free path of 50 nm. The change in k for each scattering is $\sim \pm 1\%$. The change in φ is ~ 1 radian after ~ 100 scattering events which occurs in about 1 nsec. Also, ripplons move a distance $\sim l/10$ in ~ 1 nsec. Thus, a localized state can survive for at most 1 nsec. This is also the time for a dimple of size $\sim l$ to form under the electron. We propose that in the absence of bound polarons, electrons will be relocalized at another site in a time ~ 1 nsec or will tunnel to another site in a shorter time. The mobility, given by the Einstein relation and a diffusion constant $D \sim l^2/\tau (\tau \sim 1 \text{ nsec})$, is $\sim 10^{-1}$ m^2/V.s.

POSSIBILITY OF EXPERIMENTAL REALIZATION

We estimate the mean free path required to insure $\cos(\Delta\varphi) > 0.7$ is $l < 400$ nm. This requires $E_\perp \sim 250$ kV/m, although a small negative magnetoresistance may be observed at lower fields. All other sources of scattering are absent on a bulk surface, and weak localization effects can be attributed to ripplons. However, the charged bulk surface is unstable at this value of field, and weak localization may best be observed on helium films. In this case scattering from substrate roughness may interfere. A low density of electrons is required to insure that localization is not a result of electron-electron interactions. The advantage of using electrons on a helium surface to study the transition from weak to strong localization is that the electron mean free path can be varied, in situ, by changing the holding field. Further, the electron-electron interaction can be altered by changing the density.

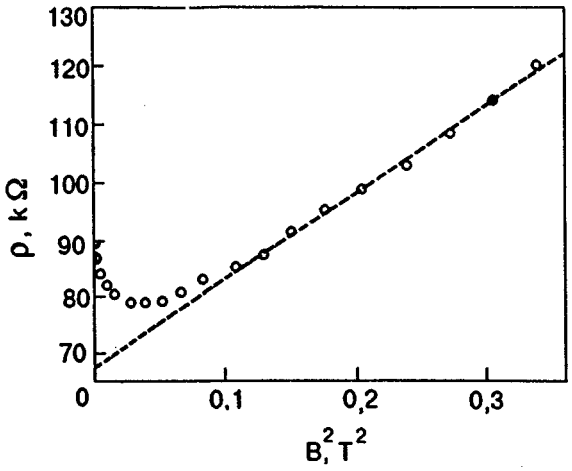

FIG. 2. Resistivity vs B^2; $n = 6 \times 10^{13}$ m^{-2}, $T = 1.3$ K.

We have some data that support our suggestion. In Fig. 2 we show the resistivity versus B^2 for electrons on a $a \sim 30$-nm-thick helium film. At low fields there is a large negative magnetoresistance, more characteristic of strong localization. At higher fields the resistivity fits the Drude formula, $\rho \sim [1 + (\mu B)^2]$. The mobility, μ, is 1.5 m^2/V.s, $l \sim 50$ nm, and $E_\perp \sim 600$ kV/m. The field at which the minimum occurs is consistent with this value of l. Scattering from substrate imperfections may occur here, but the theoretical ripplon scattering rate accounts for $\sim 40\%$ of the total scattering. We argue that since every other scattering event involves ripplons, localization effects could not be observed if ripplon scattering dephased the electronic wave function.

Localization of electrons on a helium surface is an example of classical weak localization. This has been studied both theoretically[10,11] and experimentally[6,7,12] in other systems. A search for ripplon-induced localization is underway.

The author wishes to thank H. W. Jiang for taking the data shown in Fig. 2. This work was supported, in part, by NSF grant #DMR 94-02647.

[1] V. B. Shikin, Sov. Phys. JETP **33**, 387 (1971). See also references in F. M. Peeters, *Physics of the Two-Dimensional Electron Gas*, (Eds. J. T. Devreese and F. M. Peeters, Plenum Press, N.Y.) and G. E. Marques and N. Studart, Phys. Rev. B **39**, 4133 (1989).
[2] O. Tress, Yu. P. Monarkha, F. C. Penning, H. Bluyssen, and P. Wyder, Phys. Rev. Lett. **77**, 2511 (1996).
[3] G. Bergmann, Phys. Rep. **107**, 1 (1984).
[4] P. A. Lee and T. V. Ramakrishnan, Rev. Mod. Phys. **57**, 287 (1985).
[5] S. Chakravarty and A. Schnid, Phys. Rep. **140**, 193 (1986).
[6] P. W. Adams and M. A. Paalanen, Phys. Rev. B **39**, 4733 (1989).
[7] A. M. L. Hanssen, R. W. van der Heijden, A. T. A. M. de Waele, and H. M. Gijsman, Surf. Sci. **229**, 365 (1990).
[8] A. L. Efros and B. I. Shklovskii, *Electronic Properties of Doped Semiconductors*, Springer-Verlag, New York, 1984.
[9] V. I. Nguyen, B. Z. Spivak, and B. I. Shklovskii, Sov. Phys. JETP **62**, 1021 (1985).
[10] V. V. Afonin, Yu. M. Galperin, and V. L. Gurevich, Sov. Phys. JETP **61**, 1130 (1985); V. V. Afonin, Yu. M. Galperin, V. L. Gurevich, and A. Schmid, Phys. Rev. A **36**, 5729 (1987).
[11] M. J. Stephen, Phys. Rev. B **36**, 5663 (1987).
[12] P. W. Adams and M. A. Paalanen, Phys. Rev. Lett. **58**, 2106 (1987).

This article was published in English in the original Russian journal. It was edited by S. J. Amoretty.

Mobility and localization of charge carriers in a quasi-one-dimensional electron system over liquid helium

V. A. Nikolaenko and Yu. Z. Kovdrya

B. Verkin Institute for Low Temperature Physics and Engineering, National Academy of Sciences of the Ukraine, 310164 Kharkov, Ukraine[1)]

H. Yayama and A. Tomokiyo

Department of Physics, Faculty of Science, Kyushu University, Fukuoka 810, Japan[2)]

(Submitted October 25, 1996; revised December 5, 1996)
Fiz. Nizk. Temp. **23**, 642–648 (May–June 1997)

The conductivity and mobility of charge carriers in a quasi-one-dimensional electron system over liquid helium is measured in the temperature range 0.5–1.8 K in confining electric fields up to 2.5 kV/cm. The system of quasi-one-dimensional channels is constructed by using high-quality optical diffraction gratings arranged at a certain height h over liquid helium which fill the grooves of the gratings, thus creating one-dimensional liquid channels. It is shown that the electron mobility decreases with increasing h, the value of the mobility being smaller than the corresponding value for bulk helium. As the temperature decreases, the mobility increases, passes through a peak, and then decreases. The observed effects can be explained by localization of charge carriers in quasi-one-dimensional electron systems. [S1063-777X(97)01905-1]

INTRODUCTION

The study of one-dimensional and quasi-one-dimensional electron systems is one of the most interesting problems in the physics of low-dimensional structures. Such systems are usually formed in thin metal wires and semiconducting structures. It should be interesting to obtain a one-dimensional electron system of surface electrons (SE) over liquid helium in view of the fact that the SE layer over liquid helium is characterized by extremely high purity and homogeneity. A method proposed in Ref. 1 for obtaining such a system employs the surface curvature of the liquid filling the parallel grooves of an insulating substrate mounted at a certain height h over the liquid helium surface under the action of capillary forces. The confining electric field $E_\perp$ displaces electrons to the bottom of a liquid channel, their motion across the channel being quantized, while the motion along the channel is quasi-free. It was proved that the energy corresponding to the motion of particles across the channel is defined as

$$\varepsilon_n = n\hbar\omega_0, \quad \omega_0 = \left(\frac{eE_\perp}{mr}\right)^{1/2}, \tag{1}$$

where $n = 1,2,3,\ldots;\hbar$ is Planck's constant, e and m are the electron charge and mass, and r is the radius of curvature of the liquid helium surface in the channel, which is determined by the height h.

Such a structure was created recently in experiments.[2–4] It was shown that the electron conductivity in this system is strongly anisotropic, its value being a complex nonmonotonic function of the number density of charge carriers and the confining electric field. According to estimates,[2–4] the mobility of electrons moving along the channels for small h is close to (but smaller than) the electron mobility over bulk helium.

In this research, we investigated the electron mobility in a quasi-one-dimensional electron system over liquid helium in the temperature range 0.5–1.8 K at frequencies 100 kHz and 1.1 MHz in confining electric fields up to 2.5 kV/cm. Two types of optical diffraction gratings with different separations between the grooves were used. First results on the measurements of electrical conductivity and mobility of electrons in such systems were reported earlier.[5,6] This paper contains more complete data and a detailed analysis of the obtained results.

EXPERIMENT

A quasi-one-dimensional electron system was created by using high-quality optical glass gratings without metal coating. The profile, the arrangement of gratings near the liquid helium surface, and the shape of electrodes are shown in Figs. 1a and 1b. The separation between the grooves was 5 μm in grating 1, 1.25 μ in grating 2, the depth of the grooves in both gratings being 0.2–0.3 μm. The profile of grating 1 was measured by an electron microscope. It had the shape shown in Fig. 1a, and its thickness was 0.8 mm, while grating 2 was in the form of a glass disk of diameter 30 mm and had a thickness 3 mm (Fig. 1b). Grating 1 was made of glass alone, while the surface of grating 2 was coated with a naphthagen film on which grooves were engraved. The naphthagen film with grooves had the shape of a disk of diameter 20 mm.

Experimental cells I and II in which gratings 1 and 2 were contained are shown in Figs. 1c and 1d. Liquid helium was at a distance h from the upper plane of the gratings. Electrodes A, B, and C of grating 1 were kept at zero potential, while a negative potential creating the electric field confining electrons at the surface of helium film wetting the grating was applied to the upper electrode D (Fig. 1c). Elec-

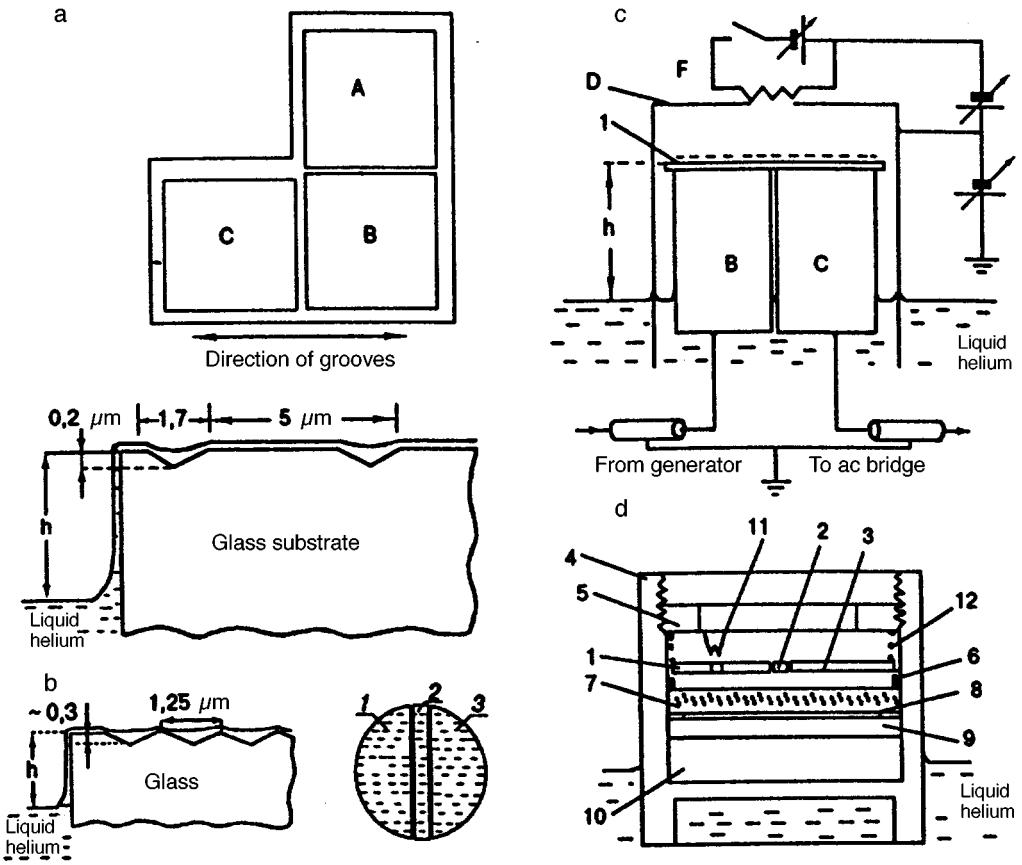

FIG. 1. Grating 1, its profile and arrangement relative to helium; the direction of grooves is indicated by arrows (a). Grating 2, the directions of grooves is indicated by dashed lines (b). Experimental cell I: optical grating (*1*), exciting and receiving electrodes (B and C), confining electrode (D), filament (F) (c). Experimental cell II: exciting, separating, and receiving electrodes (*1,2,3*), copper holder (*4*), nut (*5*), guarding ring (*6*), optical grating (*7*), electrode (*8*), insulating gasket (*9*), copper insert (*10*), filament (*11*), and spring (*12*). (d).

trode A was used for measuring anisotropy of the electron conductivity along the grooves and at right angles to them[6] and was not employed by us in this work. In the experimental cell containing grating 2, the upper measuring electrodes *1, 2, 3* were at zero potential, while a positive potential required for confining the electron charge was applied to the lower electrode δ which had the shape of a disk of diameter 25 mm. Electrodes *1, 2, 3* of grating 1 were 2 mm above the substrate surface. The voltage from the generator was applied to electrodes *B* and *1*, while the signal passing through the experimental cells was registered from electrodes C and *3*. With such a method of supplying voltage, the electric field was directed along the grooves of the substrate. Electrode *2* was earthed relative to ac voltage.

DISCUSSION OF RESULTS

We measured in experiments the variations ΔU and $\Delta\varphi$ of the amplitude and phase of the signal passing through the experimental cells during their charging with electrons. In measurements at frequency 100 kHz, an ac bridge with the output leads connected to an amplifier was used. Measurements at frequency 1.1 MHz were made by using the high-frequency phasemeter *FK*2-12. The data on the values of ΔU and $\Delta\varphi$ made it possible to determine the real (G_r) and imaginary (G_i) components of the conductance of the cell and to find the real (ρ_r) and imaginary (ρ_i) components of the resistance of the electron layer.

The quantities G_r and G_i are connected with the real ρ_r and imaginary ρ_i components of the resistance of the electron layer through the following relations:[7]

$$g_r = -n_s e^2 \sum_{q_x} \lambda_q \frac{n_s e^2 \omega^2 \rho_r}{(m\tilde{\omega}_p^2 - n_s e^2 \omega \rho_i)^2 + (n_s e^2 \omega \rho_r)^2}, \tag{2}$$

$$G_i = -n_s e^2 \sum_{q_x} \Lambda_q \frac{\omega(m\tilde{\omega}_p^2 - n_s e^2 \omega \rho_i)}{(m\tilde{\omega}_p^2 - n_s e^2 \omega \rho_i)^2 + (n_s e^2 \omega \rho_r)^2} + g_0. \tag{3}$$

Here n_s is the average electron number density in the surface layer, ω the cyclic frequency, $\tilde{\omega}_p$ the plasma frequency, and g_0 the conductance of the cell in the absence of electrons. In the case of a quasi-one-dimensional system, plasma waves cannot propagate across the electron spot, and the summation in formulas is carried out over the values of the wave vector determined by the length L_x of the electron spot:

$$L_x : q_x = \pi n_x / L_x,$$

where $n_x = 1, 2, 3, \ldots$. In our calculations we usually took three terms, which was sufficient for obtaining results with an error not exceeding 10%. The coefficient Λ_q depends on

the cell geometry; in the case when the rectangular geometry is used for a quasi-one-dimensional system in which charge carriers can move only in one direction, this coefficient can be written in the form

$$\Lambda_q = \frac{2L_y}{L_x} \frac{\sinh^2 q_x(h_0 - d)}{\sinh^2 q_x h_0} \cos q_x L_x \sin^2 q_x A_x . \qquad (4)$$

Here L_y is the width of the electron spot, A_x is the length of the exciting and receiving electrodes, h_0 the separation between the upper and lower electrodes, and d the distance from the electron layer to the receiving and transmitting electrodes.

While processing experimental results, we assumed that the plasma frequency for the system of conducting channels of the gratings is close to the plasma frequency for a two-dimensional electron layer of the corresponding concentration. For grating 2, this assumption was observed with a large margin since the separation between the grooves was $\sim 10^{-4}$ cm, which is approximately equal to the average separation between electrons. However, the situation with grating 1 is more complicated. Nevertheless, we can assume that the plasma frequencies are quite large in both cases. Under these conditions, we can omit in formulas (2) and (3) the terms containing the imaginary component of the resistance of the electron layer. Using the simplified form of expressions (2) and (3), we can determine the values of ρ_r and $\tilde{\omega}_p$ as fitting parameters from the measured values of G_r and G_i. In the case of grating 2, the electrodes having the shape of semicircles (see Fig. 1b) were replaced by rectangular electrodes of the same area. Such a substitution apparently could not lead to a considerable error since the magnitude of the signal is mainly determined by the area of the receiving and transmitting electrodes.

In order to find the electron mobility in a quasi-one-dimensional electron system, we must know the number of mobile electrons over the bulk liquid in the channels. For this purpose, we calculated the electron density distribution over the optical gratings. The calculations were based on the condition that the potential at the charged surface of the liquid wetting the gratings is constant. It turned out that, as a result of the action of image forces, the electron density over the thin helium film formed on the plane surface or above the protrusions of the gratings was higher than the value above the bulk liquid. For example, for $h = 1$ cm, the ratio of the electron density over the plane surface or the protrusions of the grating to the electron density over the bulk liquid was ~ 3.

It is well known that electrons over a thin helium film are localized and have a low mobility.[8,9] The magnitude of the mobility is determined by frequency and amounts to $\sim 10^{-4}$ m^2/V·s at a frequency of 20 kHz.[9] For frequencies used by us in this research, no data on the SE mobility in the film are available. However, it was shown in check experiments carried out by us that no signal from SE electrons was observed in smooth insulating substrates for the values of h used in a wide range of electron concentration. It follows hence that the conductivity of the system is determined only by electrons in the grooves.

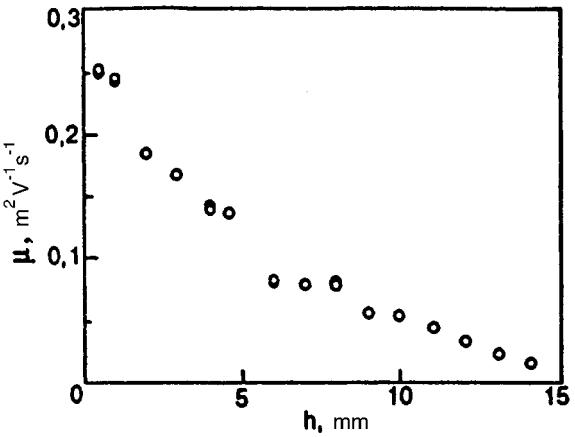

FIG. 2. Dependence of electron mobility in quasi-one-dimensional channels on height h for grating 1, $T = 1.7$ K, $f = 100$ kHz.

Andrei[9] proved that the low-frequency mobility of electrons increases sharply for liquid layers of thickness $\gtrsim 700$ Å. This allowed us to determine the number of mobile electrons for both gratings and to calculate the average electron density in the grating grooves proceeding from the total surface area of the bulk helium. It should be emphasized, however, that the condition of constant potential at the surface of a charged liquid is valid only for a high electron density. Unfortunately, such calculations are not quite accurate for the electron densities used. Nevertheless, we can apparently assume that they reflect the nature of the described phenomena.

Figure 2 presents the results obtained in experiments with grating 1. It shows the dependence of the electron mobility μ in conducting channels on h. The experiments were made at 1.7 K at a frequency of 100 kHz. It can be seen that the value of μ decreases approximately by an order of magnitude as the value of h increases from fractions of millimeter to 15 mm. Figure 3 shows typical temperature dependences of electron mobility obtained for grating 2 for different values of h. Curves *3* and *4* correspond to $h = 0.55$ and 5 mm, respectively. The figure also shows for comparison the temperature dependences of the mobility of surface electrons for bulk helium, corresponding to different electron densities and borrowed from Refs. 10–12 (curves *1* and *2*).

In order to compare the results obtained for the two gratings, we carried out check experiments for grating 2 at temperature 1.7 K. An analysis shows that the electron mobilities for gratings 1 and 2 corresponding to the same temperature and height h coincide approximately to within 30%. This means that the parameters of the quasi-one-dimensional system under investigation are virtually independent of the properties of the substrate. It should be noted that the measurements for the two gratings were made at different frequencies.

It follows from Figs. 2 and 3 that as the height h increases, the electron conductivity and mobility decrease significantly. According to the results of theoretical calculations, such a dependence should not be observed for a perfect liquid channel.

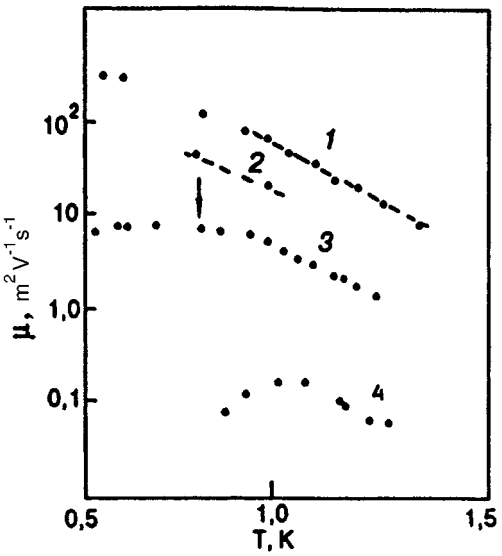

FIG. 3. Temperature dependence of electron mobility in quasi-one-dimensional channels for grating 2, $f=1.1$ MHz. Curves *1* and *2* correspond to bulk helium for electron number densities $5.5\cdot10^8$ and $13.8\cdot10^8$ cm^{-2} respectively,[10–12] curve *3* corresponds to $h=0.55$ mm, and curve *4* to $h=5$ mm, $n_s=13.8\cdot10^8$ cm^{-2}. The arrow indicates the temperature of transition to the crystalline state, corresponding to the average electron concentration in liquid channels.

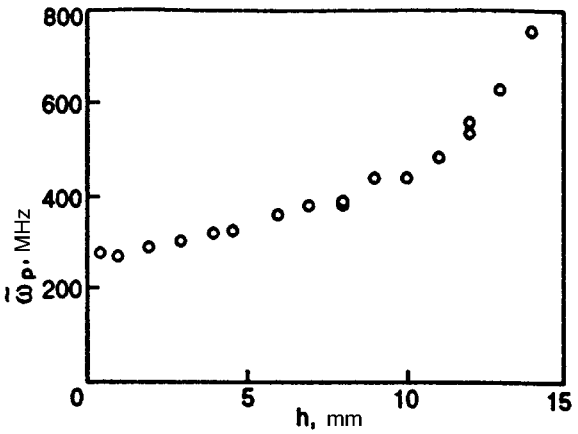

FIG. 4. Dependence of $\tilde{\omega}_p$ on height h for grating 1, $T=1.7$ K, $n_s=4.5\cdot10^8$ cm^{-2}.

Figure 3 shows that the value of μ increases with decreasing temperature T, attains a maximum, and then either decreases upon a further decrease in T (curve *4*), or becomes virtually independent of temperature (curve *3*). The arrow on curve *3* indicates the temperature T_m of transition to the crystalline state in the two-dimensional system, which corresponds to the average electron concentration in liquid grooves. Naturally the temperature of crystallization (if it takes place) in the quasi-one-dimensional case realized in our experiments can differ from the crystallization temperature for a two-dimensional layer. Nevertheless, it can be seen that curve *3* in Fig. 3 exhibits no singularities associated with possible ordering in the quasi-one- dimensional electron system over the entire temperature range under investigation.

Chaplik[13] predicted theoretically the possibility of ordering in a quasi-one-dimensional electron system, during which the electron chain aligned along the channels is rearranged into a zigzag structure. According to estimates based on the results obtained by Chaplik,[13] the ordering temperature must be ~1 K for a chain length ~1 cm (which corresponds to the average length of channels in the gratings used) and for an average distance between electrons $\sim3\cdot10^{-5}$ cm. Strictly speaking, however, this result is valid for a solitary channel. In our case, when the interaction between electrons in different channels is quite strong, it would be more correct to speak of Wigner crystallization of electrons in a system of parallel conducting strips separated by strips with localized electrons. Crystallization in such a system can be more complicated, and the crystallization temperature T_m should not necessarily coincide with the value of T_m for a two-dimensional electron layer with the same average number density. It was mentioned above that the temperature dependence of mobility does not exhibit any singularities that could be ascribed to possible ordering or crystallization of electrons. It should also be noted that the electron mobility in a quasi-one-dimensional electron system is lower than for bulk helium (see Fig. 3).

The behavior of the quantity $\tilde{\omega}_p$ defined as a fitting parameter in expressions (2) and (3) is quite interesting. Figure 4 shows the dependence of $\tilde{\omega}_p$ on height h for grating 1. It can be seen that the value of $\tilde{\omega}_p$ increases with h from the value ~300 MHz, which approximately corresponds to the plasma frequency of the electron layer of a given concentration for bulk helium, to the value ~800 MHz for $h=15$ mm. A similar dependence is also observed for grating 2. The fact that the frequency $\tilde{\omega}_p$ of plasma oscillations for $h\to0$ approximately coincides with the plasma frequency ω_p for bulk helium indicates a strong interaction between electrons in neighboring conducting channels. It should be noted, however, that this aspect is not quite clear and requires further investigation.

Analyzing the obtained results, we must bear in mind that the electron system in our experimental conditions was not strictly one-dimensional. For $h=5$ mm and the field $E_\perp=1.25$ kV/cm, the separation between energy levels for particles moving across the channels is $\Delta E=0.15$ K, while for $h=0.55$ mm we have $\Delta E=0.05$ K. In both cases, the value of ΔE is much smaller than the experimental temperature. In this case, electrons occupy not only the ground level, but also higher energy levels. If we take into account the fact that the experiments were made under the conditions of charge saturation, the pattern becomes even more complicated. Nevertheless, it should be noted that even in this case the electrons move within a narrow strip $\sim1-1.5$ μm of the bulk liquid filling the grooves, which is reflected, among other things, in a strong anisotropy of conductivity observed for various gratings.[2,4] It would be more appropriate to refer to such a system of electrons as quasi-one-dimensional.

According to Ref. 1, the electron mobility in a one- dimensional electron system can be written in the form

$$\mu=\frac{6\alpha\hbar}{meE_\perp^2}, \tag{5}$$

where α is the surface tension in liquid helium. For the confining electric field $E_\perp = 1.25$ kV/cm corresponding to the curves in Fig. 3, this expression leads to the mobility $\mu \approx 10^2$ m^2/V·s. The experimental value of mobility for this confining field amounts to ~ 10 m^2/V·s, which is an order of magnitude smaller than the theoretical value.

The electron mobility in quasi-one-dimensional electron systems was calculated by Sokolov *et al.*[14] taking into account electron scattering between sublevels both in the one-electron approximation and under the condition of complete control, when the interaction between electrons was taken into consideration. The value of mobility for $T = 0.75$ K and $E_\perp = 1.25$ kV/cm was ~ 90 m^2/V·s in the one-electron approximation and ~ 45 m^2/V·s under the condition of complete control. These values are slightly lower than the value obtained by using formula (5), but still higher than the experimental values of electron mobility in a quasi-one-dimensional system. It should be noted that the value of μ obtained in Ref. 14 at 0.5 K in the one-electron approximation is higher than the value of μ given by formula (5).

It was noted above that the electron mobility in quasi-one-dimensional conducting channels decreases significantly upon an increase in h. This fact cannot be explained in the theories describing the electron mobility in one-dimensional and quasi-one-dimensional electron systems over liquid helium. This effect is probably associated with electron localization in a quasi-one-dimensional electron system. The fact that the value of $\tilde{\omega}_p$ increases with h also speaks in favor of this assumption. In the absence of localization and in the case of free motion of charge carriers, the value of $\tilde{\omega}_p$ must coincide with the plasma frequency ω_p of the electron system, which corresponds to the stabilization of standing plasma waves in the experimental cell. In the case of electron localization, the plasma spectrum acquires a new term corresponding to the natural electron frequency ω_α in potential wells: $\tilde{\omega}_p^2 = \omega_\alpha^2 + \omega_p^2$. If the depth of potential wells in which electrons are localized is large, the value of ω_α can increase considerably. Thus, the experimentally observed increase in $\tilde{\omega}_p$ indicates the localization of charge carriers in the quasi-one-dimensional system.

Such a localization was also observed for electrons over a helium film,[8,9] but it took place for helium film thicknesses $\leqslant 700$ Å. In this case, the depth of the channels along which electrons move amounts to ~ 2500 Å, i.e., corresponds to the case of bulk helium.

The reason behind the localization of charge carriers over bulk helium in our case is probably associated with variations of potential in which charge carriers move in a quasi-one-dimensional electron system. The effect of localization is apparently connected with a peculiar charging of profiled substrates wetted with helium. Charging of such substrates begins at regions coated by a thin helium film. Electrons are localized in these regions and make no contribution to the conductivity of the system. During subsequent charging, electrons also appear above deep liquid channels in which they can move along the grooves. However, this motion occurs at a random potential associated with the presence of stationary localized electrons in the immediate vicinity of a liquid channel. According to estimates, localized electrons can cause variations of potential along a liquid channel with an amplitude of the order of several kelvins, and hence can lead to complete or partial localization of charge carriers. The decrease in the mobility of charge carriers with temperature at low temperatures is probably due to this effect. The decrease in the number of mobile electrons which can be observed upon a decrease in temperature due to a change in the relative population density of electrons in liquid channels or regions where the film is thin cannot be ruled out completely either. The effect of localization can also explain a decrease in the electron mobility with increasing height h. As the value of h increases, the radius of curvature of the surface of the liquid decreases, and the region of thin film in which electrons are localized comes closer to the center of the liquid channel. The variations of potential in which charge carriers are moving increases, while the mobility decreases. We also cannot rule out the influence of grating defects (such as inhomogeneity of grooves and various surface defects) on the emergence of potential variations.

Thus, the conductivity and mobility of charge carriers in a quasi-one- dimensional electron system over liquid helium have been measured for the first time. The obtained results show that the type of transport in such systems is determined by localization of charge carriers in liquid channels in a random potential, which is caused by the influence of stationary electrons charging the regions with a thin helium film on the substrate. The processes occurring in quasi-one-dimensional electron systems over liquid helium are obviously very complicated and require further investigations.

The authors are grateful to V. N. Grigor'ev for his interest in this research and for discussion of the results.

[1)]E-mail: kovdrya@ilt.kharkov.ua
[2)]E-mail: yayama@rc.kyushu-u.ac.jp

[1] Yu. Z. Kovdrya and Yu. P. Monarkha, Fiz. Nizk. Temp. **12**, 1011 (1986) [Sov. J. Low Temp. Phys. **12**, 571 (1986)].
[2] Yu. Z. Kovdrya and V. A. Nikolaenko, Fiz. Nizk. Temp. **18**, 1278 (1992) [Sov. J. Low Temp. Phys. **18**, 894 (1992)].
[3] O. I. Kirichek, Yu. P. Monarkha, Yu. Z. Kovdrya, and V. N. Grigor'ev, Fiz. Nizk. Temp. **19**, 458 (1993) [Low Temp. Phys. **19**, 323 (1993)].
[4] H. Yayama and A. Tomokiyo, private communication (1993).
[5] Yu. Z. Kovdrya, V. A. Nikolaenko, and P. K. H. Sommerfeld, in *Proc. 21 Int. Conf. Low Temp. Phys. LT-21*, Czech. J. Phys., **46-Suppl**, 347 (1996).
[6] H. Yayama and A. Tomokiyo, in *Proc. 21 Int. Conf. Low Temp. Phys. LT-21*, Czech. J. Phys., **46-Suppl**, 353 (1996).
[7] Yu. Z. Kovdrya, V. A. Nikolaenko, O. I. Kirichek *et al.*, J. Low Temp. Phys. **81**, 371 (1991).
[8] Yu. Z. Kovdrya, F. F. Mende, and V. A. Nikolaenko, Fiz. Nizk. Temp. **10**, 1129 (1984) [Sov. J. Low Temp. Phys. **10**, 589 (1984)].
[9] E. Y. Andrei, Phys. Rev. Lett. **52**, 1449 (1984).
[10] A. S. Rybalko, Yu. Z. Kovdrya, and B. N. Esel'son, Pis'ma Zh. Éksp. Teor. Fiz. **22**, 569 (1975) [JETP Lett. **22**, 280 (1975)].
[11] R. Mehrotra, C. J. Guo, Y. Z. Ruan *et al.*, Phys. Rev. **B29**, 5241 (1984).
[12] V. A. Buntar, V. N. Grigor'ev, O. I. Kirichek *et al.*, J. Low Temp. Phys. **79**, 323 (1990).
[13] A. V. Chaplik, Pis'ma Zh. Éksp. Teor. Fiz. **31**, 275 (1980) [JETP Lett. **31**, 252 (1980)].
[14] S. S. Sokolov, Guo-Giang Hai, and N. Studart, Phys. Rev. **B51**, 5977 (1995).

Translated by R. S. Wadhwa

Mobility of electrons in a quasi-one-dimensional conducting channel on the liquid helium surface in the presence of a magnetic field

S. S. Sokolov,[1,2] Guo-Qiang Hai,[1] and N. Studart[1]

[1]*Departamento de Física, Universidade Federal de São Carlos, 13565-905 São Carlos, São Paulo, Brazil**
[2]*B. I. Verkin Institute for Low Temperature Physics and Engineering, National Academy of Sciences of Ukraine, 310164 Kharkov, Ukraine*

(Submitted December 20, 1996)
Fiz. Nizk. Temp. **23**, 649–654 (May–June 1997)

The influence of the transverse magnetic field on the electron mobility in a quasi-one-dimensional channel along the liquid-helium surface is investigated. The mobility calculations are carried out by using the Boltzmann kinetic equation and the criteria for the validity of this approach, which are different from those for two-dimensional systems, are established. Two different limiting regimes corresponding to different roles of the electron-electron interaction in the quasi-one-dimensional electron system are considered. The mobility is shown to be a decreasing function of the magnetic field. It is shown that the temperature dependence of the mobility in the presence of the magnetic field, as in the case of zero field, is a nonmonotonic function. © *1997 American Institute of Physics.* [S1063-777X(97)02005-7]

In the last decades the investigation of low-density electron systems localized on the liquid-helium surface became one of the developing directions in the physics of systems with reduced dimensionality. In addition to the well-known features such as purity and homogeneity, these systems are very attractive because of their ability to vary their properties through external fields or constraints. The influence of a magnetic field is especially interesting because it drastically affects the energy spectrum of electrons and the character of their motion. In the case of a quasi-two-dimensional ($2D$) system of surface electrons (SE) over the flat surface of bulk helium, the energy spectrum in the presence of a magnetic field B along the z axis (electrons are located in the xy plane parallel to helium surface) is given by the Landau levels $(n + 1/2)\hbar\omega_c$, where $\omega_c = eB/mc$, in addition to the quantized energies Δ_l along the z direction.[1]

In the last years quasi-one-dimensional ($Q1D$) electron systems over the liquid helium surface were predicted theoretically and realized experimentally.[2] In such a $Q1D$ system formed due to the finiteness of the curvature radius R of liquid helium either along parallel channels on the surface of dielectric substrate with linear grooves or between two dielectric polymer sheets meeting at a sharp angle, electrons are confined across the channel near its bottom due to the holding electric field $E_\perp$ normal to the channel axis with a confinement frequency $\omega_0 = (eE_\perp/mR)^{1/2}$. In the presence of a transverse magnetic field (along the z direction) the energy spectrum of the electron in the $Q1D$ channel can be written as[3]

$$E_{n,l}=\frac{\hbar^2k_x^2}{2m^*}+(n+1/2)\hbar\Omega+\Delta_l, \tag{1}$$

where k_x is the wave number along the x direction, the hybrid frequency $\Omega = (\omega_0^2 + \omega_c^2)^{1/2}$, and the effective mass is $m^* = m\Omega^2/\omega_0^2$. The electron wave function is given as

$$\Psi_{n,l,k_x}=\frac{1}{L_x^{1/2}}\exp(ik_xx)\varphi_n(y)\chi_l(z), \tag{2}$$

where

$$\varphi_n(y)=\frac{1}{(2^n n!\,\pi^{1/2}l_c^*)^{1/2}}\exp\left(-\frac{(y-Y)^2}{2(l_c^*)^2}\right)H_n\left(\frac{y-Y}{l_c^*}\right). \tag{3}$$

Here the effective magnetic length is $(l_c^*)^2 = \hbar/m\Omega$, and $Y=-\hbar\omega_c k_x/m\Omega^2$ is the y coordinate of the center of the electron orbit; $H_n(x)$ is the Hermite polynomial, and L_x is the size of the system along the x direction.

The energy spectrum $E_{n,l}(k_x,B)$ for electrons localized in the $Q1D$ channel reveals interesting peculiarities in the electron transport coefficients. Our aim in the present work is to calculate the electron mobility along the $Q1D$ channel in the presence of B and to analyze the applicability of the Boltzmann kinetic approach in the same manner as the authors performed in Refs. 4 and 5. To begin with, we derive the criteria for the applicability of this approach in the case of $Q1D$ electrons in magnetic fields. Here the equilibrium distribution function of the electron in the nth subband is approximated by the Boltzmann factor given by

$$f_{n,0}\propto\exp\left(-\frac{\hbar^2k_x^2}{2m^*T}-\frac{n\hbar\Omega}{T}\right). \tag{4}$$

Note, however, that in the presence of magnetic fields there are constraints to be imposed on k_x due to the structure of $\varphi_n(y)$ given by Eq. (2). The magnetic field mixes electron motions along the x and y directions and the y coordinate of the center of electron orbit depends explicitly on k_x. The electron which moves along the y axis can therefore escape at some values of k_x, from the region of the applicability of the parabolic confinement. This can modify significantly the conditions for the normalization of the distribution function $f_{n,0}(k_x)$ and for the wave function $\varphi_n(y)$ in comparison with the case of $B = 0$ considered in Refs. 4 and 5. To clarify this situation let us assume that the y coordinate of the electron satisfies the condition $|y| < L_y$, where L_y is the size of the system along the y axis. In order to make reliable the applicability of a parabolic-potential approximation for the elec-

tron confinement, which is suitable for $y \ll R$, L_y must satisfy the inequality $L_y \ll R$. The condition $|Y| < L_y$ must be also satisfied. We must therefore impose the upper bound $|k_x| < m\Omega^2 L_y/\hbar\omega_c$ in order to perform the k_x integration of the Boltzmann factor. However, only the values of k_x which satisfy $k_x^2 < k_T^2 = 2m^*T/\hbar^2$ contribute substantially and k_T plays the role of the maximum k_x in the integral of $f_{n,0}$. If k_T is significantly smaller than the upper bound of k_x, then that condition does not affect the integration of $f_{n,0}$ over k_x because the effective cutoff takes place at significantly lower wave numbers than the limiting value of k_x. The standard normalization of $f_{n,0}$ with infinite limits in the normalization integral is therefore valid if the condition $2m^*T/\hbar^2 \ll (m\Omega^2 L_y/\hbar\omega_c)^2$ is satisfied. By substituting the value of m^*, which appears in Eq. (1), this inequality can be easily transformed into

$$T \ll \hbar\Omega \left(\frac{\omega_0^2}{2\omega_c^2}\right)\left(\frac{L_y}{l_c^*}\right)^2. \tag{5}$$

Assuming that the above condition is satisfied, we can write the normalized $f_{n,0}(T)$ as

$$f_{n,0}(T) = \left(\frac{2\pi\hbar^2}{m^*TL_x^2}\right)^{1/2} \frac{1}{Z_n} \exp\left(-\frac{\hbar^2 k_x^2}{2m^*T} - \frac{n\hbar\Omega}{T}\right), \tag{6}$$

where

$$Z_n = \sum_{n=1}^{\infty} \exp\left(-\frac{n\hbar\Omega}{T}\right) = \frac{1}{2}\left[1 + \coth\left(\frac{\hbar\Omega}{2T}\right)\right].$$

The quantity L_y must be larger than the scale of the electron localization across the $Q1D$ channel, which is of the order of the effective magnetic length l_c^*. As shown in Ref. 3, l_c^* is always smaller than the scale of the electron localization $y_0 = (\hbar/m\omega_0)^{1/2}$ in the case of $B = 0$. For $y_0 \cong 10^{-6}$ cm (Ref. 4), the inequality $l_c^* < y_0 \ll R$ will than be well satisfied. This assures the validity of the approximation of a parabolic confinement potential along the y axis for $y \ll R$. For this reason, $L_y^2/(l_c^*)^2 \gg 1$.

Another problem stems from the normalization of $\varphi_n(y)$. Considering the conditions under which the finiteness of the system along the y axis (finite value of L_y) does not influence the integration, we see from Eq. (3) that the range of y, which is relevant to the integration of $(\varphi_n(y))^2$, is limited by the condition $|y - Y| \leqslant l_c^*$. Since $l_c^* \ll L_y$, the effective cutoff in the integral takes place at values of y significantly smaller than L_y if, in turn, the condition $|Y| \ll L_y$ is satisfied. This can be easily seen if the integrand is rewritten in terms of the variable $|y - Y|/l_c^*$, after which the dependence of the normalization integral on Y moves into the limits of the integration. As a result, lower and upper limits of the integral can be extended to $\pm\infty$. Assuming $Y(k_T) \leqslant l_c^* \ll L_y$, we obtain the inequality which is formally the same as Eq. (5) but without the large factor $L_y^2/(l_c^*)^2$ on the right-hand side. If the inequality

$$T < \frac{\hbar\Omega\omega_0^2}{2\omega_c^2} \tag{7}$$

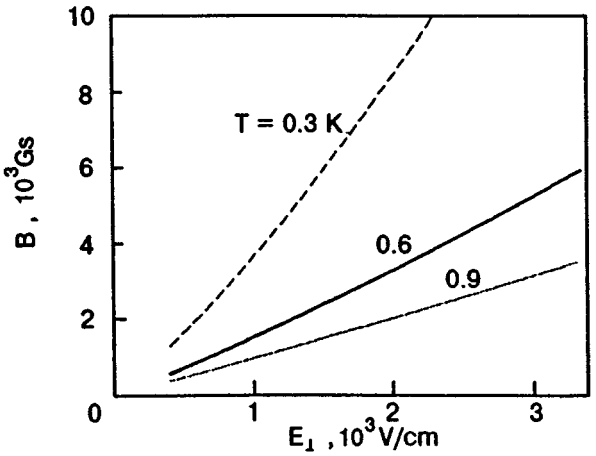

FIG. 1. Dependence of the magnetic field on the holding electric field $B(E_\perp)$, defined by the equation $\omega_c(B) = A\omega_0(E_\perp)$, for three temperatures. The curves show the region of the validity of the classical Boltzmann approach to the calculation of the electron mobility along the $Q1D$ channel, given by inequality (8).

is satisfied, then Eq. (5) is also satisfied and we obtain from Eq. (7) the following condition by substituting the expression of the hybrid frequency Ω:

$$\omega_c < A\omega_0, \tag{8}$$

where the coefficient A depends on the temperature and the frequency ω_0 as

$$A^2(T,\omega_0) = \frac{1}{8}\left(\frac{\hbar\omega_0}{T}\right)^2 \left\{1 + \left[1 + 16\left(\frac{\hbar\omega_0}{T}\right)^{-2}\right]^{1/2}\right\}. \tag{9}$$

The Eq. (8) should be satisfied in order to have reliable expressions of $\varphi_n(y)$ and $f_{n,0}$. The inequality (8) gives the estimate of the upper value of ω_c, and consequently of B, under which we can employ the usual Boltzmann transport equation, as developed in Refs. 4 and 5. Note that in $2D$ electron systems the transition from the quantum limit where $\omega_c \gg T/\hbar$ to the classical regime where $\omega_c \ll T/\hbar$ comes from the change in the occupation of the Landau levels with the temperature. In the $Q1D$ charged system with parabolic-potential confinement across the channel, limitations for the applicability of the standard classical approach given by the condition (8) are based on other grounds, i.e., due to the constraints imposed on the normalization procedure of the electron wave function and the Boltzmann distribution function. The inequality (8) relates the upper bound of the cyclotron frequency which is given not only as a function of the temperature, as in the $2D$ case, but also a function of the confinement frequency ω_0 across the channel.

The range of values of the magnetic field and the clamping electric field, which satisfies the condition $\omega_c < A\omega_0$ for the validity of the classical Boltzmann approach to the electron mobility, is shown in Fig. 1, where the coefficient A was evaluated for the curvature radius $R = 5 \cdot 10^{-4}$ cm. Note that for limited values of ω_c the separation $\hbar\Omega$ between the energy subbands is always larger than $\hbar\omega_0$ in the case $B = 0$. It was shown in Ref. 4, that $\hbar\omega_0$ is comparable to T for all reasonable values of holding electric fields. For this reason, the $Q1D$ electrons in the presence of a magnetic field still

form a multisubband system, and we must take into account all subbands in the calculations of the electron mobility.

We have calculated the electron mobility in the $Q1D$ channel in the single-particle approximation (SPA) and in the complete control approximation (CCA), where the influence of frequent two-electrons collisions is taken into account in the structure of the electron distribution function in the presence of a driving electric field $E_{\parallel}$ along the x axis. The procedure is straightforward and the formulas are quite similar to those in Ref. 4 with few replacements due to the introduction of Ω and m^*. The calculation gives the following expression for the electron mobility in the $Q1D$ system within SPA:

$$\mu(T,\Omega)=\frac{2e}{\sqrt{\pi}m^*Z_n(T,\Omega)}\left(\frac{\hbar\omega_0^2}{T\Omega}\right)^{3/2}\sum_{n=0}^{\infty}\times\exp\left(-\frac{n\hbar\Omega}{T}\right)\int_0^{\infty}\frac{\sqrt{x}e^{-\hbar\omega_0^2 x/\Omega T}dx}{\nu_{er}^{(n)}(x)+\nu_{eg}^{(n)}(x)}, \quad (10)$$

where $\nu_{er}^{(n)}(x)[\nu_{eg}^{(n)}(x)]$ is the collision frequency of an electron in the nth subband due to electron-riplon [electron-atom] scattering.

We assume in the complete control approximation (CCA) that the electron system can be characterized by a drift velocity u, when the frequency of electron-electron collisions is $\nu_{ee}^{(n)} \gg \nu_{er}^{(n)}, \nu_{eg}^{(n)}$. Under this regime, the electron momentum is efficiently redistributed between the carriers, which leads to a shifted distribution function.[6,7] The advantage of the CCA is that the kinetic equation can be used for the calculation of electron mobility in the case of strong enough electron-electron interaction without using an explicit form of such an interaction. The role of electron-electron collisions in the $Q1D$ system with a more complicated nature of the electron motion is not well established at this time. One can hope, however, that this approximation would display the main features of the electron mobility in the correlated $Q1D$ system in some range of the electron densities. Note that for $B=0$, the mobility calculated in CCA differs from the one-electron mobility, both qualitatively and quantitatively, since it is nearly three times smaller at $T<1$ K.[4,5] We also calculate the electron mobility in the CCA in the presence of B.

The results of numerical calculations of the magnetic field dependence $\mu(B)$ in SPA are plotted in Fig. 2 for $T=0.6$ K and for some values of the holding field $E_{\perp}$. As can be seen from Fig. 2, the $\mu(B)$ is a decreasing function of B at a low enough electric field $E_{\perp}$. With an increase in $E_{\perp}$, the mobility at the high electric field becomes insensitive to B. It is a consequence of the fact that, as we increase $E_{\perp}$, the frequency $\Omega=(\omega_c^2(B)+\omega_0^2(E_{\perp}))^{1/2}$ tends to ω_0 and $\mu(B)$ for fixed T becomes negligible and coincides with the mobility calculated for $B=0$. In the region where the inequality is satisfied one can estimate that B cannot exceed 1000 Gs, and the corrections to the mobility due to the magnetic field are significant for $E_{\perp}<500$ V/cm.

Figure 3 shown the temperature dependence of mobility $\mu(T)$ in SPA, calculated for two values of the magnetic field and for $B=0$. We see that $\mu(T)$ is qualitatively the same as

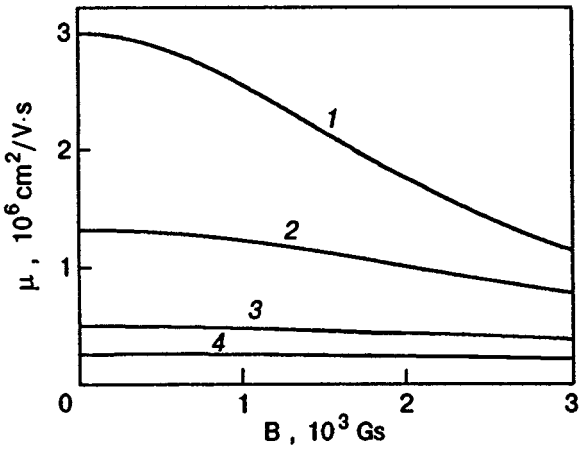

FIG. 2. Electron mobility slotted as a function of the magnetic field calculated in the one-electron approximation. The curves are numbered 1 through 4 corresponding to the clamping electric fields $E_{\perp}=500$ V/cm (*1*), 1000 V/cm (*2*), 2000 V/cm (*3*), and 3000 V/cm (*4*). The temperature is $T=0.6$ K.

in the case of $B=0$, even though the values of the mobilities become small with increasing $E_{\perp}$. At higher $E_{\perp}$, the difference in the curves $\mu(T)$, calculated for different B, becomes small for the same reason as that described before. We observe that maximum points appear in the curves of $\mu(T)$ for $T<0.2$ K. The reason for this nonmonotonic temperature dependence of the mobility and the maximum in $\mu(T)$ are discussed in detail in Ref. 4 for zero field.

The low-temperature expansion of Eq. (10) can be written as

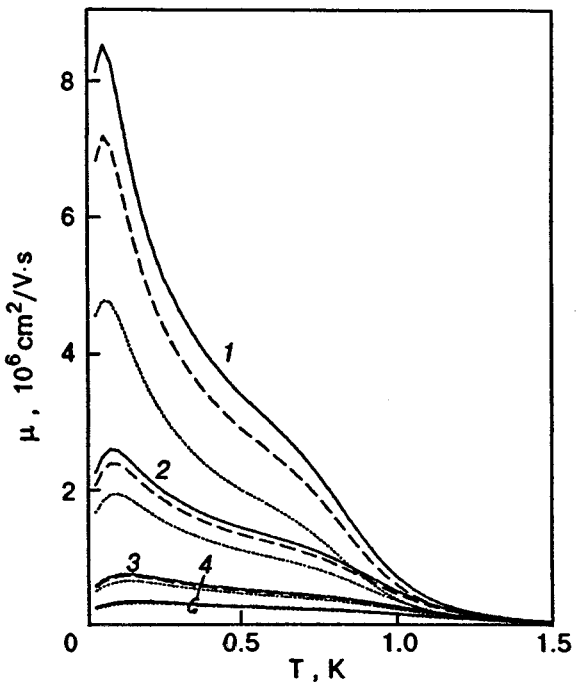

FIG. 3. Temperature dependence of the electron mobility for $B=0$ (solid line), $B=1000$ Gs (dashed line), and $B=2000$ Gs (dotted line) at $E_{\perp}=500$ V/cm (*1*), 1000 V/cm (*2*), 2000 V/cm (*3*), and 3000 V/cm (*4*).

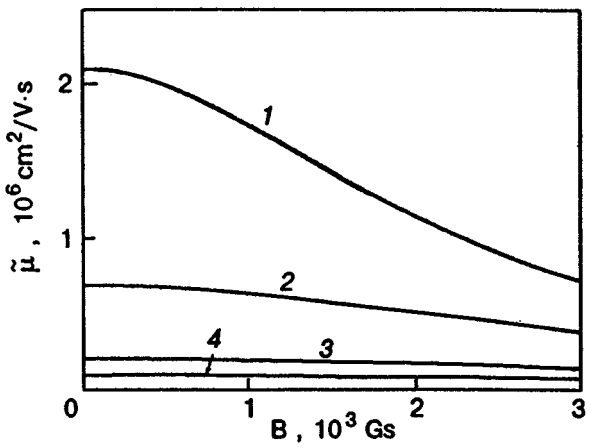

FIG. 4. The same as in Fig. 2 but in the complete control approximation.

$$\mu_0 = \mu_\perp \left[6\,\frac{\omega_0^2}{\Omega^2} + \frac{64}{\pi}\left(\frac{\omega_0^2 T}{\hbar\Omega^3}\right)^{1/2}\right], \tag{11}$$

where $\mu_\perp = \alpha\hbar/meE_\perp^2$ (α is the surface tension of liquid helium). This result explains the increase of $\mu(T)$ starting from zero until it reached the point where the contribution of the excited levels with $n > 0$ becomes dominant and leads to a decrease of $\mu(T)$ with increasing T. As one can see, increasing B causes both the mobility at $T = 0$ [the first term in Eq. (11)] and the temperature-dependent coefficient of the second term to become decreasing functions of Ω and, hence, of B. For this reason, for higher values of B, the mobilities $\mu(T)$ reach lower values and the peak becomes broader. Such a behavior of $\mu(T)$ is observed in Fig. 3.

In Figs. 4 and 5 we present our results for $\tilde{\mu}(B)$ and $\tilde{\mu}(T)$ in the CCA. As one can see, the curves $\tilde{\mu}(B)$ and $\tilde{\mu}(T)$ are qualitatively similar to those shown in Figs. 2 and 3 in the case of SPA. However, the values of $\tilde{\mu}$ are lower than those of $\mu(T)$ and for $T < 1$ K the values of $\tilde{\mu}(T)$ are nearly three times smaller than the values of $\mu(T)$ for a given B. The maximum on the $\tilde{\mu}(T)$ curve occurs at temperatures higher than those at which the maximum occurs on the $\mu(T)$ curve. The reasons for the maximum on $\tilde{\mu}(T)$ are the same as in SPA. The mobility in the CCA at a very low temperature is given by

$$\tilde{\mu}_0 = \mu_\perp \left[2\,\frac{\omega_0^2}{\Omega^2} + \frac{8}{\pi}\left(\frac{\omega_0^2 T}{\hbar\Omega^3}\right)^{1/2}\right]. \tag{12}$$

Equation (12) gives the lower limit of the mobility at $T = 0$ [the first term in Eq. (12)] for $\tilde{\mu}(T)$, which is three times smaller in comparison with the lower limit in SPA. The coefficient of the second term in Eq. (12) is eight times smaller than that in Eq. (11). As a result, the maxima in $\tilde{\mu}(T)$ are significantly smoother than in $\mu(T)$.

In conclusion, we have investigated theoretically the influence of a magnetic field on the mobility of electrons localized in a $Q1D$ channel on the liquid-helium surface. The dependence of the mobility on the magnetic field and temperature are calculated by using the classical Boltzmann approach in the framework of the usual SPA and by introducing the CCA, which takes into account the electron-electron interaction in an indirect way. The influence of the electron-electron interaction on the electron mobility seems to be more relevant in the $Q1D$ case due to the more restricted nature of the electron motion. We hope, however, that the CCA would make it possible to describe the electron mobility under certain conditions. According to the results obtained in this study and in those of Refs. 4 and 5, $\mu(T)$ in the $Q1D$ electron system in the complete control regime must differ both quantitatively and qualitatively from those conditions, under which the electron-electron interaction can be considered negligible. We should emphasize that the results obtained in our study can become invalid in the case of a sufficiently large magnetic field, for example, when the condition given by inequality (8) is not satisfied. In addition to the experimental studies,[2] the study of the electron mobility in a wide range of B and T is very desirable. The experimental evidence for the deviation of the calculated mobilities obtained by us allows us to confirm the region of B and T where the classical regime of electron system is reached.

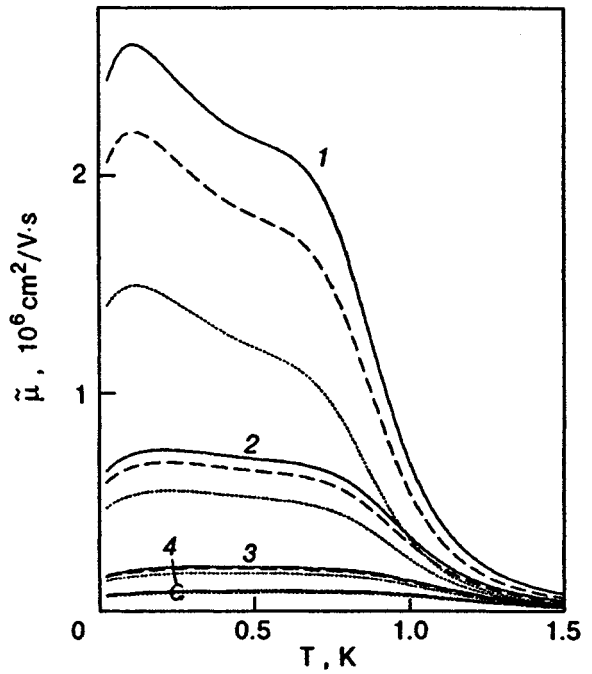

FIG. 5. The same as in Fig. 3 but in the complete control approximation.

This study was sponsored in part by the Fundacão de Amparo á Pesquisa do Estado de São Paulo (FAPESP) and the Conselho Nacional de Desenvolvimento Cientifico e Tecnológico (CNPq). One of us (S.S.S.) is grateful to FAPESP for financial support and to Yu. P. Monarkha for discussions of this subject. The other author (G.Q.H) thanks CNPq for financial support.

*E-mail: studart@power.ufscar.br

[1] V. B. Shikin and Yu. P. Monarkha, *Two-dimensional Charge Systems in Helium*, Nauka, Moscow (1989), p. 32.
[2] Yu. Z. Kovdrya and Yu. P. Monarkha, Fiz. Nizk. Temp. **12**, 1011 (1986); [Sov. J. Low Temp. Phys. **12**, 571 (1986)] D. Marty, J. Phys. **C19**, 6097 (1986); Yu. Z. Kovdrya and V. A. Nikolaenko, Fiz. Nizk. Temp. **18**, 1278 (1992) [Sov. J. Low Temp. Phys. **18**, 894 (1992)]; O. I. Kirlchek, Yu. P.

Monarkha, Yu. Z. Kovdrya, and V. N. Grigor'ev, Fiz. Nizk. Temp. **19**, 458 (1993) [Low Temp. Phys. **19**, 323 (1993)]; A. M. C. Walkering, P. K. H. Sommerfeld, P. J. Richardson, R. W. van der Heijden, and A. T. A. M. de Waele, Czech. J. Phys. 46, 321 (1996). Suppl. S1; Yu. Z. Kovdrya, V. A. Nikolaenko, and P. K. H. Sommerfeld, Czech, J. Phys. **46**, 347(1996), Suppl. S1; H. Yayama and A. Yomokiyo, Czech. J. Phys. **46**, 353 (1996), Suppl. S1.
[3] S. S. Sokolov and N. Studart, Phys. Rev. **B51**, 2640 (1995).
[4] S. S. Sokolov, G. Q. Hai, and N. Studart, Phys. Rev. **B51**, 5977 (1995).
[5] S. S. Sokolov, G. Q. Hai, and N. Studart, Phys. Rev. **B52**, 15509 (1995).
[6] F. G. Bass and Yu. G. Gurevich, *Hot Electrons and Strong Electromagnetic Waves in Semiconductor and Gas-Discharge Plasma*, Nauka, Moscow (1975).
[7] E. M. Conwell, *High Field Transport in Semiconductors*, Academic Press, New York (1967).

This article was published in English in the original Russian journal. It was edited by S. J. Amoretty.

Ultralow temperatures in a transport vessel: A dilution refrigerator to achieve 30 mK by continuous adsorption pumping

G. J. Batey, J. P. White, W. D. Duncan, A. F. Simpson, and V. A. Mikheev

*Oxford Instruments Scientific Research Division, Old Station Way, Eynsham, Witney, Oxon, OX8 1TL, England**

(Submitted November 18, 1996)
Fiz. Nizk. Temp. **23**, 655–658 (May–June 1997)

A novel design of dilution refrigerator (DR) is described for continuous operation inside a transport dewar with a neck diameter more than 51 mm. The time required for cooling the mixing chamber from room temperature to 30 mK is 3.5–4.5 h. Warming up to 300 K requires 0.5–1.0 h. The cooling power achieved is 40 at 100 mK. The DR is fitted with 6-mm line-of-sight access down to the mixing chamber. A distinguishing feature of this refrigerator is the absence of a conventional gas-handling system, which makes it easy to transport in a small car and quickly commission in a new laboratory within a few hours. © *1997 American Institute of Physics.* [S1063-777X(97)02105-1]

Many refrigerators which use the process of dilution of ^{3}He in ^{4}He to obtain ultralow temperatures have been designed in the last 30 years. The majority of them use a room-temperature ^{3}He circulation system, where one or more vacuum pumps pump ^{3}He from the still and return exhaust ^{3}He gas to condense in the insert. A modern DR has a reasonable cooling power, is typically supplied with more than 24 wires to the experimental region, often allows sample rotation and can be fitted with coaxial cables for high frequency signal pickup. All these features make it a very popular tool among physicists (and not only physicists).

It is worth emphasizing that up to now the majority of DR were made as stationary devices. Figure 1 shows an example block diagram of a typical dilution refrigerator from the popular Kelvinox family produced by Oxford Instruments. The main components of this type of standard DR (as shown in Fig. 1) is the refrigerator itself, a special dewar, a gas-handling system mounted in a frame, gas purification system including a cold trap and one or more vacuum pumps. Some of the pumps are required to be hermetically sealed for pumping ^{3}He. The development of an intelligent gas handling system (IGH in Fig. 1) provided with computer control, makes the life of the experimentalist much easier, because to operate the DR one should only fill the dewar with liquid ^{4}He and ''click'' on the cooldown button on the computer screen.

A few years ago the problem arose of how to quickly change the sample and cool it down to the millikelvin temperature range. This was solved by the top-loading design of DR[1] and more recently by the development of dilution refrigerators which are insertable directly into liquid helium (see, for example, Ref. 2). The further development of low-temperature physics of metals, semiconductors, and especially mesoscopics has created an interest in a portable dilution refrigerator, with a fast sample turnaround time.

This paper describes a novel dilution refrigerator, with a 50-mm diameter vacuum jacket, which allows it to be easily installed into the neck of the most common 100-liter helium transport dewars in Europe and worldwide. The general view of the DR is shown in Fig. 2. It is easy to see that it has no conventional gas-handling system. The only external connections are to the ^{3}He/^{4}He mixture dump and to the 1-K pot pump by two flexible lines. Only one rotary pump ($16\ m^3/h$) is used to pump the 1-K pot and the sorb heat exchangers. Special microprocessor-controlled electronics have been developed to monitor and control the operation of the refrigerator. Fully automated cooldown is possible, without the need for a computer. The operation of this DR is based on adsorption pumping by cold activated charcoal. This was first successfully realized by B. N. Eselson and his colleagues in the early 1960's for cooling liquid ^{4}He[3] and ^{3}He.[4] It is worth mentioning the growing popularity of this pumping method because of the high pumping speed, purity and absence of vibrations. Many papers have been published about using this method in the design of dilution refrigerators.[5–9]

The DR described here uses a cryogenic circulation cycle with a collector,[6] which was first realized at FTINT Kharkov.[7] Further testing of the cryogenic cycle dilution refrigerator was done in J. Saunders' group at Royal Holloway University of London (Great Britain). This proved the feasibility of this method down to below 10 mK.[10] This success convinced us to design a novel and very compact DR on this basis. All existing similar DR are fitted with external gas-handling systems (see, for example, Ref. 2 and Refs. 7–10). They also need large electronic systems for automatic control and for stable operation. It was necessary to reconsider many details of the cryogenic cycle in order to minimize the mass and size of the components, with the aim of arranging all the essential parts of the DR in the cold zone and avoiding a standard gas-handling system.

The design consists of a vacuum jacket with approximately 47-mm internal diameter. All the elements of the refrigerator are situated inside it, including the 1-K pot with a

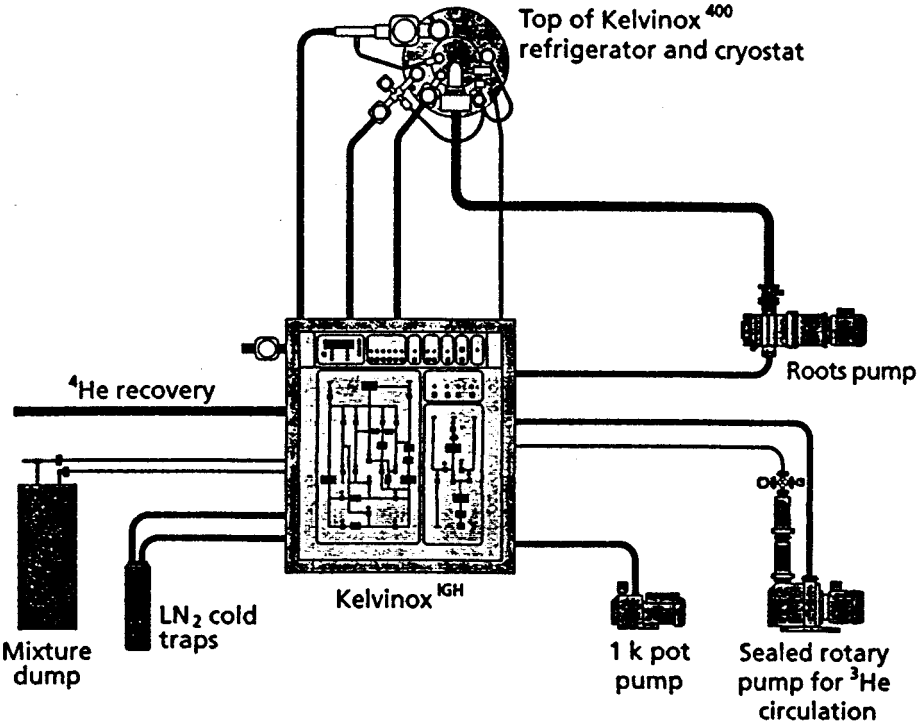

FIG. 1. Block diagram of a typical dilution refrigerator. As an example, the figure shows a Kelvinox 400 DR and its accessories.

collector, sorbs, still and mixing chamber (see Fig. 2). There is also a 6-mm line-of-sight access to the mixing chamber for experimental services. The refrigerator is fitted with a sliding seal to allow the insert to be loaded safely into the dewar. The total length of the DR from sliding seal down to the bottom of vacuum jacket is 1600 mm but it can easily be reduced to 1200 mm, which corresponds to the length of a typical transport dewar. To achieve more space in the vacuum jacket, the liquid ^{4}He supply to the 1-K pot and sorb heat exchangers enters through a tube at the bottom of the vacuum jacket with a filter and PTFE seal. This design allows us to avoid a standard cold flange with indium seal at 4.2 K and make a simple room-temperature clamp connection of the vacuum jacket at the top of the insert.

Development of the cryogenic cycle and the use of electronics for control helped us to simplify the gas-handling system and to eliminate almost all the valves and manometers. As a result, to warm up the refrigerator one only needs to pull the insert out from the dewar over approximately 30 min. The relief valves ensure that the expanding mixture is safely directed into the storage dump. To prepare the refrigerator for operation after loading it into the dewar, it is only necessary to open fully two relief valves and close them again when the mixture is sufficiently adsorbed from the dump into insert (by observing a pressure gauge on the mixture storage dump). Refrigerator operation can then be started by simply pressing a button on the electronics box. The electronics can control and monitor all of the key operating systems of the refrigerator. During operation more than ten parameters of DR can be recorded simultaneously, such as the temperatures of the sorbs and the liquid levels in the collector and still, using capacitance level gauges. Figure 3 shows typical diagnostic records for three parameters of DR-the temperature of the two sorbs and the level of liquid in the still. This picture has been taken at an early stage of the test. As can be seen, the level in the still was variable during the cycles, which was caused by some instability of 1-K pot operation at that time.

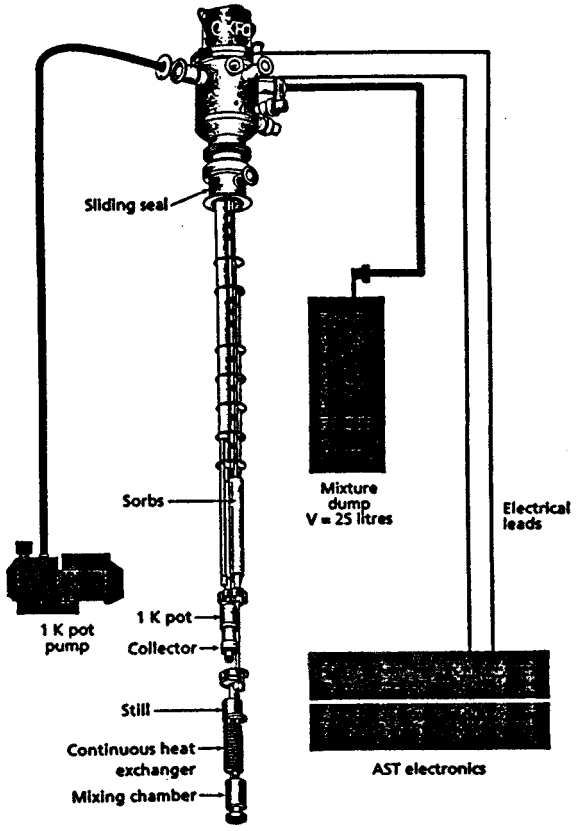

FIG. 2. General view of the new 50-mm dilution refrigerator for the transport dewar.

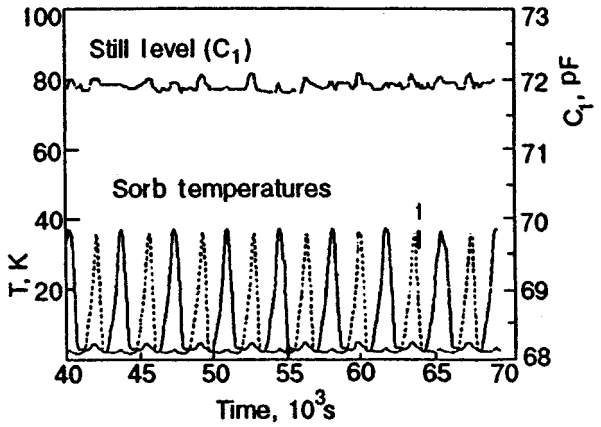

FIG. 3. An example of the diagnostic data recorded with the dilution refrigerator in continuous mode. The cycle time is approximately 30 minutes. The lower curves show the time evolution of sorb temperatures during the cycles. The upper curve shows the level in the still.

One of the remarkable features of the sorbtion pumped DR equipped with a collector is the ability to produce ''very long'' single-shot temperatures down to 10 mK without the use of silver step heat exchangers.[10] Figure 4 shows the capacitance data of a ^{3}He melting curve thermometer, fitted on the mixing chamber base during a cooldown and single shot. On part AB of the curve, one can see ordinary continuous cooling at a flow of approximately 70 micromole/sec from 250 mK down to 30 mK, in less than 1 h (B point). Between points B and C, all the ^{3}He was collected in the mixing chamber, which slightly increased the temperature to 45 mK. Further cooling to 18 mK was achieved by pumping the still with both sorbs and the flow rate between points D and E was 13 micromole/s. The ^{3}He was used at point E, when the refrigerator quickly warmed. Experimentally it takes 1 to 1.5 h to return to continuous operation from single-shot mode.

It is worth noting that the given result is similar to that described earlier in Ref. 10, and that it was achieved with a much smaller mixing chamber and total mixture volume. This can be very useful for quick tests of samples with short

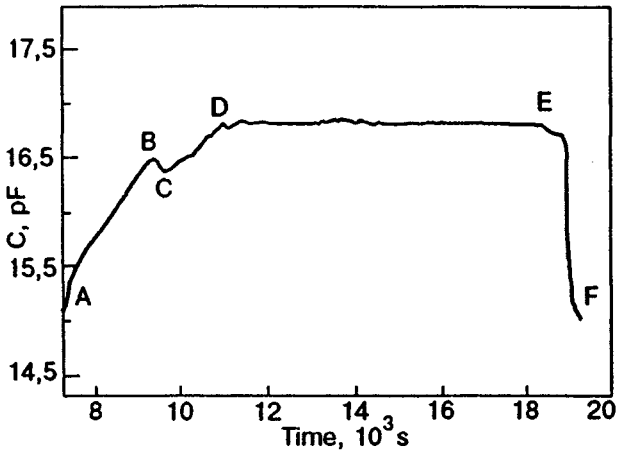

FIG. 4. The primary capacitance data of the ^{3}He melting curve thermometer, showing the typical cooling of the mixing chamber during single-shot operation. The temperature ranges from 250 mK (point A) to 18 mK (line DE).

measurement times down to below 15 mK. One can estimate the residual heat leak to the mixing chamber from single short results:[11]

$$Q_m = 84\, n_3 T_m^2, \tag{1}$$

where Q_m is the residual heat leak (watts), n_3 is the circulation rate (moles/s), and T_m is the lowest achieved temperature for given circulation rate (K). The residual heat leak to the mixing chamber of the new DR is about 0.3 μW from Eq. (1) and the measurements shown in Fig. 4. Because the lowest achievable temperature in single-shot mode is a function of the circulation rate, it is clear that the t_h length of single shots for two different temperatures and ^{3}He flows is given by the ratio

$$(T_1/T_2)^2 = n_3(T_2)/n_3(T_1) = t_h(T_1)/t_h(T_2). \tag{2}$$

Based on the data from Fig. 4 one can expect to get 14 mK for more than 1 h and 10 mK for about 30 min!

During continuous operation, the maximum circulation rate achieved was about 100 micromoles/s, with a cooling power of 40 μW at 100 mK. The continuous base temperature was below 30 mK and the still temperature was less than 0.75 K.

The test results of this dilution refrigerator, called ''Kelvinox AST Minisorb,'' allows us to draw the following conclusions:

—The portable dilution refrigerator, which has been developed for operation in a transport dewar, is convenient for a number of experiments. It has a 6-mm line-of-sight access port down to the mixing chamber. An experimental space 30-mm diameter and 80 mm long is provided. A total of 24 constantan wires for electrical measurements are fitted (with a similar quantity for the refrigerator diagnostics) and a few coaxial cables can be fitted for high-frequency measurements.

—The base temperature for continuous operation is below 30 mK. Cooling power at 100 mK exceeds 40 μW.

—The use of sorbtion pumping strongly increases the cooling power, which is normally achieved with such a dilution unit, reduces the vibration levels on the insert, and completely eliminates the possibility of blockages.

—The single-shot operation demonstrates the ability of the DR to maintain temperatures below 20 mK for a reasonably long time.

—The dilution refrigerator and mixture dump can be easily demounted with the help of a portable cryogenic pump. As a result, this type of dilution refrigerator can be accommodated inside the boot of a small car and transported to any other cryogenic laboratory. Since the commissioning of the refrigerator takes only a few hours, research can be quickly started in a new location.

The authors are very grateful to A. Adams and T. Janaway for the incredible efforts and skills they displayed during the construction and testing of this refrigerator.

*E-mail: vladimir.mikheev@oxinst.co.uk

[1] P. H. P. Reinders, M. Springford, P. Hilton, N. Kerley, and N. Killoran, Cryogenics, **27**, 689 (1987).
[2] J. P. Pekola and J. P. Kalippinen, Cryogenics **34**, 843 (1994).
[3] B. N. Eselson, B. G. Lazarev, and A. D. Shvets, Pribori I Tekhnika Experimenta (Russian) No. 5, 160 (1961).
[4] B. N. Eselson, A. D. Shvets, and N. G. Bereznyak, Pribori I Tekhnika Experimenta (Russian) No. 6, 123 (1961).
[5] V. S. Edel'man, Cryogenics **12**, 385 (1972).
[6] V. A. Mikheev, Author's Certificate of Invention No. 1103055, USSR, 1984.
[7] V. A. Mikheev, V. A. Maidanov, and N. P. Mikhin Cryogenics **24**, 190 (1984).
[8] V. M. Bunkov, D. A. Sergatskov, J. Nyeki, and I. N. Ivoilov, *Dilution Refrigerator with Internal Cryogenic ^{3}He Cycle*, in *Quantum Fluids and Solids-1989*, edited by G. G. Ihas and Y. Takano, AIP Conference Proceedings No. 194, AIP, New York, 1989, p. 397.
[9] V. E. Sivokon, V. V. Dotsenko, L. A. Pogorelov, and V. I. Sobolev, Cryogenics **32**, 207 (1992).
[10] V. A. Maidanov, N. P. Mikhin, N. F. Omelaenko, E. Ya. Rudavskii, A. S. Rybalko, V. K. Chagovets, V. A. Mikheev, P. Mohandas, B. P. Cowan, and J. Saunders, Fiz. Nizk. Temp. (in Russian) **20**, 672 (1994).
[11] O. V. Lounasmaa, *Experimental Principles and Methods Below 1 K*, Academic Press, NY, (1977).

This article was published in English in the original Russian journal. It was edited by S. J. Amoretty.